SUTMILL 99

MILLIMETRE WAVE REMOTE SENSING OF THE ATMOSPHERE

by

ROBERT ANDREW SUTTIE

Submitted for the Degree of Doctor of Philosophy

at Heriot-Watt University, Edinburgh

Department of Physics

March 1991

LIST OF CONTENTS

ACKNOWLEDGEMENTS

The work in this thesis was part of two programmes of development and testing in which many people were involved. In particular I have been working closely with Dr. G.E. Peckham and am indebted to him for his invaluable help throughout both projects.

In connection with the millimetre wave transmissometer project, which forms the main part of this thesis, I would like to thank Chris Gatley for his assistance in the atmospheric transmission and Dr. D.A. Flower for his helpful discussions and comments on the instrument. The theory of oxygen absorption in Chapter 2 is that used by all the pressure sounder projects.

There were many people involved in the Microwave Limb Sounder (MLS) project discussed in Chapter 8. I would like to thank my colleagues at the Jet Propulsion Laboratory, California for their close collaboration. I would especially like to thank Dr. J.W. Waters without whom the project would not have taken place. My thanks to my U.K. colleagues at Rutherford Appleton Laboratory and Edinburgh University for their wholehearted involvement in the MLS project and Dr. P.D. Curtis who was instrumental in setting up the project in the U.K.

I would like to thank Professors S.D. Smith and C.R. Pidgeon, in their capacity as Head and Acting Head of Department, for allowing me the use of Departmental facilities. Thanks are also due to Janice McClelland for her help and efficient typing, Sherron Gilroy for her preparation of some of the diagrams and the technical staff of the Physics Department for their assistance, especially in manufacturing parts for the satellite instrument.

I am also indebted to the SERC for their support during these projects.

ABSTRACT

Recent advances in millimetre wave technology has opened up a new region of the spectrum to remote sensing from artificial satellites. The main part of this work involves a millimetre wave proving experiment for a satellite borne millimetre wave active sounder to measure surface pressure over the oceans. The Microwave Pressure Sounder is a 6 channel, low power radar operating in the spectral range from 24 to 75 GHz. The strength of the return echoes from the sea surface determines the amount of oxygen in the path which can be directly related to the surface pressure to an accuracy of 1 mb, when corrected for sea surface reflectivity and atmospheric temperature and water content by this multichannel instrument. Measurements of atmospheric attenuation along a horizontal path were related to atmospheric pressure changes by a millimetre wave instrument built at Heriot-Watt University. The transmissometer measured the differential absorption between two frequencies (54 and 58 GHz) over a 650 metre path. The deduced atmospheric pressure was found to compare with the barometric pressure with a standard deviation of two millibars for the best data set. These results demonstrate that atmospheric attenuation can be measured with sufficient precision for a satellite borne instrument to determine the surface atmospheric pressure over the oceans to an accuracy of approximately one millibar. This accuracy would lead to significant improvements in the modelling of the atmosphere and weather forecasting. Various other techniques to remotely sense surface atmospheric pressure are reviewed.

Recently, increased awareness of the sensitivity of the environment and evidence of the effects of man-made pollutants has given rise to an increased awareness in the health of the Earth and led to several instruments being developed to monitor our planet. One of these instruments, the Microwave Limb Sounder to be flown on the Upper Atmosphere Research Satellite (launch October 1991) is described. This instrument uses millimetre wave radiometers at 63 GHz, 183 GHz and 205 GHz to measure the amount of chlorine oxide, ozone and water vapour in the upper atmosphere. These gases

are important in understanding the photochemistry of the mesosphere. Global distributions of the gases will be produced and changes in concentration will be monitored during the three year mission.

CHAPTER 1

INTRODUCTION

Remote sensing of the atmosphere is a rapidly expanding subject. In recent times, concern over the health of the Earth and our environment has become much more prominent. This has resulted in an ever increasing pressure to understand and monitor the Earth's atmosphere, especially the short and long term effects of various industrial pollutants.

Barrett and Curtis [ref. 1.1] defined remote sensing as "the observation of a target by a device separated from it by some distance". Many instruments can be included in such a definition, the camera is an example which most people understand and has been in use for remote sensing from aircraft for some considerable time. The definition of remote sensing by Barrett and Curtis is too broad and could include reading a thermometer at a short distance, but not while holding the thermometer. The more modern definition of remote sensing is the acquisition of data about objects or materials on the Earth's surface or in the atmosphere by instruments mounted on platforms some distance away (e.g. satellite, balloon or aircraft platforms). Most of these instruments make measurements of the interaction of the desired material or object with electromagnetic radiation. Remote sensing can take place from surface instruments and may use other than electromagnetic radiation, e.g. acoustic waves.

The use of satellites as platforms for remote sensing of the Earth has increased dramatically since the launch on October 4th 1957 of the first artificial Earth satellite. The present ability to launch large platforms has increased the possible complexity of the instruments in remote sensing applications. These satellite borne instruments provide global coverage in a short period of time. Polar orbiting instruments give complete

global coverage from altitudes of 500-700 km while geostationary instruments allow an instrument to observe a specific point on the globe for a long period but from an altitude of 34,000 km.

Remote sensing from artificial satellites started with images from primitive visible wavelength sensors. The 1960's saw significant developments in weather satellites, especially TIROS series of satellites. Weather pictures are now produced by geostationary satellites, such as Meteosat, as well as from polar orbiting instruments. Infrared images are used with visible images in, for example, the Multispectral Scanner on the Landsat (first launched 1972) series of satellites in the application of remote sensing to geology, agriculture, hydrology, cartography and oceanography. Cosmos (launched 1968) was the first satellite to use microwave techniques to remotely sense the water vapour and liquid water constant of the atmosphere. The advantage of the microwave sensors is in their ability to sense surface and atmospheric features through clouds. Microwave, infrared and visible sensors are extensively used in satellite instruments.

Improvements in semiconductor devices have now made millimetre wave instruments a viable option for satellite borne remote sensing experiments. The main advances, which have made this possible, have been in the fabrication of flight quality millimetre wave mixers, gunn oscillators with sufficient output power for mixer local oscillators, or to drive multiplier chains to generate mixer local oscillator power, and IMPATTS which can provide the required output power for active instruments.

The millimetre wave portion of the spectrum is very useful for remote sensing applications. The spectral features due to gaseous absorption are more widely spaced compared to infrared wavelengths which allow spectrally interference free measurements of a molecular absorption or emission spectra. Millimetre waves also offer good penetration of the clouds which normally render infrared measurements of the Earth's surface impossible.

The measurement techniques available for millimetre remote sensing are similar to other electromagnetic instruments. Measurement of the Earth's atmosphere or surface relies on either scattered, reflected, transmitted or emitted electromagnetic radiation. Passive instruments (radiometers) respond to emissions from the material being measured or to reflected or transmitted radiation from external sources, normally the Sun. Active instruments (radars, scatterometers) provide their own source of radiation which is reflected or scattered back to the detectors. The received signals are then analysed for their spectral, spatial and temporal properties [refs. 1.2, 1.3].

As mentioned earlier, there are many instruments measuring atmospheric parameters related to weather forecasting, but the one major omission is the measurement of surface atmospheric pressure especially over the oceans. Pressure measurements are fundamental to the prediction of future weather and in atmospheric modelling. There are sufficient measurements of surface atmospheric pressure over most of the land surface of the Earth but very few over the oceans. Measurements over oceans would substantially improve the modelling of the atmosphere and so improve the accuracy of weather forecasts. The improvement in millimetre wave technology has made possible a sounding technique to measure surface pressure over the oceans. The principle of operation was first proposed by Smith et al. [ref. 1.4] and later, a more detailed description of a possible instrument was published by Flower and Peckham [ref. 1.5].

The instrument is an active millimetre wave system in which six frequencies in the wings of the oxygen absorption band centred at 5 mm wavelength are transmitted from a satellite to the sea surface and measurement of the amplitude of the reflected radiation gives the attenuation in the path. By using frequencies in the wings of the oxygen absorption band a measure of the amount of oxygen in the vertical column in the sub satellite track is obtained, i.e. a nadir sounding instrument. The proportion of oxygen in dry air is a constant. Making attenuation measurements at six frequencies also allows the water vapour in the vertical column to be found, hence an estimate of the total

atmospheric pressure can then be obtained. The technique is more fully explained in Chapter 7 in a discussion of remote sensing techniques and their limitations in the measurement of surface atmospheric pressure by satellite borne instruments.

Three experiments have been conducted as proof of concept for a millimetre wave instrument to measure surface pressure. These were all two channel instruments measuring the differential absorption between two transmitted frequencies. This reduced number of channels was used to make attenuation measurements with the required precision to demonstrate the relationship between attenuation and atmospheric pressure. Because of the reduced number of channels, independent observations of atmospheric pressure, temperature and humidity were required to check the accuracy of computer models of attenuation used to optimise the satellite instrument. The six channel instrument requires no measurements from other instruments [ref. 1.6]. The three experiments were

a) An aircraft system, built at Jet Propulsion Laboratory, California, and funded by NASA. This is a two channel system in a configuration that could be implemented for a satellite system. Measurements were made over various sea conditions.

b) A ground based instrument measuring the differential attenuation through the atmosphere with the Sun as a millimetre wave source. This experiment was built by Appleton Laboratory (now part of Rutherford Appleton Laboratory) and funded by the Science and Engineering Research Council (SERC).

c) A ground based horizontal path transmissometer, this instrument measures the changes in attenuation with pressure, temperature and humidity over a fixed 650 m horizontal path at Heriot-Watt University Campus. This work was supported by the SERC.

The theory of absorption of millimetre waves in the region of the oxygen absorption band centred at 60 GHz is described in Chapter 2. A computer program, written to calculate the sensitivity of the atmospheric attenuation with respect to atmospheric

pressure, temperature and humidity is described in Chapter 3. The computer data were used to choose the best operating frequencies for the transmissometer and for the comparison of theoretical and experimental attenuations.

Details of the transmissometer instrument are given in Chapter 4. The results from several data sets are discussed in Chapter 5, along with the possible random and systematic errors. Chapter 6 summarises the horizontal path experiment and concludes the work on the transmissometer. Chapter 7 contains a discussion on remote sensing instruments which have been proposed to measure surface atmospheric pressure over the oceans, along with the problems and limitations of these measurement systems.

Also included in this thesis, in Chapter 8, is a description of a millimetre radiometer instrument for remote sensing of ozone, chlorine monoxide and water vapour in the upper atmosphere by a limb sounding technique. The instrument is called the "Microwave Limb Sounder" (MLS) and has three radiometers with local oscillator frequencies of 63 GHz, 183 GHz and 205 GHz. The project is a collaboration between the Jet Propulsion Laboratory (JPL), California, and the U.K. group of Heriot-Watt University, Rutherford Appleton Laboratory and the University of Edinburgh. The JPL part of the project is funded by NASA and the U.K. portion by the SERC.

The MLS measures atmospheric thermal emissions from ozone, chlorine oxide and water vapour at millimetre wavelengths. The intensity and spectral characteristics of these emissions as the field of view of the instrument scans vertically through the limb of the atmosphere allow the geophysical parameters to be inferred. Measurements can be made of the diurnal, spatial and temporal variations of the above gases which are important in the photochemistry of the upper atmosphere. The MLS is due for launch on the Upper Atmosphere Research Satellite in October 1991.

References

[1.1] Barrett, E.C. and Curtis, L.F., "*Introduction to environmental remote sensing*", Chapman and Hall, 1976.

[1.2] Elachi, C., "*Introduction to the physics and techniques of remote sensing*", John Wiley, New York, 1987.

[1.3] Houghton, J.T., Taylor, F.W. and Rodgers, C.D., "*Remote sounding of atmospheres*", Cambridge University Press, Cambridge, 1984.

[1.4] Smith, S.D., Colles, M.J. and Peckham, G.E., "The measurement of surface pressure from a satellite", Quart. J. Roy. Met Soc., No. 98, pp. 431-433, 1972.

[1.5] Flower, D.A. and Peckham, G.E., "A microwave pressure sounder", NASA/JPL Publication 78-68, NASA CR 157-567, 1978.

[1.6] Peckham, G.E., Gatley, C. and Flower, D.A., "Optimising a remote sensing instrument to measure atmospheric surface pressure", Int. J. Remote Sensing, 4, pp. 465-478, 1983.

[1.7] Ulaby, F.T., Moore, R.K. and Fung, A.K., *Microwave Remote Sensing Fundamentals and Radiometry*, Vols. I, II and III, Artech House, Dedhorn, MA, 1981.

CHAPTER 2

MILLIMETRE WAVE ABSORPTION IN THE ATMOSPHERE

The propagation of millimetre waves in the atmosphere is influenced by many features. The main effects are due to oxygen absorption, water vapour absorption, refraction, scintillation and scattering by hydrometeors. The attenuation due to oxygen and water vapour are the most significant features in the measurements undertaken here.

The composition of the air is well known. The most notable features in this context are that oxygen is a stable proportion of dry air, while the concentration of water vapour can vary by relatively large amounts. To be able to determine the attenuation by these gases a detailed knowledge of the absorption coefficients as a function of frequency, pressure, temperature and water vapour density is required.

2.1 Oxygen Absorption

The fundamentals of oxygen absorption were discussed quantitatively in a classic paper by J.H. Van Vleck in 1947 [ref. 2.1]. The paper describes the basic characteristics of molecular oxygen in its ground state. The symmetric diatomic molecule, O_2, is unique in having a microwave spectrum under normal conditions. The oxygen molecule differs from other symmetric diatomic molecules in that it has two unpaired electrons with parallel spin in the ground state. Consequently, the molecule has a permanent magnetic dipole moment which can couple with microwave radiation giving rise to absorption. Most gases interact with microwave/millimetre wave radiation through electric dipole/electric field coupling.

The oxygen molecule rotational states can be calculated if the total angular momentum number is J, and S is the total spin quantum and if N is the quantum number corresponding to end over end rotation of the molecule, then J may take only the values:

$$J = N+S, N+S-1, \ldots, N-S \qquad N = 0, 1, 2, \ldots$$

In the case of parallel spins, S = 1, there exists a triplet state, i.e. for each value of N there are three values of J.

$$J = N+1, N, N-1$$

The observed microwave transitions are governed by the selection rules:

$$\Delta J = \pm 1 \quad \text{and} \quad \Delta N = 0$$

This results in a group of closely spaced absorption lines around 60 GHz (5 mm wavelength) and an isolated line at ~ 118 GHz.

The absorption of energy occurs when the spin magnetic moment alters its orientation by interaction with the magnetic vector of the microwave radiation. The rotational momentum vector remains unchanged. These transitions are often described as a "spin reorientation spectrum".

The relative intensities of the individual lines vary considerably over the spectrum. The intensity of any particular line is dependent upon the probability of a transition taking place within a particular rotational energy level and on the population of that rotational energy level.

To a first approximation all transitions are equally probable, independent of the energy level. The relative intensities can be attributed only to differing populations. There are two factors governing the population levels, firstly the Boltzmann distribution:

$$P_N \propto \exp\left(-\frac{E_N}{kT}\right)$$

where E_N is the energy level for a specific rotational quantum number N, k is Boltzmann's constant and T is the absolute temperature. Secondly, a degeneracy of (2N + 1) from angular momentum considerations. Hence:

$$P_N \propto (2N+1)\exp\left(-\frac{E_N}{kT}\right)$$

Calculations of atmospheric absorption for millimetre propagation requires expressions of absorption coefficient due to oxygen as a function of frequency, temperature, pressure and water vapour density.

Attempts have been made to produce satisfactory expressions by summing lineshapes derived from isolated lines. The ratio of linewidth/pressure, constant for an isolated line, was reduced with increasing pressure to fit measurements of total absorption, especially in the band wings. Meeks and Lilley [ref. 2.2] were among many authors who used the lineshapes by Van Vleck-Weisskopf [ref. 2.3]. Also, Reber [ref. 2.4] used lineshapes by Gross [ref. 2.5] and Zhevakin and Naumov [ref. 2.6]. Their techniques were inadequate because the fit was ad hoc, giving rise to large discrepancies in other regions of frequency-pressure-temperature space.

Further developments in oxygen absorption through a theory of bands and overlapping lines were made notably by Beranger [ref. 2.7], Kolb and Griem [ref. 2.8] and Gordon [refs. 2.9,2.10]. This involves the formulisation of a collision cross-section matrix that determines the interference of lines and the result is also dependent on temperature. Computations of overlapping lines exist from Dillon and Godfrey [ref. 2.11] and Mingelgrin [ref. 2.12]. The complexity of their computations prevented their application to practical problems related to atmospheric attenuation.

Rosenkranz in 1975 [ref. 2.13] produced a much more manageable expression for attenuation due to oxygen,

$$\gamma(\nu) = CP\left(\frac{\nu}{T}\right)^2 F(\nu) \qquad (2.1)$$

where T is temperature in degrees K, P is pressure in mb, ν is frequency in GHz, C is a constant equal to 0.33 for γ in Np/km or 1.434 for γ in dB/km. The function $F(\nu)$ is the lineshape factor and, together with ν^2, describes the spectral intensity distribution. Rosenkranz, by taking the first order pressure approximation to the impact theory of overlapping lines, and by using a weak coupling approximation which reduces the interaction matrix, arrived at the following expression for the line shape:

$$F(\nu) = p\left\{\sum_N \theta_N \left[f_N^+(\nu) + f_N^+(-\nu) + f_N^-(\nu) + f_N^-(-\nu)\right] + \frac{0.70 w_b}{\nu^2 + (p w_b)^2}\right\} \tag{2.2}$$

where

$$f_N^{\pm}(\nu) = \frac{w_N (d_N^{\pm})^2 + (\nu - \nu_N^{\pm})\, y_N^{\pm}}{(\nu - \nu_N^{\pm})^2 + (p w_N)^2} \tag{2.3}$$

The summation is over a set of lines at both positive and negative frequencies with lineshapes of approximately Lorentzian form modified by the interference coefficients $y_N^{\pm}$. The final term in equation (2.2) is the contribution from merging the zero frequency lines where ω_b is the non-resonant linewidth.

θ_N is the population factor and given by

$$\theta_N = \frac{2N+1}{0.725T} \exp\left(-2.0685\, N(N+1)\, T\right) \tag{2.4}$$

and the line amplitudes $d_N^{\pm}$ are

$$d_N^+ = \left[\frac{N(2N+3)}{(N+1)(2N+1)}\right]^{1/2} \tag{2.5}$$

$$d_N^- = \left[\frac{(N+1)(2N-1)}{N(2N+1)}\right]^{1/2} \tag{2.6}$$

The interference coefficients $y_n^{\pm}$ are given by:

$$y_N^{\pm} = d_N^{\pm}\left[\frac{2 d_{N+2}^{\pm} w_N^{\uparrow}}{\nu_N^{\pm} - \nu_{N+2}^{\pm}} + \frac{2 d_{N-2}^{\pm} w_N^{\downarrow}}{\nu_N^{\pm} - \nu_{N-2}^{\pm}} - \frac{w_b}{\nu_N^{\pm}} - \frac{w_b}{\nu_N^{\pm} + 60}\right] \tag{2.7}$$

$w_N^{\uparrow}$ and $w_N^{\downarrow}$ are the near-diagonal elements of the interaction matrix. The weak coupling approximation allows each positive frequency line to couple to the two adjacent lines in the same branch, to the line at zero frequency and to its corresponding negative frequency lines. $w_N^{\uparrow}$ and $w_N^{\downarrow}$ can be related by two equations. The first arises due to the probability of conversion and states that the elements in any column of the w matrix must sum to zero.

$$w_N^{\downarrow} = w_b - w_N - w_N^{\uparrow} \tag{2.8}$$

where w_b is the non-resonant linewidth.

The second is due to the fact that the product $w_N \theta_N$ is symmetric, i.e.:

$$w_{N-2}^{\uparrow} = w_N^{\downarrow} \frac{\theta_N}{\theta_{N-2}} \tag{2.9}$$

Equation (2.9) is exact, but (2.8) involves weak coupling assumptions and is therefore only approximate. The evaluation of these elements was initiated by setting

$$w_{39}^{\uparrow} = 0 \tag{2.10}$$

The arbitrary cut-off at N = 39 introduces a large error in the interference coefficient for large N but this is insignificant as these are weak lines and the error is progressively damped by application of equations (2.8) and (2.9).

The experimentally derived values of frequency, $\nu_N^{\pm}$ and linewidths $w_N^{\pm}$, are given in Table 2.1. These values were used to compute the millimetre spectrum of oxygen. The non-resonant linewidth is given a value of

$$w_b = 0.48 \left(\frac{300}{T}\right)^{0.89} \text{ MHz mb}^{-1} \tag{2.11}$$

which is the average of measurements made by Kaughman [ref. 2.14] and Maryott and Birnbaum [ref. 2.15]. The theory provided by Rosenkranz was an improvement in fit compared with Reber [ref. 2.4], who had produced the best fit, especially with respect to absorption in the wings of the bands. Birnbaum [ref. 2.14] has produced a further refinement of the collision broadening, again improving the fit away from the absorption bands.

Liebe [refs. 2.17-2.20] has made a significant attempt to reduce the errors between theory and experiment. Liebe gives a formula for reduced broadening due to O_2-N_2 collisions compared to O_2-O_2 collisions and a linewidth contribution due to water vapour as:

Table 2.1. Frequencies and Linewidth of the Oxygen Millimetre Wave Spectrum

N	Frequencies, GHz		Linewidths, MHz mb^{-1}	
	ν^+_N	ν^-_N	$w^+_N(300)$	$w^-_N(300)$
1	56.2648	118.7503	1.66	1.61
3	58.4466	62.4863	1.47	1.49
5	59.5910	60.3060	1.39	1.42
7	60.4348	59.1642	1.34	1.36
9	61.1506	58.3239	1.30	1.32
11	61.8002	57.6125	1.27	1.29
13	62.4112	56.9682	1.24	1.25
15	62.9980	56.3634	1.22	1.23
17	63.5685	55.7838	1.20	1.20
19	64.1278	55.2214	1.18	1.18
21	64.6789	54.6712	1.16	1.16
23	65.2241	54.1300	1.13	1.13
25	65.7647	53.5957	1.12	1.12
27	66.3021	53.0668	1.10	1.10
29	66.8368	52.5422	1.08	1.08
31	67.3695	52.0212	1.06	1.06
33	67.9007	51.5030	1.04	1.04
35	68.4308	50.9873	1.02	1.02
37	68.9601	50.4736	1.00	1.00
39	69.4887	49.9618	0.98	0.98

$$w_N = w_N(300)\left[m\left(\frac{300}{T}\right)^{0.9} + m_w \beta\left(\frac{300}{T}\right)\right] \text{MHz mb}^{-1} \qquad (2.12)$$

where $w_N(300)$ is the measured linewidth at 300 K and the nitrogen gas broadening coefficient, m, has a value of 0.929 for dry air. The second term accounts for the water vapour effects through the mass mixing ratio β and the coefficient m_w which has a value of 0.52.

The preceeding equations allow the attenuation to be calculated with a reasonable amount of computer time, for changes in pressure, temperature and humidity of the atmosphere.

2.2 Water Vapour Absorption

Water vapour is the major deterrent to propagation of infrared frequencies and to a lesser extent for millimetre and microwave frequencies. The estimation of absorption by water vapour in the atmosphere is considerably more difficult than the estimation of absorption by oxygen. The amount of water vapour in the air varies with time along the length of long propagation paths.

The microwave spectrum of water vapour is caused by electric dipole transitions between rotational states of the molecule as described by Van Vleck [ref. 2.21]. Water vapour is a nonlinear asymmetric molecule which means that no two of its three principal moments of inertia are equal. Rotational spectral lines of water vapour are distributed from microwave through far infrared frequencies. The spectrum has been extensively measured and studied, the most notable papers are by Burch [ref. 2.22] and Liebe [ref. 2.23].

The lines of particular interest here are those at 22, 68 and 183 GHz, though the many lines at higher frequencies contribute to a continuum background in the millimetre wave region. Many lineshapes have been used to obtain a fit to experimental data but they all fail to account for the absorption in the wings of absorption lines. Waters [ref. 2.24] shows that for frequencies below 100 GHz the discrepancies can be satisfactorily

accounted for by grouping together in a single term the contributions from lines other than 22 GHz and including an empirical correction. The absorption coefficient in dB/km is given by:

$$\gamma_w(\nu) = \frac{\rho \nu^2 \Delta\nu}{T^{3/2}} \left\{ \frac{3.12 \times 10^6}{T} \frac{\exp(-644/T)}{(22.235^2 - \nu^2)^2 + 4\nu^2\Delta\nu^2} + 0.012 \right\} \qquad (2.13)$$

where the linewidth in GHz is

$$\Delta\nu = 2.96 \left(\frac{p}{1013}\right) \left(\frac{300}{T}\right)^{0.626} \left(1 + 0.018 \frac{\rho T}{p}\right) \qquad (2.14)$$

where ρ is water vapour density in gm^{-3}. These equations allow the computation of atmospheric coefficient for values of p, T, ρ and ν. Many ad hoc formula are available to allow calculation of atmospheric transmission.

The values obtained agree within 5% of measured values of this difficult gas. Many measurements have been made of water vapour attenuation, mostly using non-resonant chambers. The anomalously high absorption away from line centres obtained by many workers has no satisfactory theoretical basis. The water polymer $(H_2O)_n$ hypothesis has the inherent weakness that, except for dimers $(H_2O)_2$ no other forms have been observed. The probability of dimer formation in natural atmospheric environments is very low and would appear to be insignificant in the estimation of the water vapour absorption. The only redemption for a contribution from dimers is that the absorption has the correct temperature dependence, Bohlander et al., [ref. 2.25], Harris and Ade [ref. 2.26].

The other contender for the extra water vapour attenuation is the uptake of water vapour by submicron aerosol particles with diameter < 1 μm c.f. fog and haze diameter > 1 μm. These are much smaller particles than found in fog, haze or cloud but they do have a large probability of existence compared with dimers, Carlon and Harden [ref. 2.27]. Insufficient measurements have been reported at this time to consider the effectiveness of the submicron aerosol theory to extra water vapour attenuation.

There is still a large amount of research required before a full understanding of water vapour absorption can be obtained.

2.3 Other Gaseous Constituents of the Air

The atmosphere contains many other gases but none of these occur in sufficient concentration to have a detectable influence on atmospheric attenuation in the range 50 to 70 GHz. Ozone has many lines in this frequency band but ozone concentration is low in the atmosphere. Ozone absorption is important in measurements of the zenith attenuation through the atmosphere.

Isotopic species of oxygen ^{16}O, ^{17}O and ^{18}O are present in the atmosphere at fixed relative abundancies

^{16}O	99.76%
^{17}O	0.037%
^{18}O	0.204%

The oxygen absorption is based on $^{16}O_2$ but $^{16}O^{18}O$ has a small influence on the total attenuation. The spectrum of $^{16}O^{18}O$ differs from $^{16}O_2$ in having twice as many lines. Because the molecule is now asymmetric, even, as well as odd values of rotational quantum numbers are allowed. The line intensities are about half as strong as the $^{16}O_2$ lines. Typically the $^{16}O^{18}O$ lines are displaced from the $^{16}O_2$ lines by a few hundred megahertz. The even resonance will be in the $^{16}O_2$ valleys but has little effect on the absorption of electromagnetic radiation except on the line centres. The ozone attenuation is not significant in this application.

2.4 Condensed Water Attenuation

Condensed water or hydrometeors can produce major attenuation in propagation of microwave frequencies. Rain drops both absorb and scatter the electromagnetic wave. Other rain effects are depolarisation, amplitude and phase fluctuations,, antenna gain degradation and bandwidth coherence reduction.

Any shower of rain has a large range of drop sizes. The distribution may be represented by

$$n(r) = N_0 e^{-\Lambda r}$$

where r is the raindrop radius in mm, N_o and A are empirical constants determined from measured distribution. The above distribution can be found in many papers but the three most often referenced distributions are those of Laws and Parsons [ref. 2.28], Marshall and Palmer [ref. 2.29] and Joss et al. [ref. 2.30]. The relationship between rate and attenuation was first analysed by Mie [ref. 2.31]. Later researchers have obtained the relation:

$$\alpha = aR^b$$

where a and b are frequency and temperature dependent constants, α is the attenuation and R is the rain rate. This form was observed by early investigators Ryde and Ryde [ref. 2.32] and Gunn and East [ref. 2.33]; the analytical basis of the above relation has been published by Olsen et al. [ref. 2.34]. The relation aR^b is found in nearly all models for prediction of attenuation due to rain.

The measurement of attenuation related to rain is very difficult due to large variations in drop size and rate and due to large temporal variations. Fog and clouds affect radio propagation to a lesser extent than rain for horizontal paths at sea level. Water droplet sizes of less than 0.1 mm in diameter occur in clouds and fog which allows the Rayleigh approximation to be used in the calculation of attenuation up to about 100 GHz. The attenuation for clouds and fog is proportional to the liquid water content rather than the drop size. The liquid water varies widely from 0.05 to 5 g/m^{-3}. Fair weather cumulus averages less than 1 g/m^{-3} and cumulonimbus about 2.5 g/m^{-3}. Some of the most recent and commendable works on rain and cloud effects on the propagation of electromagnetic radiation are by Ippolito [ref. 2.35] and Crane [ref. 2.36].

2.5 Summary

The theory for calculation of atmospheric attenuation of millimetre waves is well advanced. The oxygen absorption is well understood with reasonably good agreement

between theory and experimental results. Water vapour absorption of millimetre waves, on the other hand, does not show the same degree of agreement between theory and measurement but should be sufficient for the measurements described later.

A useful summary of the attenuation of electromagnetic waves by the various constituents of the atmosphere is shown in Fig. 2.1 after Preissner [ref. 2.37]. Absorption in the microwave and millimetre wave portion of the spectrum is dominated by oxygen and water vapour. Water vapour absorption is highest in the submillimetre and far infrared regions. Carbon dioxide is an important feature of the absorption at infrared frequencies.

Rain has a similar effect on signal attenuation from visible through the infrared wavelengths and then reduces through the millimetre and microwave portion of the spectrum. The plot also shows how the attenuation due to fog increases with frequency from the microwave up to and including submillimetre wave frequencies. The attenuation remains relatively constant through the infrared and visible regions of the spectrum. Because of the difficulties involved in measuring rain and fog water contents no attempt was made to model these quantities.

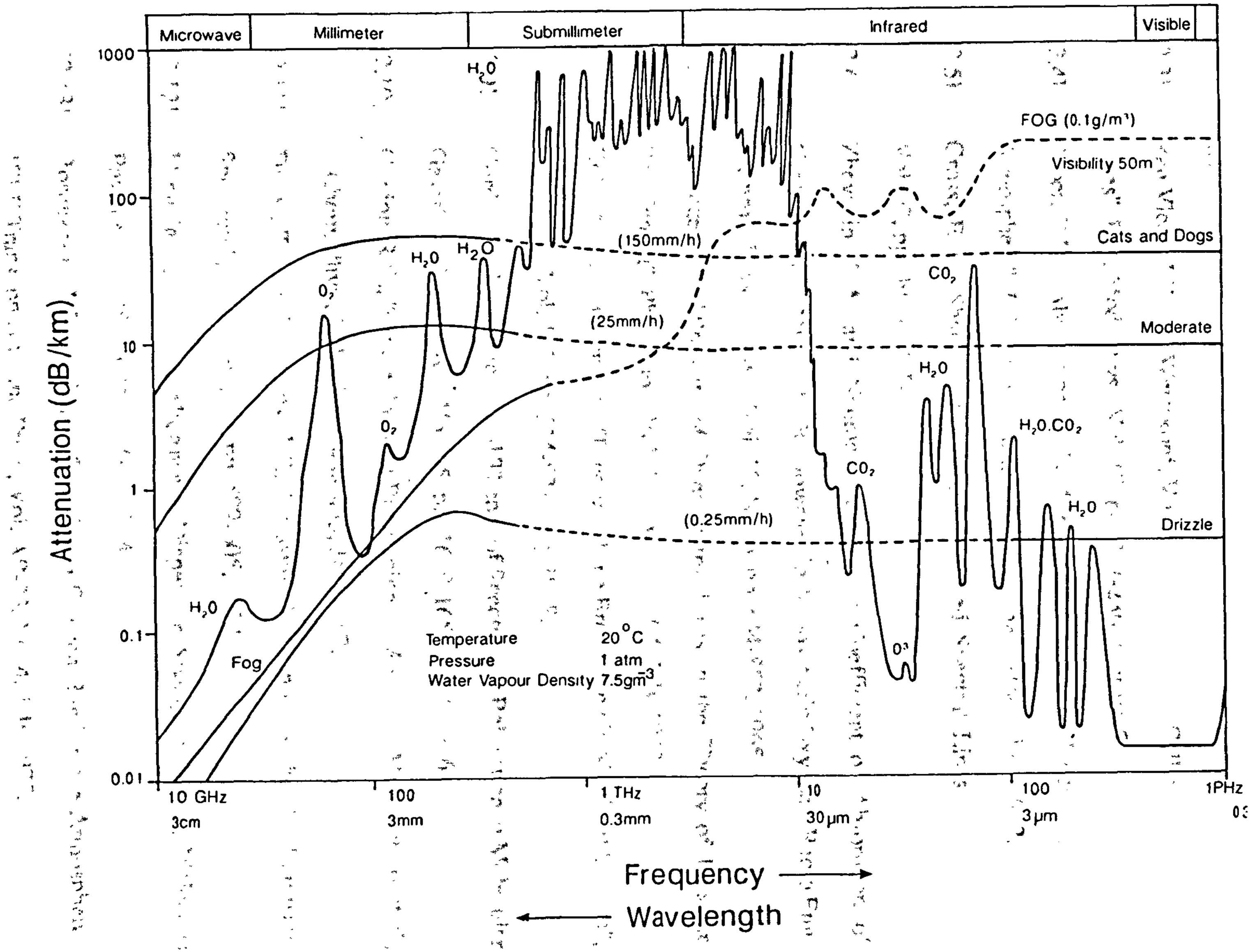
Microwave
Millimeter
Submillimeter
Infrared
Visible
Attenuation (dB/km)
1000
100
10
1
0.1
0.01
H_2O
O_2
H_2O
H_2O
O_2
H_2O
FOG (0.1g/m³)
Visibility 50m
(150mm/h)
Cats and Dogs
(25mm/h)
Moderate
CO_2
H_2O
$H_2O.CO_2$
CO_2
H_2O
(0.25mm/h)
Drizzle
O_3
H_2O
Fog
Temperature 20°C
Pressure 1 atm
Water Vapour Density 7.5gm⁻³
10 GHz
3cm
100
3mm
1 THz
0.3mm
10
30μm
100
3μm
1PHz
Frequency
Wavelength

References

[2.1] Van Vleck, J.H., "The Absorption of Microwaves by Oxygen", Physical Review, Vol. 71, No. 7, pp. 413-423, April 1947

[2.2] Meeks, M.L. and Lilley, A.E., "The Microwave Spectrum of Oxygen in the Earth's Atmosphere", J. Geophys. Research, Vol. 68, No. 6, pp. 1683-1703, march 15, 1963.

[2.3] Van Vleck, J.H. and Weisskopf, V.F., "On the Shape of Collision-Broadened Lines", Rev. Mod. Phys., Vol. 17, pp. 227-236, July 1945.

[2.4] Reber, E.E., "Absorption of the 4 to 6 Millimetre Wavelength Band in the Atmosphere", J. Geophys. Res., Vol. 77, pp. 3831-3845, July 1972.

[2.5] Gross, E.P., "Shape of Collision-Broadened Spectral Lines", Phys. Rev., Vol. 97, pp. 395-403, Jan., 1955.

[2.6] Zhevakin, C.A. and Naumov, A.P., "The Coefficient of Absorption of Centimeter and Millimeter Radiowaves in Atmospheric Oxygen", Radio Eng. Electron. Phys. (USSR), Vol. 10, No. 6, pp. 844-852, 1965.

[2.7] Beranger, M., "Problem of Overlapping Lines in the Theory of Pressure Broadening", Phys. Rev., Vol. 111, pp. 494-504, July 1958.

[2.8] Kolb, A.C. and Griem, H., "Theory of Line Broadening in Multiplet Spectra", Phys. Rev., Vol. 111, pp. 514-521, July 1958.

[2.9] Gordon, R.G., "Semiclassical Theory of Spectra and Relaxation in Molecular Gases", J. Chem. Phys., Vol. 45, pp. 1649-1655, Sept. 1966.

[2.10] Gordon, R.G., "On the Pressure Broadening of Molecular Multiplet Spectra", J. Chem. Phys., Vol. 46, pp. 448-455, Jan. 1967.

[2.11] Dillon, T.A. and Godfrey, J.T., "Pressure Broadening of the O_2 Microwave Spectrum", Phys. Rev., A5, pp. 599-605, 1972.

[2.12] Mingelgrin, U., "The Microwave Dispersion Spectrum of O_2", Molecular Physics, Vol. 28, pp. 1591-1602, 1974.

[2.13] Rosenkranz, P.W., "Shape of the 5 mm Oxygen Band in the Atmosphere", IEEE Trans. on Ant. and Prop., Vol. AP-23, No. 4, July 1975.

[2.14] Kaufman, I.A., "Microwave Pressure Broadening in O_2 and H_2O above one Atmosphere", Ph.D. Thesis, Columbia University, N.Y.

[2.15] Maryott, A.A. and Birnbaum, G., "Microwave Absorption in Compressed Oxygen", J. Chem. Phys., Vol. 32, pp. 686-691, 1960.

[2.16] Birnbaum, G., "The Shape of Collision Broadened Lines from Resonance to the Far Wings", Journal of Quantitative Radiative Transfer, Vol. 21, pp. 597-607, 1979.

[2.17] Liebe, H.J., "Molecular Transfer Characteristics of Air Between 40 and 140 GHz", IEEE Trans. on Microwave Theory and Techniques, Vol. MTT-23, No. 4, pp. 380-386, April 1975.

[2.18] Liebe, H.J., Gimmestad, G.G., Hopponen, J.D., "Atmospheric Oxygen Microwave Spectrum - Experiment Versus Theory", IEEE Trans. on Ant. and Prop., Vol. AP-25, No. 3, pp. 327-335, May 1977.

[2.19] Liebe, H.J., "Modelling Attenuation and Phase Radiowaves in Air at Frequencies Below 1000 GHz", Radio Science, Vol. 16, No. 6, pp. 1183-1199, Nov.-Dec. 1981.

[2.20] Liebe, H.J., "Atmospheric EHF Window Transparencies Near 35, 90, 140 and 220 GHz", IEEE Trans. on Ant. and Prop., Vol. AP-31, No. 1, pp. 127-135, Jan. 1983.

[2.21] Van Vleck, J.H., "The Absorption of Microwaves by Uncondensed Water Vapour", Physical Review, Vol. 71, No. 7, pp. 425-433, 1 April 1947.

[2.22] Burch, D.E., "Absorption of Infrared Radiant Energy by CO_2 and H_2O. III. Absorption Between 0.5 and 36 cm^{-1}, Journal of Opto. Soc. of America, Vol. 58, No. 18, pp. 1383-1394, October 1968.

[2.23] Liebe, H.J., "A Nemesis for Millimeter Wave Propagation", Atmospheric Water Vapour, edited by Deepak, Wilkerson and Rubuke, Academic Press, pp. 143-201.

[2.24] Waters, J.W., "Absorption and Emission by Atmospheric Gases", in Methods of Experimental Physics, Vol. 12B, edited by M.L. Meeks, Academic Press, 1976.

[2.25] Bohlander, R.A., Emery, R.J., Llewellyn-Jones, D., Gimmestad, G.G., Gebbie, H.A., Simpson, O.A., Gallagher, J.J. and Perkowitz, S., "Excess Absorption by Water Vapour and Comparison with Theoretical Dimer Absorption", in Atmospheric Water Vapour, pp. 241-254, Edited by Deepak, Wilkerson and Rubuke, 1980.

[2.26] Harries, J.E. and Ade, P.A.R., "The High Resolution Millimeter Wavelength Spectrum of the Atmosphere", Infrared Phys., Vol. 12, pp. 81-94, 1972.

[2.27] Carlon, H.R. and Harden, C.S., "Mass Spectrometry of Ion-Induced Water Clusters: An Explanation of the Infrared Continuum Absorption", Appl. Optics, Vol. 19, No. 11, pp. 1776-1786, 1980. (Addenda Appl. Opt., Vol. 20, No. 5, pp. 726-727).

[2.28] Laws, J.O. and Parsons, D.A., "The Relationship of Raindrop Size to Intensity", Trans. Am. Geophys. Un., Vol. 24, pp. 452-460, 1943.

[2.29] Marshall, J.S. and Palmer, W.McK., "The Distribution of Raindrops with Size", Journal of Meteorology, Vol. 5, pp. 165-166, 1948.

[2.30] Joss, J., Thams, J.C. and Waldvogel, A., "The Variation of Raindrop Size Distributions at Locarno", Proc. Int. Conf. Cloud Physics (Toronto), pp. 367-373, 1968.

[2.31] Mie, G., "Beitrage zur Optik ...", Ann. Phys., XXV, p. 377, 1908.

[2.32] Ryde, J.W. and Ryde, D., "Attenuation of Centimeter and Millimeter Waves by Rain, Hail, Fog and Clouds", Report No. 8670, GEC, England, 1945.

[2.33] Gunn, K.L.S. and East, T.W.R., "The Microwave Properties of Precipitation Particles", Quart. J. Royal Meteor. Soc., Vol. 80, pp. 522-545, 1954.

[2.34] Olsen, R.L., Rogers, D.V. and Hodge, D.B., "The aR^b Relation in the Calculation of Rain Attenuation", IEEE Trans. Ant. and Prop., Vol. AP-26, pp. 318-329, march 1978.

[2.35] Ippolito, L.J., "Radio Propagation for Space Communications Systems", Proc. IEEE, Vol. 69, No. 6, pp. 6978-727, June 1981.

[2.36] Crane, R.K., "Fundamental Limitations Caused by RF Propagation", Proc. IEEE, Vol. 69, No. 2, pp. 196-209, Feb. 1981.

[2.37] Preissner, J., "The Influence of the Atmosphere on Passive Radiometric Measurements", Symposium Millimeter and Submillimeter Wave Propagation Circuits, AGARD Conf. Proc. No. 245, pp. 48/1-48/3.

CHAPTER 3

MILLIMETRE WAVE ATMOSPHERIC ATTENUATION CALCULATIONS

This chapter describes the computer program to calculate the atmospheric attenuation and describes the sensitivity of the atmospheric attenuation to pressure, temperature and humidity.

3.1 Computer Program

A computer program was written to calculate the atmospheric attenuation from the equations and line data in the previous chapter. The line data is the same as used by Peckham et al. [ref. 3.1] in their work in optimising a satellite instrument to measure atmospheric surface pressure. The program was initially written in double precision Fortran on a Nova computer. Due to operational difficulties the program was rewritten in 'basic' on the Acorn Atom computer which was also used for controlling the digital demodulator (see Chapter 4). This allowed one computer to be used for all the instrument requirements. The reduction in precision of the calculation on changing to the Atom was a concern, but a series of calculations over various atmospheric conditions showed the differences in calculated attenuation to be less than 0.0007 dB for the worst case and about 0.0002 dB for most cases. This error is insignificant compared to other errors in the system as shown in Chapter 5. If the difference between the Nova and Atom calculations had been larger, this would have contributed to the systematic errors in the comparison of the theoretical and experimental attenuations. Any other mistake in the program could also contribute to the errors of the instrument.

The program calculates the atmospheric attenuation for a given frequency, barometric pressure, air temperature and humidity. The flow chart of the program is shown in Fig. 3.1. The program starts by loading the values for the look up tables into arrays. The water vapour density and water vapour partial pressure are calculated from the humidity and temperature. The Rosenkranz interference coefficients are calculated

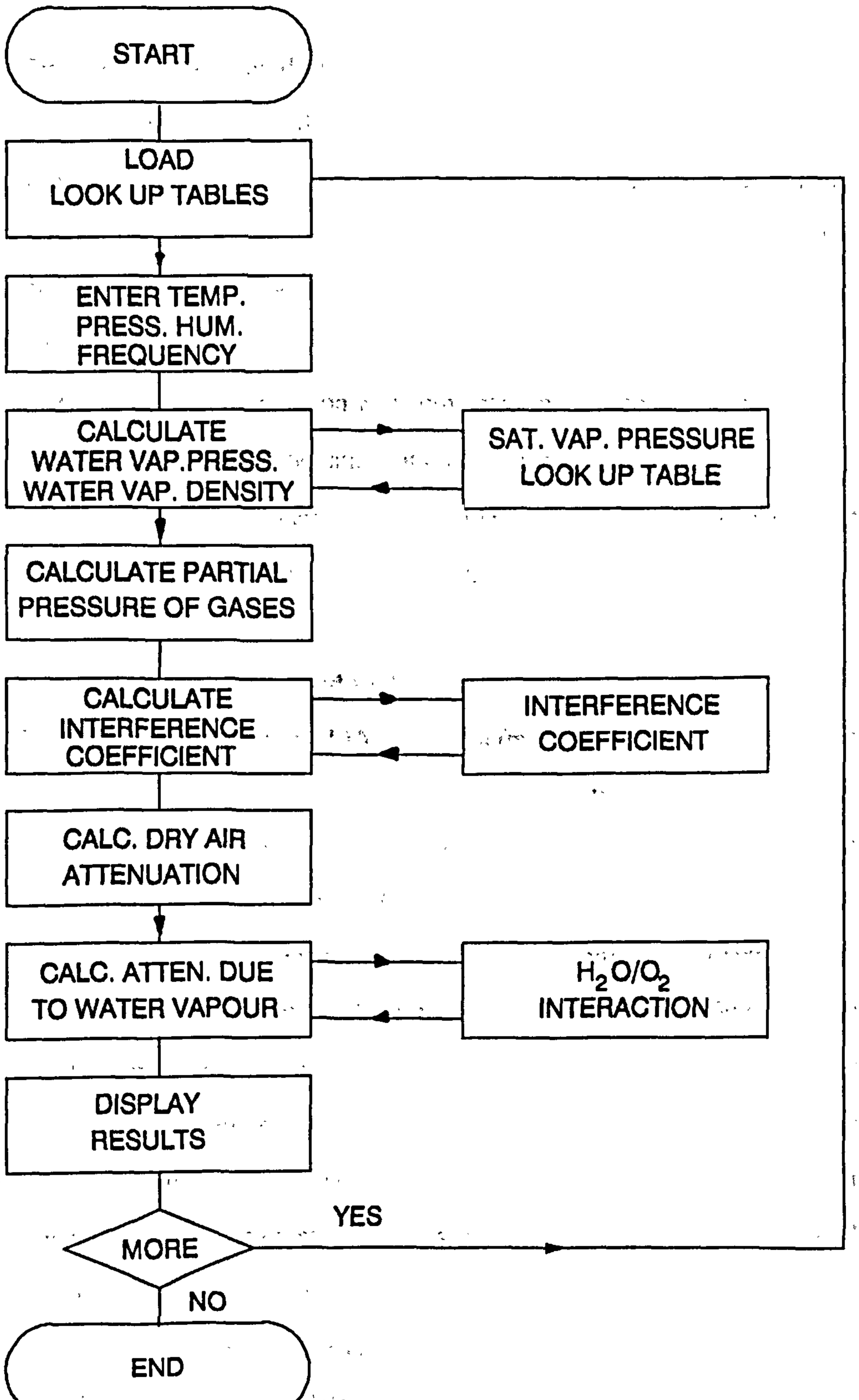

Fig. 3.1 Atmospheric attenuation program flow chart.

to give the dry air attenuation. The contribution of the water vapour is then calculated and added to the dry air attenuation to give the displayed result. A listing of the computer program is given in Appendix A.

The computer program does not include any expressions to calculate attenuation due to rain, fog or cloud. The difficulties associated with such measurements, such as finding the rain drop size, distribution and allowing for changes in antenna gain, make this an added degree of complexity in the atmospheric attenuation above an already difficult measurement. Losses due to rain and cloud have been characterised by many other groups.

Each attenuation computation was completed in 15 seconds. The program listed in Appendix A computes the attenuation for the two fixed frequencies of the transmissometer and for the path length of 650 metres. The total calculation time for each data point was approximately 30 seconds.

3.2 Comparison with Allen and Liebe

The calculated attenuation (dB/km) against frequency is compared with the values obtained by Allen and Liebe [ref. 3.2]. The two sets of results are shown in Fig. 3.2. The attenuations are for a range of frequencies from 42 to 78 GHz, with an atmospheric pressure of 1013 mb, temperature of 15°C and relative humidity of 100%. The two data sets are in fairly good agreement except for two main features. The attenuation is lower for Allen and Liebe's model at the absorption peak, due to slight differences in the line shapes and water vapour/oxygen interaction term. The differences in the attenuations in the wings of the absorption are due to Allen and Liebe using a theoretical model for water vapour absorption compared to the empirical model used in this computation. Unfortunately, there are no other data points available in the paper by Allen and Liebe. More data points at other pressures, temperatures and humidities would have improved the comparison between the two calculations. Allowing for these differences, the agreement between the two models is good.

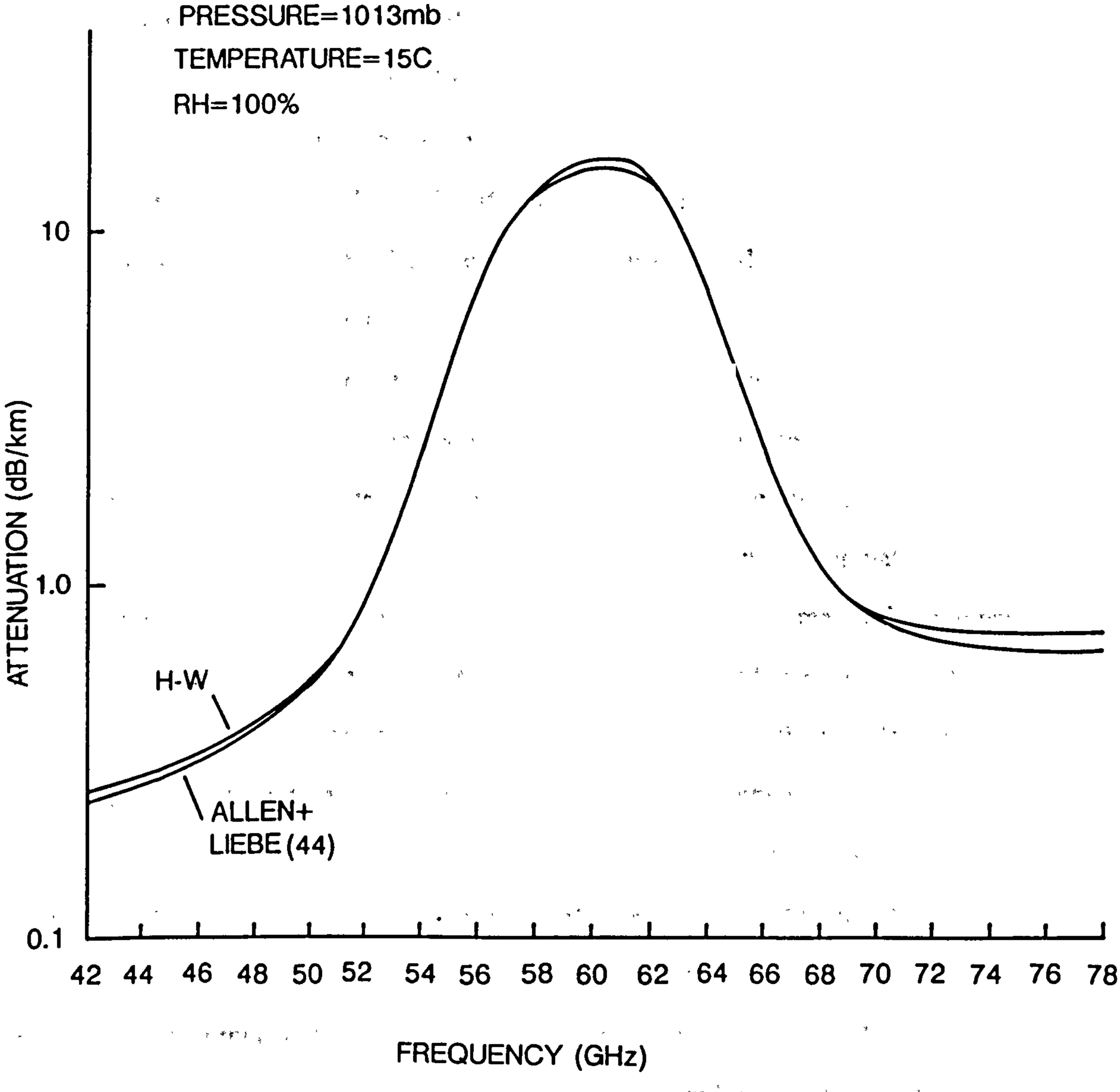

Fig. 3.2 Comparison of atmospheric attenuation with Allen and Liebe [ref. 3.2].

3.3 Calculation on Pressure, Temperature and Water Vapour Sensitivities

One of the main purposes of the computer program was to assist in choosing the operating frequencies for the instrument, as well as calculating the theoretical attenuations for each data set.

The sensitivity of the attenuation with pressure versus frequency is shown in Fig. 3.3. The vertical scale is the logarithmic change in attenuation for a 1 mb change in pressure when the pressure is initially 1013 mb, temperature is + 15°C and the relative humidity is 70%. The plot shows the increase in attenuation due to oxygen as the frequency approaches 60 GHz. The difference in the attenuation at low and high frequency is due to the 118 GHz line. The two arrows indicate the final operating frequencies for the instrument.

A plot of temperature sensitivity versus frequency is shown in Fig. 3.4. The vertical scale is the change in attenuation for a one degree Kelvin change in temperature for a pressure of 1013 mb, initial temperature of 15 C and a relative humidity of 70%. The large dip in the attenuation coefficient is due to the change in the population levels of the oxygen molecules with temperature. As the temperature increases the number of molecules in the higher energy state increases, and so reduces the probability of absorption. The overall absorption is still higher near 60 GHz than for frequencies in the wings of the absorption band, but the rate of change of attenuation with temperature is negative and also greater near 60 GHz than in the wings of the band. The positive change in attenuation away from the absorption band is due to the change in the water vapour density as the temperature changes. The amount of water vapour is entered in the program as a relative humidity, the calculation of the water vapour density involves the saturated vapour pressure which is temperature dependent. With no water vapour present there is no positive change in attenuation with temperature.

The sensitivity of the attenuation with water vapour density is shown in Fig. 3.5. The expected trend of the water vapour continuum in the region of the spectrum has a slight dip near the oxygen absorption peak. This arises from the interaction term between

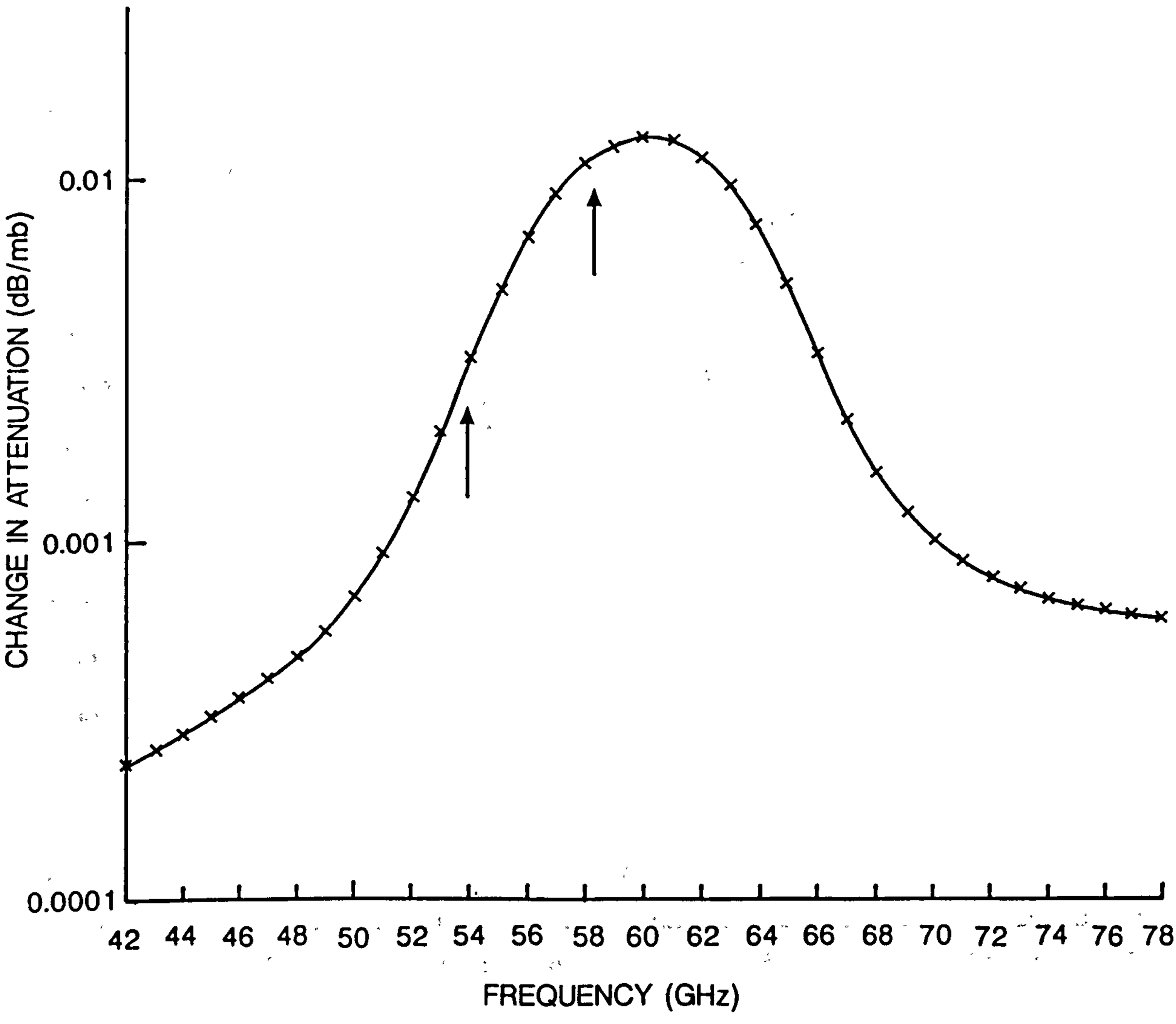

Fig. 3.3 Atmospheric attenuation sensitivity to pressure vs. frequency.

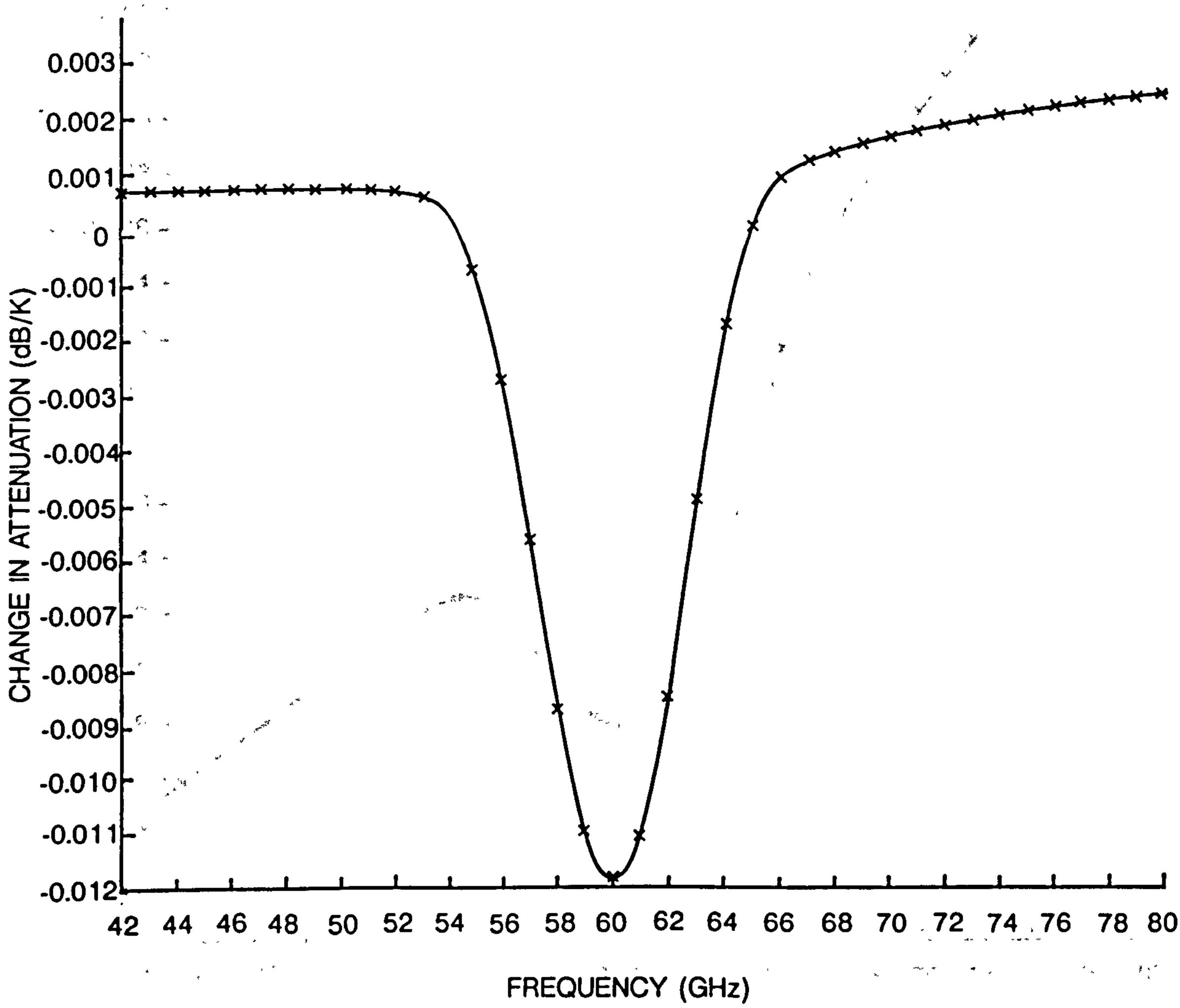

Fig. 3.4 Atmospheric attenuation sensitivity to temperature vs. frequency.

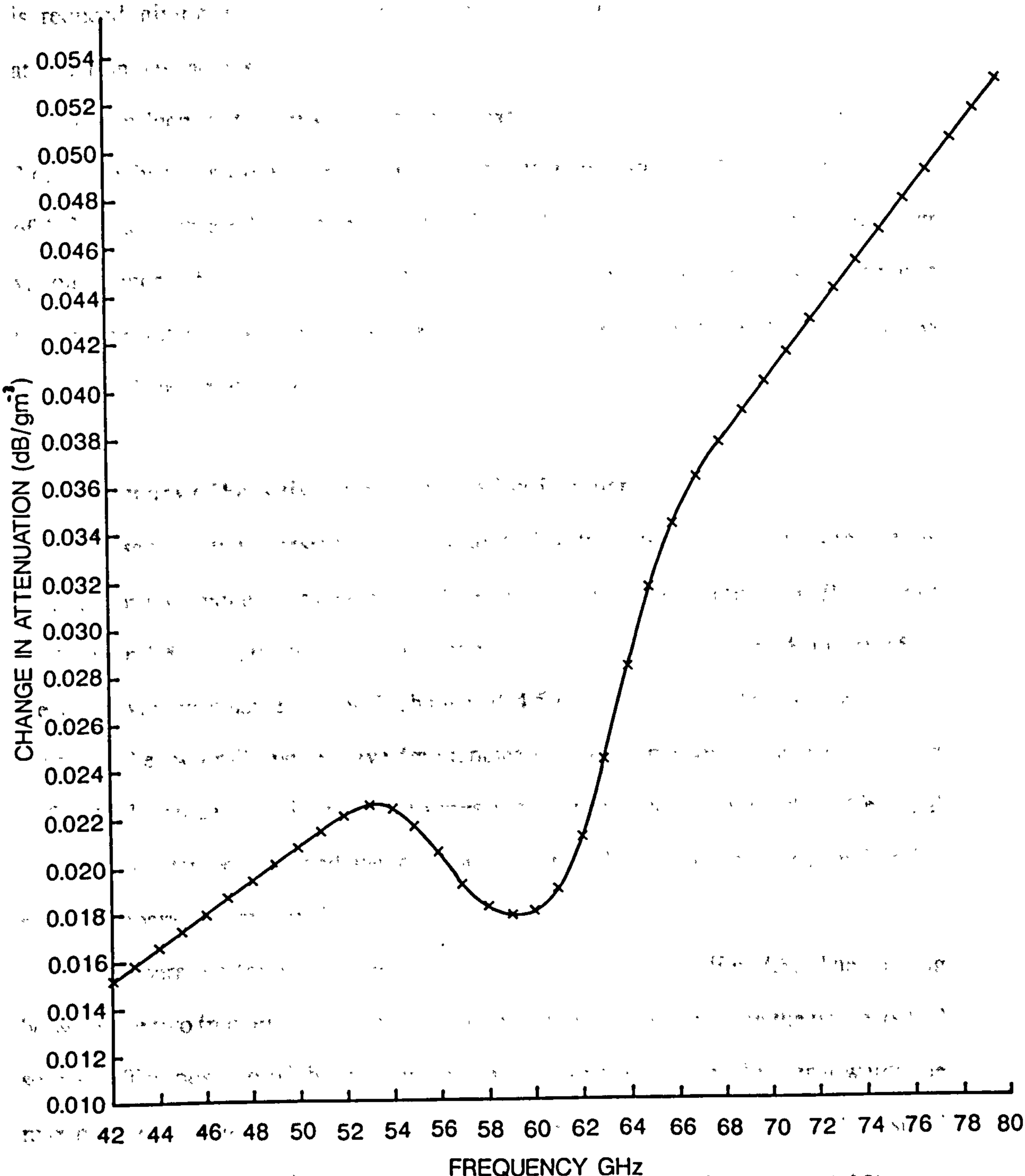

Fig. 3.5 Atmospheric attenuation sensitivity to water vapour density vs. frequency.

oxygen and water vapour. As the water vapour density increases the oxygen absorption is reduced giving a nett decrease in attenuation even although the water vapour attenuation has increased.

The influence of water vapour on the atmospheric attenuation is also shown in Fig. 3.6. where the two plots are for an atmosphere with a pressure of 1013 mb, a temperature of 15°C and with a relative humidity of 70% and 0%. The contribution of the water vapour is more obvious away from the oxygen band absorption due to the logarithmic plot but the water vapour does provide a relatively constant increase in attenuation across the range of frequencies in the graph.

3.4 Summary of Sensitivities and Operating Frequencies

The sensitivity to pressure, temperature and water vapour have been combined in Fig. 3.7 for the frequency range 50 to 60 GHz. The pressure change is a 10% change of 10 mb in 1000 mb, the temperature change is a -0.5% change of -1.44 K in 288.15 K, the water vapour change is a 50% change of 4.5 gm^{-3} in 9 gm^{-3}. The requirement in choosing the two millimetre wave frequencies for the instrument is to maximise the differential attenuation with respect to pressure changes and minimise the differential attenuation to temperature and water vapour changes. The two dashed lines on Fig. 3.7 mark the operating frequencies.

The operating frequencies are indicated by the arrows on Fig. 3.8. The spacing between the two frequencies was controlled by hardware constraints in the phase locked sources. The position of the frequencies could have been moved further towards the maximum of the oxygen absorption lines but this would have provided only a small increase in sensitivity. Choosing frequencies nearer the centre of absorption peak also decreases the system signal to noise ratio. The final frequencies were a reasonable compromise.

A further constraint on the frequencies was that the operating frequencies would not be near a line centre. The nearest line centres to the 53.975 GHz operating frequency

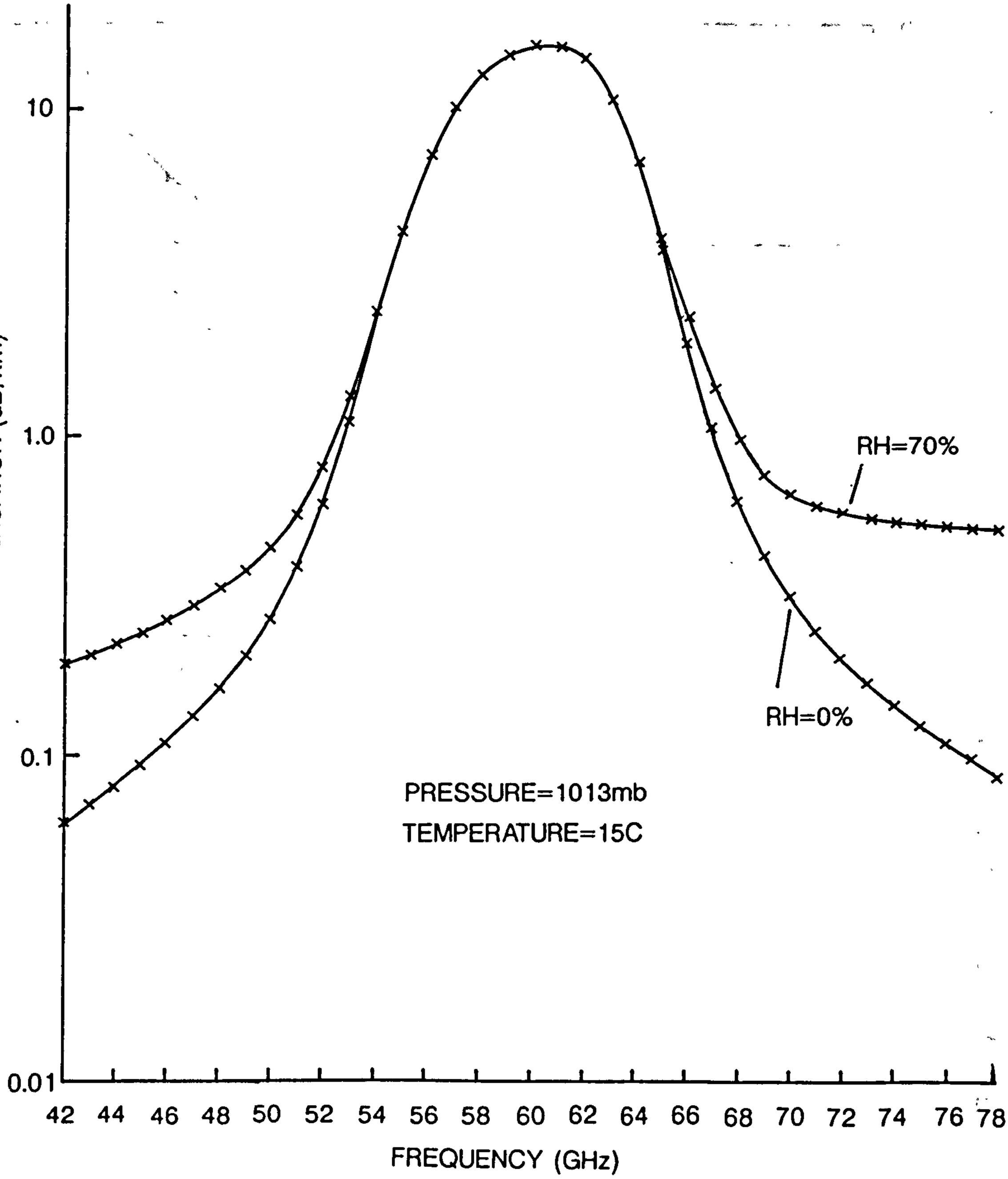

Fig. 3.6 Plot of atmospheric attenuation for two values of relative humidity.

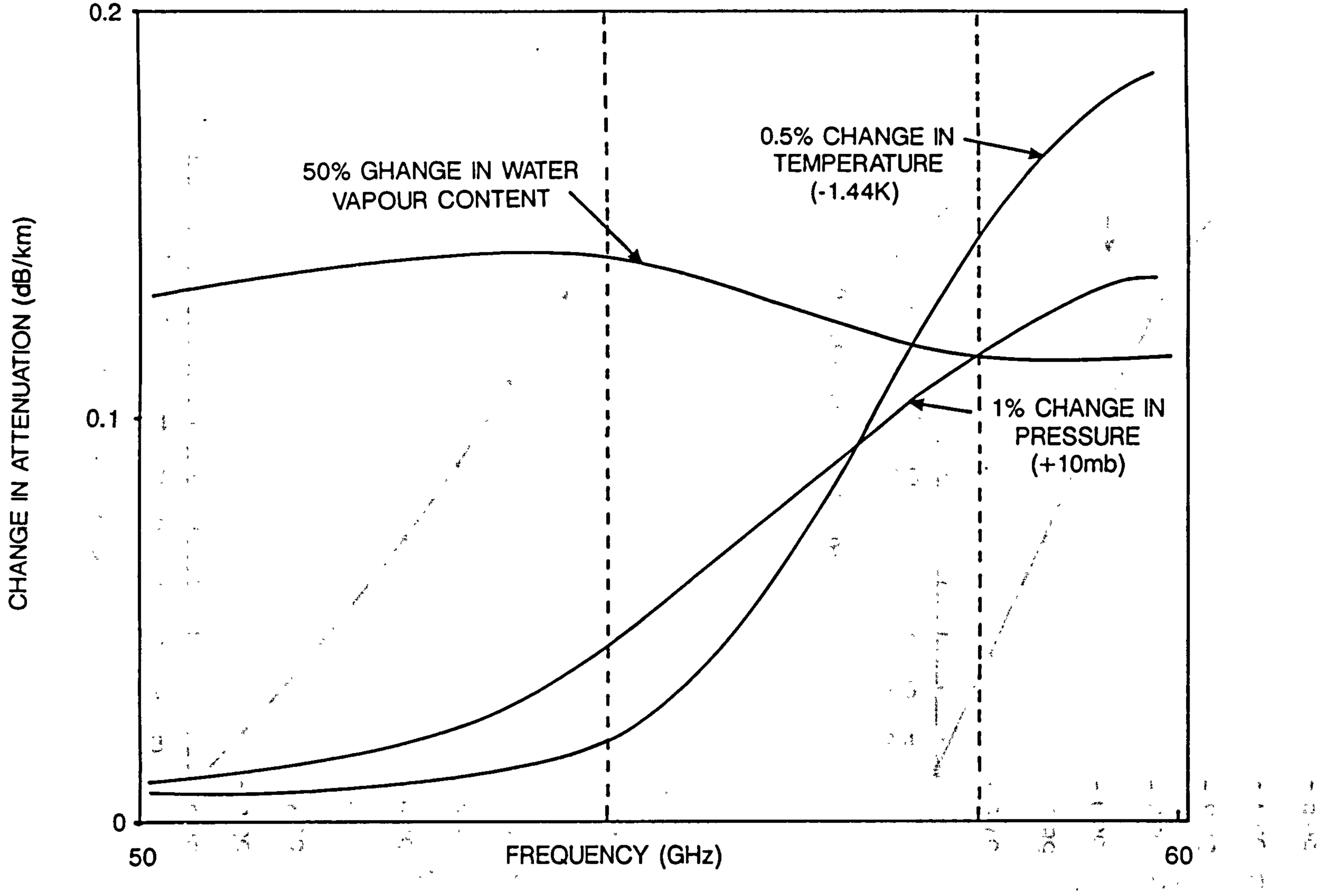

Fig. 3.7 Summary of atmospheric attenuation sensitivity to pressure, temperature and water vapour density.

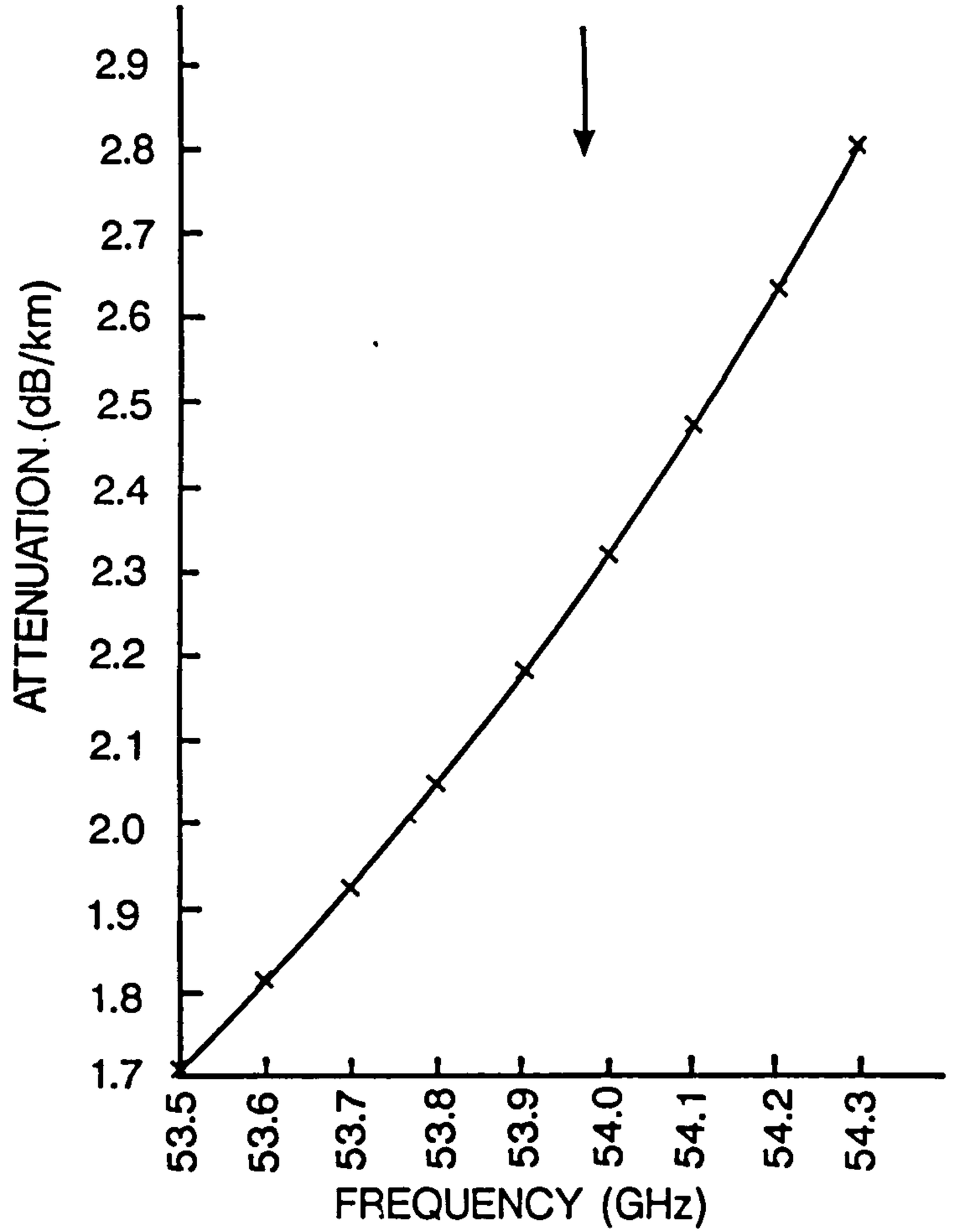

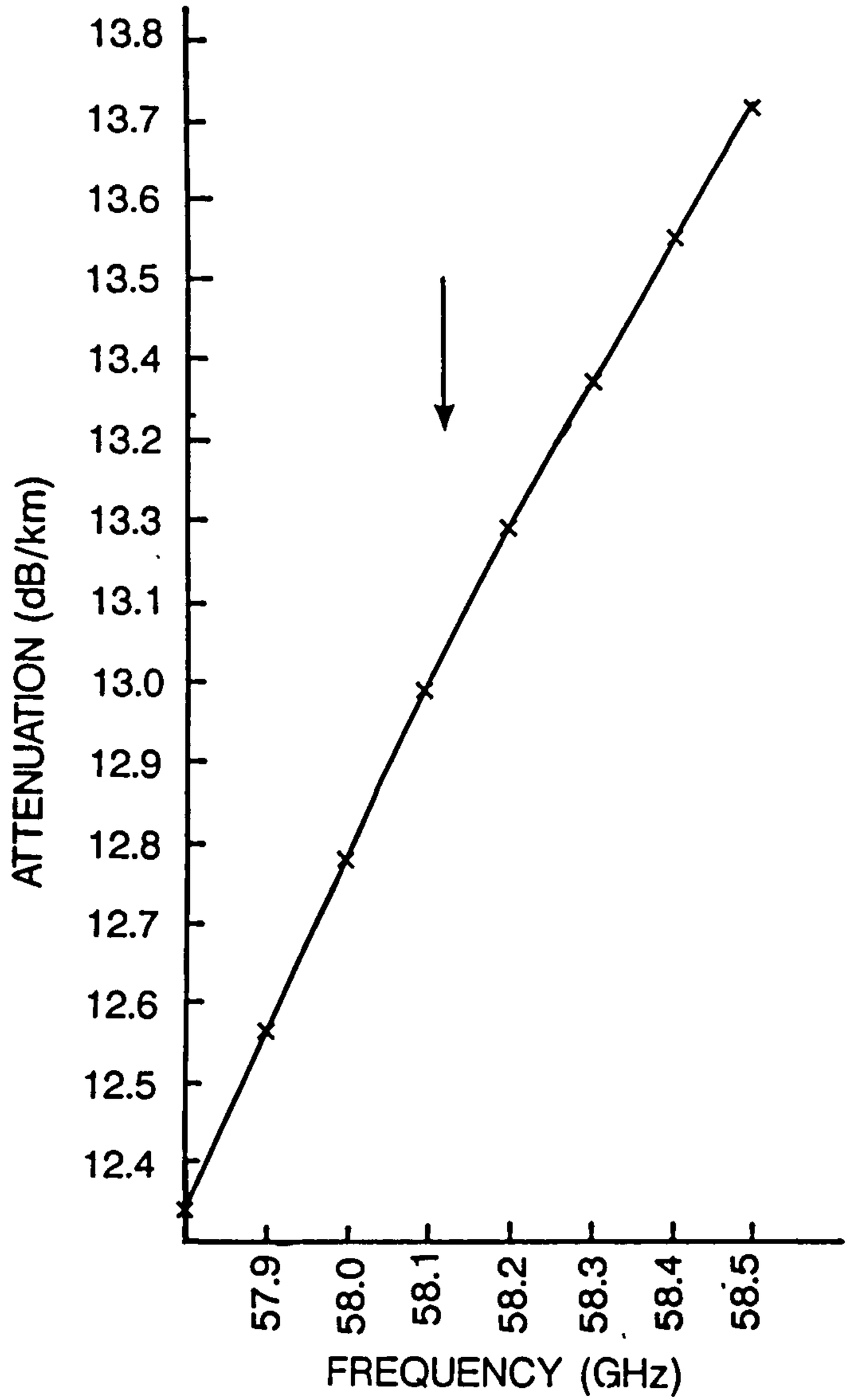

Fig. 3.8 Atmospheric attenuation in region of operating frequencies.

are at 54.1300 and 53.5957 GHz and the nearest line centres to the 58.11875 GHz operating frequency are at 57.6125 GHz and 58.3239 GHz. The choice of operating frequencies is further discussed in Chapter 4.

References

[3.1] Peckham, G.E., Gatley, C. and FLower, D.A., "Optimising Remote Sensing Instrument to Measure Atmospheric Surface Pressure", Int. J. Remote Sensing, No. 4, pp. 465-478 (1983).

[3.2] Allen, K.C. and Liebe, H.J., "Tropospheric Absorption and Dispersion of Millimeter and Submillimeter Waves", IEEE Transactions on Antennas and Propagation, Vol. AP-31, No. 1, pp. 221-223 (1983).

CHAPTER 4

INSTRUMENT DESCRIPTION

4.1 General Design Considerations

All measurements of radio or microwave propagation require some method of calibration to give good reproducibility over extended periods of observations. In instruments where there is a transmission from one point to another some means of controlling the transmit power must be used as well as some means of keeping the detector in calibration for all operating conditions. The physical arrangement used here was to transmit the signal to a reflector and receive the reflected signal at the same site as the transmitter. An advantage of the transmitter and receiver being on the same site is that all reference frequencies and all the equipment can be in the same laboratory and coherent detection techniques can then be used, giving advantages in the rejection of noise. The main advantage of this double pass system is that a balanced amplitude bridge can be employed to give corrections for changes in transmitter power and changes of gain in the intermediate frequency (IF) gain stages in the receiver. The system used was not an exact bridge but allowed the signals in the transmit and reference paths to be adjusted to be of nearly equal amplitude. An attenuator was adjusted in the reference path to equalise the powers arriving at the detector from the transmit and reference paths. The attenuator settings chosen for the two millimetre wave frequencies approximately matched the difference in the atmospheric attenuation (~ 7 dB). Fixed attenuator settings were maintained throughout each measurement set.

This transmissometer is a double pass, coherent system using two fixed millimetre wave frequencies transmitted over a horizontal atmospheric path. The two millimetre frequencies were chosen to give as large a sensitivity to atmospheric pressure, and as low a sensitivity to atmospheric temperature and humidity as possible. There was also some restriction in the choice of frequencies which could be conveniently generated

with good stability. A tunable source could have been used but the importance of reproducibility of frequency was given a high priority. Retuning the same millimetre source can produce problems with stability. When the frequency is changed in a Gunn oscillator or IMPATT oscillator this requires a change in voltage and current which in turn changes the heat dissipation and efficiency of the source. It was felt that two fixed frequency sources operating under stable conditions throughout the measurements were important and made operation of the instrument more convenient.

The attenuation changes with frequency are quite large in the wings of the oxygen absorption band centred at 60 GHz. Two frequencies in the lower wing were chosen, namely 58.11875 GHz and 53.975 GHz, the exact frequencies being constrained to be multiples of the crystal reference frequency. The components were chosen to ensure that the same waveguide system, transmit and receiver dishes and detection system would respond equally well to both frequencies.

The path length of 650 m is relatively short compared to other atmospheric paths. The position of the reflector was chosen as the best direction of propagation from the laboratory which would give reasonably unobstructed propagation and minimal multipath effects. Another consideration was accessibility for monitoring temperature at the reflector and along the transmission path.

The sensitivity of the differential attenuation to pressure, temperature and humidity is

Pressure	0.00524 dB/mb	P = 1 atm
Temperature	-0.0585 dB/°K	T = 15 C
Humidity	-0.0098 dB/gm^{-3}	RH = 70%

The differential attenuation being simply the difference in attenuation between the two millimetre wave frequencies. These sensitivities vary by a small amount depending on the atmospheric conditions. The sensitivities quoted are a guide and are not correct over all pressures, temperatures and humidities. The temperature sensitivity is quite high and therefore requires accurate measurements of atmospheric temperature so that changes in atmospheric attenuation due to changes in pressure can be observed. The sensitivity

to humidity was low and this was an advantage in relating the observed attenuations to the measured barometric pressures. For this locality, the maximum change in difference attenuation due to temperature ranging from +20°C to -5°C is approximately 1.5 dB. The maximum variation in attenuation due to a pressure change of 960-1030 mb is approximately 0.36 dB. These attenuations were calculated using the computer program described in Chapter 3.

The other main design feature, which was introduced into the heterodyne system, was that the transmitted and reference signals were modulated at separate frequencies (approximately 120 Hz and 70 Hz, respectively) to allow both signals to be measured simultaneously. This reduced the effects of power change and gain drift in the instrument. Another benefit was the removal of waveguide switches from the transmitted atmospheric path and internal reference path. There had been doubts as to the resettability of waveguide switches to the accuracy required for these measurements. The transmitted signal was modulated at the retroreflector so that coherent reflections from the retroreflector could be retrieved from other stray coherent reflections.

The accuracy required was defined as that sufficient to be able to observe pressure changes of the order of 5 mb. This is equivalent to 0.03 dB in differential attenuation and is also the required attenuation accuracy for a satellite borne instrument to measure the surface atmospheric pressure to an accuracy of 1 mb. This would be an important check of the spectroscopic models used to calculate the atmospheric attenuation and of the attenuation accuracy that can be achieved. These spectroscopic models were used in determining the feasibility of satellite borne instruments to measure pressure over the sea surface on a global scale.

A schematic of the transmissometer system is shown in Fig. 4.1. It shows several main sections, namely an atmospheric path, a reference path, millimeter wave sources, a signal downconvertion scheme and a digital demodulator controlled by a computer. The use of a digital demodulator required a signal carrier frequency not greater than 1 kHz, hence the need for the offset generator and downconvertion scheme to convert the millimeter waves to a < 1 kHz carrier frequency. A digital demodulator was used

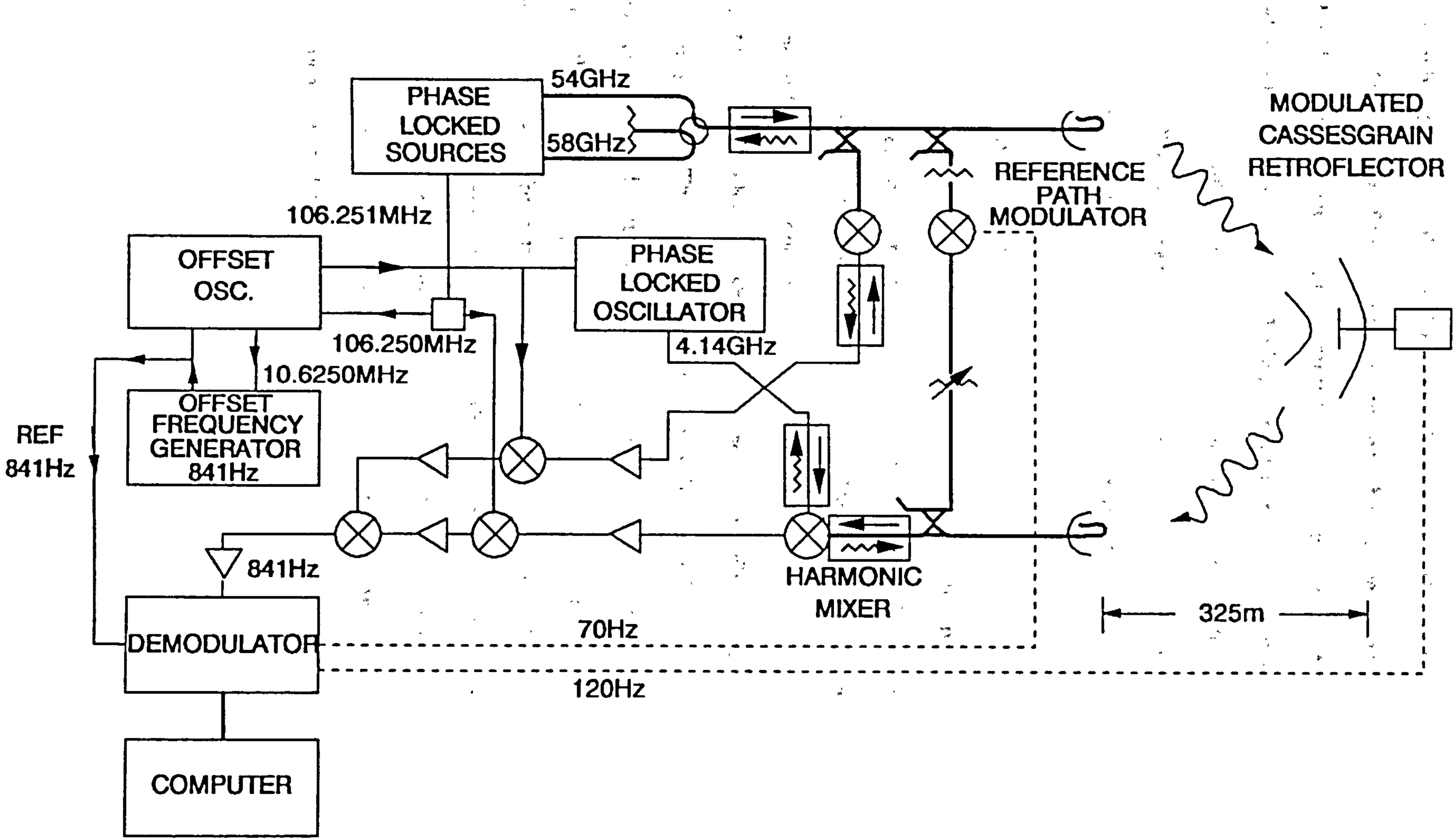

Fig. 4.1 Schematic of millimetre wave transmissometer.

because the signal retrieval can be made sensitive to only the fundamental modulation frequency and not sensitive to the odd harmonics of the modulation frequency as is the case with standard analogue phase sensitive detectors (PSD's).

More details of the instrument are described in the following sections along with details of the measurement of barometric pressure, atmospheric temperature and the relative humidity of the air. The instrument was developed over a period of time with a large amount of effort expended in reducing effects which were sometimes difficult to identify. The instrument discussed here is the final system with, in some cases, some explanation of the problems and solutions employed.

4.2 Atmospheric Path

The atmospheric path is a double pass system with separate transmit and receive dishes at one end of the path and a reflector at the other end of the path. The dishes were situated in a laboratory on top of the Physics Department giving an unobstructed view of the reflector positioned in a field. The distance from the laboratory to the reflector is 325 metres, which is shorter than most atmospheric paths used in absorption measurements. The other disadvantage was the lack of clearance over the intervening roofs which could contribute to multipath effects. The position of the reflector was close enough to the buildings to ease any problems in laying cables for power to drive the modulator and for returning information on the modulation frequency and the atmospheric temperature at the end of the transmission path.

The path length was measured with surveying instruments used in the construction industry. The total path difference between the atmospheric path and the reference path was measured to be 650.02 ± 0.01 metres.

4.2.1 Transmit and Receive Antennae

The transmit and receive dishes were 30 cm diameter parabolic reflectors with swan neck waveguide feeds purchased from EMI. The beam patterns for one of the dishes are shown in Figs. 4.2 and 4.3. The E-plane pattern is fairly symmetric with the first sidelobes at about 25 dB down from the peak. The H-plane pattern shows an asymmetry which is due to the waveguide feed partly blocking one side of the dish.

The transmit and receive dishes were positioned close to one another and fitted into a window of the laboratory to give an unobstructed view of the retroreflector. Each dish was mounted by four adjustable bolts to an aluminium plate which was also bolted to the frame of the building. Mechanical stability was important to avoid any signal changes due to movement of a dish. If the dish moves, the gain for each operating frequency will change, leading to errors in the attenuation measurements. The adjustable bolts were used during alignment of the dishes and then locked in position. The dishes were about 2.5 metres above the surface of the flat roof outside the laboratory.

The isolation between the dishes was increased by placing a metal tube (about 10 cms long) lined with microwave absorber over each dish. This reduced any spill-over between the two dishes. The absorber used was AN72, a foam based material impregnated with absorber from Emerson and Cuming [ref. 4.1], which has reasonably good absorption qualities at 50-60 GHz frequencies. The tubes also have the beneficial effect of absorbing some of the energy in the sidelobes which could have contributed to standing waves between the dish and the window surround. This could have made small, subtle changes in the transmitted or received powers.

The ends of the tubes were fitted with expanded polystyrene covers to protect the dish from the weather, especially rain. Expanded polystyrene was chosen because it has low absorption for millimetre wavelength radiation. This was found to be unsatisfactory as water would ingress into the polystyrene, especially after it had been weathered for a few months. It was found that the attenuations would change by a large amount as the

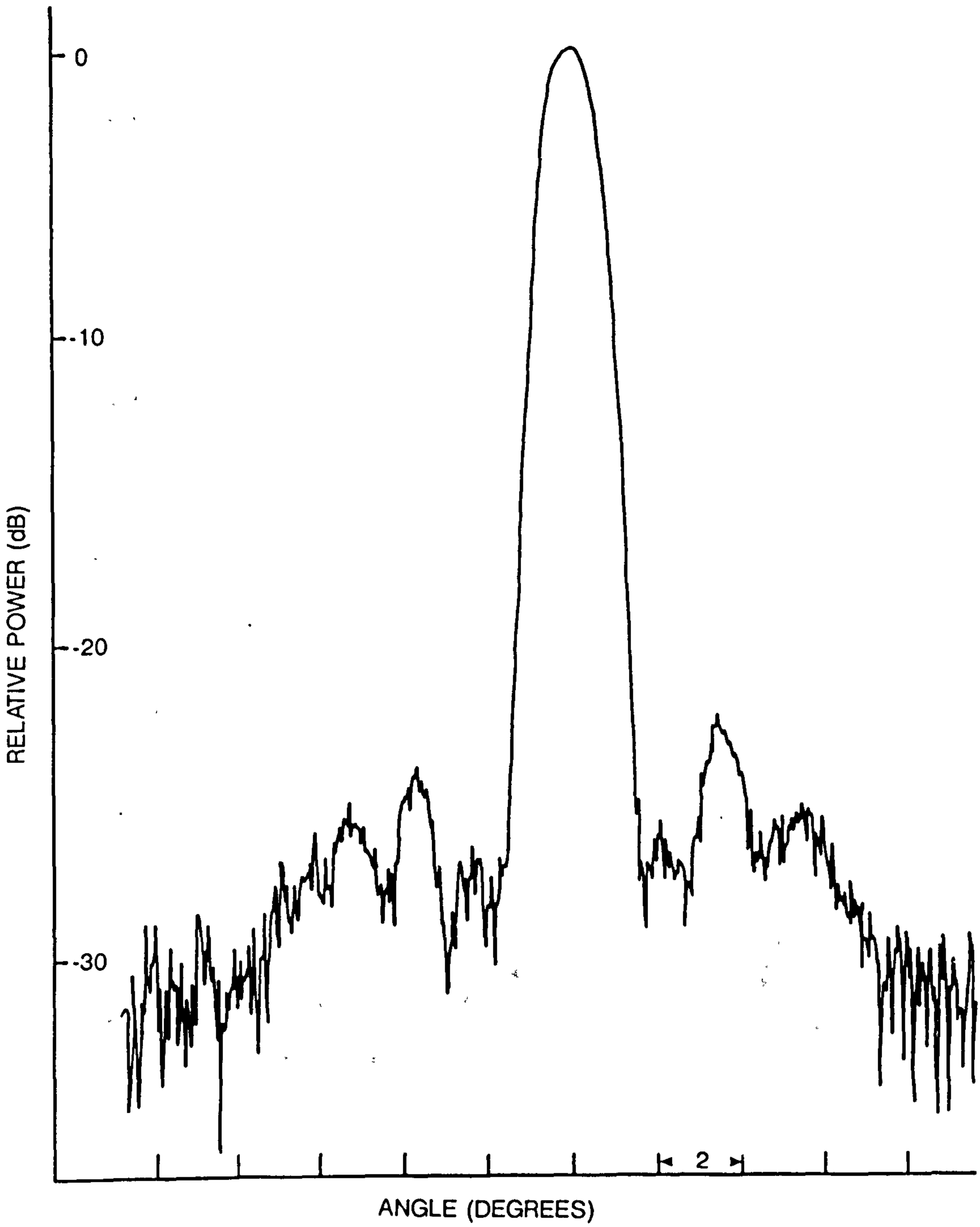

Fig. 4.2 E-plane beam pattern for transmit and receive antennae.

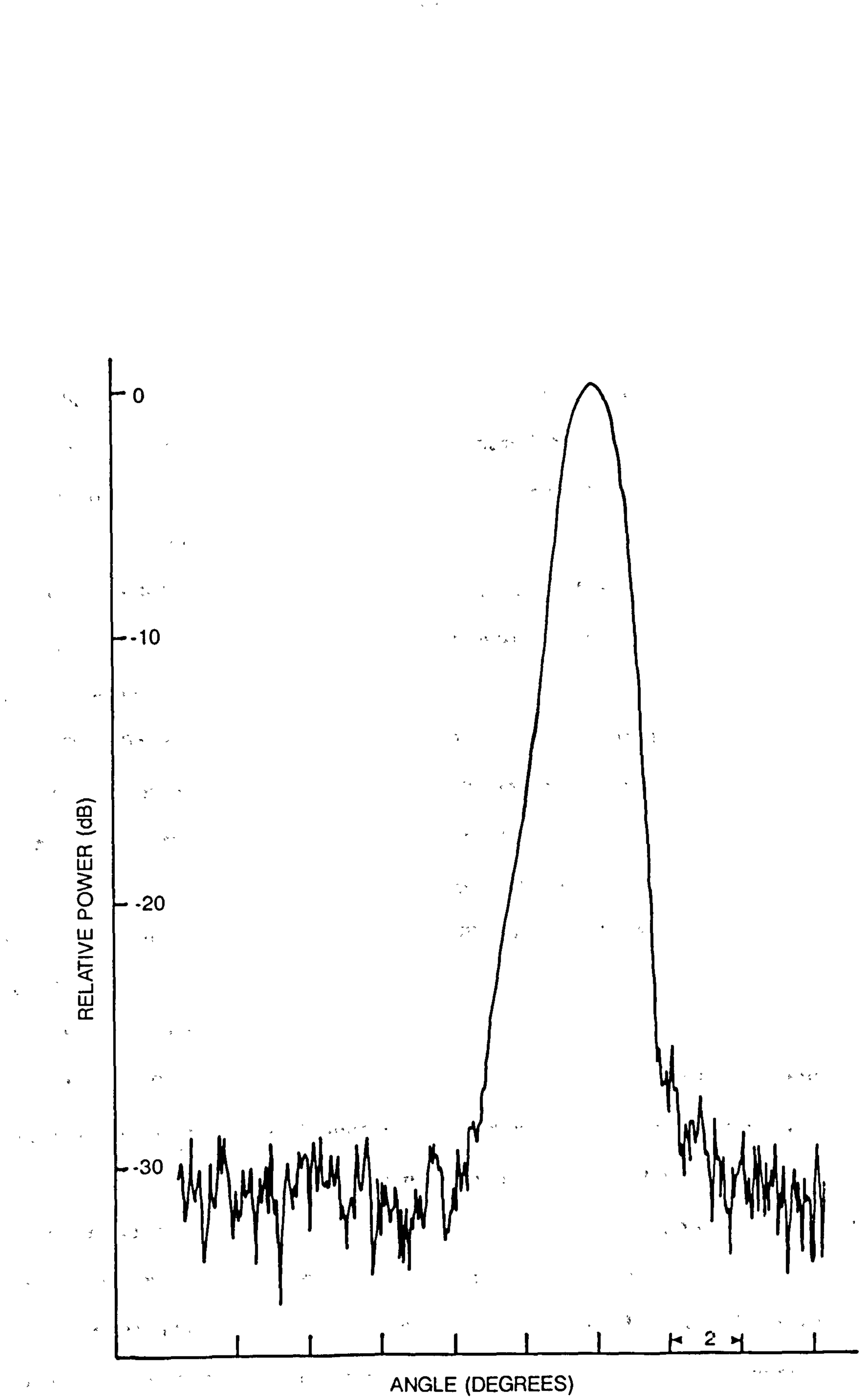

Fig. 4.3 H-plane beam pattern for transmit and receive antennae.

air temperature increased and even more alarmingly when heated by the sun's rays. The solution to the protection of the dishes was to have no protective covers while the instrument was in operation and to fit a cover when the instrument was not in use.

Due to the polarisation rotation on the reflector (described later) it was possible to site the transmit dish with its E field horizontal to the direction of propagation and the receive dish with the E field vertical to the direction of propagation. This had two benefits

a) the spill-over from the transmit dish to the receive dish was greatly reduced

b) only signals which had been reflected from the reflector at the end of the path would propagate into the waveguide feed of the receive dish, decreasing unwanted coherent reflections.

The transmit dish was also positioned with the waveguide feed on the upper half of the dish to provide the sharpest beam pattern taper towards the roof under the transmission path, to reduce the possible multipath signal.

The efficiency of the dishes was 42% and was calculated from the manufacturer's data of gains measured at frequencies near to the operating frequencies. The effective gain for each operating frequency was calculated from the theoretical gain and reduced by the efficiency, assuming the efficiency did not change with frequency. The efficiency will change depending on how well the feed fills the dish. At 58.11875 GHz the gain was 41.5 dB; at 53.975 GHz the gain was 40.8 dB.

4.2.2 Retroreflector

A retroreflector was formed by placing a plane mirror at the focus of a cassegrain antenna. The cassegrain was chosen for the convenience of the mirror position. Moving the mirror along the axis of the parabola produces a modulated reflected beam. Having the mirror supported through the centre of the parabola allowed good access for the control electronics without interfering with the microwave beam.

The cassegrain used for the microwave region is an adaptation of the optical technique invented by William Cassegrain in the seventeenth century. The reflector consists of a 61 cm diameter parabolic primary reflector with a 20 cm diameter hyperbolic subreflector and a 76 mm diameter mirror at the focus. The mirror diameter

was chosen to be at least three times the diameter of the expected spot size, but small enough not to obstruct the beam. One of the two foci of the hyperbola is a real focal point and the mirror is positioned at this point. This was chosen to be 25 mm in front of the parabolic surface. The other focus of the hyperbola is a virtual focal point and is coincident with the focus of the parabolic surface [ref. 4.2]. The focus of the parabola was 22.86 cms from the vertex. The diameter (20 cm) of the hyperbolic subreflector was chosen to be reasonably small to keep the aperture blocking to a minimum but large enough so that the curvature of the hyperbola was not so severe as to make its manufacture difficult. The surface was lightly polished to reduce the surface roughness. The hyperbola was mounted on the parabola by four tufnol rods with metal threaded sections at the end for adjustment. The hyperbola was positioned by dead reckoning initially and only required a slight adjustment when the patterns were measured. The reflectance patterns are shown in Fig. 4.4.

The mirror required to form the reflector and produce a modulation was initially a flat mirror which vibrated in the direction of the cassegrain axis. The mirror movement was controlled by electronics to a quarter wavelength, thus producing a 180° phase modulation for the reflected radiation. As the mirror moved through the focus there would also be a small amplitude modulation, but this was sufficiently small and stable not to cause any problems in the signal demodulation. The flat mirror modulator was prone to mechanical failure after short periods of operation because the springs retaining the mirror tended to break. As no reasonable springs could be found, a new modulator design was required. Another problem with this technique was the high amplitude stability required for accurate demodulation could not be maintained over any acceptable period of time.

The new modulator, Fig. 4.5, was a grooved aluminium plate. The depth of the grooves were a quarter wavelength deep and the width of each groove was less than half a wavelength (2.38 mm). When a polarised wave is incident normal to the plate and the grooves are aligned perpendicular to the E field then the signal wave will penetrate the groove and the reflected wave will emerge with a $\lambda/2$ phase delay. When the E field is

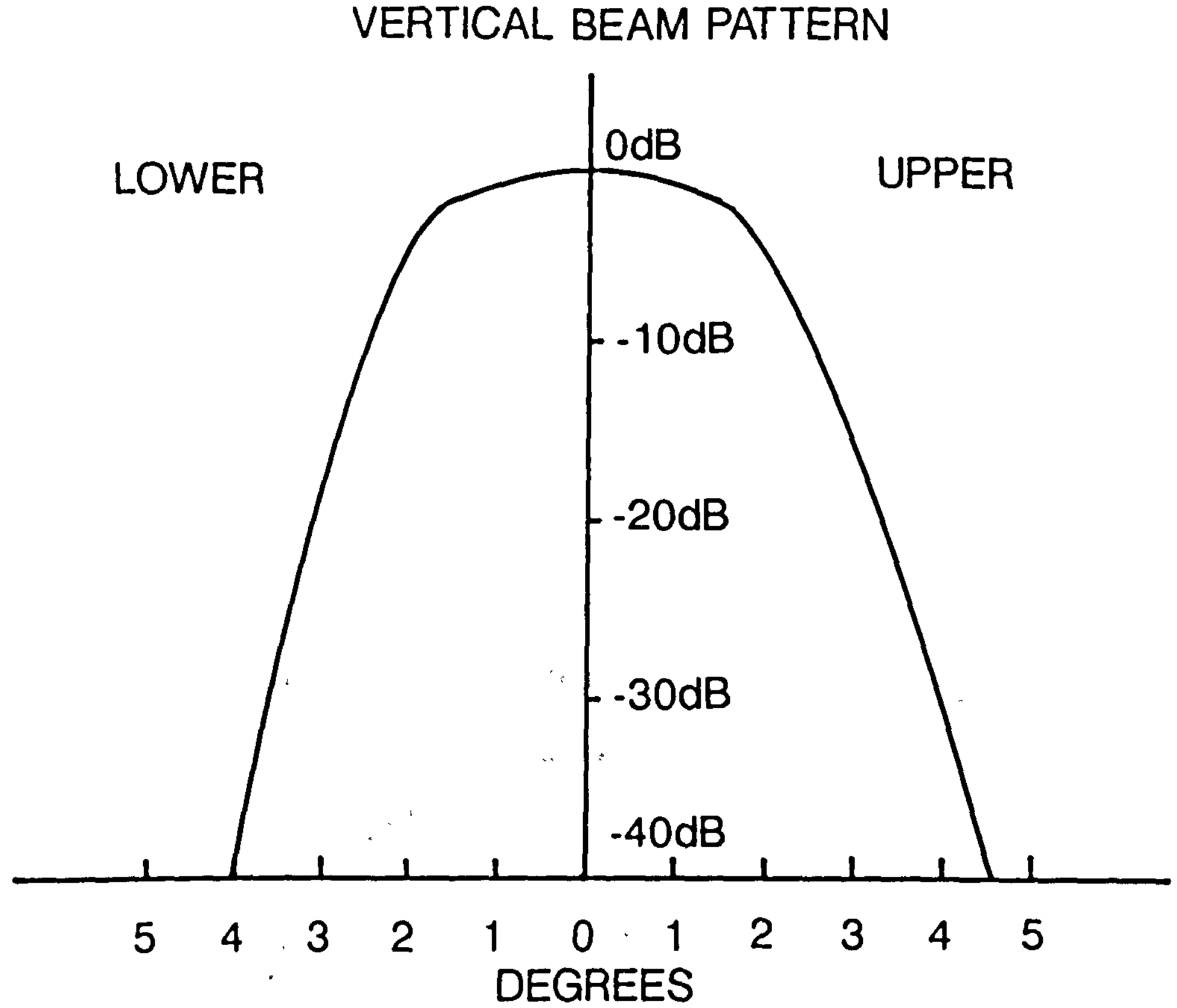

Fig. 4.4 Cassegrain retroreflector patterns.

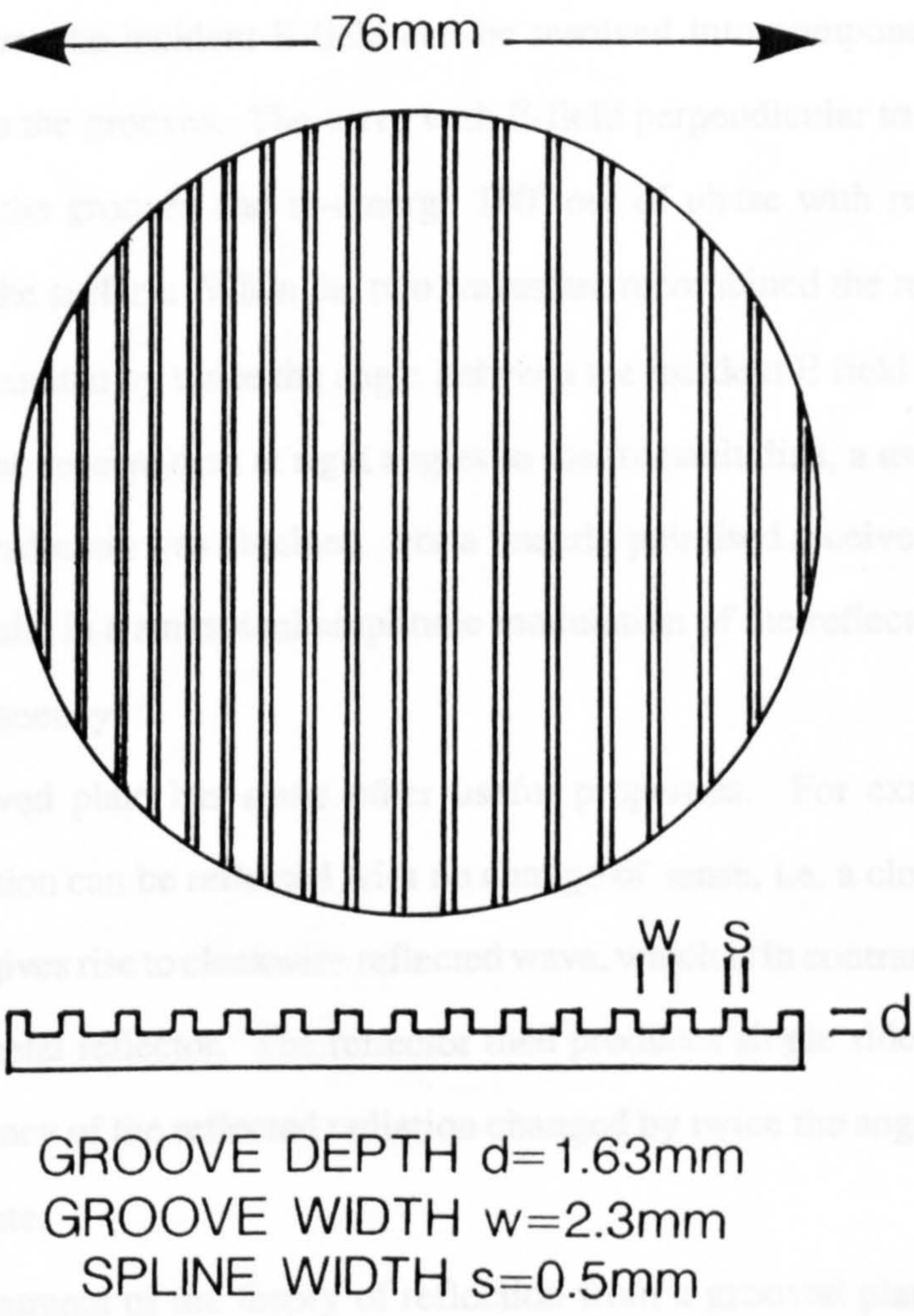

Fig. 4.5 Sketch of grooved plate modulator.

parallel to the grooves, the signal will reflect off the front surface of the reflector because the grooves are then cut-off for that polarisation. As the plate rotates the wave will be phase modulated. The width of the splines was chosen to be 0.6 mm, this was considered thick enough so the spline would not be deformed during machining or during operation. This ensures a periodicity of less than a wavelength and so avoids diffraction of the near normal incident radiation.

The plate also has the property of rotating the plane of polarisation. Fig. 4.6 depicts the plate with the grooves at 45° to the plane of polarisation of the incident wave. For an incident wave, the incident E-field can be resolved into components parallel and perpendicular to the grooves. The wave with E-field perpendicular to the grooves will propagate into the grooves and re-emerge 180° out of phase with respect to a wave reflected from the surface. When the two waves are recombined the resultant reflected wave has been rotated by twice the angle between the incident E field and the grooves. By polarising the receive dish at right angles to the transmit dish, a useful reduction of stray coherent radiation was obtained. For a linearly polarised receiver, steady rotation of the plate results in a sinusoidal amplitude modulation of the reflected wave at twice the rotation frequency.

The grooved plate has some other useful properties. For example, circularly polarised radiation can be reflected with no change of sense, i.e. a clockwise polarised incident wave gives rise to clockwise reflected wave, which is in contrast to the reflection from a plane metal reflector. The reflector then produces single sideband modulation with the frequency of the reflected radiation changed by twice the angular frequency of the grooved plate.

A full treatment of the theory of reflection from a grooved plate modulator was published in IEEE Transactions on Antennas and Propagation, July 1988, Vol. 36, No. 7 by G.E. Peckham and R.A. Suttie, entitled "Microwave Reflection Properties of a Rotating Corrugated Metallic Plate used as a Reflection Modulator". The paper is attached as Appendix B. The paper describes how an electromagnetic field reflected

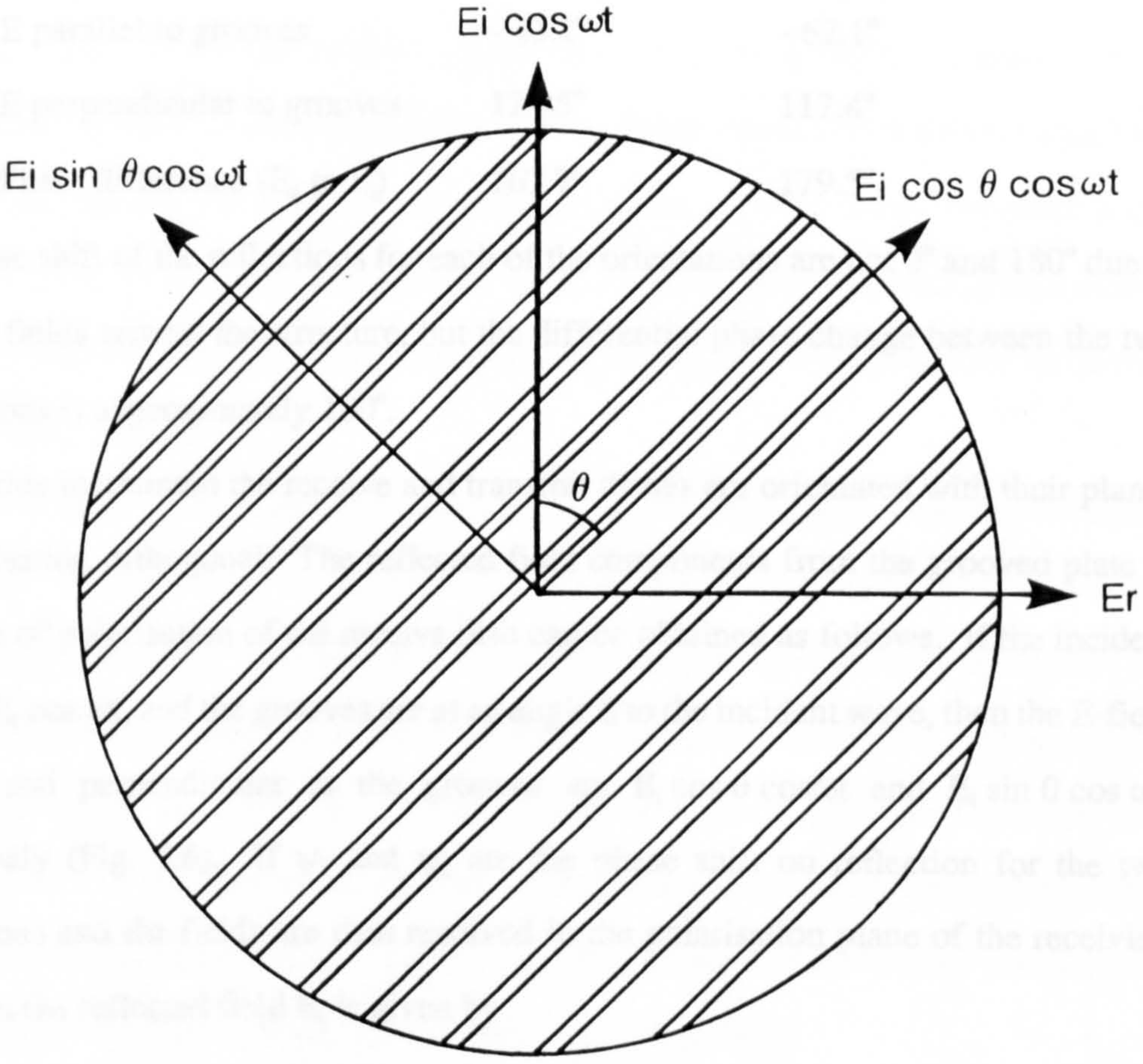

Fig. 4.6 Field components at the surface of the grooved plate.

from a grooved (or corrugated) plate can be calculated by matching plane wave and waveguide mode expansions at the surface of the plate. The numerical results compared favourably with laboratory measurements of various grooved plates.

The calculated phase shifts for a reflected wave from the modulator, for the two orientations of the grooves and the two operating frequencies with respect to the front face, are

	53.975 GHz	**58.11875 GHz**
E parallel to grooves	- 43.2°	- 62.1°
E perpendicular to grooves	124.5°	117.4°
Phase difference ($E_{\|}$ to $E_{\perp}$)	167.7°	179.5°

The phase shift of the reflections for each of the orientations are not 0° and 180° due to fringing fields around the structure, but the differential phase change between the two orientations is approximately 180°.

In this instrument the receive and transmit dishes are orientated with their planes of polarisation orthogonal. The reflected field components from the grooved plate in the plane of polarisation of the receive dish can be obtained as follows. If the incident wave is $E_i \cos \omega t$, and the grooves are at an angle θ to the incident wave, then the E-field parallel and perpendicular to the grooves are $E_i \cos\theta \cos\omega t$ and $E_i \sin\theta \cos\omega t$, respectively (Fig. 4.6). If ψ_1 and ψ_2 are the phase shift on reflection for the two orientations and the fields are then resolved in the polarisation plane of the receiving dish, then the reflected field E_r is given by

$$E_r = E_i \sin\theta \cos\theta \cos(\omega t + \psi_1) - E_i \cos\theta \sin\theta \cos(\omega t + \psi_2) \qquad (4.1)$$

which can be rewritten as

$$E_r = E_i \sin\theta \cos\theta (\cos(\omega t + \psi_1) - \cos(\omega t + \psi_2))$$

$$= E_i \sin 2\theta \sin\left(\frac{2\omega t + \psi_1 + \psi_2}{2}\right) \sin\left(\frac{\psi_2 - \psi_1}{2}\right) \qquad (4.2)$$

The sin 2θ term indicates that the electric field is varying at twice the rotation angle of the modulating disc. The second term is the time varying part of the signal with a phase shift. The $\sin\left(\frac{\Psi_2-\Psi_1}{2}\right)$ shows that for maximum signal the phase difference between the two phase reflection coefficients must be 180°.

Evaluating the $\sin\left(\frac{\Psi_2-\Psi_1}{2}\right)$ for $\theta = 45°$ for the phase differences for the two operating frequencies gives a 1 part in 100,000 reduction in signal strength compared with the maximum possible for the 58 GHz signal and a 6 parts in 1000 reduction for the 53.975 GHz signal, assuming no resistive losses. These signal losses are very small and do not introduce any problem to the operation of the instrument. More important is that there should be no change in these losses. This would most likely result from a change in the dimensions of the structure. The grooved plate proved to be a very stable method of modulating a signal.

A schematic of the cassegrain reflector and the arrangement for mounting the motor to drive the modular is shown in Fig. 4.7. The motor has a continuous shaft extending from both ends allowing an optical pick-off for the modulation frequency to be mounted on one end and the modulator on the other end. The control electronics to maintain the preset modulation frequency and the optical reference pick-off were contained in a watertight unit on the back of the parabola. Details of the modulator frequency control circuit are given in Appendix C. The dc motor had lever graphite brushes and the shaft was mounted with ball bearings for good mechanical stability.

A plastic shield was added around the grooved disc but fixed to the parabola to prevent the wind from disturbing the rotation velocity. Sudden changes in the modulation frequency resulted in noisy output from the demodulator. The modulator was only sensitive to side winds.

The photograph in Fig. 4.8 shows the cassegrain retroreflector. The retroreflector was mounted to an aluminium plate which was hinged to a horizontal base plate fitted with a threaded section to adjust the elevation. The base plate could be rotated on a fixed

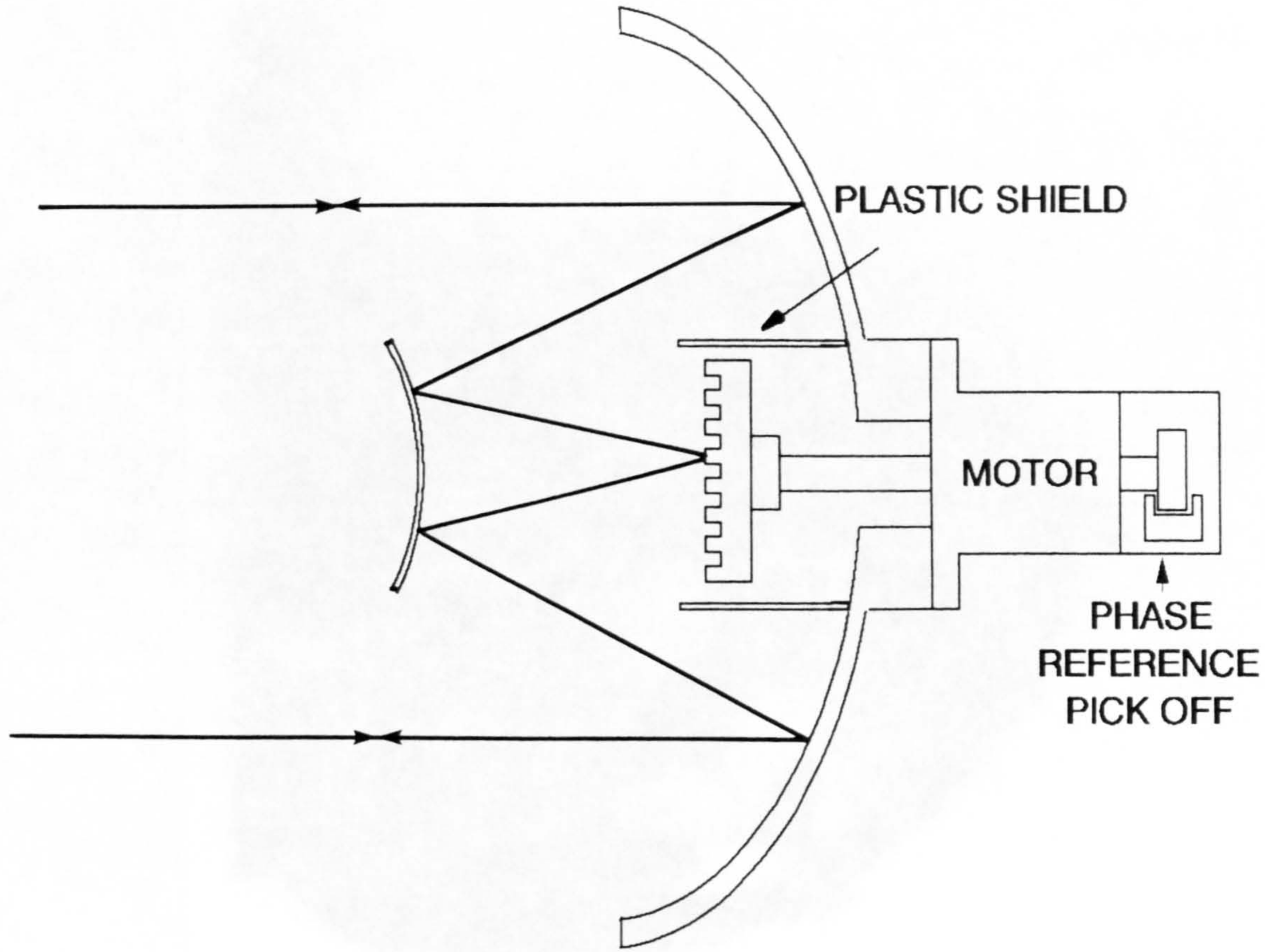

Fig. 4.7 Schematic of modulating cassegrain retroreflector.

Fig. 4.8 Photograph of modulating cassegrain retroreflector.

plate to give horizontal adjustment of the pointing direction of the dish. The fixed plate was bolted to a small platform on three concrete pillars. The photograph in Fig. 4.9 shows the reflector mounted on its concrete pillars. The centre of the dish was approximately 2 metres from the ground. The retroreflector was initially supported on a scaffolding tower but this was not sufficiently stable during windy conditions. The demodulated signal was unsteady due to phase shifts in the return signal, slight changes in the pointing of the dish or slight distortions of the shape of the parabola changing the efficiency of the retroreflector.

The effective cross-sectional area (A_r) of a cassegrain retroreflector is the area of the parabola less the effect of blocking by the hyperbola and an allowance for the efficiency. The reduction in area due to hyperbola blocking is given by [ref. 4.3]

$$\rho_H = \left[1 - 2\left(\frac{D_H}{D}\right)^2\right]^2$$

where ρ_H is the factor describing the reduction in area, D_H is the diameter of the hyperbola and D is the diameter of the parabola. A value of 0.5 was assumed for the efficiency of the retroreflector. This gives A_r as 0.09 m^2.

4.2.3 Signal Losses in Transmission Path

The two main signal losses are geometric losses and atmospheric losses. The atmospheric losses for the two operating frequencies are approximately 9 dB for 58.11875 GHz and 2 dB for 53.975 GHz for average values of pressure, temperature and humidity. Calculation of the losses was used as a guide to the alignment of the system rather than an exact calculation of the atmospheric losses.

An expression for the geometric losses can be formulated by following the ideas of the radar equation for which there are many references. The power density at a distance from the transmit dish is that of a directive antenna at a distance R from the dish, i.e. power transmitted divided by the surface area of an imaginary sphere of radius R and multiplied by the gain of the transmit dish.

Fig. 4.9 Photograph of the retroreflector on the concrete pillars.

$$\text{Power density at retroreflector} = \frac{P_T G_T}{4\pi R^2}$$

where P_T is the power transmitted, G_T is the gain of the transmit dish and R is the distance from the transmit dish to the retroreflector. The amount of power collected by the retroreflector depends on the effective area (A_r) allowing for the efficiency of the retroreflector.

$$\text{Power incident on mirror} = \frac{P_T G_T A_R}{4\pi R^2}$$

The power transmitted by the retroreflector was assumed to be the same as the incident power with no losses on reflection from the aluminium modulator plate. The power density at the receive dish is again the power transmitted multiplied by the gain of retroreflector (G_R) divided by the surface area of an imaginary sphere at radius R at the receive dish. R is 325 metres.

$$\text{Power density at receive dish} = \frac{P_T G_T A_R}{4\pi R^2} \frac{G_R}{4\pi R^2}$$

Note the distance between the retroreflector and the transmit and receive dishes is the same distance R. The power collected by the receive dish (P) depends on the effective area of the dish (A) with an allowance for the efficiency of the receive dish.

$$\text{Power received by receive dish} = P = \frac{P_T G_T A_R}{4\pi R^2} \cdot \frac{G_R A}{4\pi R^2}$$

The geometric losses are then

$$\frac{P}{P_T} = \frac{G_T A_R G_R A}{(4\pi)^2 R^4}$$

The frequency sensitive components in the above equation are the gains of the transmit and receive dishes and the retroreflector. The geometric losses for 58.11875 GHz frequency is 59.3 dB and for 53.975 GHz frequency is 60.6 dB. Adding the atmospheric losses gives the total signal losses in the atmospheric path as 68.3 dB at 58.11875 GHz and 62.6 dB at 53.975 GHz. These losses agree well with the measured signal levels.

4.2.4 Multipath Signals

Multipath signals are signals which propagate from the transmit dish to the receive dish but not by the expected main path or vice versa. These unwanted signals can be a problem if they contribute to a change in the received signal with changes in the atmospheric conditions. In this case by adding signals that change phase with respect to the main signal, changes in amplitude can be produced which are indistinguishable from the required changes due to atmospheric attenuation. Other ray refraction multipath effects should not be a problem here due to the short path length of 325 m. Refraction can be a problem on long communication paths.

The most significant multipath for this instrument is caused by the close proximity of the roof, of other buildings under the main transmission path. Fig. 4.10 shows plan view of the transmission path. The elevation view of the path near the laboratory is shown in Fig. 4.11. The distance from the centre of the beam to the parapet of the neighbouring roofs is 1.7 metres. The angle between the line from the transmit dish to the retroreflector and the line from the transmit dish to the furthest parapet (angle θ_1 on Fig. 4.10) is 2.25°. For this angle the signal level at the parapet for the H-plane is approximately 26 dB down with respect to the main beam, for the E-plane the signal at the parapet is approximately 27 dB down with respect to the ray propagating directly to the retroreflector. The efficiency of the reflection from the parapet is difficult to quantify, but even a 10% efficiency would mean that a signal propagating via the parapet on one pass and then directly to the receive dish on the return pass would be more than 36 dB down with respect to the direct path. The possible signals reflecting from the other parapets have a similar attenuation. Therefore any reflection from the roof should not cause a significant change in the measured signal amplitude when the phase of multipath signal changes with respect to the main signal.

The difference in number of wavelengths for the two paths at 58.11875 GHz was 5.72 λ and at 53.975 GHz was 5.31 λ. This is a very small difference and even over the most extreme changes in refractive index of the air, the phase difference would remain almost constant and produce a negligible change in the measured signal amplitude.

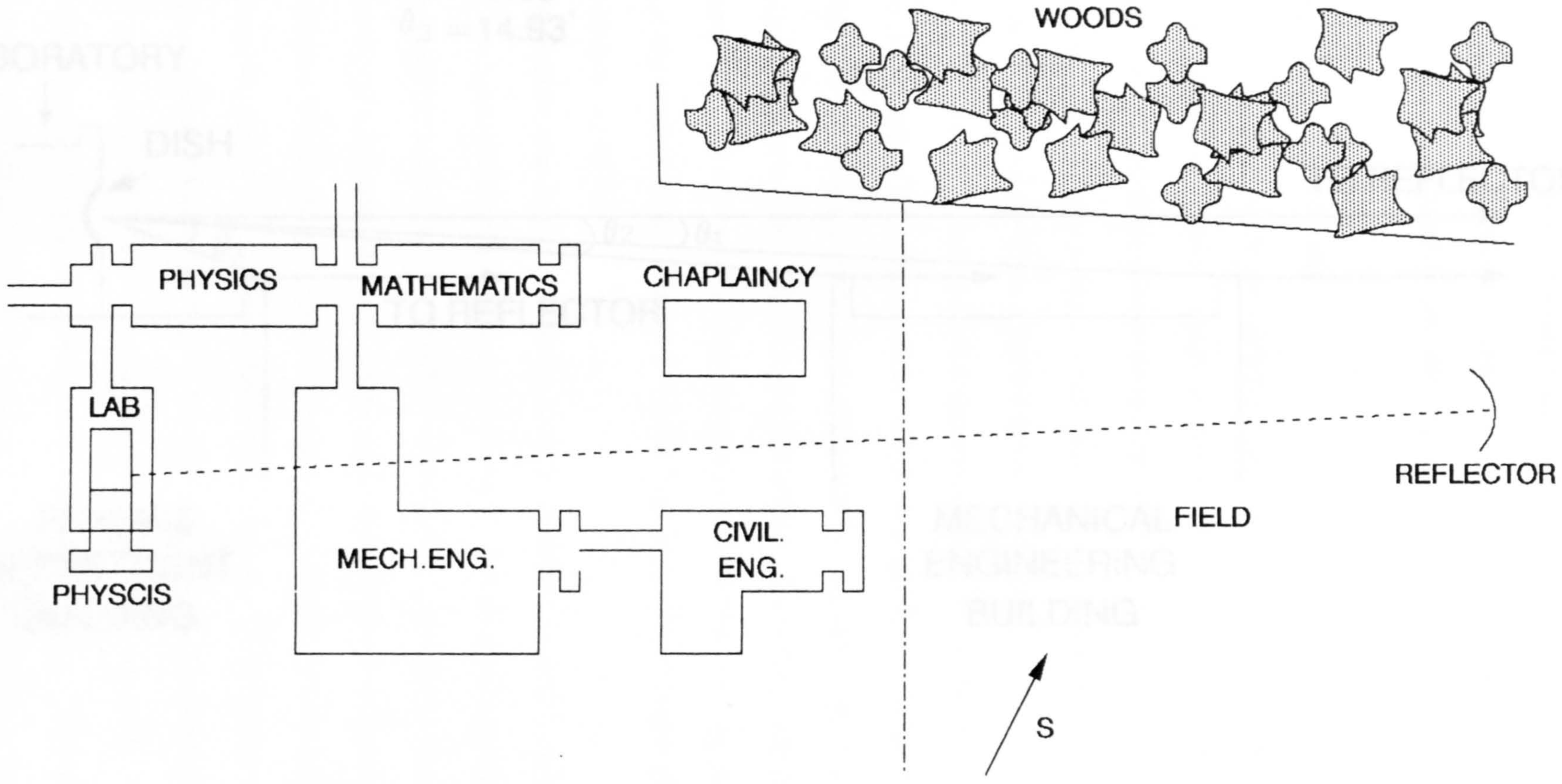

Fig. 4.10 Plan view of the atmospheric path.

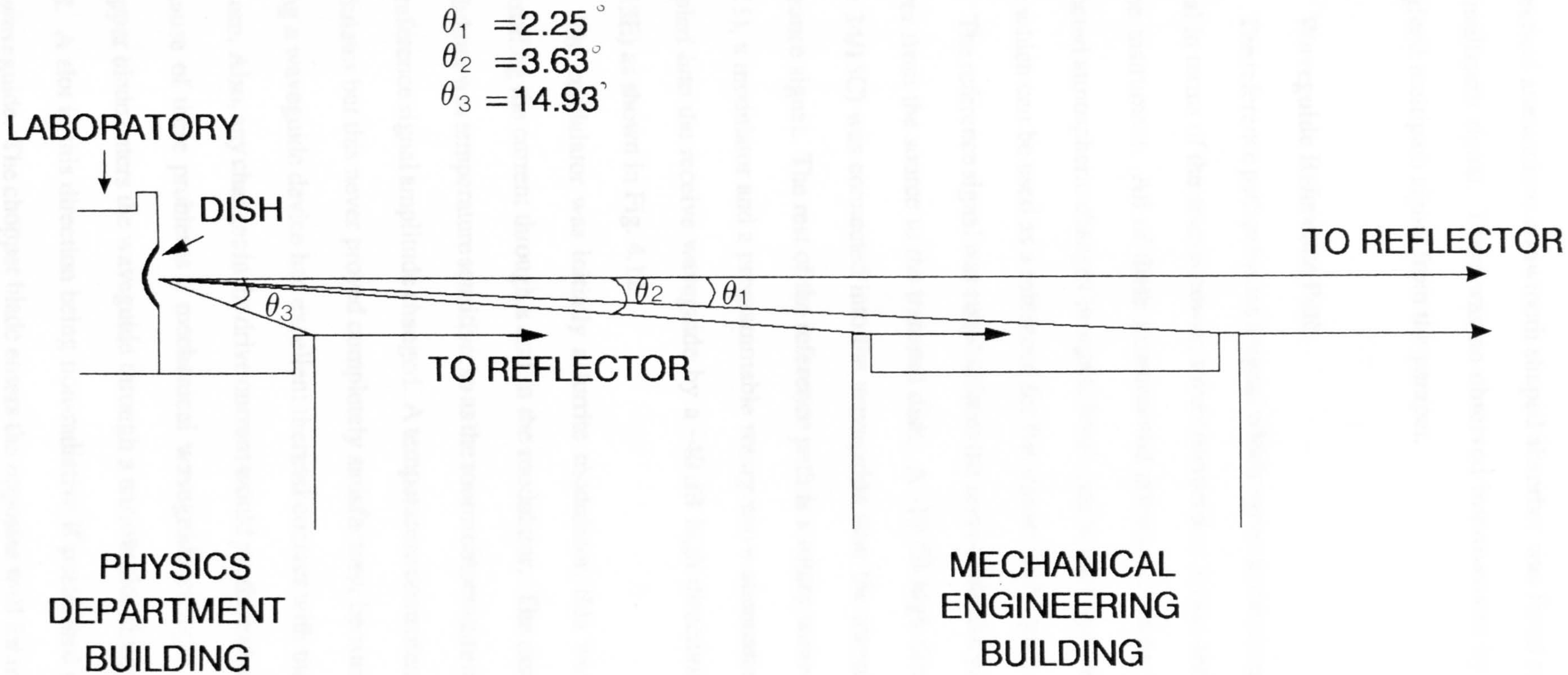

Fig. 4.11 Elevation view of the atmospheric path in the vicinity of the buildings.

In an attempt to find some of the smaller variations between the measured and theoretical attenuations a sawtooth shaped absorber was fitted to the parapet to deflect any multipath signal. There was no observed improvement by deflecting any real or imagined multipath signal from the parapet.

4.3 Waveguide Reference Path

The reference path provides a signal which varies in the same way as the transmitted signal in terms of the source power, mixer conversion losses and the gain of amplifiers in the instrument. All of these instrumental effects would be large compared to the expected atmospheric changes in signal level, hence the requirement for a stable signal path which can be used as a reference for the transmitted signal.

The reference signal was coupled from the waveguide carrying the millimeter wave power from the source to the transmit dish. A -10 dB high directivity coupler (Flann type 24/13C) was connected into the waveguide near the transmit dish to provide the reference signal. The rest of the reference path is a rotary wave attenuator (Flann type 24/11), a modulator and a programmable rotary wave attenuator. The signal was then coupled into the receive waveguide by a -40 dB high directivity coupler (Flann type 24/13E) as shown in Fig. 4.12.

The modulator was initially a ferrite modulator, this was easily modulated by controlling the current through a coil in the modulator. The disadvantage was that the modulator was temperature sensitive, so as the room temperature increased and decreased the reference signal amplitude changed. A temperature controller was fitted to the ferrite modulator but this never proved completely satisfactory, because the ferrite modulator being a waveguide device had excellent thermal contact with the rest of the waveguide system. Also, any changes in the drive current would produce changes in the modulation. Because of these problems a mechanical waveguide chopper was built. The metal chopper blade enters the waveguide through a narrow slot along the centre of the broad wall. A slot in this direction being non-radiative if positioned exactly at the centre of the waveguide. The chopper blade enters the opposite wall for maximum reflection and

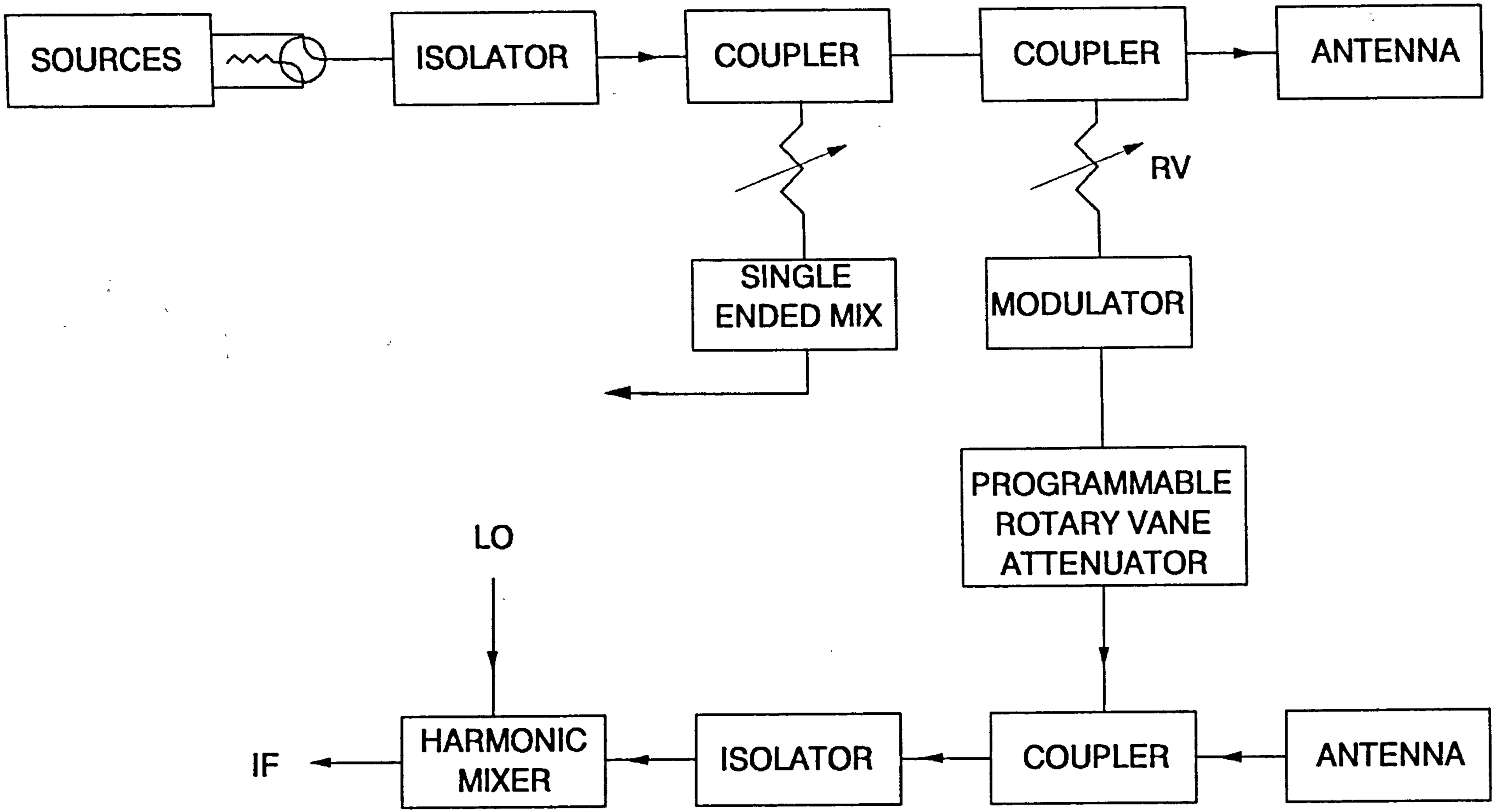

Fig. 4.12 Schematic of waveguide path.

is completely out of the waveguide for maximum transmission. The reflected power is attenuated and most of it will be dissipated in the load in the coupler, some of the power will propagate into the main line in the direction of the isolator and be dissipated. The coupling and attenuation are sufficient to ensure that any reflected power from the chopper will not contribute to the reference signal via the transmission path. The chopper was found to be very stable. The isolation between the two paths is greater than 40 dB, which is sufficient to ensure no interference between the two modulated signals.

The chopper blade is mounted on the shaft of a dc motor. The motor speed is sensed by an optical pick-up on the chopper blade and the speed control circuit is identical to the circuit used to control the corrugated reflector (Appendix C) except the loop components are slightly different due to the different motor and chopper blade.

The attenuators are used to equalise the signal levels between the two paths at the mixer and throughout the intermediate frequency (IF) stages. Equal signals should be influenced in a similar manner thus ensuring a good reference for the transmitted signal. Because the two millimetre frequencies have different attenuations, the attenuators in the reference path are required to be reset for each operating frequency. To give good resettability, a programmable rotary vane attenuator (Flann type 1124/02) was used. The rotary vane is driven by a stepper motor with an optical reference point and limit indicators for maximum and minimum positions. A schematic of the control circuit for the attenuator is shown in Fig. 4.13. The circuit has a timer to provide a pulse generator with variable frequency control for rapid movement of the attenuator. The maximum and minimum limit switches can disable the pulse stream to ensure the stepper motor does not jam against the end of the travel and damage the mechanism. LED indicators show when the limit switches have been tripped. The stepper motor can still be moved using the single shot facility to move away from the end stops. The programmable attenuator requires pulses to either increase or decrease the attenuation. These pulses are also fed to 4-decade counters with numerical displays. The counters can be set to a preset value at the optical reference point. Before each set of atmospheric attenuation measurements the programmable attenuator was reset using the optical reference to

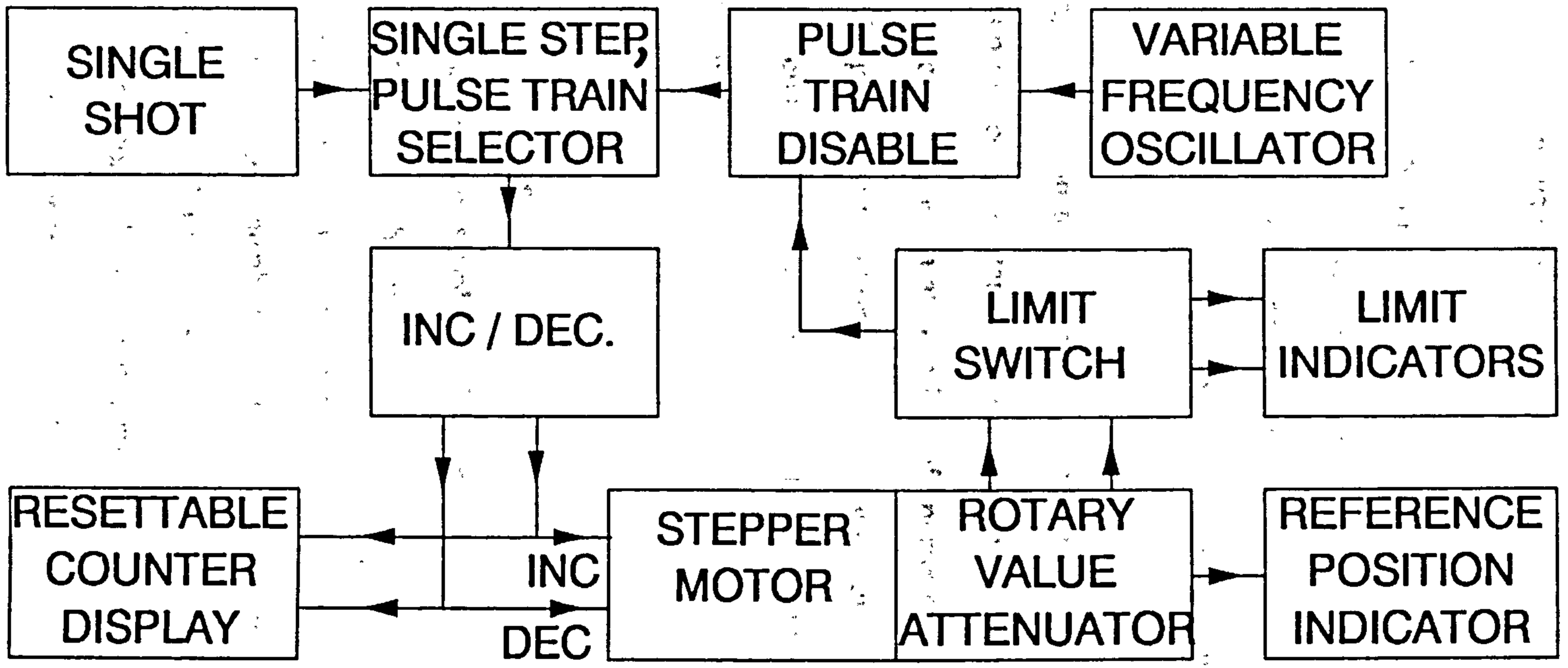

Fig. 4.13 Schematic of rotary vane control circuit.

ensure the correct attenuation setting for each operating frequency. The programmable rotary vane attenuator was set to as low an attenuation as possible as the resettability of the attenuator was best at this end of the attenuation range.

The programmable attenuator does not give exactly the same attenuation for increasing and decreasing the attenuation to a specific setting. The attenuation would vary by ~ 0.02 dB at the 10 dB attenuation setting. Therefore care was required when changing the attenuation for the two operating frequencies that the setting was approached from the same side each time with no overshoot. The attenuator settings could have been computer controlled but the number of changes in the setting was not large, so this was not implemented.

The remaining attenuation to equalise the signal levels between the signal and reference paths was provided by a rotary vane attenuator which was locked in position during measurement sets. This extra attenuation, of approximately 10 dB, also helps reduce the reflected signal from the chopper to an insignificant level. If the reflected signal was too large then a signal at the reference modulation frequency could reach the receiver via the transmit path at sufficient level to upset the stability and usefulness of the reference path.

4.4 Millimetre Wave Sources

The millimetre wave sources supply the electromagnetic radiation which interacts with the atmosphere. Because of the large change in attenuation with frequency in the region of the oxygen absorption line it is essential that the two sources are locked to a very stable frequency reference. The phase locked sources were purchased from Hughes Aircraft Corporation of USA. Figure 4.14 shows the system supplied with an additional waveguide switch and isolator. The waveguide switch was used to select the desired operating frequency while the other source is dissipated in a waveguide load. This allows both sources to be powered up at all times, which improves their stability.

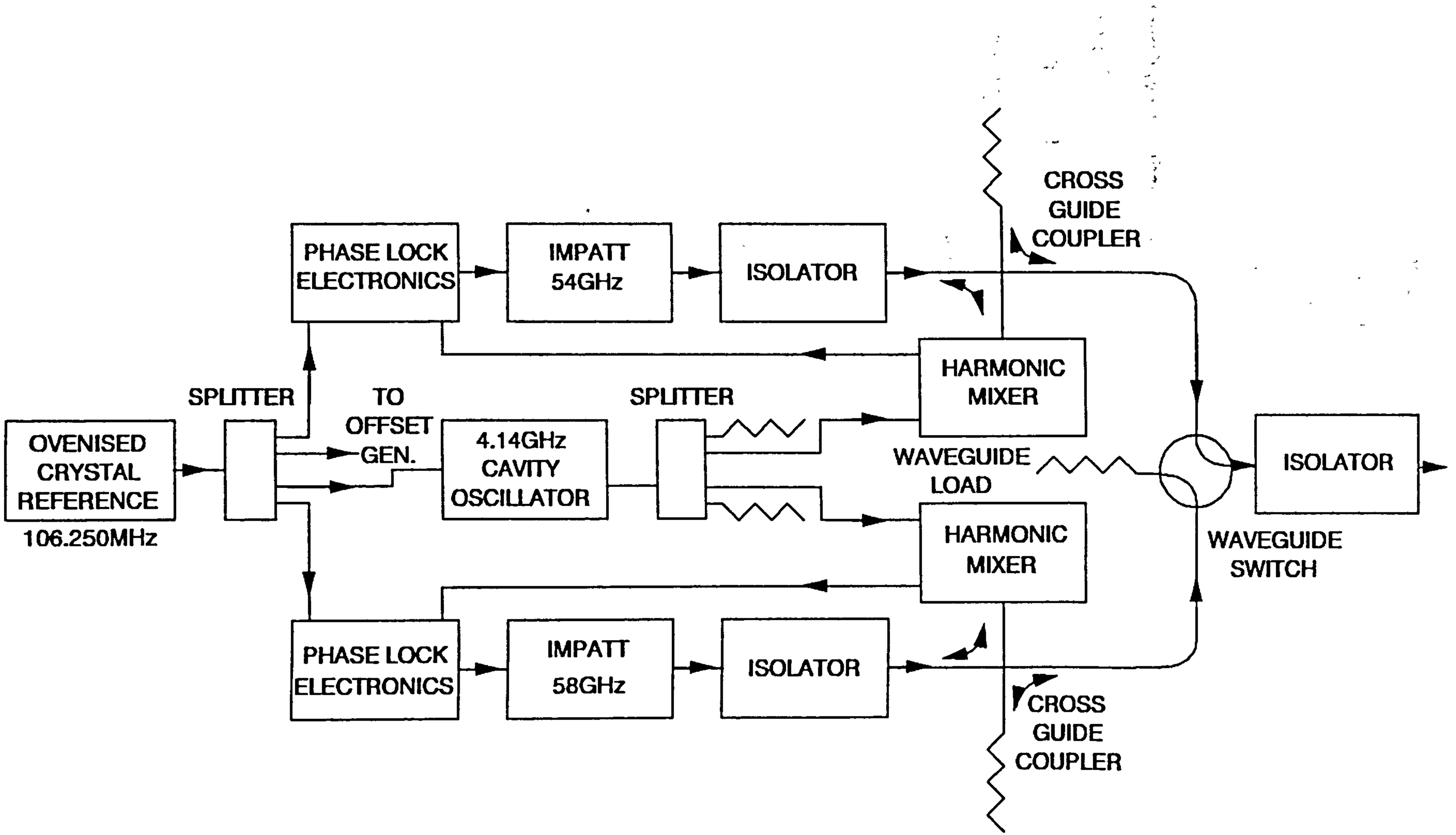

Fig. 4.14 Millimetre wave source schematic.

The millimetre wave sources are IMPATT oscillators. These were chosen in preference to Gunn oscillators to give experience in operating IMPATTS for a future satellite based system, where the required transmit powers are at least several watts. IMPATTS are the only solid state sources near capable of these output power levels. The power output of the sources for the transmissometer were less than 100 mW, which could have been provided by a gunn oscillator. The disadvantage of IMPATTS is that they have a higher noise level than gunns and their operating conditions are much more critical.

The IMPATTS were phase locked to an ovenised crystal reference with an output frequency (f_R) of 106.250 MHz. The crystal reference was also used as the main frequency reference for the rest of the system. The crystal reference has an output power of 14 dBm which is then split into four approximately equal signals by a 4 port splitter.

Two of the reference outputs are connected directly to the phase lock electronic units for each of the IMPATTS. One of the outputs is connected to the offset generator which is described in Appendix D. Another of the outputs is fed to a high Q cavity oscillator which is phase locked to the 39th multiple of the reference. The oscillator gives an output power of + 23 dBm at a frequency of 4.14375 GHz which is connected to a 4 way splitter. Two of the outputs are terminated, the other two outputs provide the local oscillator for the harmonic mixers in the phase locked loops for the two IMPATTS.

The phase lock electronics compares the phase of the reference signal with the signal from the harmonic mixer and then controls the frequency from the IMPATT. Each IMPATT is bolted directly onto an isolator. The isolator protects the IMPATT from reflections from the rest of the system which could upset the oscillation efficiency and frequency. The signal for the phase comparison is coupled from the main waveguide with a - 20 dB cross guide coupler to the harmonic mixer. The signal is then downconverted, amplified and then fed to the phase lock electronics. The harmonic conversion for the 54 GHz source is from the 13th harmonic. The harmonic conversion for the 58 GHz source is from the 14th harmonic of the cavity oscillator.

Therefore the final output frequency is

$$f_{RF} = f_R \times 39 \times n + f_R$$

n = 13 for the 54GHz source,

n = 14 for the 58 GHz source,

f_R = 106.250 MHz.

Therefore,

$f_{FR} = 508 \times f_R = 53.975$ GHz (54 GHz)

$f_{FR} = 547 \times f_R = 58.11985$ GHz (58 GHz).

There were a few difficulties in operating these sources. The first problem was that as the IMPATTS aged, over a few months, it became necessary to reset the voltage control for the IMPATTS. This could have been easy except the control was inside the phase lock electronics unit which if tampered with violated the warranty. The system was returned to the manufacturer many times before the operation of these sources was satisfactory. Several months after the warranty had expired the 54 GHz IMPATT failed to operate. Instead of sending the whole unit back to Hughes, it was decided to buy a Plessey IMPATT and use it in place of the failed oscillator. After some trials, the Plessey IMPATT (type ATO 242) was phase locked using the Hughes phase lock electronics and this source was used for all the measurements presented in Chapter 5. The output power from the Plessey device was only 6.5 mW measured after the second isolator compared to the 58 GHz IMPATT whose output power was 38 mW at the same point. As the atmospheric attenuation at 54 GHz is about 6-7 dB less than at 58 GHz then the received signal levels were approximately the same.

All the connections in the system are either waveguide or semi-rigid cable to improve the immunity to outside interference. The sources required a 40 V and a 28 V regulated power supply. The unit has lock indicators and outputs to sample the spectrum at the downconverted input to the phase lock electronics unit.

4.5 Signal Downconvertion

The millimetre wave signals from the atmospheric path and waveguide reference path must be downconverted to the digital demodulator input carrier frequency (841 Hz) for comparison of the amplitude of the two signals. The schematic of the system is shown again in Fig. 4.15 with the mixers in the downconvertion chain labelled for identification. The input and output frequencies for each mixer are shown in Table 4.1.

The first attempt at downconvertion involved mixers labelled M1, M3 and M5. This is a three stage downconvertion to the final carrier frequency. The system was changed to that shown in Fig. 4.15 because the phase jitter was so large that the demodulated signals were very unsteady. The phase jitter arose from the large number of multiplications of the reference frequency required to produce the phase-locked millimetre wave frequencies and the downconvertion ratio is also very large. The problem was solved by taking a sample of the millimetre wave signal, before transmission, and downconverting this to produce the LO for the final downconvertion stage so reducing the phase jitter between the RF signal and LO at mixer M5. The improvement was sufficient to allow the instrument to operate satisfactorily.

This downconvertion scheme required a frequency source which was offset in frequency from the crystal reference frequency (106.250 MHz) by the final carrier frequency (841 Hz). The particular offset frequency was chosen to make the IF frequencies as similar as possible for the 54 and 58 GHz operating frequencies. The offset oscillator was built using a phase locked emitter coupled logic crystal oscillator. The required output frequency was 106.250841384 MHz. Appendix D contains details of the offset oscillator. The output from this oscillator was used as the reference for a cavity locked oscillator (Continental type PE4.2N) at 4.14 GHz which supplies the LO for the harmonic mixers.

The millimetre wave signals from the atmospheric and reference paths are combined in the -40 dB coupler (Flann type 24/13E). The two signals then pass through a waveguide Faraday isolator (TRG type V112) to the harmonic mixer (Hughes type 47484H-025). The isolator reduces reflections from the harmonic mixer travelling back

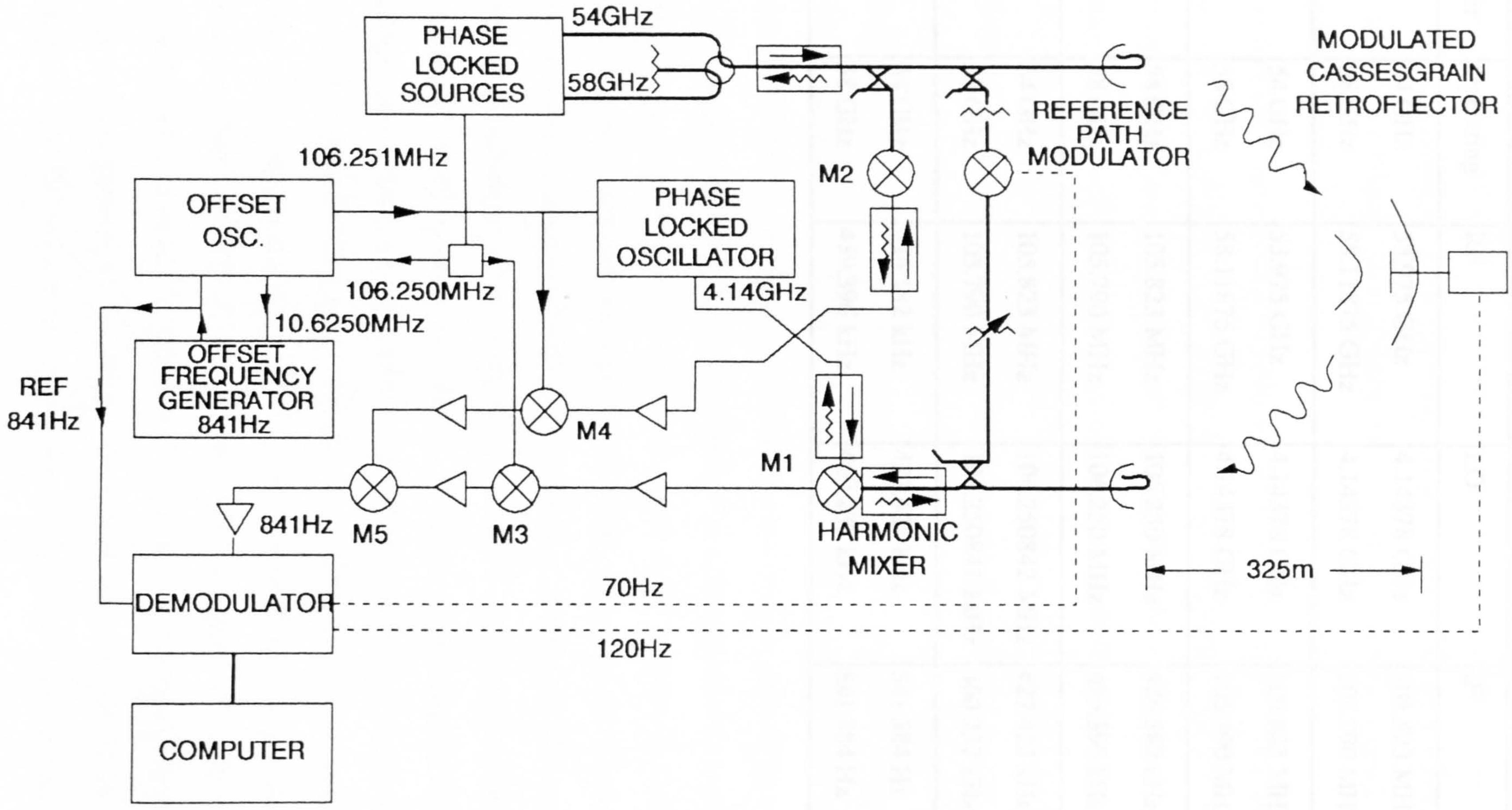

Fig. 4.15 Millimetre wave transmissometer schematic.

Table 4.1. RF Frequencies

Mixer	Operating	RF	LO	IF
M1	54 GHz	53.975 GHz	4.14378 GHz	105.823 MHz
	58 GHz	58.11875 GHz	4.14378 GHz	105.790 MHz
M2	54 GHz	53.975 GHz	4.14378 GHz	105.823 MHz
	58 GHz	58.11875 GHz	4.14378 GHz	105.790 MHz
M3	54 GHz	105.823 MHz	106.250 MHz	426.582 kHz
	58 GHz	105.790 MHz	106.250 MHz	459.396 kHz
M4	54 GHz	105.823 MHz	106.250842 MHz	427.423 kHz
	58 GHz	105.790 MHz	106.250841 MHz	460.237 kHz
M5	54 GHz	426.582 kHz	427.423 kHz	841.384 Hz
	58 GHz	459.396 kHz	460.237 kHz	841.384 Hz

along the waveguide to the antenna and being reflected back to the harmonic mixer to interfere with the initial signal. The phase of these reflections can vary with the temperature of the waveguide and so cause changes in the amplitude of the received signals. The extra loss of 1.5 dB due to the isolator decreases the signal to noise ratio of the instrument but this is outweighed by the improvement in operating conditions for the harmonic mixer.

The harmonic mixer (M1) is a simple and direct way of downconverting millimetre waves with a relatively low frequency local oscillator (LO = 4.14 GHz). Downconvertions is accomplished by mixing the millimetre wave signal with the appropriate harmonic of the LO, generated in the silicon Schottky barrier diodes. The LO is fed to the mixer by a semi-rigid coaxial line fitted with a microstrip isolator (Ferranti type 3HD350) to stop any back reflection from the mixer pulling the frequency of the 4.14 GHz cavity oscillator. The LO power at the input to the mixer was +16.7 dB which is sufficient to ensure the conversion loss will be insensitive to changes in the LO power.

The conversion loss of the harmonic mixer, when operated at the 13th and 14th harmonics for the 54 GHz and 58 GHz frequencies respectively, is approximately 30 dB. This is a high loss for the first stage of a receiver but the signal to noise ratio is still good. The mixer has an IF amplifier built into the unit with a gain of just over 30 dB. The amplifier bandwidth is 50-500 MHz which adequately covers the IF frequencies at ~ 106 MHz. The net signal loss from RF to IF was 2 dB at 58 GHz and 0 dB at 54 GHz.

The other millimetre wave mixer, M2, is a single ended mixer operated as a harmonic mixer. The LO and IF frequencies enter and leave the mixer by a common coaxial port and the millimetre wave port is in waveguide. The LO source for this mixer comes from the same 4.14 GHz cavity locked oscillator as the harmonic mixer LO. The 4.14 GHz oscillator output is equally split by a -3 dB stripline hybrid coupler. A stripline coupler was used as it can also serve as a diplexer for the single ended mixer, i.e. the LO can be fed to the mixer and the returning IF signal is guided to a separate port from the cavity oscillator port. A stripline coupler has a d.c. connection between diagonally opposite ports. The LO can couple across to the other port but any frequency outside

the design range will not couple. Therefore the IF signal coming from the mixer will follow the dc connection and not couple to any other port. The 4 GHz isolator between the coupler and the mixer M2 is a microstrip isolator which also has a dc connection from output to input which allows a low frequency, such as the IF frequency, to propagate in either direction. The stripline coupler has been used to split the local oscillator power and diplex the LO and IF signals for the single ended mixer.

The IF signals from the millimetre mixers were each amplified by their respective amplifiers. Each amplifier had a centre frequency of 100 MHz and 50 MHz bandwidth. The two signals were downconverted again in the double balanced mixers (Minicircuits type SRA-1), M3 and M4.

The IF from mixer M3 is further amplified, filtered and then mixed in mixer M5. Details of the amplifier, filter and mixing stage are shown in Appendix E. The IF from mixer M4 forms the LO for mixer M5. The signal passes through an amplifier, a 3 pole Butterworth LC bandpass filter and an emitter coupled logic limiting amplifier to produce the LO to mixer M5. Details of these circuits are also shown in Appendix E.

A notch filter based on switched capacitor filters removes the carrier frequency from the IF from mixer M5. Details of the notch are also given in Appendix E. The carrier was removed because when the two signals (one derived from the reference path and one from the transmit path) are combined the resultant carrier amplitude varies with the relative phases of the two signals. The signal gain would then have to be set such that the amplitude could not cause the analogue to digital converter in the digital demodulator to overflow. Removing the carriers allows the best sensitivity to be achieved by the digital demodulator. It is only the sidebands that are required to calculate the atmospheric attenuation.

The signal level to the digital demodulator was controlled by a variable attenuator to approximately three volts peak to peak. The spectrum of the carrier (841 Hz) with the modulation sidebands due to the retroreflector is shown in Fig. 4.16. The modulation

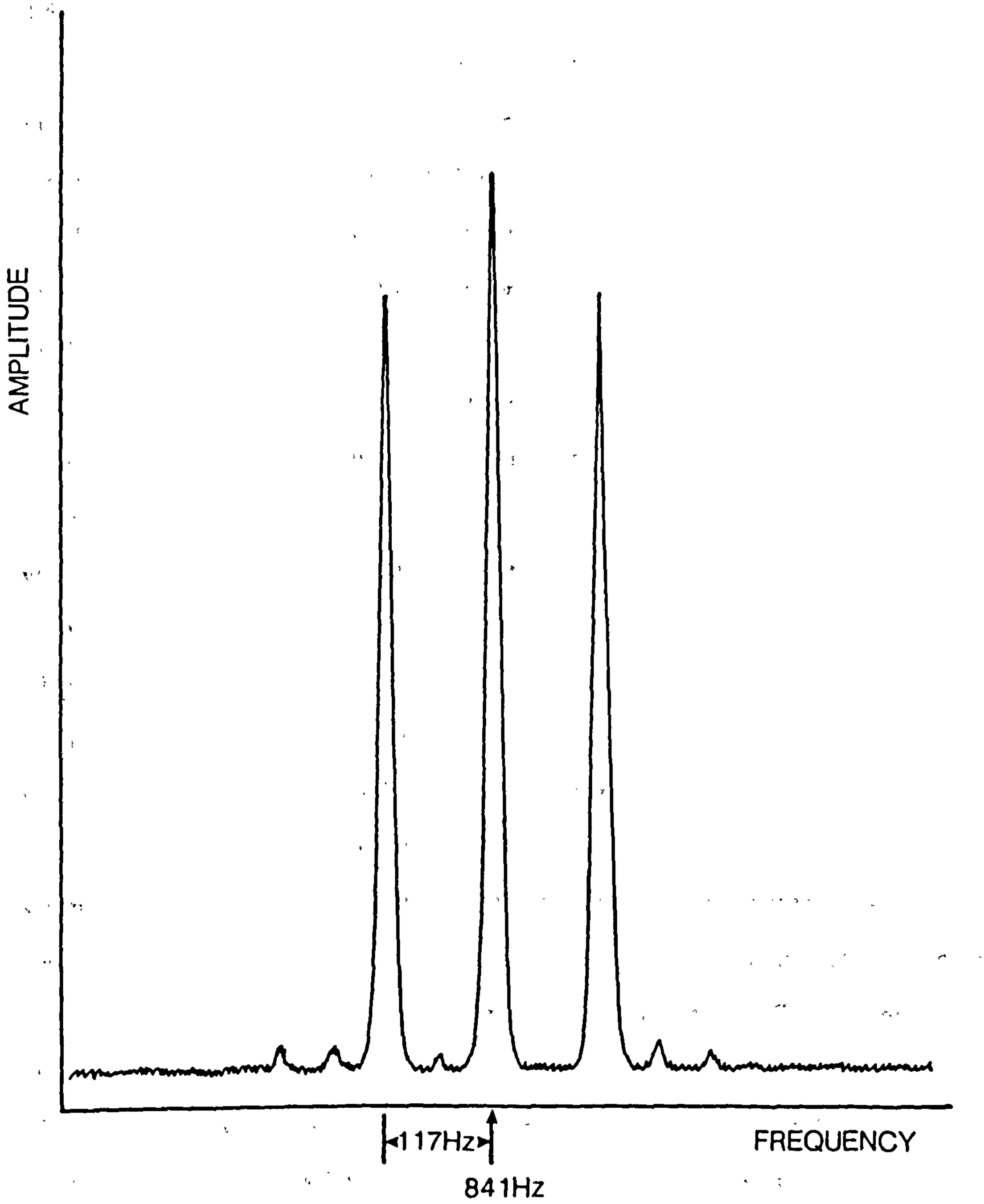

Fig. 4.16 Spectrum of the carrier with the sidebands due to the modulating cassegrain retroreflector.

is almost sinusoidal at a frequency of 117 Hz. The spectrum of the carrier and the modulation sidebands due to the waveguide chopper is shown in Fig. 4.17. The modulation is at 70.5 Hz and is almost square wave.

4.6 Digital Demodulator

A digital demodulator, consisting of a digital electronic unit controlled by a microcomputer, was built to compare the amplitudes of the two modulated signals. The suppressed carrier frequency was 841 Hz with modulation frequencies offset by 70.5 and 117 Hz. The signal was demodulated with respect to the carrier frequency and a second set of PSDs (phase sensitive detectors), one for each modulation frequency was implemented using digital algorithms.

The demodulator was initially an analogue device but suffered from several disadvantages. Dual frequency demodulation schemes involve using two separate PSDs to demodulate each signal. These PSDs will have different drift error characteristics which will not cancel. Also the analogue filters following the PSD are almost impossible to make identical. The response of these filters to transients is important in this case where the power from the IMPATTs will drift up and down with the temperature of the diode. In phase and quadrature measurements of a signal, the calculated power and phase will be affected by gain mismatch in the separate channels.

Digital demodulation or digital PSDs overcome most of these problems. In this system the signal is sampled and digitised near the input. All further processing including demodulation and filtering are carried out by digital processing algorithms. The main disadvantage of digital PSD's is that of a reduced dynamic range. The dynamic range of a good analogue PSD is approximately 10^6:1 whereas the dynamic range of a digital PSD is restricted by the range of the digitiser. In this case the analogue to digital convertor (ADC) has 12 bits, giving a dynamic range of 4096:1. This is much less than the analogue PSD but more than sufficient for this instrument.

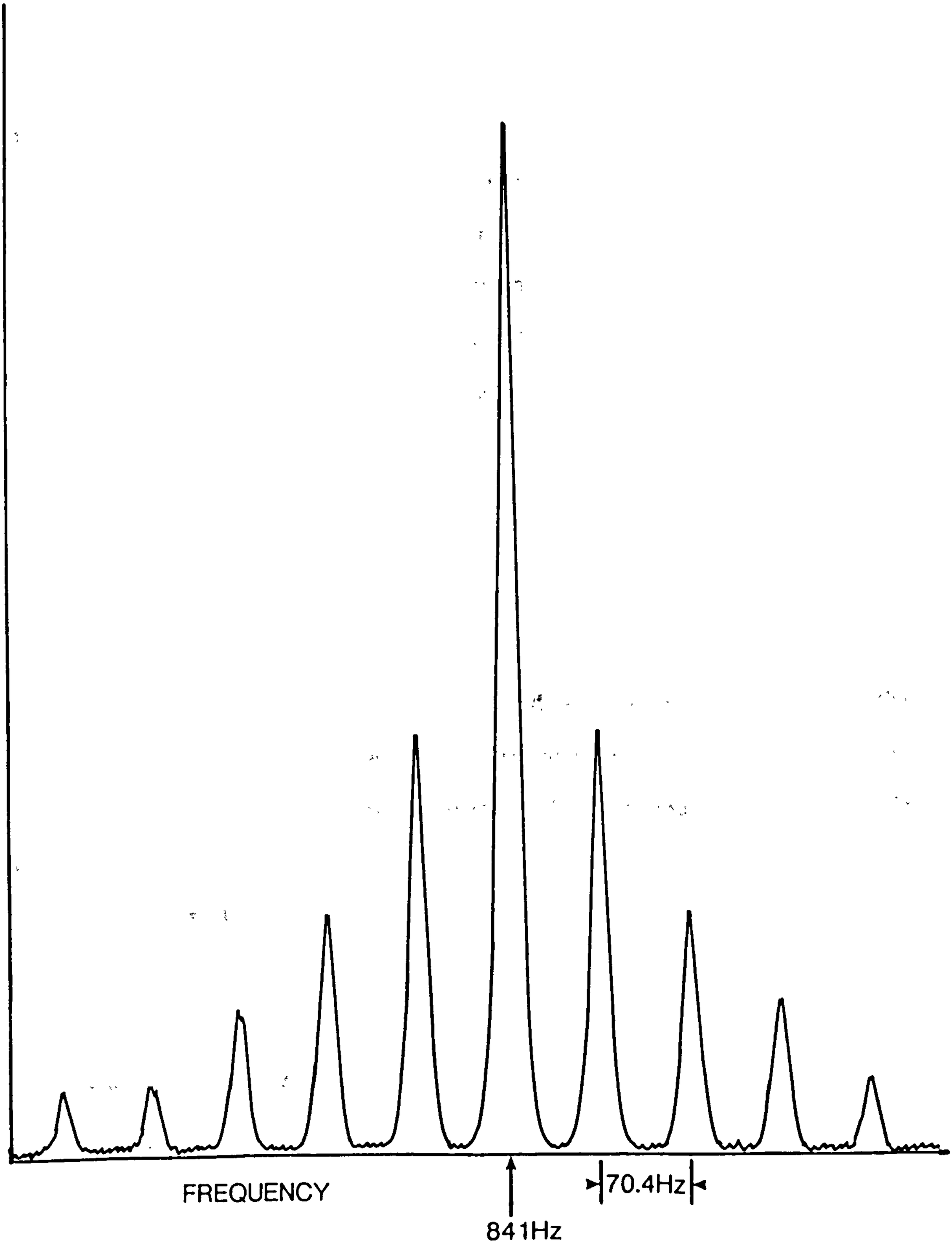

Fig. 4.17 Spectrum of the carrier with the sidebands due to the waveguide chopper.

The digitial PSD also has the advantage that the same hardware can be used to provide more complex demodulation functions, i.e. to double demodulate a signal, to provide phase and quadrature amplitudes for signals at different frequencies simultaneously. Multistage post demodulation low pass filters can be implemented. All these features can be written into the software and changed, at will, without the need to modify the hardware.

In this case where a ratioing system with dual modulation is being used the channels are not separated until after digitisation so there is no possibility of differential gain or offset drifts affecting the ratio. Digital filtering ensures that the filters on each channel have identical responses hence their response to transients and drift will be identical. The phase and quadrature components are measured through the same digitiser so they will have a common offset and gain.

The demodulation scheme employed was to sample the waveform at four equally spaced times per cycle of the carrier period, i.e. the sample frequency is exactly four times the carrier frequency. This was ensured by using an oscillator phase locked to the carrier frequency reference supplied by the offset oscillator (Appendix D).

In Fig. 4.18, if we let the four equally spaced samples be a, b, c and d. Let the phase difference between a crossover of the wave and sample 'a' be ϕ degrees, then the phase to each of samples b, c and d will increase by 90° for each sample. The amplitude of the wave can be expressed by

$$\text{Amplitude}^2 = (a-c)^2 + (b-d)^2$$

now

$$a = A \sin \phi$$

$$b = A \sin (\phi + 90) = A \cos \phi$$

$$c = A \sin (\phi + 180) = - A \sin \phi$$

$$d = A \sin (\phi + 270) = - A \cos \phi$$

where A is the amplitude of wave.

substituting

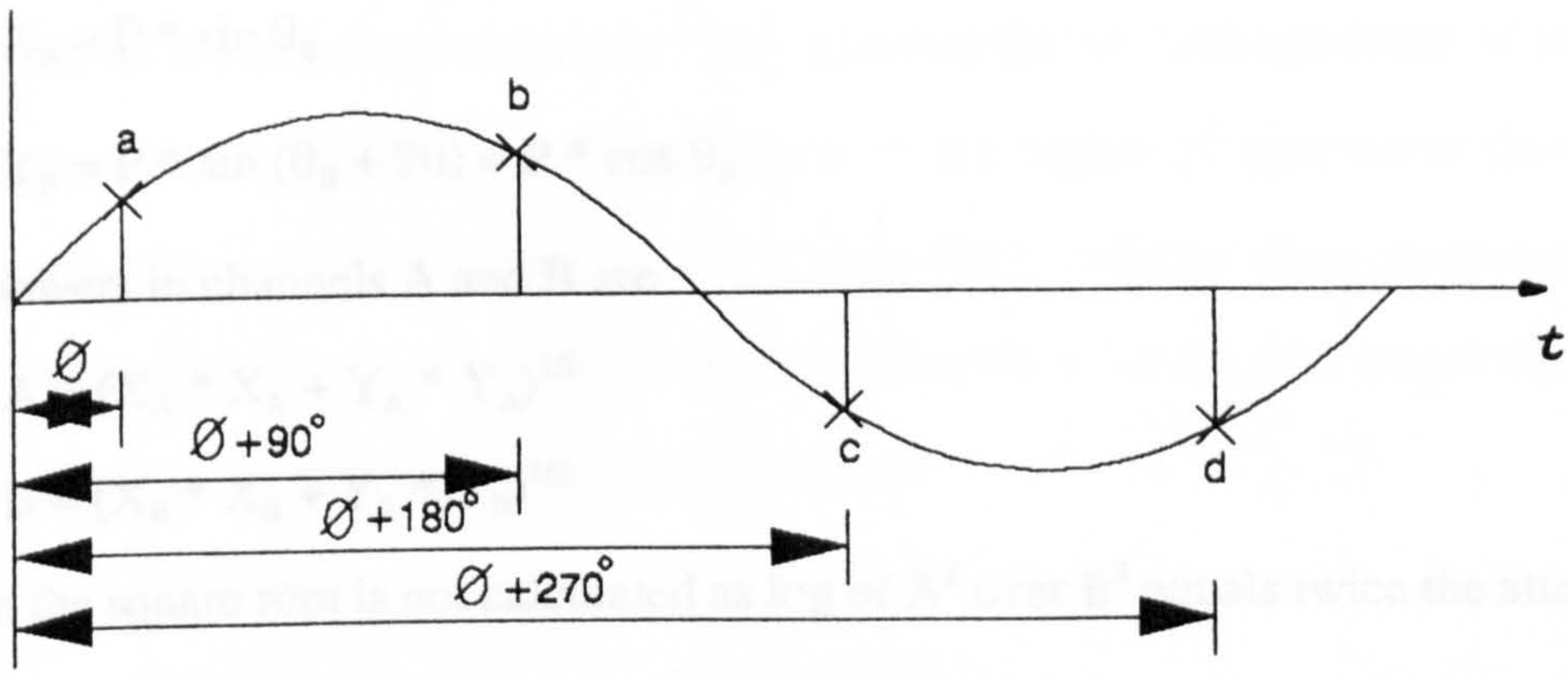

Fig. 4.18 Digital demodulator signal sampling.

$$\text{Amplitude}^2 = (\dot{A}\sin\phi + A\sin\phi)^2 + (A\cos\phi + A\cos\phi)^2$$

$$= 4A^2[\sin^2\phi + \cos^2\phi]$$

$$= 4A^2$$

The amplitude calculated by this technique is twice the real amplitude. The calculated amplitude could be scaled but in this case this is unnecessary as the resultant outputs will be ratioed.

The PSD for each of the modulation frequencies was implemented by multiplying the demodulated power by the phase and quadrature components of the reference from each modulator. The four quantities are

$$X_A = P * \sin\theta_A$$

$$Y_A = P * \sin(\theta_A + 90) = P * \cos\theta_A$$

$$X_B = P * \sin\theta_B$$

$$Y_B = P * \sin(\theta_B + 90) = P * \cos\theta_B$$

The powers in channels A and B are

$$A = (X_A * X_A + Y_A * Y_A)^{1/2}$$

$$B = (X_B * X_B + Y_B * Y_B)^{1/2}$$

Again the square root is not calculated as log of A^2 over B^2 equals twice the attenuation or

$$\text{Difference Attenuation} = 10 \log (A/B)$$

$$= 5[\log A^2 - \log B^2]$$

The accuracy of the program was checked by changing a rotary vane attenuator in the reference path and checking for the correct change in the calculated attenuation.

Digital filtering was carried out on the phase and quadrature components of the PSD section. The digital filters were second order low pass recursive Butterworth filters. These filters are based on analogue designs and their implementation is discussed in Appendix F, along with details of the hardware and software that make up this digital demodulator.

The digital demodulator proved to be accurate and stable over a wide range of carrier and modulation frequencies. There was no sensitivity to harmonic frequencies. Each demodulated channel gave identical results when fed with the same reference frequency and signal. The response of the digital demodulator to modulation frequencies is shown in Fig. 4.19. The resultant 3 dB bandwidth of the digital demodulator was 1.9 Hz. Higher than second order digital filters were impossible to implement due to the time restrictions of the sampling frequency. Machine coded sections of the program were essential in achieving reasonable processing speeds.

4.7 Atmospheric Measurements

Measurements of the atmospheric pressure, temperature and humidity are required to calculate the expected atmospheric attenuation for comparison with the value measured by the microwave system. The accuracy of the measurements of pressure, temperature and humidity are of importance to the degree of agreement that can be obtained between theory and experiment. The coefficients for pressure, temperature and water vapour density are repeated below, from Chapter 3, for the path length of 0.65 km at a nominal pressure, temperature and humidity.

Pressure:	0.0052 dB/mb
Temperature:	-0.058 dB/°C
Water Vapour Density:	-0.01 dB/gm^{-3}

The main feature of the coefficients is the relatively large sensitivity to temperature. To calculate attenuations with an equivalent accuracy of a millibar the air temperature must be known to 0.1 K. The change in attenuation due to water vapour is small. The measurement of pressure, temperature and humidity are discussed in the next three sections.

4.7.1 Atmospheric Pressure

The pressure was measured by a Cassella Microbarograph type W2600. The available pressure range was 960 to 1040 mb. The sensing unit is an evacuated flexible tensioned metal bellows made of tempered steel with welded edges. As the pressure of

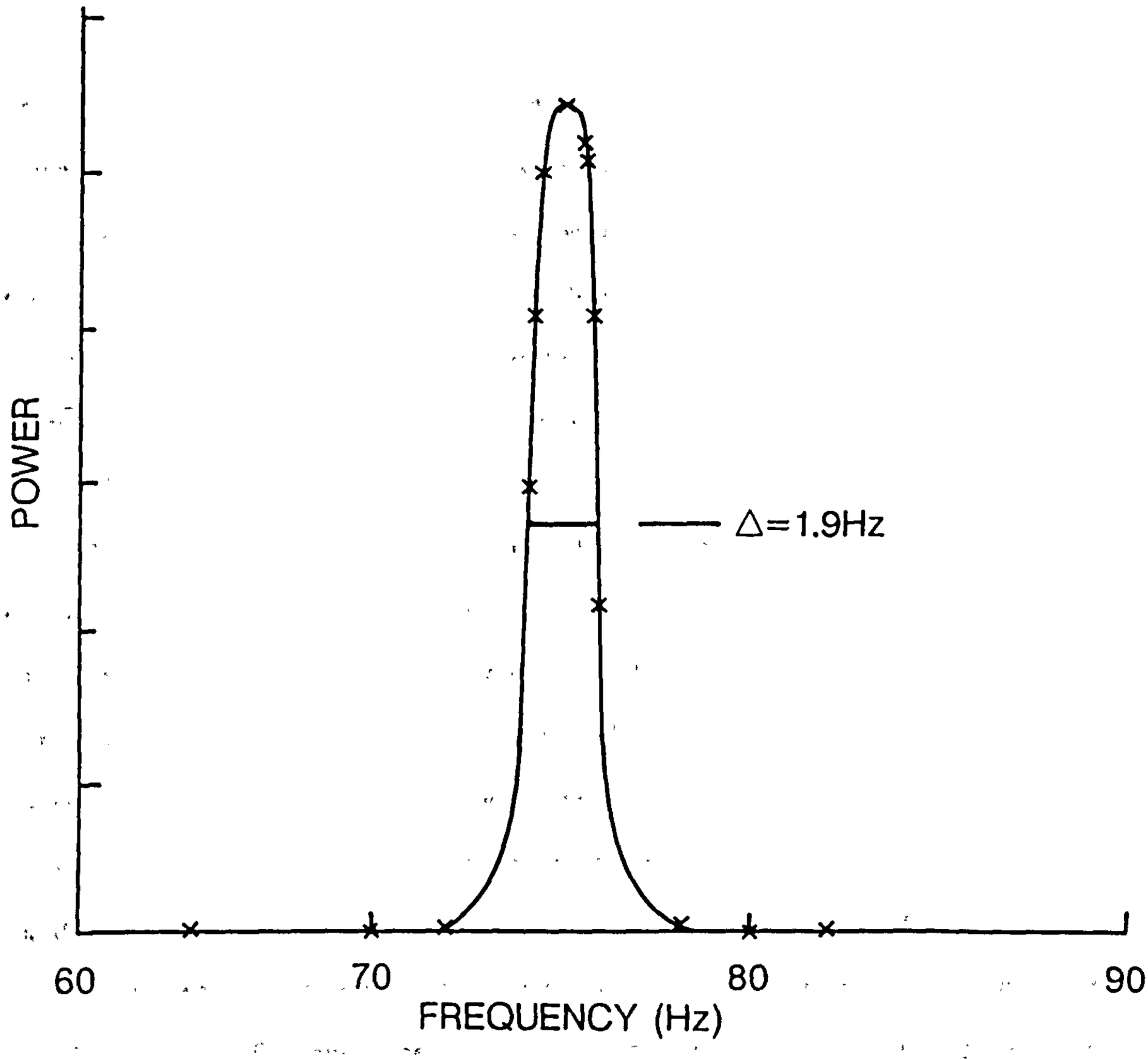

Fig. 4.19 Digital demodulator frequency response.

the atmosphere increases the vacuum chamber contracts and when the pressure decreases it expands, resulting in a change in the overall length of the sensing unit. The change in length is transmitted through a lever system to an indicator on the chart. The indicator moves 2 mm for every 1 mb change in atmospheric pressure. The instrument is temperature compensated. The microbarograph was sited in the laboratory in an easily accessible position. Only one measurement site was needed as the change in pressure over the 325 metre distance from the laboratory to the reflector is expected to be less than a millibar.

The atmospheric pressure was recorded to the nearest millibar. The readings were periodically calibrated against a mercury barometer. The microbarograph did not require any adjustment during the measurement sets and provided consistent measurements.

The microbarograph was used for all measurements except for one data set where the pressure fell to 942 mb. In that instance the mercury barometer readings were taken and these were also checked against the nearby Meteorological Station readings, allowing for the difference in altitude between the two sites.

4.7.2 Atmospheric Temperature

The atmospheric temperature is required to be measured to 0.1 C due to the strong temperature coefficient compared to the pressure coefficient. Unlike the pressure, variations in the atmospheric temperature can be expected over the length of the transmission path (325 m). There are several solutions to measuring the temperature at the remote location of the retroreflector. The temperature could have been measured by a standard platinum resistor thermometer, recorded and read at a later time. This had the disadvantage that, (a) the data must be physically retrieved each day, and (b) that any fault in the temperature measuring system would not be found until some time later.

The choice of temperature measurement system was to use a three terminal adjustable current source whose sense voltage is used to establish the operating current, which is directly proportional to absolute temperature. The sensor element was an LM134H which has a true floating current source with no separate power supply connection. This makes the device ideal for remote sensing applications because changes

in the series resistance in long wire runs do not affect the current flow. The output current is directly proportional to absolute temperature in degrees Kelvin. The absolute value of the current was controlled by an external resistor. Details of the circuitry and setting up procedure for the temperature sensing unit are discussed in Appendix G. The unit measures both the wet and dry bulb temperatures.

The dry bulb measurements gave good agreement with a mercury bulb thermometer in a Stevenson screen, within the limits of the measurement accuracy of 0.1 C. The readings on the DVM could have been read to more digits but this was not done as even although the reading would be correct for the air in the sensor, it would not necessarily be correct for the air along the path. How well the air is mixed to an even temperature is a source of error. Meteorological standards assume that a temperature measurement only represents the true air temperature to within ± 0.3 C. The error depends on how well the air is mixed. The measurement of air temperature makes a large contribution to the final errors between theoretical and experimental atmospheric attenuations.

4.7.3 Relative Humidity

Although the atmospheric attenuation sensitivity to water vapour was not large, it was still significant in the calculations of the relative attenuations of millimetre waves in air. The initial intention was to measure the water vapour density by a wet bulb and dry bulb measurement incorporated in the temperature sensors described in Appendix G. Several difficulties were found.

(a) The wet bulb temperature depression was only half that of a whirling psychrometer. This was due to a lack of air flow over the sensor. This could have been corrected by either increasing the air flow or recalculating the water vapour density for a lower temperature depression.

(b) The overriding problem was that the wick on the temperature sensor dried out on occasions. The reason for this is uncertain. The length of wick from the distilled water bottle in the sensor is quite long, but is shielded in a small pipe and only exposed near the sensor. Standard wet bulb wicks were used and several alternatives were tried but the problem persisted.

The alternative was to use a hair hygrometer. The type used was a Casella T9154, which is thermohygrograph. The relative humidity (RH) is sensed by changes in length of specially treated human hair. A series of levers are connected to a pointer to indicate the relative humidity on a chart. The chart can be read to an accuracy of 1% RH with a quoted accuracy of ± 3% RH. The accuracy was found to be about ± 1% RH when compared with a whirling psychrometer. Comparisons were made at various times throughout the measurements to check for changes in calibration. No changes were observed.

The thermohygrograph was placed in a Stevenson screen, not far from the laboratory, so readings could be taken at frequent intervals.

4.8 Instrument Signal to Noise Ratio

The signal to noise of the millimetre wave system can be calculated by first estimating the equivalent noise power at the input to the harmonic mixer and comparing it with the signal level at the same point in the system. The comparison could be made at any other point in the system, but the input to the harmonic mixer is the most convenient. Fig. 4.20 shows a schematic of the microwave system starting from the harmonic mixer, through to the second IF amplifier.

The standard formula [ref. 4.4] for calculating the contribution of later stages to the overall noise temperature is given by

$$T_e = T_1 + \frac{T_2}{G_1} + \frac{T_3}{G_1 G_2} + \ldots$$

where T_e is the effective noise temperature at the input to the harmonic mixer assembly, T_1, T_2 and T_3 are the equivalent noise temperature of the first three stages and G_1 and G_2 are the gains associated with the first two stages respectively. Later stages than the third have not been included as their contribution is very small in comparison with the early stages. The noise figure and gain for each stage is shown in Fig. 4.20. The noise temperature of a stage is given by

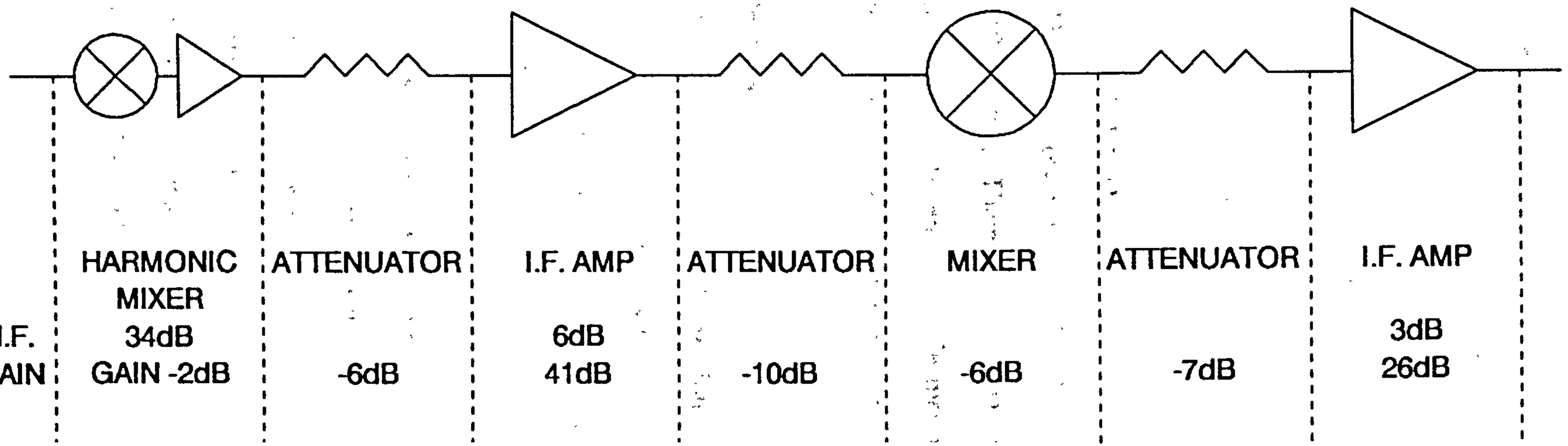

Fig. 4.20 Schematic of the receiver system from the harmonic mixer to the second I.F. amplifier.

$$T_n = (F_n - 1) \times T_o$$

where T_n is the n^{th} stage noise temperature, F_n is the noise figure for the n^{th} stage and T_o is the physical temperature of the n^{th} stage in degrees Kelvin.

Substituting the values for noise temperature and gain into the equation for T_e gives the effective noise temperature at the input to the harmonic mixer as 735943 K. This value is almost completely dominated by the harmonic mixer noise temperature.

The noise power at input to the harmonic mixer is given by

$$P = kB\,T_e$$

where P is the noise power, k is Boltzmann's constant and B is the final 3 dB bandwidth of the system (1.9 Hz). The noise power is 1.9×10^{-17} Watts. The signal level at this point is - 56 dBm (2.5×10^{-9} Watts). Therefore the signal to noise is approximately 1.3×10^{8}. The signal to noise is sufficient to enable measurements of atmospheric attenuation to be made to an accuracy consistent with the aims of the experiment.

4.9 Measurement Procedures

All the measurements reported in the results section were made using a similar measurement technique and procedure. Before any readings were taken the instrument was allowed to stabilise for about two hours to avoid rapid gain or power changes. The main source of change was the IMPATT output power which took a substantial time to stabilise.

A measurement cycle was about 8 minutes duration. The measurement sequence was to measure the attenuation difference between the atmospheric path and the reference path at 54 GHz, for just over 1.6 minutes, measure the attenuation difference at 58 GHz for the same period of time, record the atmospheric pressure, temperature, relative humidity, and other information such as was it sunny, cloudy, windy, etc. The microwave measurements then resumed with the 58 GHz differential attenuation followed by the

54 GHz differential attenuation again for the same period of time as before. The sequence of the frequency measurements was to remove any drift effects during the period of measurement, especially temperature changes.

All the data were recorded on standard record sheets which included such information as the date and time of day of the measurement, the theoretical attenuation, all the measured quantities and any notable occurrences during the measurement, such as if it rained or if any of the frequency sources lost phase lock. The standard record sheets were invaluable in ensuring all the data was recorded.

References

[4.1] "*High Loss Dielectric Microwave Absorbers*", Published by Emerson and Cuming, U.S.A.

[4.2] "*Antennas*", second edition, p. 594, by J.D. Kraus, published by McGraw-Hill Book Company, 1988.

[4.3] "*Introduction to Radar Systems*", second edition, p. 240, by M.I. Skolnik, published by McGraw-Hill International Book Company, 1980.

[4.4] "*Introduction to Radar Systems*", second edition, p. 344, by M.I.Skolnik, published by McGraw-Hill International Book Company, 1980.

CHAPTER 5

EXPERIMENTAL RESULTS AND ERRORS

The first section of this chapter contains the results from measurements of atmospheric attenuation and comparison with the theoretical attenuation calculated using the computer program in Chapter 3. The second section of the chapter discusses the random errors and the third section the systematic errors possible in the measurements and their relevance to the observed results.

5.1 Results

Three sets of results are presented. Many sets of results were recorded but these were during the period of development of the instrument, when various faults and unwanted effects were being traced. The three sets shown all have specific differences and because of changes in the instrument the data sets are not continuous.

The results are analysed and presented in three ways for each data set:

(a) The measured attenuation difference between the two frequencies is plotted against the theoretical difference attenuation, calculated from the measured barometric pressure, temperature and humidity. An unknown instrument offset is removed by equating the calculated and measured attenuation means.

(b) The attenuations are plotted as a function of time, either chronologically or as in data set II by linear time. Data Set II time span is less than sixty hours whereas the other data sets cover weeks of data with gaps in the measurements due mainly to rain, high winds or other operational difficulties.

(c) An atmospheric pressure can be deduced from the atmospheric coefficients, the measured attenuation, and temperature and humidity. This was compared with the measured pressure and plotted against time.

5.1.1 Data Set I

Data Set I represents the first series of measurements where there were some signs of a correlation between the theoretical attenuation and the measured attenuations. The instrument, at the time of these measurements, had an analogue demodulator, and a ferrite modulator for the reference path. The analogue demodulator was replaced for later data sets by a digital demodulator to improve the tracking between the two modulation channels.

The twenty-four data points which make up this set were recorded over a period of approximately three weeks. The temperature ranged from 9 to 13.9 C, the pressure from 962 to 1004 mb and the relative humidity from 58 to 86%. The two transmission frequencies were measured for a period of 10 minutes, with interleafed readings to reduce the effects of instrument and atmospheric drift.

The plot of experimental attenuation versus theoretical attenuation (calculated from the measured pressure, temperature and humidity) is shown in Fig. 5.1. The plot shows a reasonably good correlation.

Fig. 5.2 shows the theoretical and experimental attenuations as a function of time. The time between points varies from half an hour to several days. The main variation in the attenuation is due to air temperature changes. The barometric pressure is also compared with the deduced atmospheric pressure in Fig. 5.3. The standard deviation between the two pressures was 4.1 mb.

This data set shows that the atmospheric pressure can be obtained even when the attenuation is dominated by changes in the air temperature.

5.1.2 Data Set II

This data set was recorded over a three day period as a large depression, centred near Edinburgh, moved away. There are only ten data points in the set taken during a short dry spell. The lowest pressure was 942 mb recorded with a mercury barometer as the microbarograph normally used for measuring the pressure was out of range. All the pressure measurements in this data set were made with the mercury barometer. The data

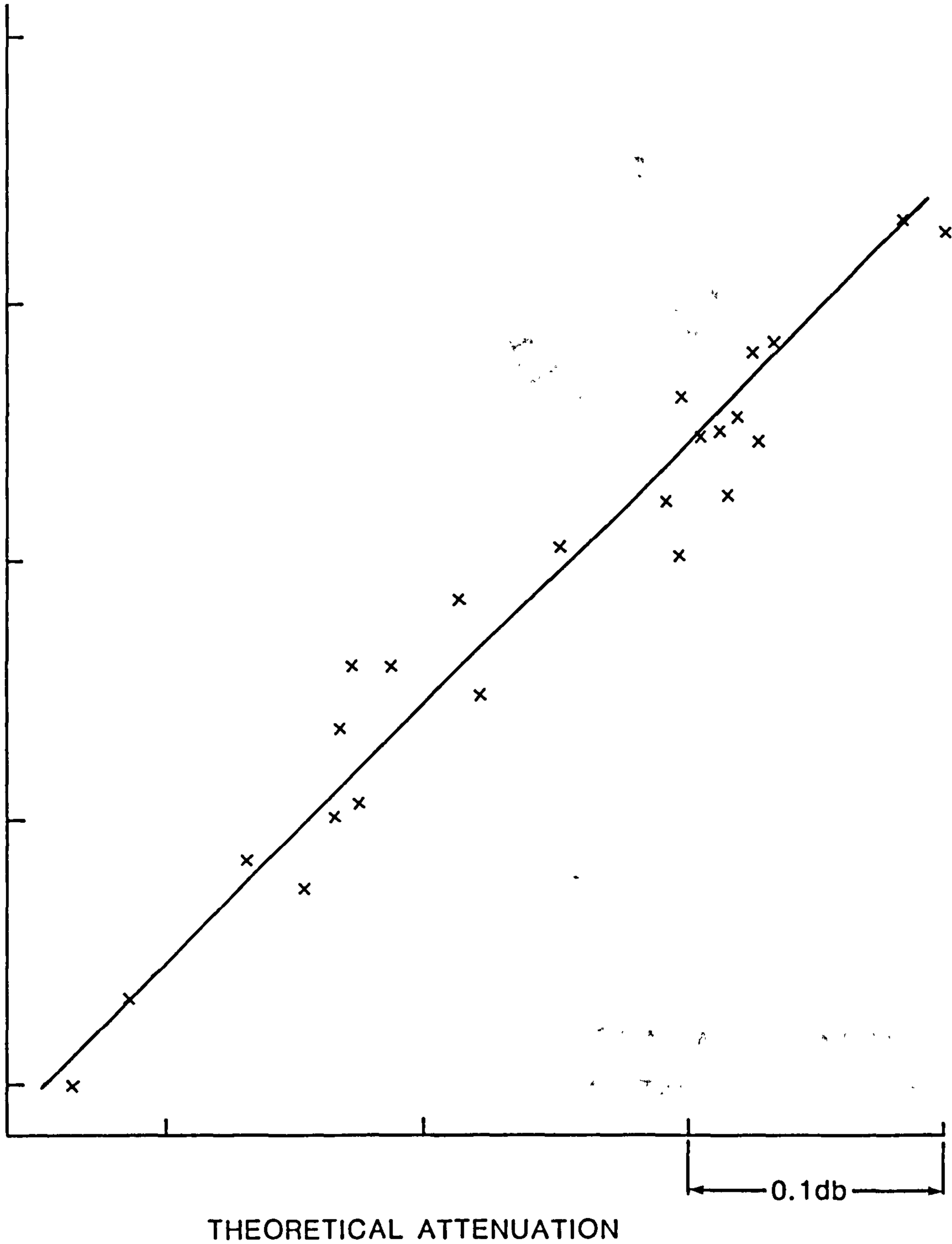

Fig. 5.1 Data Set I: Experimental attenuation vs. theoretical attenuation.

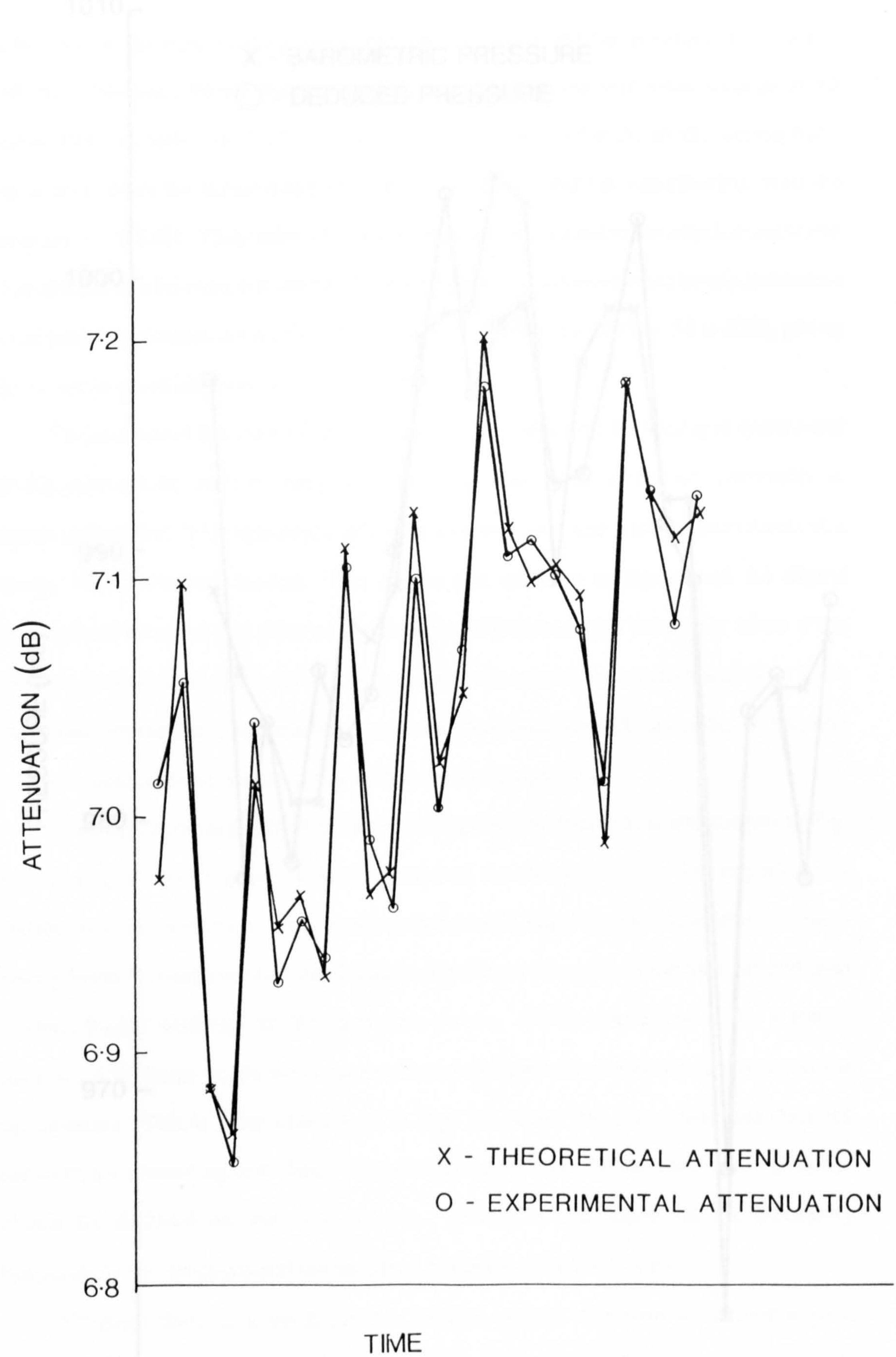

Fig. 5.2 Data Set I: Experimental and theoretical attenuation vs. time.

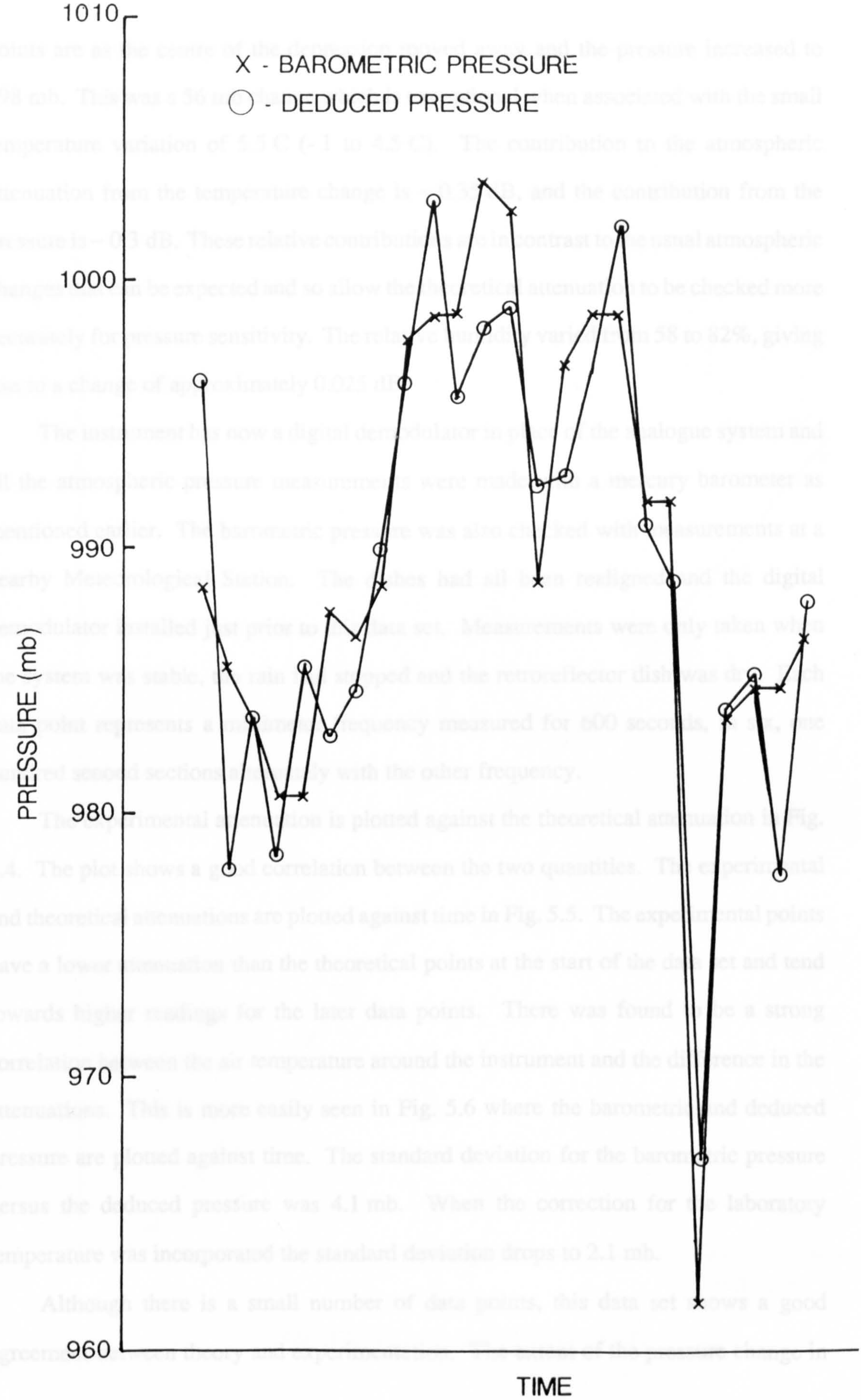

Fig. 5.3 Data Set I: Barometric and deduced pressure vs. time.

points are as the centre of the depression moved away and the pressure increased to 998 mb. This was a 56 mb change which is exceptional when associated with the small temperature variation of 5.5 C (- 1 to 4.5 C). The contribution to the atmospheric attenuation from the temperature change is ~ 0.35 dB, and the contribution from the pressure is ~ 0.3 dB. These relative contributions are in contrast to the usual atmospheric changes that can be expected and so allow the theoretical attenuation to be checked more accurately for pressure sensitivity. The relative humidity varied from 58 to 82%, giving rise to a change of approximately 0.025 dB.

The instrument has now a digital demodulator in place of the analogue system and all the atmospheric pressure measurements were made with a mercury barometer as mentioned earlier. The barometric pressure was also checked with measurements at a nearby Meteorological Station. The dishes had all been realigned and the digital demodulator installed just prior to this data set. Measurements were only taken when the system was stable, the rain had stopped and the retroreflector dish was dry. Each data point represents a millimeter frequency measured for 600 seconds, in six, one hundred second sections alternately with the other frequency.

The experimental attenuation is plotted against the theoretical attenuation in Fig. 5.4. The plot shows a good correlation between the two quantities. The experimental and theoretical attenuations are plotted against time in Fig. 5.5. The experimental points have a lower attenuation than the theoretical points at the start of the data set and tend towards higher readings for the later data points. There was found to be a strong correlation between the air temperature around the instrument and the difference in the attenuations. This is more easily seen in Fig. 5.6 where the barometric and deduced pressure are plotted against time. The standard deviation for the barometric pressure versus the deduced pressure was 4.1 mb. When the correction for the laboratory temperature was incorporated the standard deviation drops to 2.1 mb.

Although there is a small number of data points, this data set shows a good agreement between theory and experimentation. The extent of the pressure change in

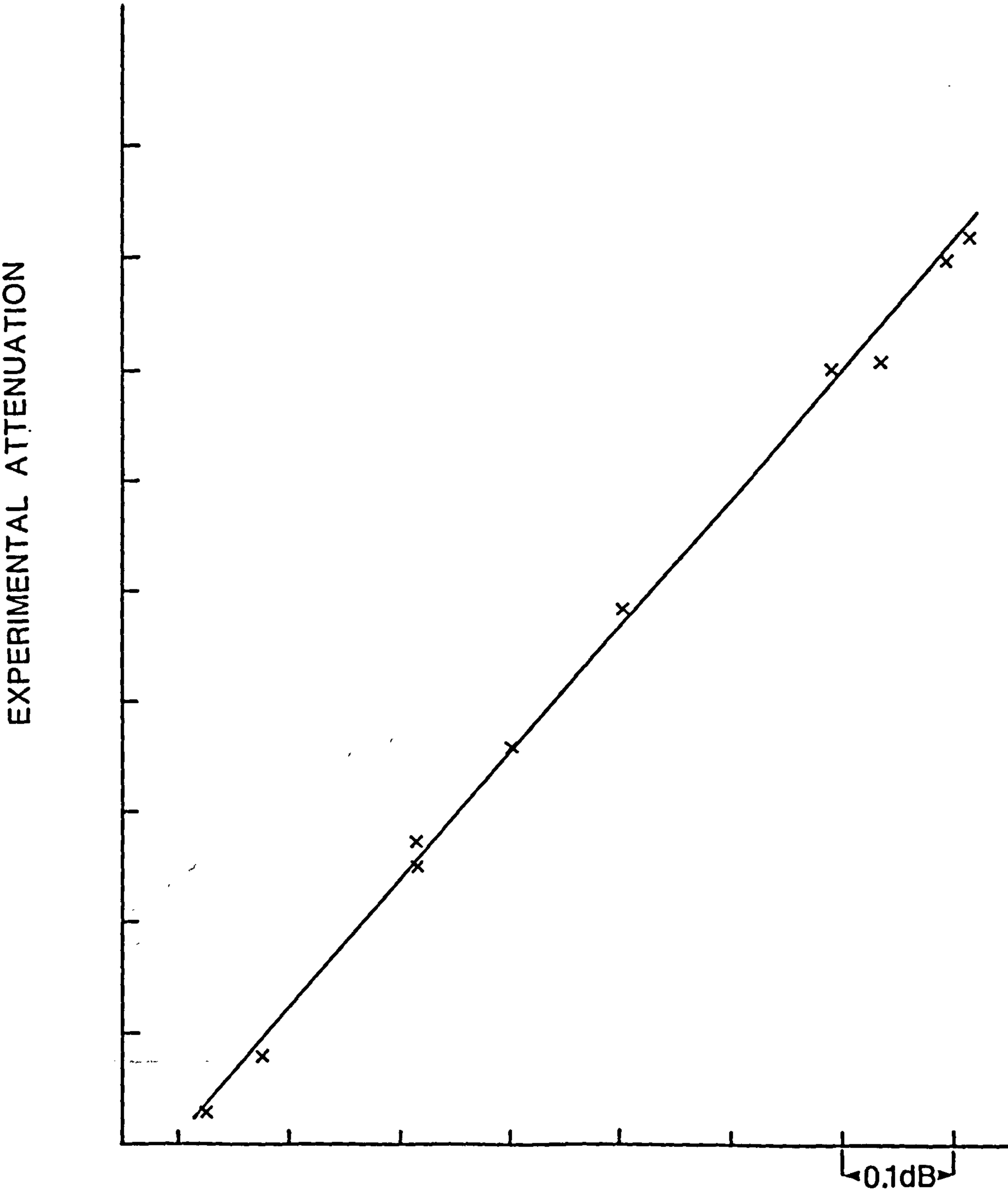

Fig. 5.4 **Data Set II: Experimental attenuation vs. theoretical attenuation.**

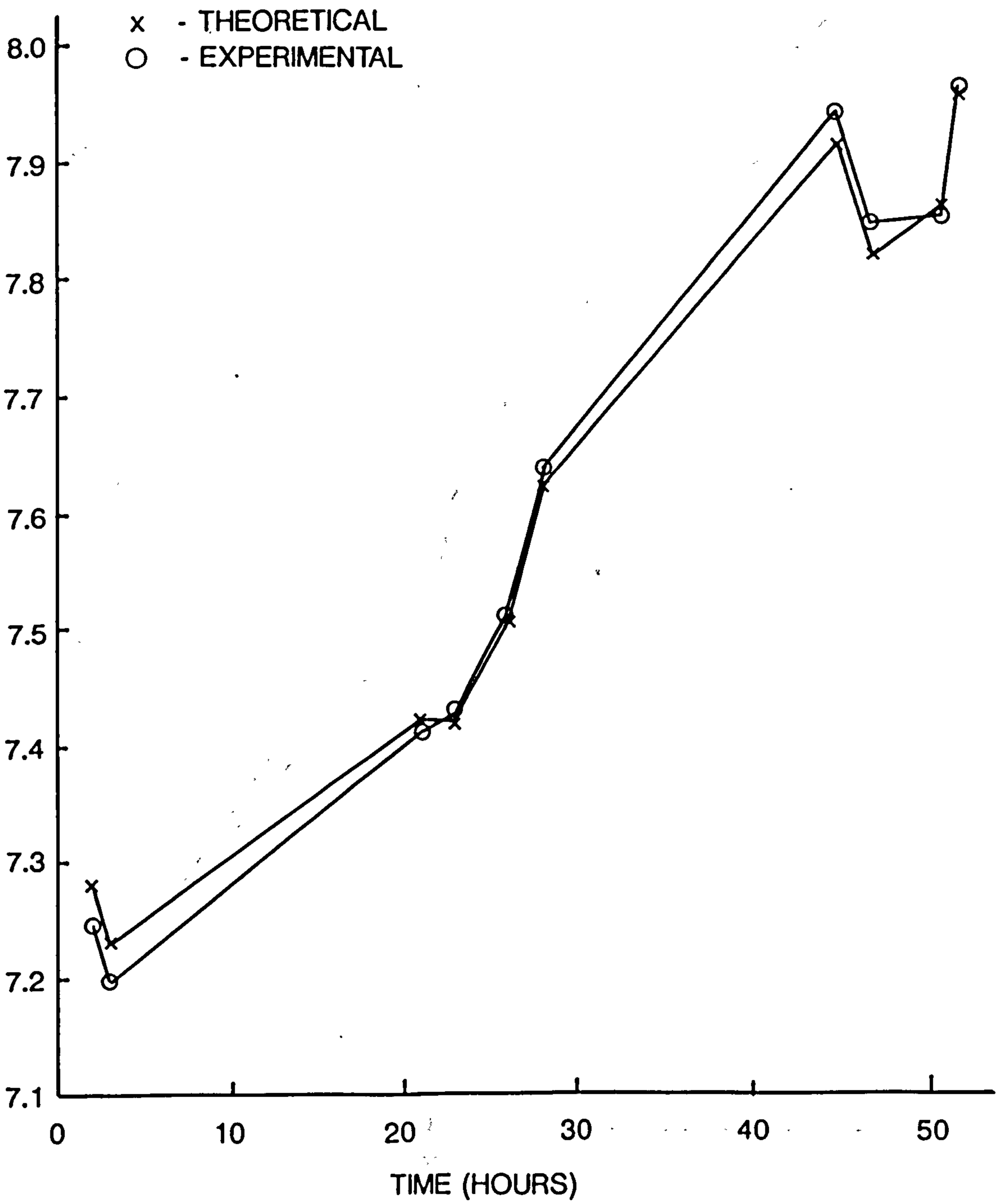

Fig. 5.5 Data Set II: Experimental and theoretical attenuation vs. time.

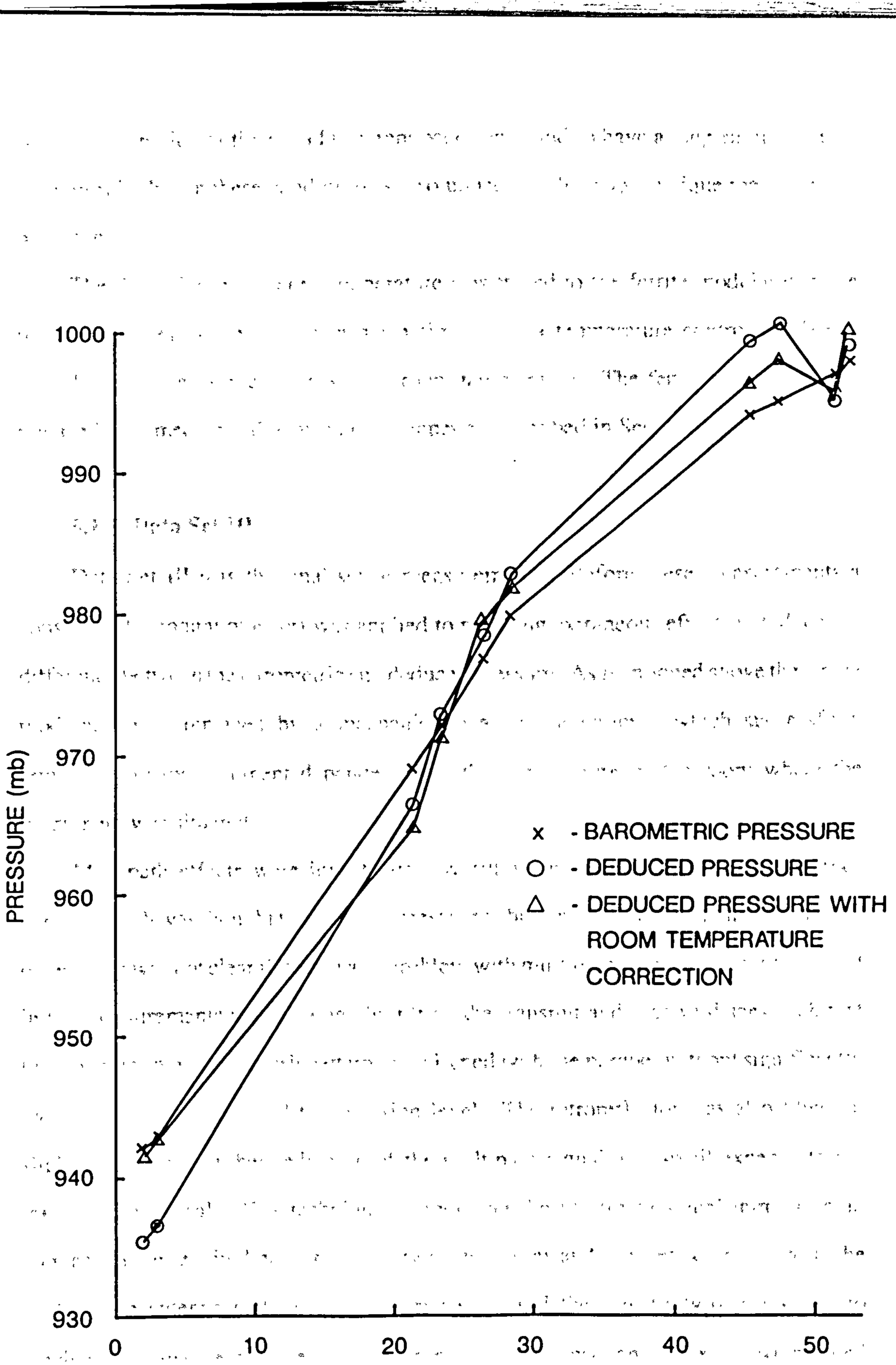

Fig. 5.6 Data Set II: Barometric and deduced pressure vs. time.

such a short period of time is a fairly rare occurrence and to have a long enough period without rain during these conditions is also unusual. This was a unique measurement opportunity.

The dependence on room temperature was traced to the ferrite modulator in the reference waveguide path. Even when fitted with a temperature control the ferrite modulator showed some sensitivity to room temperature. The ferrite modulator was replaced by a mechanical waveguide chopper as described in Section 4.3.

5.1.3 Data Set III

Data Set III was the final set of measurements. Before these measurements a considerable amount of effort was applied to reducing extraneous effects to reduce the difference between the barometric and deduced pressure. As mentioned above the ferrite modulator was replaced by a mechanical waveguide chopper which successfully removed any measurement dependence on the temperature of the room where the instrument was situated.

Multipath effects were investigated by fitting microwave absorber to the roof parapet which was thought to give the largest contribution. Even after extensive amounts of testing it was not clear if there was a problem with multipath signals. An improvement in the measurements was obtained by tilting the transmit and receive dishes such that the first minimum of the dish pattern was aligned with the parapet without significantly reducing the wanted signal transmission level. The retroreflector was also tilted up slightly to give a further reduction of the multipath signal at a small expense to the transmission signal. This technique of reducing the multipath signal introduces an increase in the required pointing stability of the dishes and retroreflector. Because the peak of the antenna pattern is no longer being used the sensitivity of the signal to mechanical movement of the dishes is increased. The mechanical fixings were found to have an adequate stability, but the dishes and consequently the signal level, would be more sensitive to strong winds. This introduced a further restriction on the weather conditions under which measurements of atmospheric attenuation could be recorded.

This data set has 112 readings taken over a period of 6 weeks. The sample time was reduced from 600 seconds in previous data sets to 200 seconds due to improvements in signal stability. This reduction in integration time also reduces the possible changes in temperature during the sampling period. Previously, a measurement would span a period of 30 minutes, due to changing frequencies and resetting the rotary vane attenuator. By reducing the sampling time to 2×100 second periods per frequency, a measurement could be completed in six minutes, thus minimising any drift in air temperature during the measurement.

The changes in pressure range for this data set is 962 to 1013 mb. The range is reasonably large and has the advantage of long periods where the pressure is almost constant. The temperature varies from - 7 to + 7 C and the humidity ranges from 65 to 84% relative humidity which is equivalent to a change in water vapour density from 1.9 to 6.5 gm^{-3}. The total change in differential attenuation was approximately 1.4 dB as shown in Fig. 5.7. The correlation between theoretical and experimental attenuation is good. Fig. 5.8 shows the theoretical and experimental attenuations plotted against time. Again the time scale is not linear but chronological data points plotted at regular intervals. The deduced pressure and barometric pressure are plotted in Fig. 5.9. The deduced pressure follows the barometric pressure closely except at several places where there is an obvious offset. The standard deviation for the data set is 3.7 mb. For some parts of the plot the standard deviation is much lower, for example, the standard deviation for the first 28 points in 2.3 mb. An important feature is that even although the elapsed time between data points 66 and 67 is 14 days, there is no apparent sign of a discontinuity in the agreement between the theoretical and experimental attenuations. The alignment of the system has remained stable.

The error between the experimental and theoretical differential attenuations is plotted with respect to time in Fig. 5.10, along with the calculated errors for each of the millimetre wave frequencies. The benefit of using two frequencies, in which one is used as a reference for the other, is clearly seen. The reason for changes in the two millimetre

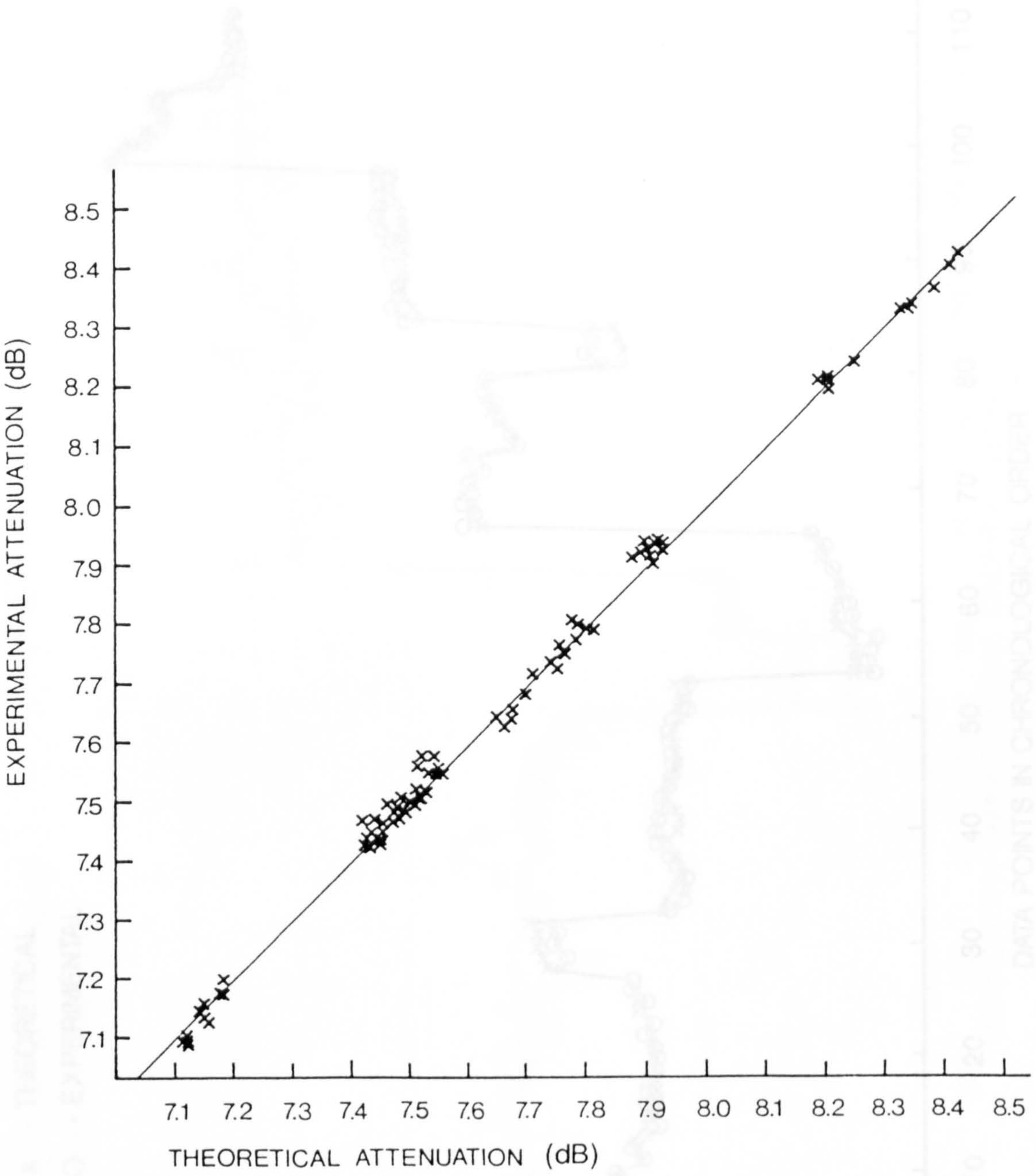

Fig. 5.7 Data Set III: Experimental attenuation vs. theoretical attenuation.

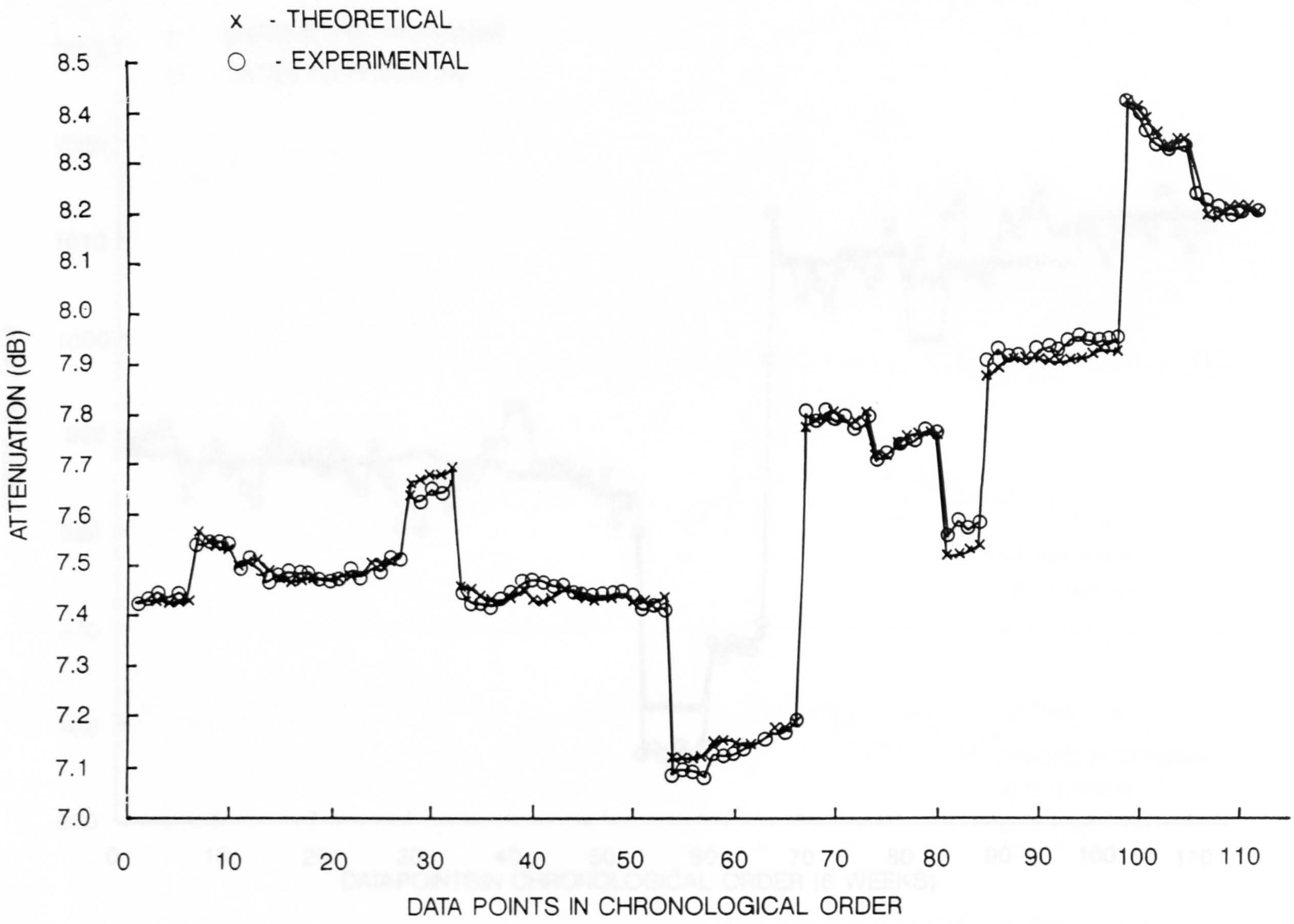

Fig. 5.8 Data Set III: Experimental and theoretical attenuation vs. time.

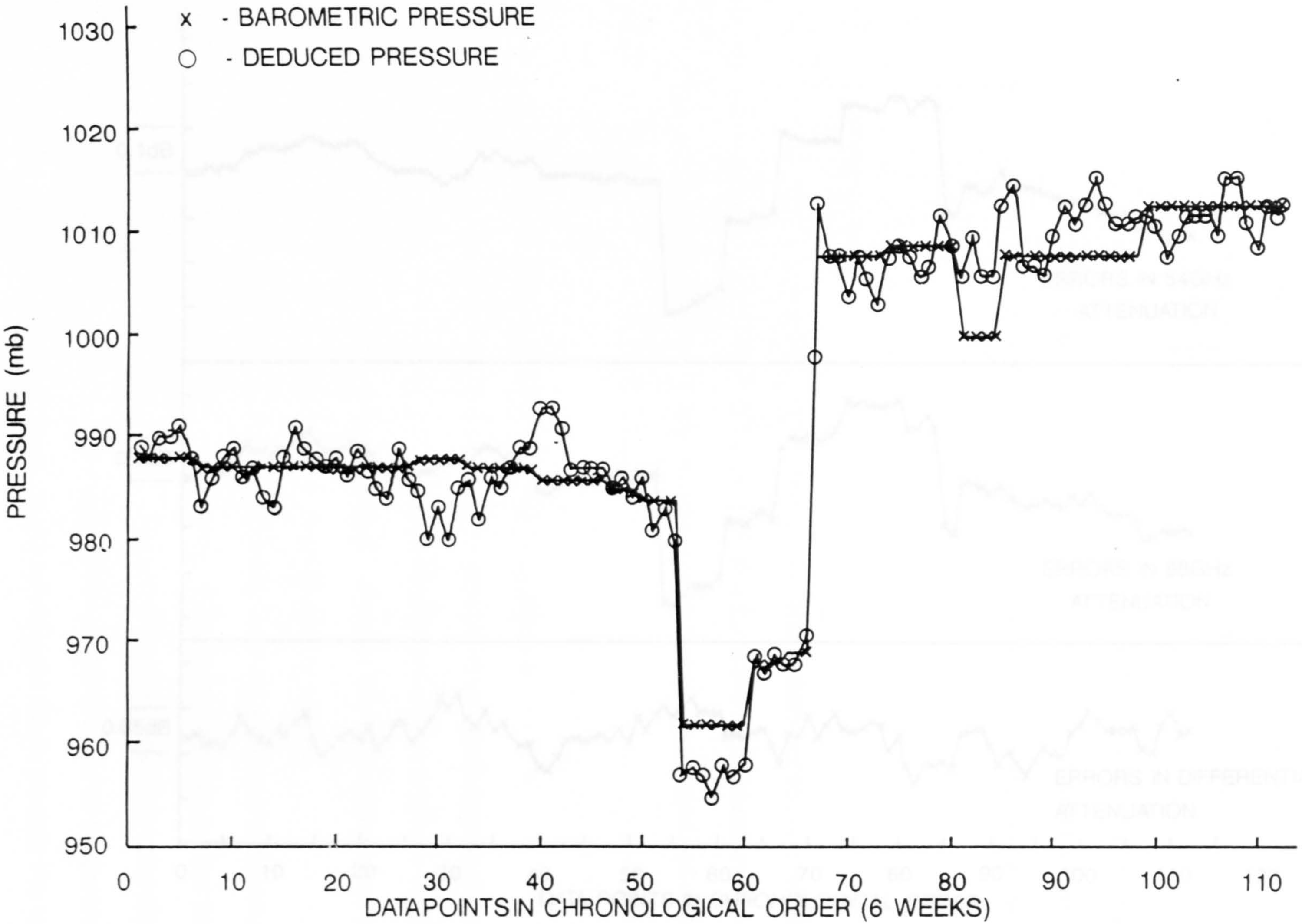

Fig. 5.9 Data Set III: Barometric and deduced pressure vs. time.

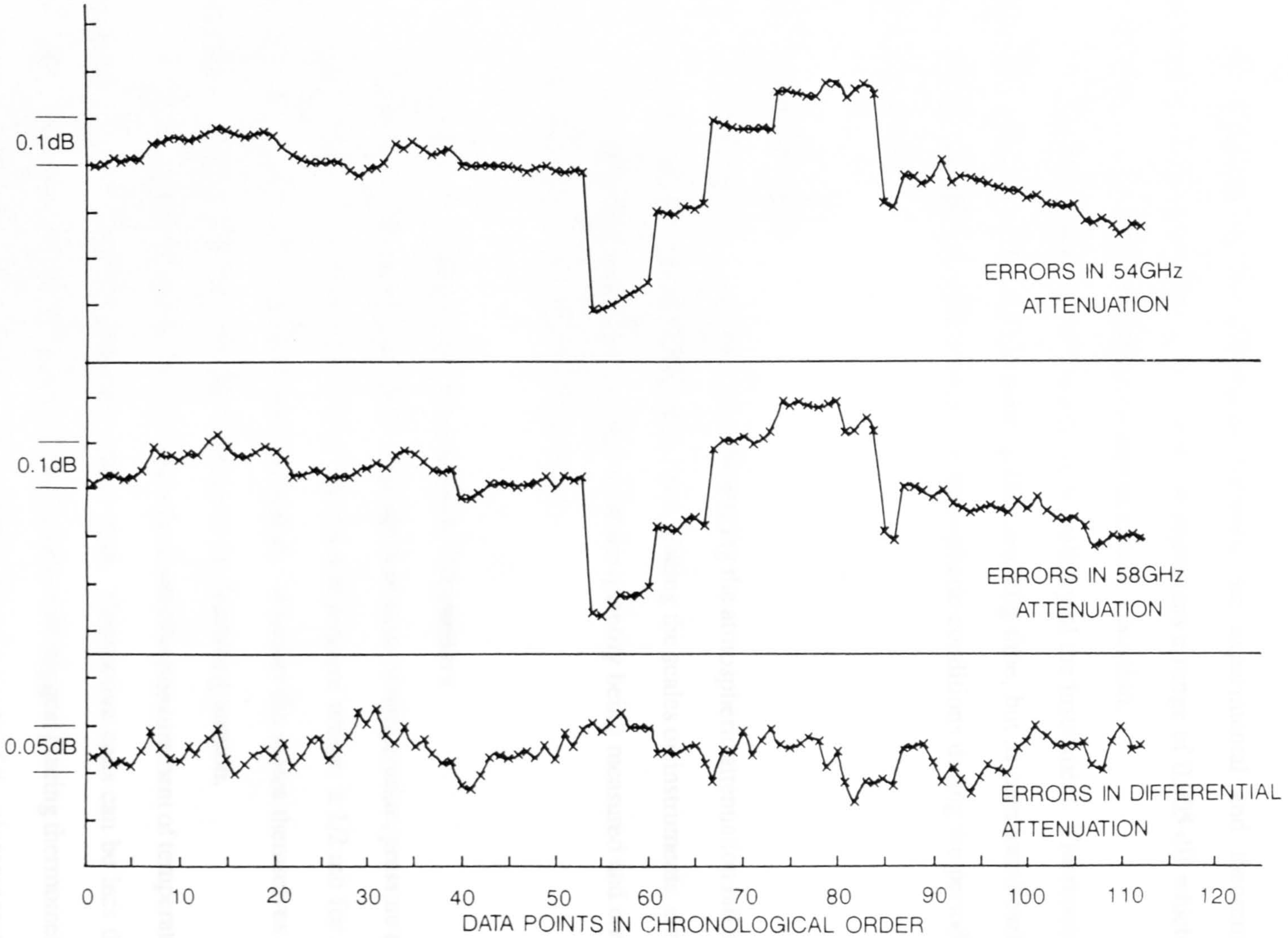

Fig. 5.10 Data Set III: Variations in attenuation errors for 54 GHz, 58 GHz and the differential attenuation vs. time.

signals is uncertain, but may be due to small changes in the alignment of the antennas, though this seems unlikely, or an error in the meteorological readings could also produce this effect.

A histogram of the differences between the experimental and theoretical attenuations is shown in Fig. 5.11. Each bar represents a range of 0.005 dB which is equivalent to ~ 0.95 mb. The shape is approximately Gaussian.

This data set demonstrates the long term stability of the instrument. The standard deviation could be reduced by increasing the sampling time, but as mentioned earlier this introduces problems with changes in atmospheric conditions during the period of the measurement.

5.2 Random Errors

The random errors associated with measuring the atmospheric attenuation fall into three main categories. Errors originating from reading the scales on instruments, errors due to how well these measurements represent the quantity being measured and errors which are not associated with direct readings.

5.2.1 Errors in Measuring Atmospheric Parameters

The errors in scale readings apply to the measurement of temperature, pressure and humidity. The scale errors are ± 0.05 K for the temperature sensor, ± 1/2 mb for the microbarograph and ± 1% RH for the hygrograph. Whether the scales themselves are accurate is discussed under systematic errors in the following section.

The more difficult quantity to estimate is how well the measurement of temperature represents the air along the millimetre wave path. Convective cells can be less than 10 metres across in a lateral direction [ref. 5.1], this would suggest placing thermometers at 10 metre intervals along the path. Ideally many measurements of the air temperature would be made at equal intervals along the length of the path, but in practice this was not possible.

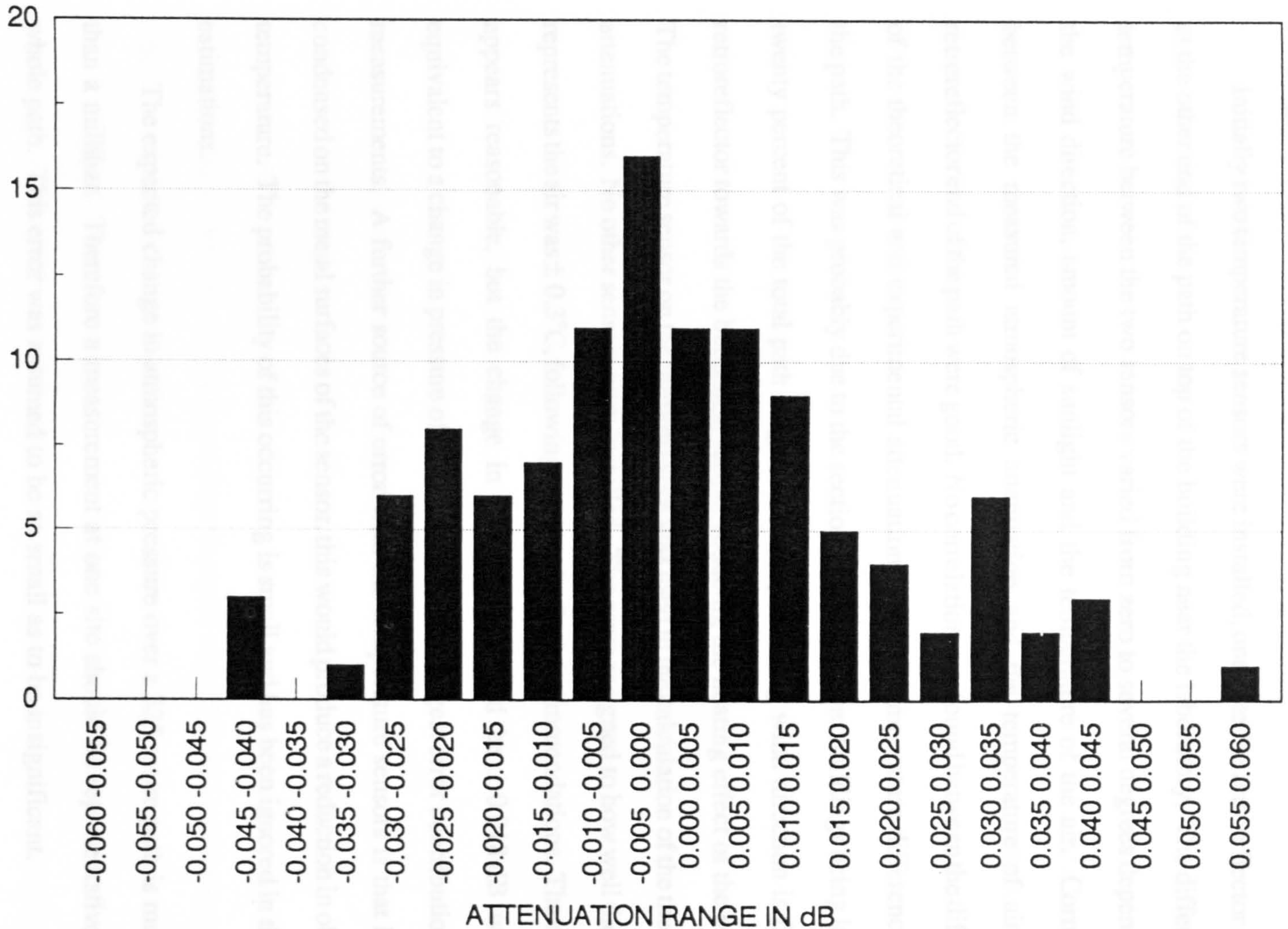

Fig. 5.11 Data Set III: Histogram of errors between theoretical and experimental differential attenuations.

The path has the disadvantage of passing across some buildings near the laboratory end of the path. This introduces heating of the air in the vicinity of the buildings, the effect being more pronounced during winter when the air temperature is lowest and the buildings are heated.

Initially two temperature sensors were installed, one near the retroreflector and one at the other end of the path on top of the building near the laboratory. The difference in temperature between the two sensors varied from zero to several degrees depending on the wind direction, amount of sunlight and the temperature of the air. Correlations between the measured atmospheric attenuation and the temperature of air at the retroreflector end of the path were good. No correlation was found between the difference of the theoretical and experimental attenuations and the temperature difference along the path. This was probably due to the section of the path over buildings being less than twenty percent of the total path length, also the prevailing wind direction is from the retroreflector towards the buildings, further reducing the heating effect of the building. The temperature sensor on the retroreflector was used in the calculation of the theoretical attenuations. No other sensors were installed. The error assigned to how well the sensor represents the air was $\pm$ 0.3°C, following meteorological recommendations. The estimate appears reasonable, but the change in attenuation would be $\pm$ 0.018 dB which is equivalent to a change in pressure of 3.4 mb. This is the largest error contribution to the measurements. A further source of error with the temperature sensors is that if water condensed on the metal surfaces of the sensor, this would produce a reduction in observed temperature. The probability of this occurring is small and has been ignored in the error estimations.

The expected change in atmospheric pressure over a 325 metre path is much less than a millibar. Therefore a measurement at one site should be representative of the whole path. This error was assumed to be so small as to be insignificant.

Humidity measurements do vary with position along the transmission path and the ambient temperature. An allowance of $\pm$ 3% RH was assigned for this random error following the recommendation in the manufacturer's literature.

5.2.2 Errors in Waveguide System and Demodulation

Random errors associated with the waveguide system, downconvertion and demodulation of the signals was measured using two internal waveguide paths each with a separate modulator at separate frequencies. The deviations were less than ± 0.003 dB for each transmission frequency and using a 100 second sample period. This figure applies to data set III only, as were instrument changes between each data set which would have improved the stability. Each data point had 2 × 100 second sample periods for each millimetre wave frequency. These are then ratioed to produce the final attenuation. The maximum random error for each data point was ± 0.0056 dB. This does not include the setting of the programmable rotary vane attenuator for each frequency. This error is less than 0.0002 dB and therefore insignificant in comparison with other errors.

5.2.3 Errors Due to Propagation Effects

Multipath signals can cause a random error in the signal level if the difference in path length is sufficient to allow a significant change in relative phase with changes in the refractive index of the air. As described in Section 4.2.4, the difference in number of wavelengths between the signal path and possible multipaths is just over five wavelengths. Therefore any change in refractive index would not produce a significant change in the relative phases of the two signals.

A multipath signal could produce a random error from changes in the efficiency of the multipath reflecting surfaces. With the alignment procedure used to reduce the multipath signals for data set III the multipath signal should be insignificant and so no random error has been included for these signals.

Distortion of the antenna surfaces by wind is a source of error. Also, because of the tilting of the antennas to minimise multipath signals the angular position of each antenna was more critical than a system aligned for maximum signal. The error due to the effects of wind were counteracted by only recording measurements during periods of calm or light wind.

Unknown errors could also have been introduced through temperature effects on the antennas. Either changes in the parabola surface or changes in the relative positions of the feed and the parabola or in the case of the retroreflector changes between the parabola and hyperbola. This effect was probably reduced to an insignificant level by employing a dual frequency system where both signals would track to a large extent. No allowance has been made for this error.

5.2.4 Summary of Random Error

A summary of the random errors is shown in Table 5.1. The equivalent change in atmospheric attenuation for each error is also shown. The total equivalent random error in terms of atmospheric pressure is ± 3.65 mb. The limits chosen for the random errors are probably about the 95% confidence level, i.e. 3.65 mb ≡ 2σ. Therefore the expected standard deviation for a data set would be ± 1.8 mb compared to the recorded value of 3.7 mb for data set III. Sections of data set III were approaching a 2 mb standard deviation.

The most likely cause of the discrepancy is how well the temperature sensor represents the air along the path or another error may have been underestimated or overlooked.

5.3 Systematic Error

The most difficult part of estimating systematic errors is recognising their existence. Usually once the error has been found it can then be eliminated.

5.3.1 Errors in Pressure, Temperature and Humidity

The systematic errors associated with measuring the atmospheric pressure, temperature and humidity arise from whether the scale is correct. All the instruments were carefully calibrated against a reliable standard at regular intervals to reduce systematic errors to an insignificant level.

Table 5.1

Random Errors

Source	**Errors**	**Error in dB**
Temperature Measurement	± 0.05 K	± 0.0029
Pressure Measurement	± 1/2 mb	± 0.0026
Relative Humidity	± 1%	± 0.001
Air Temperature Variation	± 0.3 C	± 0.0176
Air Humidity Variation	± 3%	± 0.003
Millimetre Wave Instrument	± 0.13%	± 0.0056
Programmable R.V. Resetting	± 0.0002 dB	± 0.0002
Total Random Error		± 0.019 dB
Equivalent Pressure Random Error		± 3.65 mb

The pressure was calibrated to better than a millibar which is sufficient for this instrument. A one millibar systematic error will change the calculated atmospheric attenuation but the difference in attenuation for each data point will not be significantly different from the value obtained from the pressure readings without the systematic errors. The instrument only compares changes in pressure or attenuation and no attempt is made to measure the absolute attenuation of the air in the path. Also the pressure offset is not a large error in a quantity of 1000 millibars over a range of ± 50 millibars.

Similar arguments apply to the temperature calibration. The temperature sensor was calibrated to better than 0.1 K, but, as in the case of the pressure measurements, the change in attenuation between data points is very small when there is an offset of 0.1 K in 280 K over the relatively small range of ± 15 K.

The same arguments apply to the relative humidity measurements. The maximum offset was 1% RH which results in a very small error across the expected range of values. All these limits were verified as insignificant by computing the changes in attenuation.

Another source of systematic error is the computer program calculating the atmospheric attenuation from the measured pressure, temperature and humidity. As mentioned in Chapter 3, the program was checked against calculations made by other groups, but this is not a guarantee of accuracy. The program agrees well with the measurements, which gives some confidence in its accuracy.

The temperature measurements are also subject to another possible systematic error introduced by the digital voltmeter (DVM) measuring the voltage across the load resistor. The zero was checked before every measurement and the accuracy of the DVM was checked against a voltage standard at regular intervals. The DVM was found to be consistently accurate.

5.3.2 Errors in Waveguide System, Downconvertion and Demodulation

The accuracy of the millimetre wave frequencies is dependent on the ovenised crystal reference oscillator. The random errors will be small but a drift in the reference frequency would produce a systematic error in the attenuation. The sensitivity to

pressure, temperature and humidity would all be changed. The quoted ageing rate of the oscillator is 1 part in 10^5 maximum over five years. A 1 in 10^5 error produces only a 0.00028 dB change in the observed differential pressure. The frequency was also measured at regular intervals to ensure the drift was acceptable.

The digital demodulator could introduce systematic errors due to the offset voltage of the analogue to digital convertor (ADC). An error in the algorithms of the digital filter could also introduce an offset. The digital demodulator has a high quality ADC and was carefully tested for accuracy.

A nonlinearity in the system could produce a change in one signal and not the other. The result would be to reduce the sensitivity of the measured signal to the changes in signal level. The system was built so that no amplifier or mixer was operating near a nonlinear region, i.e. the signal levels were more than 15 dB down from the 1 dB compression point of amplifiers and mixers. There should be no offset or systematic error due to nonlinearities.

5.3.3 Errors in Atmospheric Path

The most common error in atmospheric transmission systems are due to multiple signal paths. In this case, the difference in the path length between the signal path and the most likely multipath is only 5-6 wavelengths compared with 60,000 wavelengths in the total path length. There will be a phase difference between the two paths, which remains almost constant with changes in the refractive index but will give rise to a systematic error in the amplitude of the received signal. Such a systematic error is not a problem for this transmissometer as it is the change in the received signal that is monitored and a measurement of the absolute signal is not required. The multipath signal was also estimated to be sufficiently small as to be an insignificant contribution to the received signal.

Any error in the path length will produce a systematic error in the measurements. The theoretical attenuation is dependent on the path length. The path length was

determined by a combination of surveying and calculation. The length was 650.02 metres with a 1 centimetre estimated error. This error is sufficiently small as to not contribute to the errors in the measurements.

Antenna reflectivity changes could also contribute to systematic errors. This error would be reduced by employing two transmission frequencies whose attenuations should track to a reasonable degree. The error associated with changes in reflectivity were assumed to be negligible.

5.4 Summary of Results and Errors

There are no contributing systematic errors to the overall errors in the results. The total contribution from the random errors was ± 3.65 mb which although does not match the experimental errors exactly, is reasonably consistent. The main doubt in the calculation of the errors is in how well the air temperature was represented. This could be improved by installing more temperature sensors along the length of the path.

The results show good correlation between the barometric and deduced atmospheric pressure. In conclusion, the results support the theory and technique of determining the atmospheric pressure from measurements of millimetre wave absorption.

CHAPTER 6

SUMMARY

The way in which the work outlined in the preceding chapters contributes to the confidence in the technique of remotely sensing surface atmospheric pressure by a satellite borne instrument is described in the introduction. The overall objective was to build a millimeter wave atmospheric transmissometer which could measure the atmospheric attenuation with sufficient accuracy to monitor the atmospheric pressure and to acquire some experience of operating millimeter wave systems to better assess the problems involved in designing a satellite borne instrument.

6.1 Measurements

The standard deviation between theory and experimental results is about twice that of the estimated errors assuming that the estimated errors represent a 95% confidence level or two standard deviations. But during very stable atmospheric conditions or over short periods of time the standard deviations were comparable. There are two main possible causes for the difference in the standard deviations

(i) the estimate of the error associated with the measured air temperature compared to the real air temperature. As the temperature error is the largest contributor, then any underestimate or overestimate will greatly affect the total error.

(ii) there still remains some doubt as to the existence or otherwise of a multipath signal. Extensive tests were made in an attempt to pinpoint the source of any effect but there still might exist an atmospheric propagation effect. This is in contradiction to calculations which show that the multipath signals should be insignificant compared to the direct signal path.

There may be other reasons for the remaining discrepancies in the errors but they are not apparent at this time. A more critical examination of the atmospheric absorption models would have been possible with smaller random errors.

6.2 Instrument

There were three major developments which contributed to the instrument stability. The most effective development being the use of a grooved plate at the focus of a cassegrain antenna to modulate the signal beam. Synchronous detection of the received signal then allowed the signal that had propagated to the reflector and back to the receiver to be extracted from other coherent signals. This development should be useful to many microwave and millimeter wave system builders in producing more accurate measurements of beam patterns.

The introduction of the digital demodulator provided a substantial improvement in the system stability through ensuring identical demodulation and filtering for the modulated atmospheric and reference signals. The ability to change the filtering characteristic through the computer software was invaluable in producing an efficient demodulator.

The development of a remote temperature sensing unit improved the measurement and accuracy of the air temperature. Readings of the air temperature from the far end of path were made from the laboratory, hence giving instant readings and avoiding the need to record the information and retrieve it at some later time. The unit outputs a current proportional to the temperature. The current source means that changes in resistance of the connecting wires do not affect the measurement accuracy. The voltage developed across a resistor located in the stable temperature environment gives the temperature at the remote location.

There were many other smaller developments, each providing an important step forward in the evolution of the millimeter wave transmissometer but those mentioned above provided the most significant improvements.

6.3 Further Improvements

The development of any instrument is a continuous process which results in the measurement of the required parameters to an acceptable degree of accuracy. This transmissometer is no different in that an acceptable level of accuracy has been achieved but there is also the desire to produce an even better instrument. The following ideas might enhance the millimeter wave transmissometer.

6.3.1 Temperature and Humidity Measurements

Some of the errors in the results are probably due to insufficient characterisation of the air along the propagation path. Even for the relatively short distance of 325 metres between the ends of the path, the probability for temperature changes of the order of 0.1 C are large. A 0.1 C error would translate to approximately 1 mb error. Also the relative humidity may also have some variation along the path but this would have a much smaller effect on the total error of the measurements. Extra sensor units distributed along the path would improve the characterisation of the air. These units cannot be placed too close to the millimeter wave beam as they would disturb the propagation of the signal and introduce multipath signals.

6.3.2 Path Length

An increase in the length of the propagation path would increase the attenuation changes due to the atmosphere and so proportionately reduce the contribution of non-atmospheric errors. Any increase in path length also requires the stability of the antenna alignments to be improved so that changes in alignment are not misinterpreted as changes in atmospheric attenuation.

6.3.3 Millimeter Wave Operating Frequencies

The operating frequencies for the measurements were to a large extent dictated by what was commercially available. Altering the frequency of the millimetre wave sources could have marginally improved the sensitivity to atmospheric pressure and

reduced the temperature sensitivity. A more useful improvement would be to increase the number of operating frequencies to reduce the reliance on accurate measurements of air temperature. This would also be much closer to the proposed satellite system which employs six frequencies to determine the surface atmospheric pressure. An increase to four operating frequencies for the transmissometer would be sufficient as there are no effects due to cloud, rain or changes in reflector reflectivity to be compensated for in the transmissometer.

6.3.4 Circularly Polarised Radiation

Circularly polarised radiation would reduce multipath signals. Any reflection will change the sense of polarisation. With a circular polarisation sensitive receiver there will be an increase in immunity to multipath signals. The corrugated modulator on the retroreflector has the property of maintaining the sense of circularly polarised radiation so other coherent reflections will also be rejected by the receive antenna.

6.3.5 Computer Control

The human error factor in the measurements could be removed by enabling the computer to perform all the tasks associated with recording data and changing of settings. The changing of the setting of the programmable rotary vane attenuator in the reference path for each millimeter wave frequency is an obvious use of the computer. Also changing the waveguide switch which selects the operating frequency. The readings of air temperature, pressure and relative humidity could all be converted to a computer read system. Also, the monitoring of the phase lock indicators would be a straightforward task. The main advantage of a computer controlled system would be to continuously operate without operator assistance. This would significantly increase the number of measurements recorded and reduce human error and boredom.

6.4 Comparison of Ground Based and Satellite Instruments

The horizontal path millimeter wave system was designed to test the basis of a technique to measure surface atmospheric pressure. The main feature of the technique being the absorption of millimeter wave radiation by oxygen and water vapour. The millimeter transmissometer also uses similar millimeter wave components as would be used in a satellite instrument.

The IMPATTs were chosen especially because this type of source would be necessary in a satellite instrument to produce the very high continuous wave output powers of up to 3 watts. Gunn oscillators would have been acceptable for the ground based measurements as they are simpler to use and less prone to electrical damage, but they do not produce the output powers required for a satellite borne instrument. Each channel in the satellite system has an internal attenuation path to calibrate the transmitted signal against a known reference as in the horizontal path instrument. The two instruments use the same absorption effects and millimeter wave components but there are several differences in the systems which require special consideration.

6.4.1 Coherent Radiation

Due to the short path length and uniform retroreflector, the received signals for the horizontal path instrument are coherent. All the unwanted reflections are also coherent. This was overcome by the introduction of the corrugated modulator at the focus of the retroreflector which allowed the correct signal to be retrieved from the other coherent reflections. The satellite system has no coherence problems. The millimeter wave signal reflects from the ocean surface producing an incoherent signal. The coherence problems for the horizontal path instrument do not exist for the satellite instrument.

6.4.2 Frequency of Operation

The horizontal path measurements were taken using only two operating millimeter wave frequencies. This was sufficient for these measurements as the temperature, pressure and humidity could all be measured. Operation from a satellite requires all the atmospheric information to be sensed by the instrument or by another instrument viewing the same scene. The satellite microwave pressure sounder employs six frequencies. Frequencies at 52.8 and 67.7 GHz, in the wings of the oxygen absorption band, principally measure the total oxygen in the air column. The other four frequencies, at 24.5, 27.7, 42.6 and 74.6 GHz, compensate for perturbations due to the variability in the sea surface reflectivity and in the atmospheric column temperature, humidity and cloud content. The surface pressure can then be deduced from these six absorption measurements. The frequencies in the oxygen absorption band are further away from the band centre compared to the horizontal path instrument as the nadir attenuation from a satellite at band centre is approximately 200 dB. This level of attenuation would require impossibly large transmitter powers to maintain a sufficient signal to noise ratio, even with the reduction in system noise figure that could be obtained by changing the mixer from harmonic to fundamental operation.

6.5 Conclusions

These measurements, over a horizontal path, are an important demonstration of the feasibility of an instrument to measure surface atmospheric pressure based on the absorption by oxygen of millimeter wave radiation.

CHAPTER 7

SURVEY OF TECHNIQUES FOR REMOTE SENSING OF SURFACE ATMOSPHERIC PRESSURE

The measurement of the surface atmospheric pressure from satellites has long been the aim of many groups of researchers. Pressure is an essential parameter in the description of the atmosphere. Meteorologists have historically used surface pressure maps to analyse and forecast the weather. Measurements of surface pressure are needed, together with temperature, water vapour, liquid water and wind fields, to define the dynamic state of the atmosphere. Pressure gradients produce forces which drive the Earth's atmosphere.

Forecasters rely heavily on results from numerical weather prediction models. These require a description of the mass and motion of the air throughout the depth of the atmosphere, and surface pressure is an essential component. Forecasting of the time and position of severe weather is still not at a satisfactory standard.

The surface pressure requirements for observational parameters for large scale dynamic studies and weather prediction have been set by the World Meteorological Office (WMO) as:

Pressure accuracy	± 1 mb
Spatial resolution	100 km
Repetition rate	12 hr

These requirements form the basis of a specification for all remote sensing instruments.

Observation of atmospheric pressure measurements show that pressure gradients vary by typically less than 1 mb/100 km except in storm conditions and on frontal systems.

The surface pressure is currently reported from a global network of land-based manned stations, and in the oceanic areas, from islands, buoys, weather ships and a large number of merchant ships. These sources are generally regarded as adequate over the

land areas of the northern hemisphere but some improvement of coverage is desirable from the more remote land regions of the southern hemisphere. Over the oceans, which comprises about 70% of the earth's surface, there are insufficient measurements for numerical models. Reports from ships of surface atmospheric pressure could form the basis of a numerical model if they were uniformly distributed. However, the observations are concentrated in the major shipping lanes and therefore leave large areas with no data, particularly in the southern hemisphere.

7.1 Drifting Buoys

The inadequate number of observations over the southern oceans led to the establishment of a system of drifting buoys for the first GARP Global Experiment in 1979. These buoys made measurements of surface pressure and a few other parameters such as sea temperature and atmospheric temperature. The data were collected by satellite along with the position of the buoys. The coverage when the number of buoys was near the maximum of 180 is shown in Fig. 7.1. Guymar and LeMarshall [ref. 7.1] showed that these observations had a significant impact on the accuracy of Australian forecasts. The life of these buoys was relatively short and by summer of 1981 only about fifty were still providing reliable pressure measurements. This reduced number of measurements does not provide the necessary observational spacing for numerical forecasting. This technique would be inoperable on a global scale due to the large number of buoys required to give suitable coverage, especially if the WMO recommendation that measurements be attempted every 100 km.

7.2 Satellite Instruments

Satellite borne instruments offer the best opportunity for measuring the surface pressure over the ocean with the required accuracy and spatial resolution on a global scale. There are no reported measurement techniques for the measurement of surface pressure over land because this is in general a well reported area of the earth's surface. It is the development of weather systems at sea which is of most interest to weather

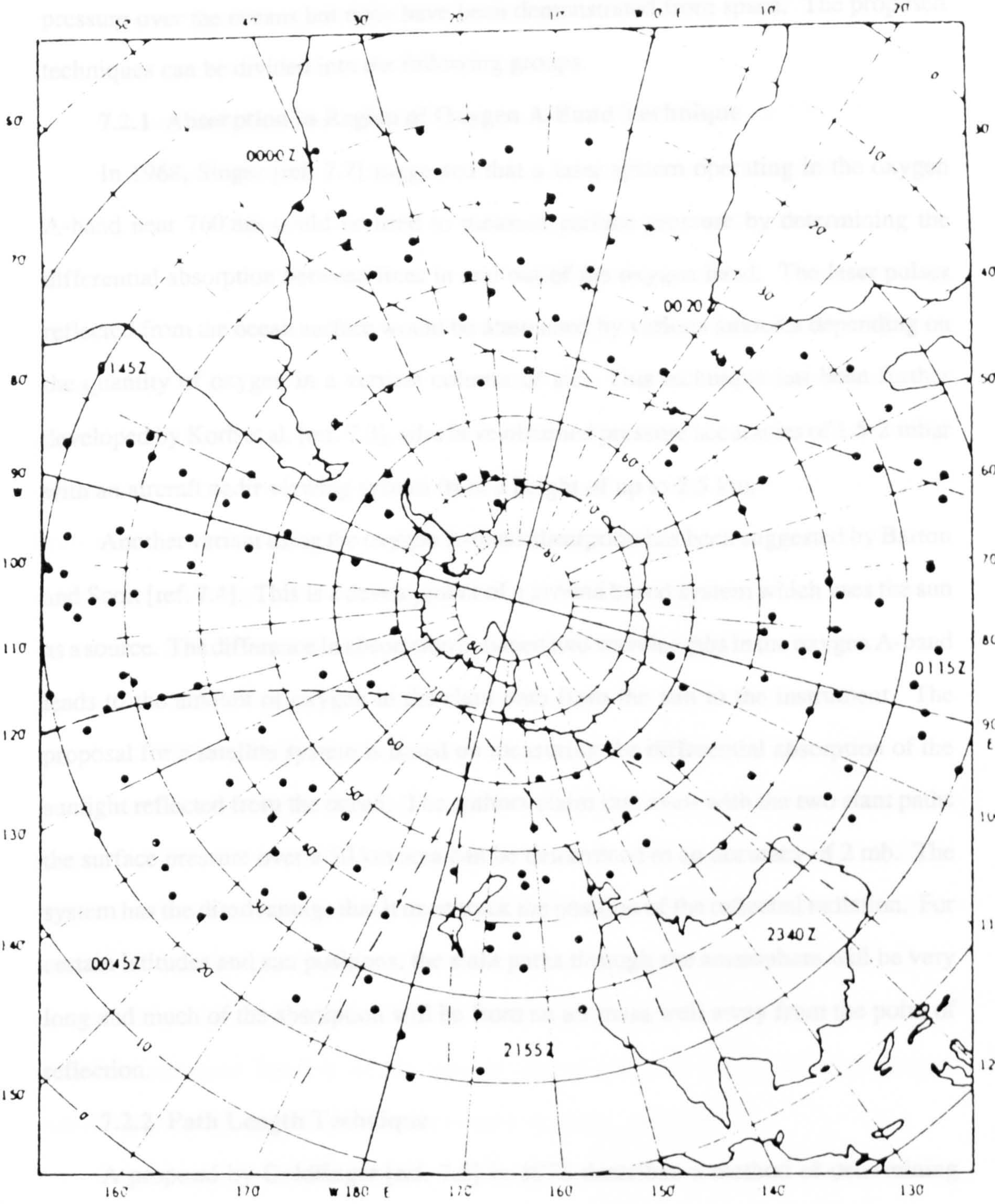

Fig. 7.1 Position of drifting buoys in the southern hemisphere.
From Guymer and Le Marshall [ref. 7.1].

forecasters. There have been many proposals for satellite instruments to measure surface pressure over the oceans but none have been demonstrated from space. The proposed techniques can be divided into the following groups.

7.2.1 Absorption in Region of Oxygen A-Band Technique

In 1968, Singer [ref. 7.2] suggested that a laser system operating in the oxygen A-band near 760 nm could be used to measure surface pressure by determining the differential absorption between lines in and out of the oxygen band. The laser pulses reflected from the ocean surface would be attenuated by various amounts depending on the quantity of oxygen in a vertical column of air. This technique has been further developed by Korb et al. [ref. 7.3], who have obtained pressure accuracies of 1.5-2 mbar with an aircraft nadir viewing system from a height of up to 2.5 km.

Another variant using the oxygen A-band absorption has been suggested by Barton and Scott [ref. 7.4]. This is a development of a ground based system which uses the sun as a source. The difference in absorption between two wavelengths in the oxygen A-band leads to the amount of oxygen in the slant path from the sun to the instrument. The proposal for a satellite system is based on measuring the differential absorption of the sunlight reflected from the ocean. The authors claim that even with the two slant paths the surface pressure over a 50 km area can be determined to an accuracy of 2 mb. The system has the disadvantage that it must track the position of the reflected radiation. For certain latitudes and sun positions, the slant paths through the atmosphere will be very long and much of the absorption will be from an air mass well away from the point of reflection.

7.2.2 Path Length Technique

A proposal by Goldfinger [ref. 7.5] in 1978 describes a method of determining surface pressure from measurements of refractivity of the atmosphere. An optical pulse is transmitted from one satellite, reflected from the ocean surface and received by a second satellite. The time of travel depends on the refractivity of the atmosphere which

is dependent on the pressure. This would appear to be a difficult technique to maintain over a large area of the globe due to the requirement of having satellites in suitable positions.

A more viable technique was proposed by Gardner et al. [ref. 7.6] in 1983. Gardner suggests measuring the propagation time of a laser pulse reflected from the ocean surface, but the pulse would be transmitted and received by the same satellite instrument. The proposed "two-colour" laser altimeter uses fixed frequency lasers and the technique is relatively insensitive to changes in the laser wavelengths. One of the disadvantages of the technique is that picosecond timing accuracies are required to make millibar-level pressure measurements. The pressure error would be ~ 1 mb for a 2 picosecond timing error. A practical demonstration was made by Abshire and Kalshoven [ref. 7.7] on a horizontal path ranging system. With their system, they were able to measure the differential path length with an accuracy of about 6 picoseconds. Abshire also reported measurements from an airborne instrument at an altitude of 2.5 km which showed a pressure accuracy of about 3 mb for nadir sounding.

7.2.3 Millimetre Wave Absorption Technique

A technique to measure surface atmospheric pressure was proposed by Smith et al. [ref. 7.8] in 1972 in which the absorption by the broad oxygen band near 60 GHz (5 mm wavelength) is used as a monitor of the surface pressure. The technique involves the differential absorption between frequencies in the oxygen band and frequencies close to the absorption band. The measurements at these frequencies are preferable for a satellite instrument because of the greater transparency of clouds at these longer wavelengths compared with the lidar systems mentioned earlier.

A disadvantage of the technique is the presence of water vapour absorption in this region of the spectrum. This is overcome by introducing measurements near the water vapour line at 27 GHz. This leads to the instrument having the ability to determine the water vapour content of the air in the vertical column sounded by this instrument. The number of sounding frequencies was extended to six in a theoretical optimisation by Peckham et al. in 1983 [ref. 7.9]. Table 7.1 shows the characteristic of such a satellite

Table 7.1.Characteristics of a 6 channel satellite pressure sounder

(from Peckham et al. [ref. 7.9])

Operating frequencies, GHz:

24.591, 27.705, 42.497, 52.808, 67.697, 74.588

Instrument design parameters:

Total system power	180 W
Total weight	80 kg
Antenna dimensions	100 × 19 cm
Satellite altitude	675 km
Transmitter power (total)	12 W
Receiver bandwidth	75 kHz
Pulse length	4.5 ms
Integration time	9 s

Predicted retrieval errors:

Surface pressure	1.04 mb
Water vapour	0.13 g/cm^{-2}
Liquid water	0.18 mm
Sea surface wind speed	2 ms^{-1}

borne instrument. This large number of frequencies would allow the surface pressure to be determined with a 1 mb standard deviation, as well as water vapour to 0.13 g/cm^2, liquid water to 0.18 mm and surface wind speed to 2 ms^{-1} accuracy.

In addition to the horizontal path absorption measurements described in earlier chapters, aircraft trials of a two frequency differential absorption instrument, Flower et al., [ref. 7.10] gave an r.m.s. error of 0.87 millibar for altitudes up to 10 km. These measurements required a knowledge of the temperature of the column of air which was obtained by flying the aircraft through the measurement area at various altitudes.

This technique appears to offer the best prospects for an instrument measuring surface atmospheric pressure on a global scale. The requirements of pressure accuracy can be met over a large range of atmospheric conditions. This instrument was proposed in 1988 to NASA for inclusion on the Earth Observing System, a series of satellite instruments investigating the health of the atmosphere.

7.3 Problems with Remote Sensing of Atmospheric Pressure

All the systems discussed in Section 7.2 suffer to a larger or smaller degree from sensitivity to atmospheric effects, which are not directly involved in the measurement, and from a lack of spatial coverage. Atmospheric effects can significantly affect the required dynamic range of the instrument and consequently the viability of the technique in providing the required parameters over all conditions.

7.3.1 Atmospheric Problems

Cloud cover will drastically change the return signals for the laser type instruments and to a small degree for a millimetre wave instrument. It is not only the presence of cloud cover but the partial filling of the field of view which can make retrieval of surface pressure difficult. For an instrument operating with several frequencies the beam footprints must match to a close tolerance to ensure the same cloud beam filling for each frequency to avoid erroneous interpretation of the received signals.

A similar problem arises from the presence of rain in the field of view. This is especially a problem for millimetre wave systems because in this wavelength region the losses due to rain vary with wavelength. This is not so for the much shorter wavelength radiation where the losses are almost constant with wavelength. Also the ratio of the wavelengths in the millimetre wave instrument have a three to one ratio for the longest to the shortest wavelength in comparison to the small percentage change in wavelength for the instruments using the oxygen A-band absorption. The millimetre wave instrument has turned this effect into an advantage by being able to estimate the amount of precipitating water in the signal path by the use of six transmission frequencies.

The reflection coefficient or amount of backscattered radiation from the ocean surface is influenced by many local conditions. The ocean surface is made up of gravity waves and capillary waves. The backscatter of radiation at normal incidence is dependent on the number and size of specular point reflectors in the field of view of the instrument.

Modern work on the analysis of optical backscattered radiation began with the mean-square slope statistics of Cox and Munk [ref. 7.11]. Their work was based on the analysis of sun glitter patterns in aerial photographs obtained over the ocean under various wind and wave conditions. They reported a near Gaussian distribution of wave slopes and proposed a relationship for the two dimensional mean-square slope and backscattered radiation. There are many publications to be found on the theory of optical backscatter, but Bufton et al. [ref. 7.12] have made comparisons with measured backscatter using airborne lidar systems both nadir viewing and up to 15° off nadir. Their data shows an up to 10-fold decrease in signal as the viewing angle moves to 10-15° off nadir, depending on wavelength and wind speed.

The microwave, and to a much less degree the millimetre wave, backscatter of the ocean with wind speed was modelled by Wilheit [ref. 7.13]. There have been many microwave instruments, such as altimeters involved in satellite monitoring of the oceans, providing a large fund of measurements. Townsend [ref. 7.14] presents good measurements of microwave backscatter at 13.9 GHz versus wind speed from Seasat-1 data.

The reflection coefficient of the ocean is a function of surface roughness, complex dielectric constant (salinity), temperature, signal frequency, polarisation and angle of incidence. There is still extensive work being carried out to improve the modelling of these effects. More measurements in a larger variety of conditions would significantly improve the progress in modelling the backscatter from the ocean, especially off nadir backscatter.

7.3.2 Spatial Coverage Problem

An instrument to measure surface atmospheric pressure would be mounted on an orbiting polar platform. Similar to many satellite platforms already in operation monitoring and measuring aspects of the atmosphere and surface properties. Typically these platforms orbit the earth every ~ 100 minutes at an altitude of 600 to 700 km. Therefore a platform will make 14.4 orbits per day and the distance between crossover points on the equator will be approximately 2,800 km. For complete spatial coverage an instrument will have to scan out to 1,400 km on both sides of the platform subtrack point so that the next swath will then join onto the previous swath.

The diagram in Fig. 7.2 shows the orbit crossover for two consecutive orbits, labelled A and B, at the equator where the spatial coverage is most severe for a polar orbiting platform. The required scan angle, θ is ~ 58°, and the angle between the radiation and the normal to the surface, ϕ, is ~ 71°. These two angles are not identical due to the curvature of the earth. For a useful sounding measurement there must be an adequate reflection of the incident radiation back to the instrument for all likely surface conditions and at all incident angles.

Barrick [ref. 7.15] has calculated the possible reflection coefficients for various angles of incidence using a specular point theory. Fig. 7.3 from Barrick shows the changes in backscatter cross-section against various angles of incidence and sea surface conditions. The vertical axis is the backscatter cross-section σ^0 normalised by the Fresnel reflection coefficient $|R(0)|^2$ at normal incidence and expressed in decibels. $\sigma^0 / |R(0)^2$ is independent of frequency. The horizontal axis is the angle made with the ocean surface by radiation from a satellite platform with respect to the normal to the surface. The lines

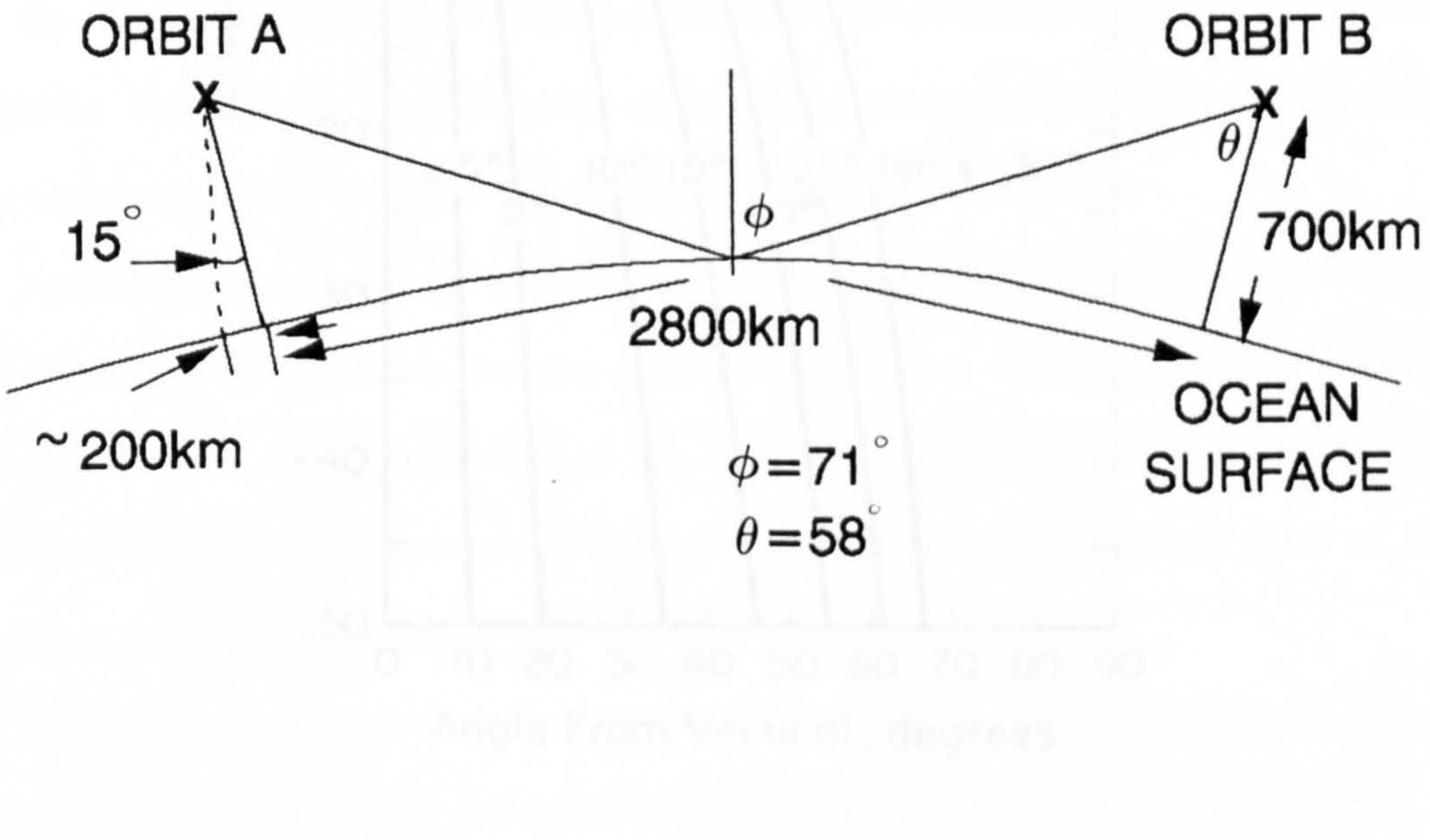

Fig. 7.2 Geometry of scanning satellite instruments.

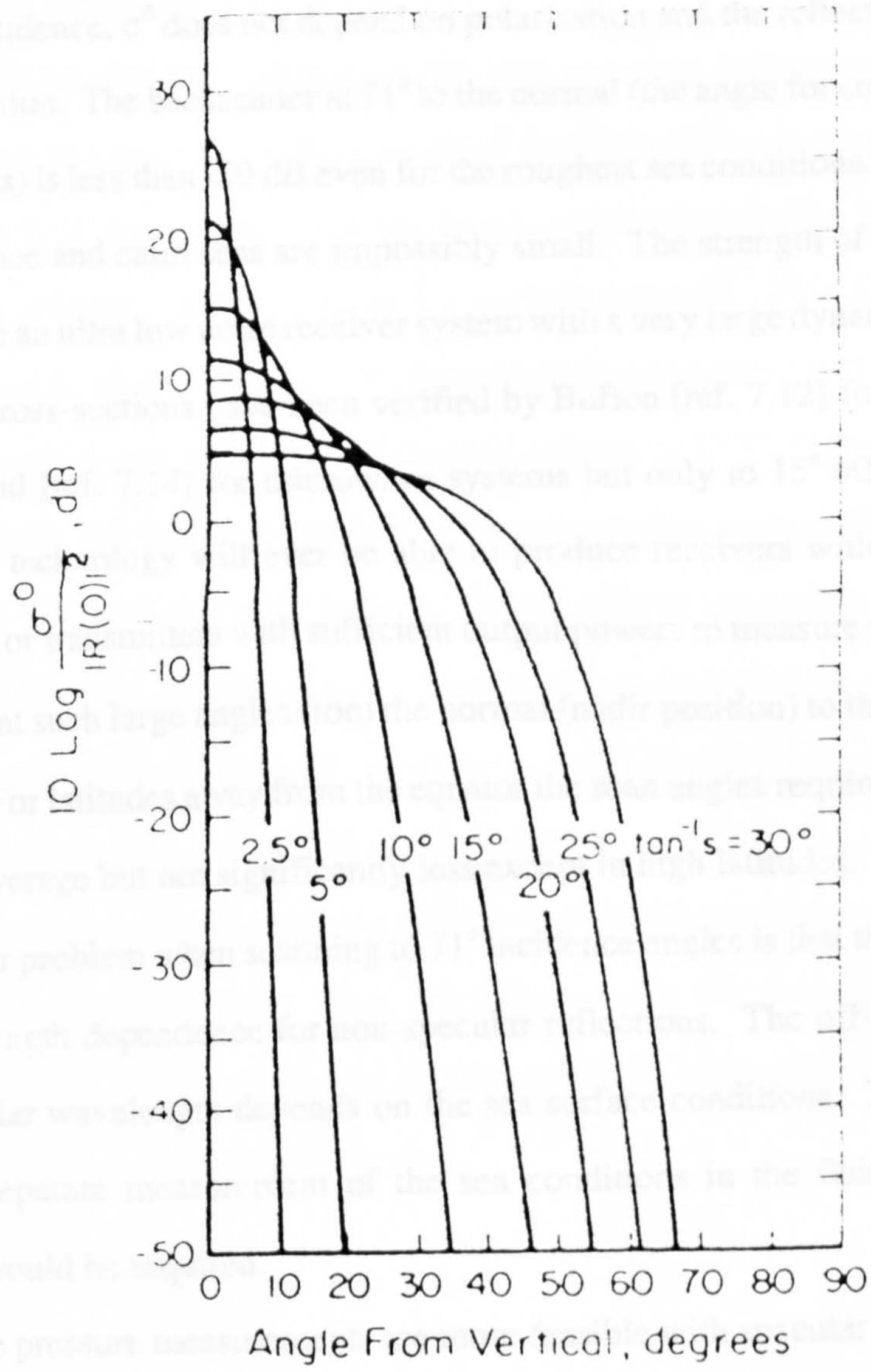

Fig. 7.3 Sea surface backscatter cross-section vs. incident angle. After Barrick [ref. 7.15].

on the graph represent various roughness conditions dependent mainly on wind speed. S is the r.m.s. roughness slope which has a Gaussian distribution. The values on the graph represent calm to very heavy seas.

Values for $\sigma^0 / |R(0)^2$ vary from 5 to 27 dB for various sea states at normal incidence. At normal incidence, σ^0 does not depend on polarisation and the reflected signal suffers no depolarisation. The backscatter at 71^0 to the normal (the angle for complete coverage measurements) is less than -50 dB even for the roughest sea conditions. The backscatter at 71° incidence and calm seas are impossibly small. The strength of the return signal would require an ultra low noise receiver system with a very large dynamic range. These backscatter cross-sections have been verified by Bufton [ref. 7.12] for optical systems and Townsend [ref. 7.14] for microwave systems but only to 15° off nadir. It seems unlikely that technology will ever be able to produce receivers with sufficiently low noise figures or transmitters with sufficient output powers to measure the return signals from the sea at such large angles from the normal (nadir position) to the surface in calm conditions. For latitudes away from the equator the scan angles required will be less for complete coverage but not significantly less except in high latitudes.

Another problem when scanning to 71° incidence angles is that the returned signal has a wavelength dependence for non-specular reflections. The off-nadir backscatter for a particular wavelength depends on the sea surface conditions. To overcome this problem a separate measurement of the sea conditions in the field of view of the instrument would be required.

Surface pressure measurements are more feasible with specular reflection. There is no reason why the transmit and receive systems have to be on the same platform. A bistatic arrangement with an orbiting satellite transmitting to the surface and the reflected radiation being received by a series of geostationary satellites would appear possible. This arrangement requires a large number of satellites. As the orbiting satellite moves away from the equator there would be several swathes of specular reflection points for each of the geostationary satellite receivers. The difficulty with using geostationary

platforms is that the distances involved are much greater and so the geometric losses are much greater. To maintain the signal to noise ratio for the measurements the transmit powers must be increased by about a factor of one thousand if the same size of antenna is used. The transmit powers already used are at the limit of technology, therefore this technique does not appear to be feasible.

A recent proposal for a millimetre pressure sounding instrument by Flower [ref. 7.16] for the Earth Observing System series of satellites outlines viewing the surface at nadir and at ± 13.7° from nadir. This has the advantage of providing the gradient of the local surface pressure field as well as the surface pressure. This does not give full coverage as can be seen in Fig. 7.4 from the proposal which shows daily global coverage for a single satellite instrument. By pointing an antenna at 13.7° off nadir measurements at approximately 208 km on either side of the sub-satellite track at 10 second intervals can be made. The inset shows the smeared field of view at the surface of approximately 20×100 km, oriented along the track. Though this technique does not give the ideal coverage required by meteorologists it would be a significant step forward in improving the understanding of the atmosphere and forecasting.

Complete daily coverage with the millimetre pressure sounder can only be achieved by using five orbiting satellites. This is a large number of satellites but insignificant compared with the present number of orbiting satellites being used for meteorological measurements and surface remote sensing.

7.4 Summary

The remote sensing of surface atmospheric pressure on a global scale to allow better modelling and forecasting of weather is not at present equal to the requirements set out by the WMO. Significant progress has been made towards this goal by both millimetre and optical systems. But, for a complete global specification of the surface pressure over the oceans, the problem of coverage must be solved. The effects of the atmosphere on the sensing signals also has some severe limitations especially for optical systems. There is still an opportunity for new instruments to overcome the problems in existing

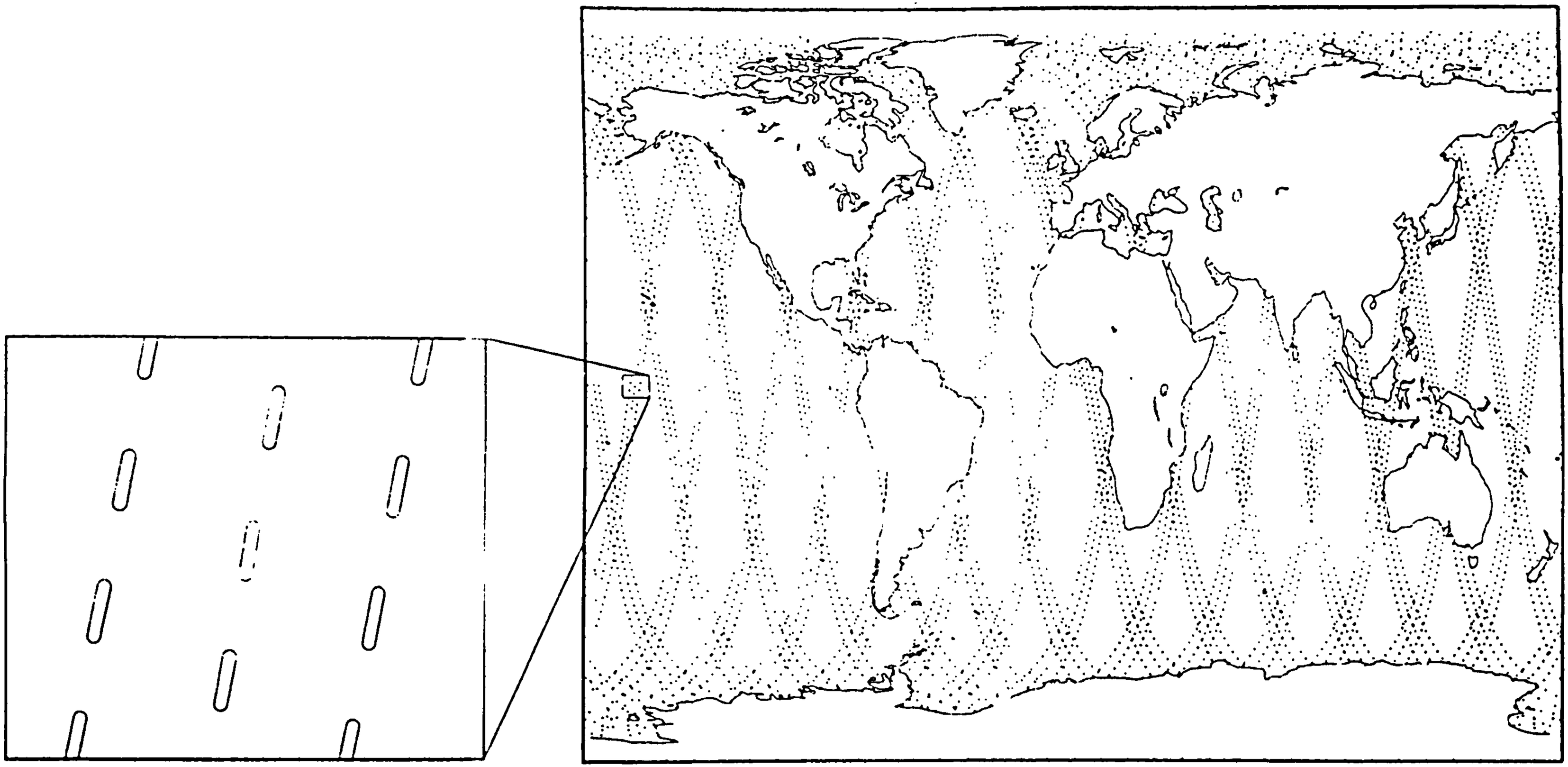

Fig. 7.4 Typical daily global coverage. Inset shows sampling pattern. From Flower [ref. 7.16].

proposals for the global measurement of surface atmospheric pressure. Some combination of monostatic and bistatic systems may produce an instrument which will satisfy the WMO requirements.

REFERENCES

[7.1] Guymer, L.B. and J.F. Le Marshall, "Impact of FGGE buoy data on southern hemisphere analysis", Bull. Am. Meteorological Society, No. 62, pp. 38-47 (1981).

[7.2] Singer, S.F., "Measurement of atmospheric surface pressure with a satellite borne laser", Appl. Opt., No. 7, pp. 1125-1127, (1968).

[7.3] Korb, C.L., Schwemmer, G.K., Dombrowski, M. and Weng, C.Y., "Airborne and ground based lidar measurements of the atmospheric pressure profile", Appl. Opt., No. 28, pp. 3015-3023 (1989).

[7.4] Barton, I.J. and Scott, J.C., "Remote measurement of surface pressure using absorption in the oxygen A-band", Appl. Opt., Vol. 25, pp. 3502-3507 (1986).

[7.5] Goldfinger, A.D. et al., "A satellite system for measuring atmospheric surface pressure", APL Report SDO 5077, John Hopkins University (1978).

[7.6] Gardner, C.S., Tsai, B.M. and Im, K.E., "Multicolor laser altimeter for barometric measurements over the ocean: theoretical", Appl. Opt., Vol. 22, No. 17, pp. 2571-2577 (1983).

[7.7] Abshire, J.B. and Kalshoven, J.E., "Multicolor laser altimeter for barometric measurements over the ocean: experimental", Appl. Opt., Vol. 22, No. 17, pp. 2578-2585 (1983).

[7.8] Smith, S.D., Colles, M.J. and Peckham, G.E., "The measurement of surface pressure from a satellite", Quart. J. R. Met. Soc., No. 98, pp. 431-433 (1972).

[7.9] Peckham, G.E., Gatley, C. and Flower, D.A., "Optimising a remote sensing instrument to measure atmospheric surface pressure", Int. J. Remote Sensing, No. 4, pp. 465-478 (1983).

[7.10] Flower, D.A., Peckham, G.E. and Bradford, W.J., "Experimental validation of a millimetre wave radar technique to remotely sense atmospheric pressure at the Earth's surface", Proc. of IGARSS'84 Symposium. Strasbourg, August 27-30 1984. ESA SP-215.

[7.11] Cox, C. and Munk, W., "Measurement of the roughness of the sea surface from photographs of the sun's glitter", Journal of the Optical Society of America, Vol. 44, No. 11, pp. 838-850 (1954).

[7.12] Bufton, J.L., Hoge, F.E. and Swift, R.N., "Airborne measurements of laser backscatter from the ocean surface", Appl. Opt., Vol. 22, No. 17, pp. 2603-2618 (1983).

[7.13] Wilheit, T.T., "A model for the microwave emissivity of the ocean's surface as a function of windspeed", NASA Technical Memorandum 80278 (1979).

[7.14] Townsend, W.F., "An initial assessment of the performance achieved by the Seasat-1 radar altimeter", IEEE J. of Oceanic Engineering, Vol. OE-5, No. 2, pp. 80-92 (1980).

[7.15] Barrick, D.E., "Rough surface scattering based on the specular point theory", IEEE Trans. on Antennas and Propagation, Vol. AP-16, No. 4, pp. 449-454 (1968).

[7.16] Flower, D.A., "Microwave pressure sounder - a proposal for the Earth Observing System", Jet Propulsion Laboratory, CA. Earth Observving System Proposal (1988).

CHAPTER 8

MICROWAVE LIMB SOUNDER INSTRUMENT

8.1 Introduction

The microwave limb sounder instrument (MLS) is one of nine complementary experiments to be flown on the Upper Atmosphere Research Satellite (UARS). The UARS mission will provide the most complete data gathered so far on atmospheric chemical composition, photochemical reactions, winds and energy input. These data sets will yield the first simultaneous comprehensive global coverage of these closely coupled upper atmospheric properties. Additional correlative data will complement the UARS observations to provide a systematic approach to understanding and monitoring the upper atmosphere.

The inaccessibility of the upper atmosphere has long hindered its global study. Tropospheric absorption impedes direct observation by surface instruments, which are confined mainly to land areas. Balloons can carry large instruments and rockets permit smaller payloads to reach high into the atmosphere, but extensive geographic coverage by these means is not feasible. Global study of the upper atmosphere requires remote sensing from an orbiting platform to achieve systematic coverage of the atmospheric properties.

The first TIROS satellite, launched in 1960, initiated the remote sensing of the atmosphere from space. These first satellite instruments predominantly carried out weather observations. Microwave remote sensing of the earth's atmosphere from satellites was initiated by the Nimbus 5 satellite and results were published by Staelin et al. [ref. 8.1]. These series of satellites have demonstrated the potential of remote sensing of the atmosphere from instruments in an earth orbit. The UARS orbiting

observatory will allow the physical and chemical processes and concentrations of molecules in the upper atmosphere (~ 15-80 km) to be measured on a near daily basis over the globe. The UARS satellite and payload characteristics are shown in Table 8.1.

One serious concern is the high altitude ozone depletion which is thought to be caused in part by various man-made pollutants. The most dramatic evidence of depletion is the ozone hole found over Antarctica by Forman [ref. 8.2]. The current explanation of this phenomenon combines the chemical mechanisms initiated by man-made chlorofluorocarbons (CFC's) with the low temperatures, long periods of darkness and unique atmospheric dynamics found in the polar region. The full impact of CFC's on ozone levels worldwide can not be predicted with a high degree of confidence due to the complexity of stratospheric chemistry. Many chemical species need to be measured if numerical simulations of global ozone levels changes are to become reliable. Simultaneous measurements of the stratospheric winds and energy input are also essential in providing a more complete understanding of the upper atmosphere. Only remote sensing from space can provide the temporal and spatial coverage needed to study such processes worldwide.

Apart from the interaction of CFC's with ozone, UARS instruments will also monitor other source molecules which yield highly reactive free radicals in the stratosphere which are involved in the depletion of ozone. Nitrous oxide (N_2O), arising from natural processes and from the use of synthetic nitrogen fertilisers, is thought to contribute to the depletion of ozone. Methane (CH_4), arising from swamps, marshes, rice fields, ruminant animals and oil and gas drilling, is the parent of a group of reactive species that play a key role in stratospheric chemistry. MLS will measure ClO, O_3 and H_2O. The upper atmospheric water vapour concentration is not well known and is thought to be a source of OH in ozone reactions.

Table 8.1

UARS Mission and Payload Characteristics

Launch Date	Late 1991
Design Lifetime	36 months
Orbit	600 km circular
Inclination	57°
Period	97 minutes
Latitude Coverage	80°N to 80°S
Global coverage interval for full diurnal measurements	36 days
Weight of instruments	2,500 kg (5,500 lb)
Total spacecraft weight	6,800 kg (15,000 lb)
Total launch weight	7,700 kg (17,000 lb)
Total instrument power	786 W
Total power	1.6 kW
Telemetry rate	32 kbps
Data storage	Two tape recorders
Tape playback	512 kbps
Data relay	Tracking and Data Relay Satellite System (TDRS), 10 min/orbit
Thermal range	-10 to 45°C
Stabilisation	Three-axis to less than 0.1 degree

8.2 Microwave Limb Sounding

The microwave limb sounding technique involves the measurement of thermal emissions from molecules in the atmosphere as the field of view of the instrument is scanned through the limb of the atmosphere. Fig. 8.1 shows diagrammatically the vertical and horizontal projection of the limb sounding configuration. The microwave limb sounder (MLS) views the atmosphere at right angles to the direction of flight of the satellite.

Limb sounding at millimetre wave frequencies has several advantages.

1) Most of the molecules and radicals associated with ozone depletion emit in the millimetre and sub-millimetre wave range of the spectrum. The spectroscopic data base is more accurate in this region and there are fewer overlapping lines compared to the infrared wavelength region.

2) Limb geometry allows the emissions to be viewed against the background of space. Because of the rapid decrease in atmospheric pressure with height, the bulk of the emission originates close to the tangent point (limb point).

3) The spatial resolution can be ~ 2 km in the vertical and ~ 300 km in the horizontal direction along the line of sight. This is adequate for zonal mapping of the concentrations of molecules.

4) Thermal emissions can be observed at any time of day or night without the need for background sources such as the sun or intermediate processes such as backscattering.

5) Aerosols and ice clouds have a negligible effect on the measurements.

6) The spectral lines can be resolved to much better than the linewidths. The only limiting factor is the overlapping of lines which is not a serious problem in the millimetre and submillimetre wave region.

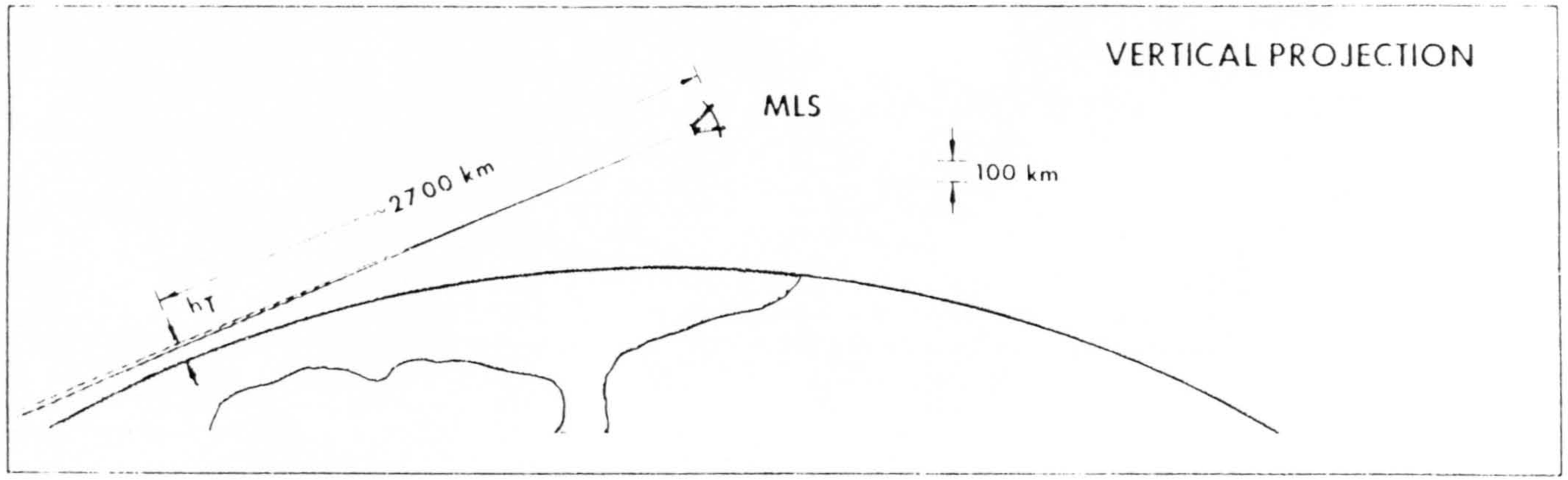

Fig. 8.1 MLS measurement geometry.

8.3 The Microwave Limb Sounder Experiment

The main objective of the microwave limb sounder (MLS) is to simultaneously measure the concentrations of chlorine oxide (ClO), ozone (O_2) and water vapour (H_2O) in the stratosphere and lower mesosphere [ref. 8.3]. A summary of the geophysical parameters, altitude range and sensitivity are shown in the following table.

Band	Frequency (GHz)	Molecule	Altitude Range (km)	Sensitivity
B1	63.998	O_2	30-60	1%
	63.569			
B2	204.352	ClO	25-45	0.2 ppb
B3	204.573	H_2O_2	30-40	0.9 ppb
B4	206.132	O_3	15-60	1%
B5	183.310	H_2O	15-85	1%
B6	184.378	O_3	15-80	1%

The measurement of oxygen (O_2) at 63 GHz is to provide pressure information to improve the pointing knowledge of the antenna. The measurement of H_2O_2 is a secondary goal and it is unknown at this time if, even with long integration times, any meaningful measurements can be made. H_2O_2 is believed to be an important molecule in ozone photochemistry. The ClO measurements are essential for understanding the catalytic destruction of ozone in the stratosphere by chlorine from industrial products such as CFC's. The O_3 measurements will allow estimation of the total amount of ozone present in the stratosphere, if its concentration is increasing or decreasing and monitor seasonal changes. The measurement of H_2O is important in relation to the hydrogen cycle and as a pointer to the amount of OH in the atmosphere which has an effect on ozone concentration.

This experiment has been developed by the Jet Propulsion Laboratory, California in collaboration with Heriot-Watt University, Rutherford Appleton Laboratory and the University of Edinburgh in the U.K. The satellite instrument has been developed from balloon and aircraft versions of MLS [refs. 8.4-8.8].

8.4 Microwave Limb Sounder Instrument

The MLS instrument has three main assemblies: sensor, spectrometer and power supply. A signal flow diagram of the MLS is shown in Fig. 8.2. The thermal radiation from the atmospheric limb is collected by the antenna and optically diplexed and polarisation split to the three millimeter wave radiometers. The local oscillator frequencies for these are 63.28 GHz, 184.78 GHz and 203.28 GHz. Each radiometer downconverts the signal to a common I.F. frequency of 400 MHz. These signals are then analysed by the spectrometer filter banks and the data passed to the UARS data bus for transmission to a ground station for analysis.

8.4.1 Antenna

The antenna along with the radiometer box form the sensor assembly. Fig. 8.3 is a sketch of the MLS sensor assembly. The antenna is an offset Cassegrain type with a main parabolic disk aperture of 1.6 m by 0.8 m giving a half power beam width in the vertical plane of 0.25° for B1 and 0.07° for B2-B4, corresponding to a 3.5 km resolution at the limb for B2-B4. The surface of the parabola has an rms accuracy of 15 μm to reduce scattering losses to no more than a few percent. The signal is then reflected from a hyperbolic secondary to a tertiary mirror whose optical axis is positioned on the axis of rotation so that the instrument remains fixed during an antenna scan. The signal is reflected from the tertiary mirror into the radiometer box (Fig. 8.3). The antenna system can be moved in a vertical plane to scan the field of view vertically through the earth's atmosphere. The antenna views the limb of the earth in a direction perpendicular to the satellites orbital path and depressed by 22° from the horizontal.

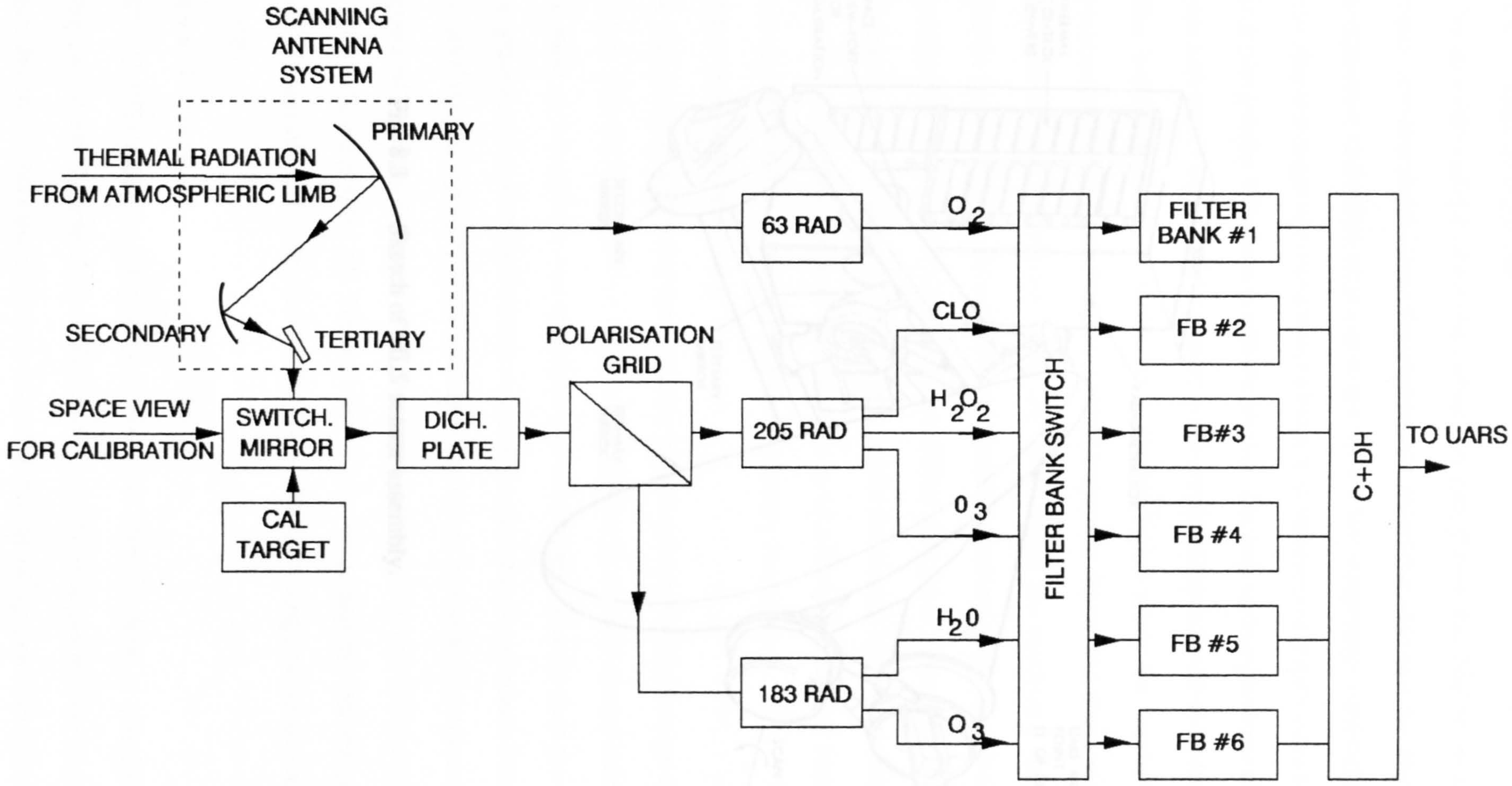

Fig. 8.2 Signal flow block diagram of the MLS instrument.

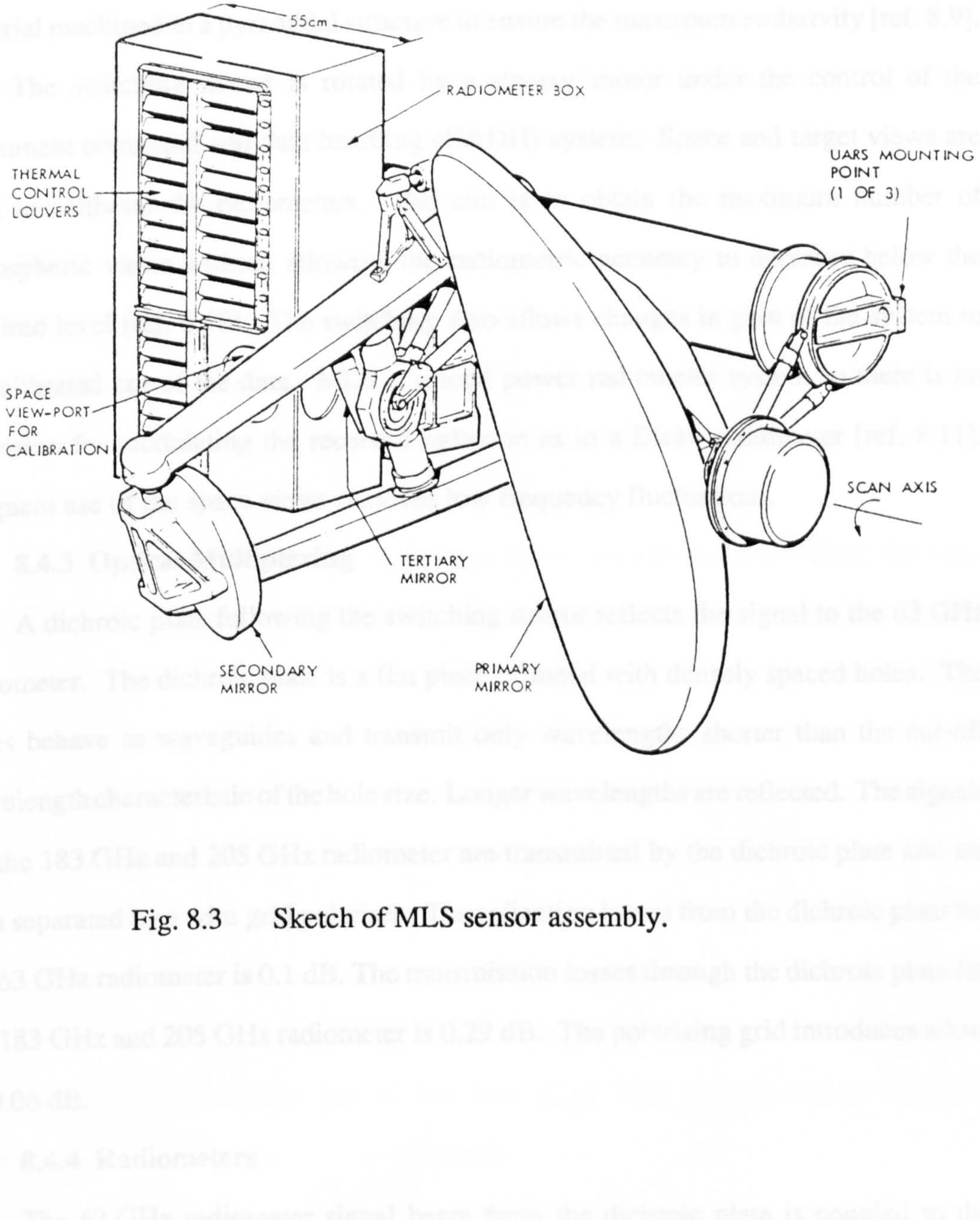

Fig. 8.3 Sketch of MLS sensor assembly.

8.4.2 Calibration System

The switching mirror inside the radiometer box allows the field of view of the radiometer to be directed to either the atmospheric signal from the antenna, an internal room temperature calibration target, or to space for a low temperature calibration. The internal calibration target approximates to a black body source so that it provides a known signal for comparison with the atmospheric signal. The targets are made from absorber material machined in a pyramidal structure to ensure the maximum emissivity [ref. 8.9].

The switching mirror is rotated by a stepper motor under the control of the instrument command and data handling (C&DH) system. Space and target views are used to calibrate the radiometers. The aim is to obtain the maximum number of atmospheric views without allowing the radiometric accuracy to decrease below the required level [ref. 8.10]. The switching also allows changes in gain of the system to be calibrated out of the data. MLS is a total power radiometer system so there is no provision for modulating the received radiation as in a Dicke radiometer [ref. 8.11]. Frequent use of the space views removes low frequency fluctuations.

8.4.3 Optical Multiplexing

A dichroic plate following the switching mirror reflects the signal to the 63 GHz radiometer. The dichroic plate is a flat piece of metal with densely spaced holes. The holes behave as waveguides and transmit only wavelengths shorter than the cut-off wavelength characteristic of the hole size. Longer wavelengths are reflected. The signals for the 183 GHz and 205 GHz radiometer are transmitted by the dichroic plate and are then separated by a wire grid polariser. The reflection losses from the dichroic plate for the 63 GHz radiometer is 0.1 dB. The transmission losses through the dichroic plate for the 183 GHz and 205 GHz radiometer is 0.29 dB. The polarising grid introduces a loss of 0.06 dB.

8.4.4 Radiometers

The 63 GHz radiometer signal beam from the dichroic plate is coupled to the feedhorn by a beam shaping mirror. The mirror is astigmatic and has the appropriate curvature in the two orthogonal planes, to correct for the difference in the phase front

radii of curvature to a circularly symmetric beam to match to the feedhorn. The signal then propagates along a short section of waveguide to the balanced Schottky mixer where the signal is heterodyned with a phase locked Gunn local oscillator. The I.F. is then amplified and downconverted for analysis in the spectrometer.

The higher frequency radiometers require a different configuration from the 63 GHz radiometer as there are no balanced mixers available at 183 GHz and 205 GHz of flight quality and packaged diodes have too large a capacitance for such high frequency operation. These high frequency radiometers use single ended mixers with whisker contacted Schottky diodes [ref. 8.12]. The mixers and triplers for the 183 GHz radiometer were supplied by Rutherford Appleton Laboratory.

The local oscillator and signal are optically combined in a Fabry-Perot interferometer (FPI). A schematic of the 183 GHz front end is shown in Fig. 8.4. The 205 GHz radiometer configuration is identical to the 183 GHz radiometer. Only the 183 GHz will be discussed as the two are identical, apart from the number of I.F. outputs and local oscillator frequencies.

The FPI marked in Fig. 8.4 is a Fabry-Perot ring resonator in which the local oscillator (L.O.) is transmitted and is combined with the signal reflected from the FPI input. Both signals are then reflected into the mixer horn by a focussing mirror as in the 63 GHz radiometer. The tripler converts the 61.59 GHz output from a phase locked gunn oscillator to the 184.78 GHz local oscillator required to downconvert the signals from the atmospheric limb. A focussing mirror matches the beam from the tripler horn to the instrument beam parameters for transmission through the FPI. The tripler and mixer horns are dual mode with suppressed sidelobes and nearly equal beam shape in the E and H field patterns [ref. 8.13]. This particular modification of the Potter horn [ref. 8.14] is dimensionally less critical than other horn designs and so easier to manufacture for millimetre wave applications.

This coupling arrangement has the advantage over alternative systems based on interferometers that the reflectivity of the Fabry-Perot for the signal is high over a relatively broad band [refs. 8.15, 8.16]. Fig. 8.5 shows a diagram of an FPI with the

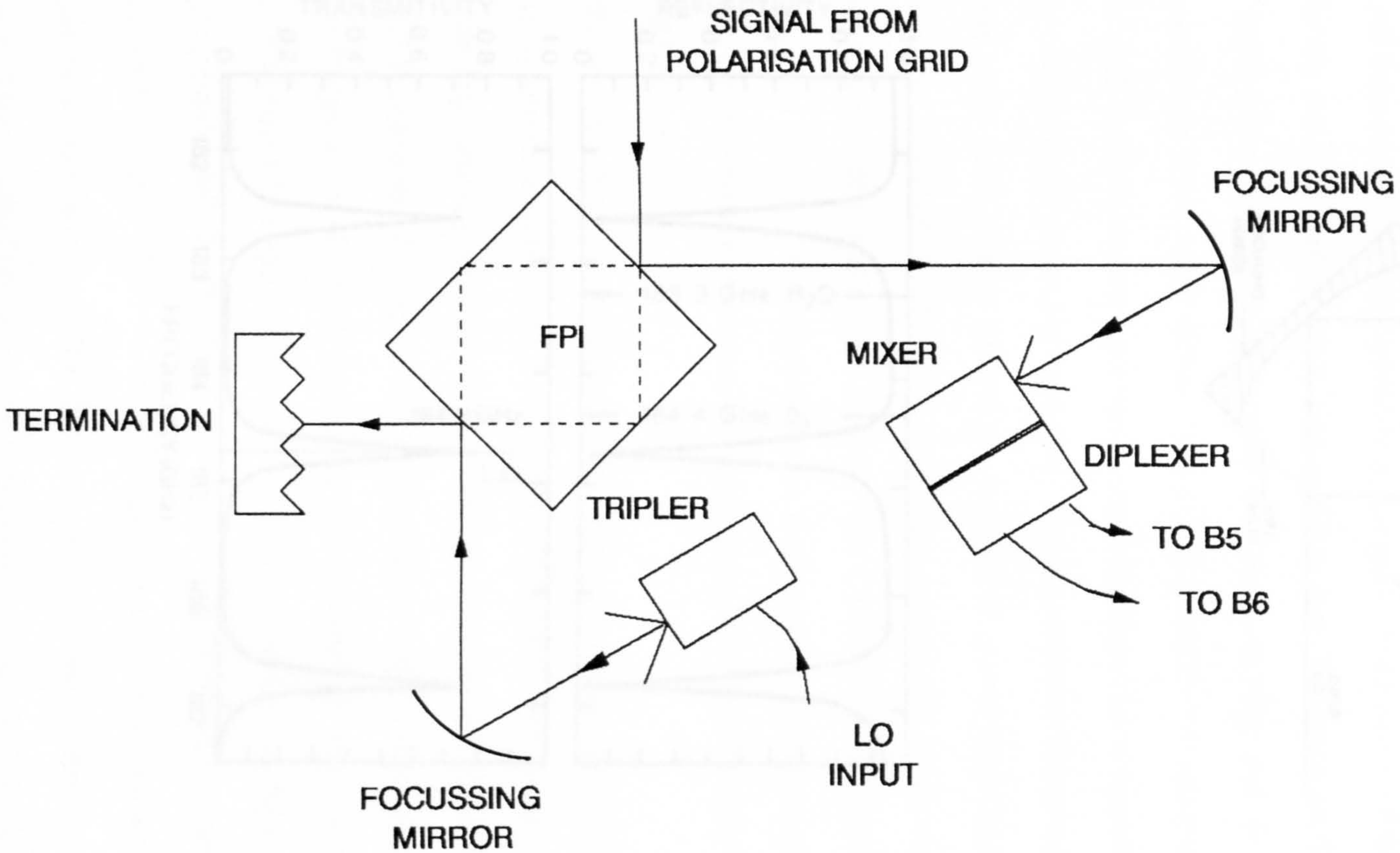

Fig. 8.4 183 GHz radiometer front end.

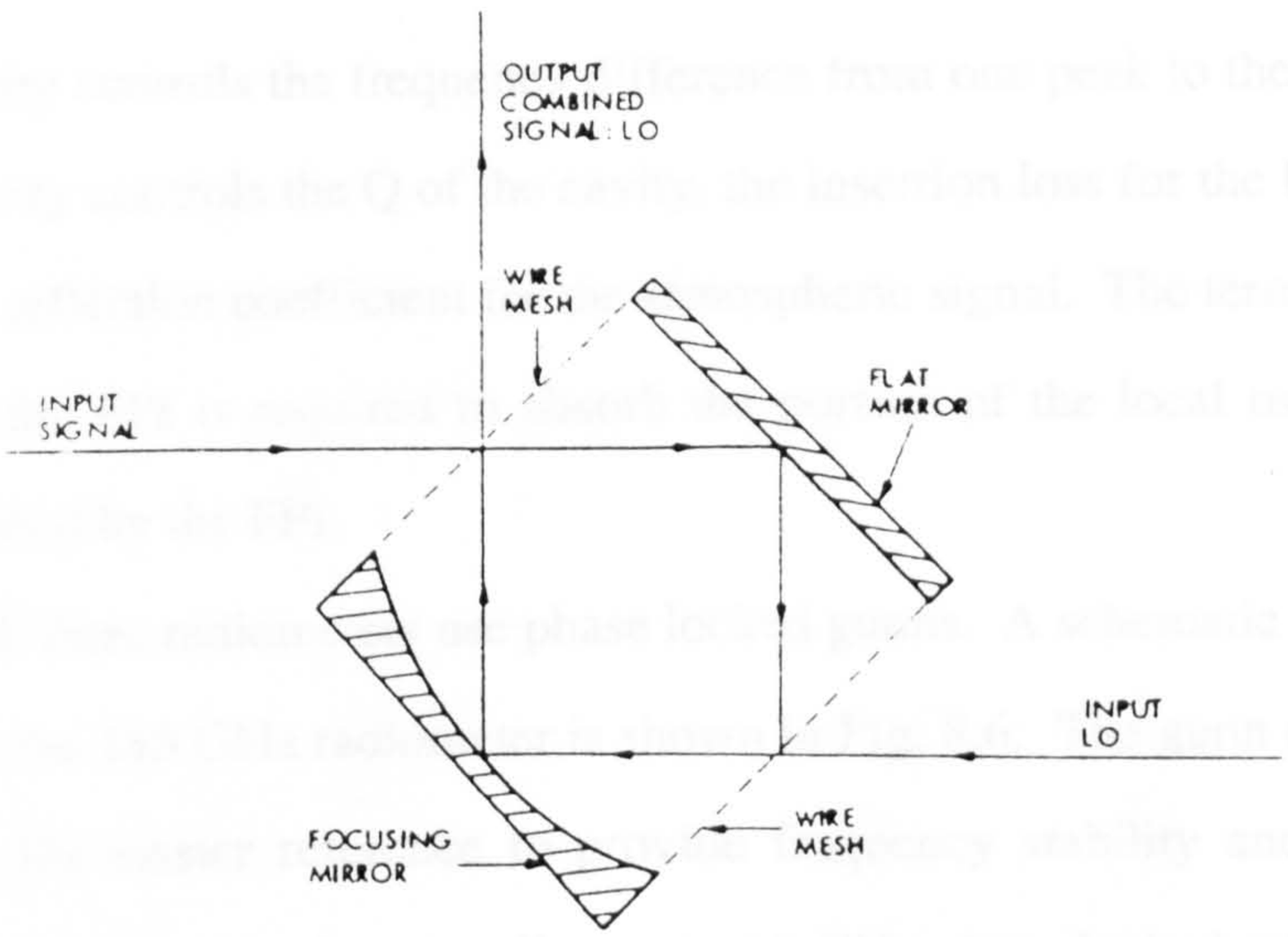

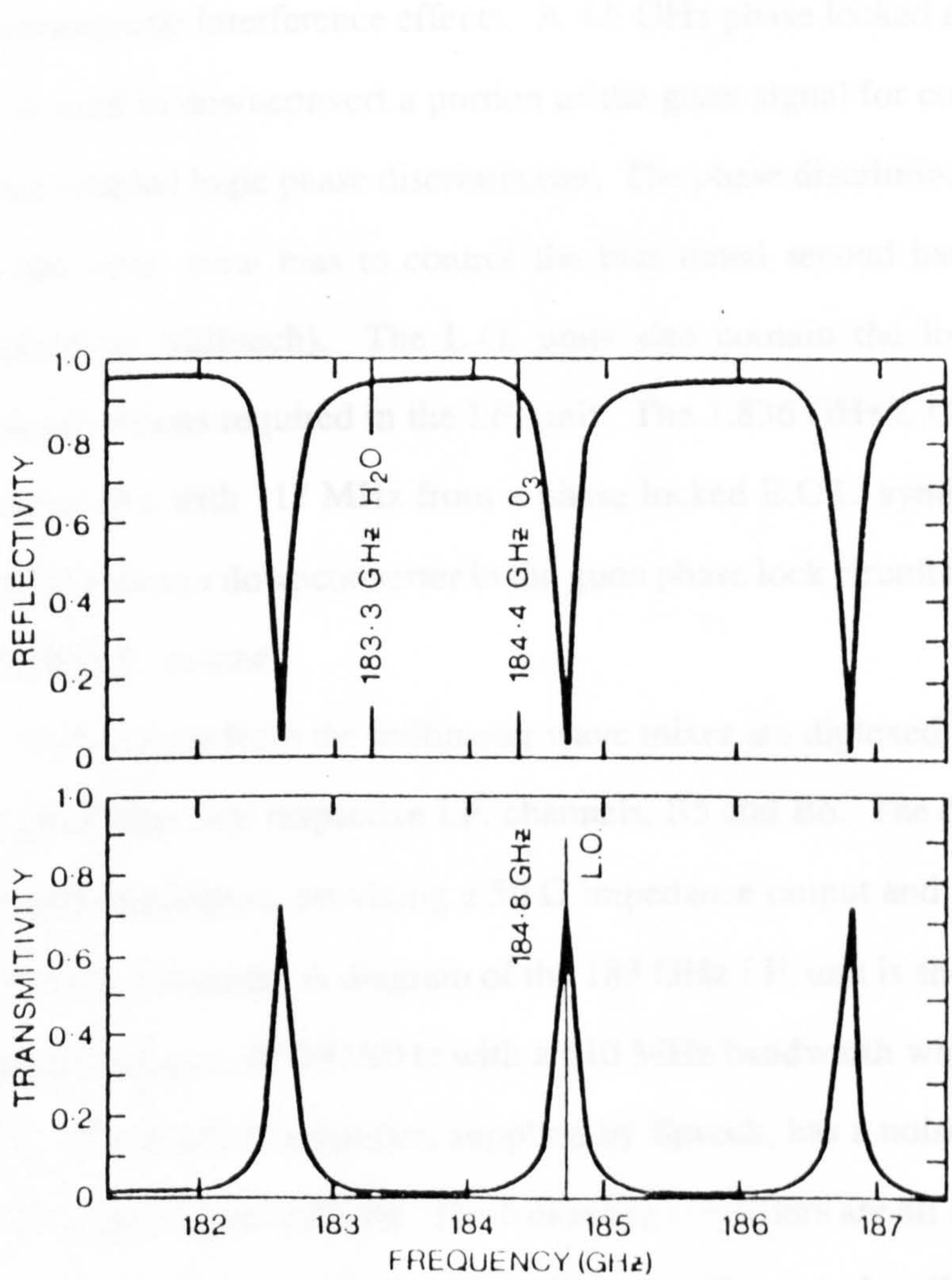

Fig. 8.5 FPI configuration and frequency response.

transmission and reflection characteristics for the 183 GHz radiometer. The size of the FPI cavity controls the frequency difference from one peak to the next while the mesh reflectivity controls the Q of the cavity, the insertion loss for the local oscillator signal and the reflection coefficient for the atmospheric signal. The termination on the fourth part of the FPI is required to absorb the portion of the local oscillator which is not transmitted by the FPI.

All three radiometers use phase locked gunns. A schematic of the local oscillator unit for the 183 GHz radiometer is shown in Fig. 8.6. The gunn oscillator is locked to a 4.7 MHz master reference to provide frequency stability and to control possible electromagnetic interference effects. A 4.5 GHz phase locked reference, from another unit, is used to downconvert a portion of the gunn signal for comparison in the digital emitter coupled logic phase discriminator. The phase discriminator output is combined with the static gunn bias to control the bias tuned second harmonic gunn oscillator (supplied by Millitech). The L.O. units also contain the local oscillators for any downconvertions required in the I.F. unit. The 1.836 GHz L.O. is generated by a x16 multiplier fed with 117 MHz from a phase locked E.C.L. synthesiser. The multiplier output is split to a downconverter in the gunn phase lock circuit and for downconvertion in the B5 I.F. channel.

The outputs from the millimeter wave mixer are diplexed to separate the H_2O and O_3 signals into their respective I.F. channels, B5 and B6. The diplexer also matches to the diode impedance, providing a 50 Ω impedance output and some isolation between the two I.F. channels. A diagram of the 183 GHz I.F. unit is shown in Fig. 8.7. B6 has a centre frequency of 400 MHz with a 510 MHz bandwidth which is controlled by two filters. The first I.F. amplifier, supplied by Spacek, has a noise figure of 1.3 dB and a gain of approximately 30 dB. The following amplifiers are all cascadable amplifiers in TO-8 style packages. The final amplifier provides gain levelling across the band and commandable gain control. The nominal output power to the filter bank switch is -10 dBm. All the amplifiers have sufficiently high compression points to avoid nonlinear responses. I.F. channel B5 has a centre frequency of 1468 MHz and a 510 MHz

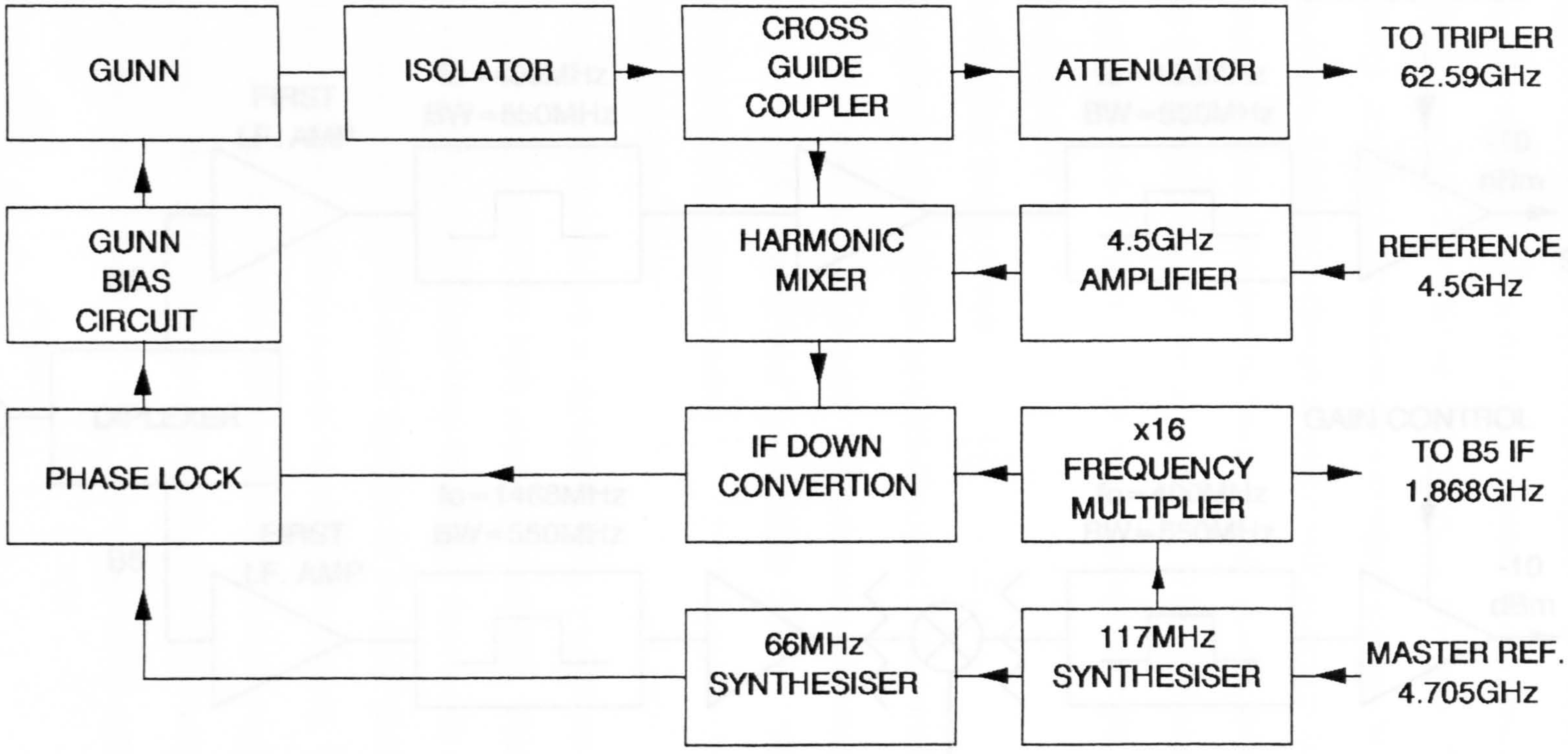

Fig. 8.6 183 GHz radiometer L.O. unit.

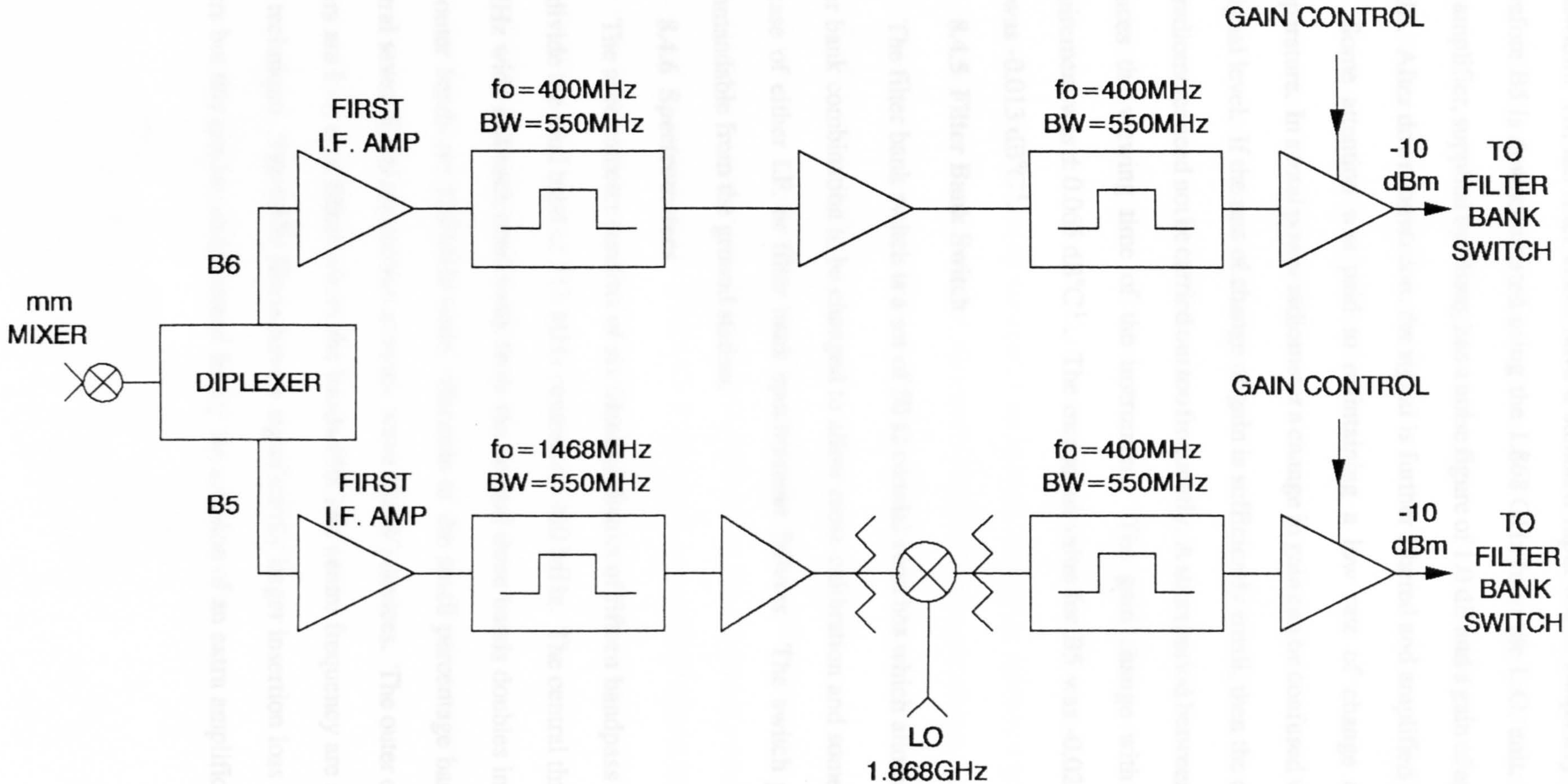

Fig. 8.7 183 GHz radiometer I.F. unit.

bandwidth. All the filter banks have a standard input centre frequency of 400 MHz, therefore B5 is downconverted using the 1.868 GHz from the L.O. unit. The B5 first I.F. amplifier, supplied by Miteq, has a noise figure of 1.0 dB and a gain of approximately 34 dB. After downconvertion, the signal is further filtered and amplified as in B6.

Some attention was paid to maintaining a low rate of change of gain with temperature. In a total power radiometer a change in gain can be confused with a change in signal level. If the rate of change of gain is sufficiently small, then the calibration of the radiometer need not be carried out too frequently. A short period between calibrations reduces the viewing time of the instrument. The gain change with temperature requirement was ± 0.065 dB°C^{-1} . The measured value for B5 was -0.027 dB°C^{-1} and B6 was -0.013 dB°C^{-1}.

8.4.5 Filter Bank Switch

The filter bank switch is a set of 50 Ω coaxial switches which allows the I.F. and filter bank combination to be changed to allow cross-calibration and some redundancy in case of either I.F. or filter bank spectrometer failures. The switch positions are commandable from the ground station.

8.4.6 Spectrometers

The spectrometer consists of six identical banks of fifteen bandpass filters which subdivide the total band of 512 MHz centred on 400 MHz. The central three bands are 2 MHz wide and each band away from the central three bands doubles in bandwidth , the outer bands are 128 MHz wide. Because of the small percentage bandwidths the central seven filters are surface acoustic wave (SAW) devices. The outer eight channel filters are L-C type filters where the bandwidth and centre frequency are attainable by this technique. The SAW filters have a significantly larger insertion loss than the L-C filters but this can be compensated for by the addition of an extra amplification stage.

The output power from each filter is rectified by a tunnel diode operated in the square law region. The filtered output from the diode is amplified and digitally integrated by a voltage to frequency converter and a counter. All ninety filter outputs are read every 2 seconds by the data system.

8.4.7 Command and Data System

The microprocessor based command and data system (C&DH) assimilates data from the spectrometer, temperature sensors and instrument monitors, and formats these data for transmission to UARS and subsequent transmission to the ground station with a bit rate of approximately 1,000 bits per second. The C&DH also relays all the control commands from the ground station to the subsystems such as the scan and calibration mechanisms, the switching network, bias control for gunns, mixers, triplers, I.F. gain and synthesisers. The system can also store command sequences for execution at a later time. All C&DH operations are synchronised within MLS and with UARS.

8.4.8 Power System

The power system controls and conditions spacecraft power bus inputs to the voltages required by the subsystems. Each radiometer has a separate power supply. The total power requirement for MLS is 185 W which is achieved with a 75% efficiency from the power system. Subsystems sensitive to noise on the power supply have local regulation.

8.4.9 System Performance

The double sideband noise temperatures for the six bands at room temperature are

B1	457 K
B2	1083 K
B3	1126 K
B4	1681 K
B5	1740 K
B6	1893 K

These are all within the instrument requirements. Figs. 8.8, 8.9 and 8.10 show the measured radiometric sensitivities for various integration times for ClO_3, H_2O and O_3, respectively. Channel 8 has the smallest bandwidth of 2 MHz and channels 1 and 15 have a bandwidth of 128 MHz, hence the difference in sensitivities shown in the graphs. The stability and lack of interference in the system is demonstrated by the linear improvement in sensitivity with increasing integration time. If the above stability is reproduced during flight conditions then the number of calibrations required may be reduced allowing more viewing time of the atmospheric limb.

Temperature changes during each orbit may upset the system stability but these will be reduced to a minimum by the louvred thermal control panels and by using the UARS cooling system. The MLS instrument has passed all its requirements and environmental tests consistent with a shuttle launch.

Table 8.2 from the UARS handbook [ref. 8.3] summarises the MLS instrument parameters.

8.5 Conclusions

The MLS instrument data will form part of a large number of measurements to be made by experiments on the UARS observatory due for launch in October 1991. These measurements will be of immense value in furthering our understanding of the photochemistry and dynamics of the atmosphere. Chlorine and ozone concentrations will be monitored and depletion of ozone during the Antarctic spring will be studied. Studies of the radiation budget and dynamics of the atmosphere will be made possible by simultaneous measurements of water vapour and ozone.

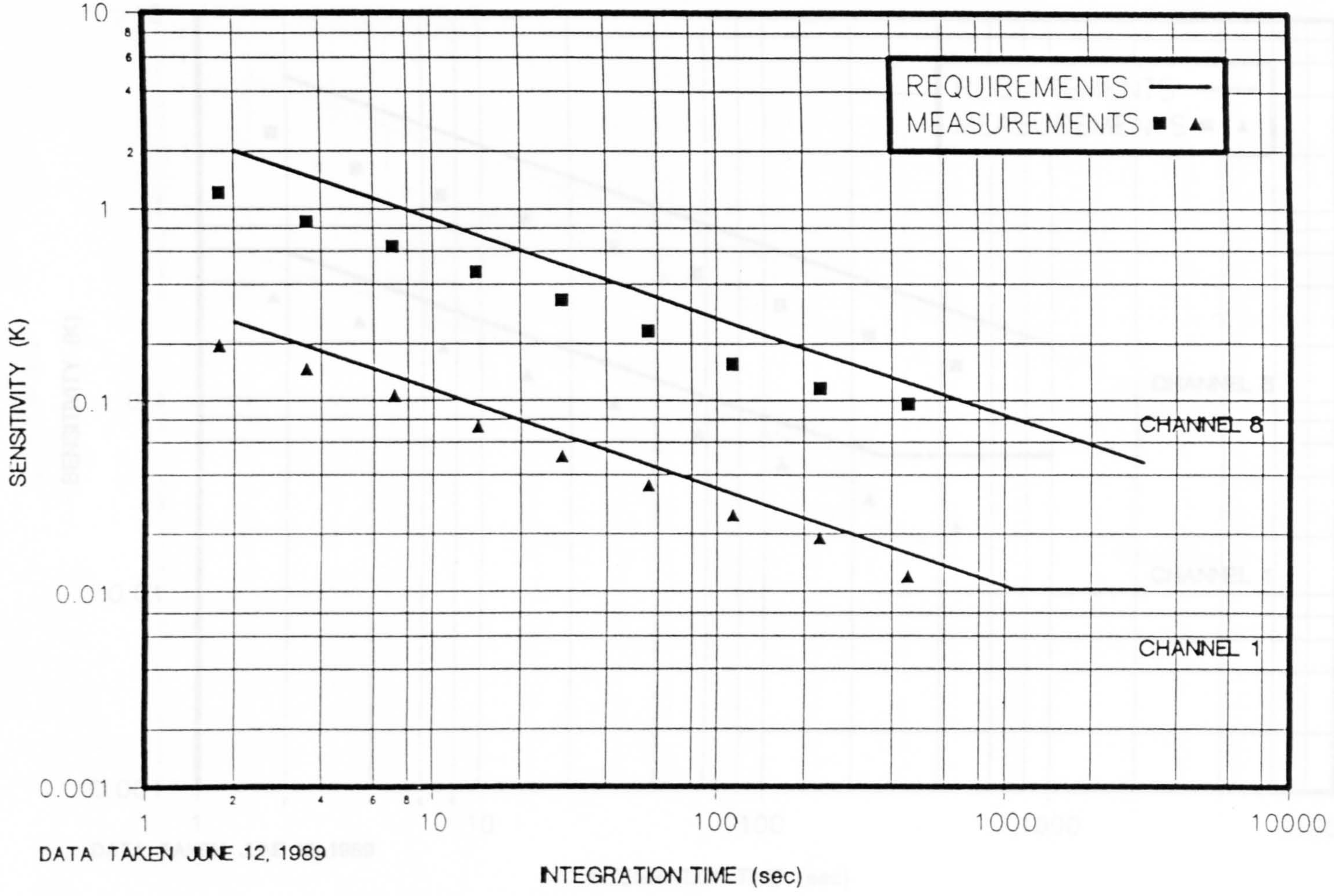

Fig. 8.8 Band 2 (ClO) radiometric sensitivity.

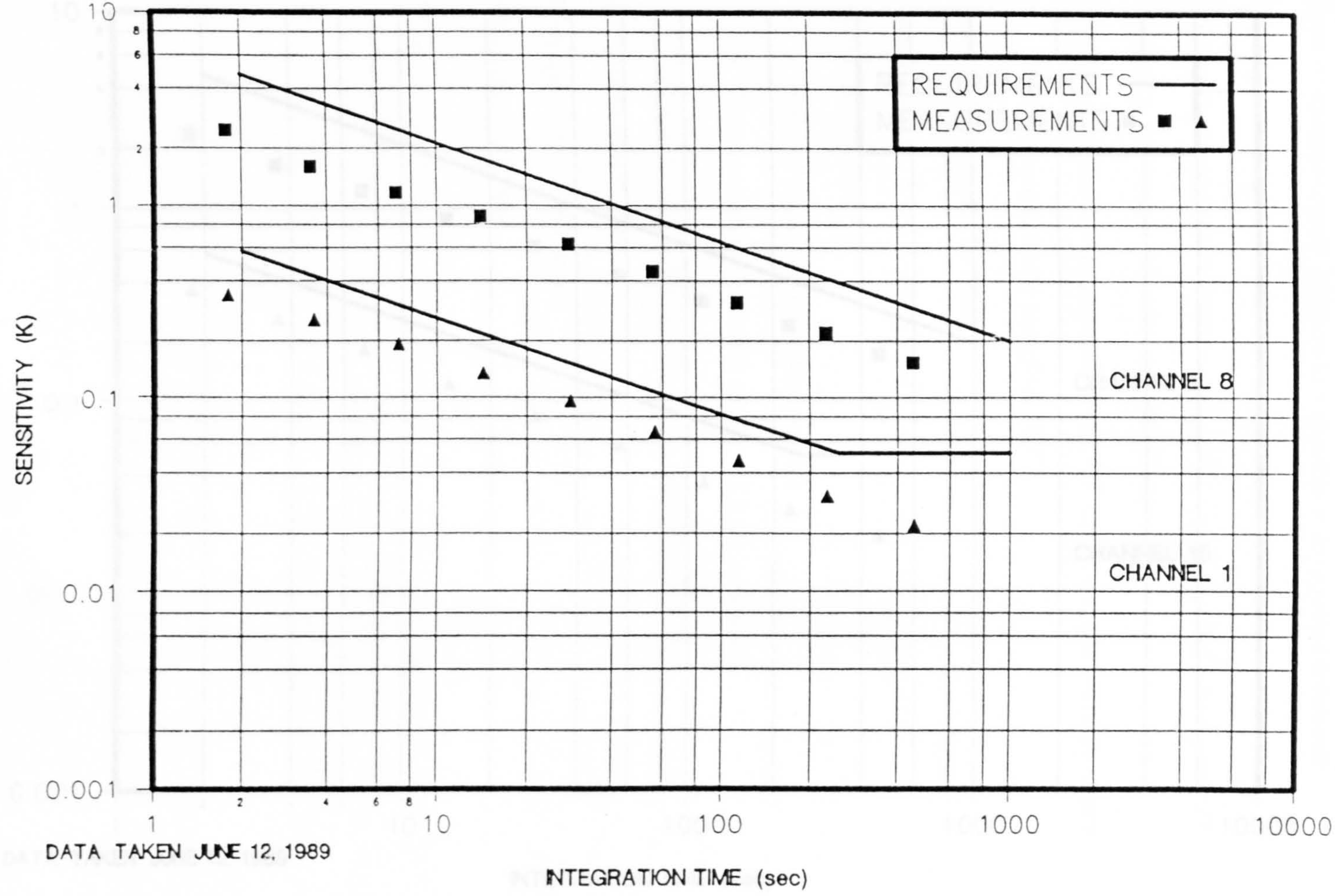

Fig. 8.9 Band 5 (H_2O) radiometric sensitivity.

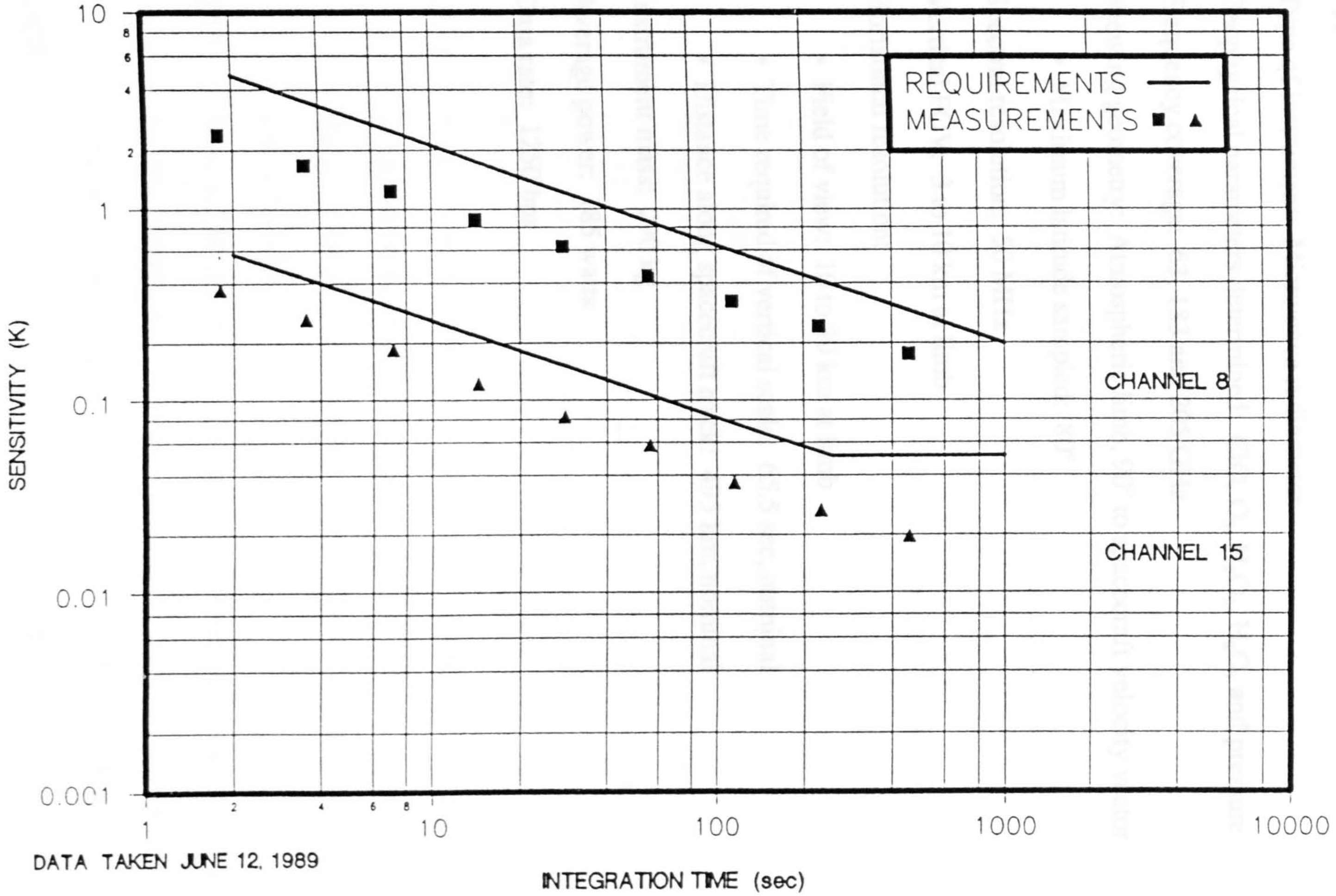

Fig. 8.10 Band 6 (O_3) radiometric sensitivity.

Table 8.2

MLS Instrument Parameters

Type of measurement: Microwave thermal atmospheric emission

Type of instrument: Microwave radiometer

Geophysical parameters determined: ClO, O_3, H_2O_2, H_2O, and pressure

Frequency coverage: 63, 183 and 205 GHz

Viewing geometry: Atmospheric limb, 90° to spacecraft velocity vector

- Maximum latitude sampled: 80°

Spectral resolution: 50 MHz

Vertical FOV: 3 to 10 km at limb

Horizontal resolution:

- Field of view: 10 to 30 km at limb
- Time required of vertical scale: 65.5 sec, nominal
- Distance along spacecraft track: 495 km, nominal

Instrument mass: 290 kg

Average power: 185 watts

Data rate: 1250 bps

References

[8.1] Staelin, D.H., Barrett, A.H., Waters, J.W., Barath, F.T., Johnston, E.J., Rosenkranz, P.W., Grant, N.E. and Lenoir, W.B., "Microwave spectrometer on the Nimbus 5 satellite: meteorological and geophysical data", Science, 182, pp. 1339-1341, 1973.

[8.2] Farman, J.C., Gardiner, B.G. and Shanklin, J.D., "Large losses of total ozone in Antarctica reveal seasonal ClO_x/NO_x interaction", Nature, 315, p. 207, 1985.

[8.3] NASA, UARS Project Data Book, 1987.

[8.4] Waters, J.W., Hardy, J.C., Jarnot, R.F., Pickett, H.M. and Zimmermann, P., "A balloon-borne microwave limb sounder for stratospheric measurements", J. Quant. Spectrosc. Radiat. Transfer, 32, pp. 407-433, 1984.

[8.5] Waters, J.W., Stachnik, R.S., Hardy, J.C. and Jarnot, R.F., "ClO and O_3 stratospheric profiles: balloon microwave measurements", Geophys. Res. Lett., 15, pp.780-783, 1988.

[8.6] Waters, J.W., Gustincic, J.J., Kakar, R.K., Roscoe, H.K., Swanson, P.M., Phillips, T.G., De-Graauw, T., Kerr, A.R. and Mattauch, R.J., "Aircraft search for millimeter wavelength emission by stratospheric ClO", J. Geophys. Res., 84, pp. 7034-7040, 1979.

[8.7] Waters, J.W., Gustincic, J.J., Swanson, P.N. and Kerr., A.R., "Measurements of upper atmospheric H_2O emission at 183 GHz. In: Deepak, Wilkerson and Ruhnke (Editors), Atmospheric Water Vapour, Academic Press, London, pp. 229-240, 1980.

[8.8] Waters, J.W., Hardy, J.C., Jarnot, R.F. and Pickett, H.M., "Chlorine monoxide radical, ozone, and hydrogen peroxide: stratospheric measurements by microwave limb sounding", Science, 214, pp. 61-64, 1981.

[8.9] Goldsmith, R.A., Kot, and Iwasaki, R.S., "Microwave radiometer black body calibration standard for use at millimeter wavelengths", Rev. Sci. Instrum., 50(9), pp. 1120-1122, 1979.

[8.10] Peckham, G.E., "An optimum calibration procedure for radiometers", Int. J. Remote Sensing, 10, pp. 227-236, 1989.

[8.11] Dicke, R.H., "The measurement of thermal radiation at microwave frequencies", Rev. Sci. Instrum., No. 17, pp. 268-275, 1946.

[8.12] Archer, J.W. and Mattauch, R.J., "Low noise single-ended mixer for 230 GHz", Electron Lett., 17, pp. 180-181, 1981.

[8.13] Pickett, H.M. Hardy, J.C. and Jam Farhoomand, "Characterisation of a dual-mode horn for submillimeter wavelengths", IEE Trans. on Microwave Theory and Techniques, MT-32, 8, pp. 936-937, 1984.

[8.14] Potter, P.D., "A new horn antenna with suppressed sidelobes and equal beamwidths", Microwave Journal, p. 71, June 1963.

[8.15] Gustincic, J.J., "A quasi-optical receiver design", IEEE MTT-S Int. Microwave Symp. Digest, pp. 99-101, 1977.

[8.16] Pickett, H.M. and Chiou, A.E.T., "Folded Fabry-Perot quasi-optical ring resonator diplexer; theory and experiment", IEEE Trans. Microwave Theory and Techniques, MT-31, pp. 373-380, 1983.

APPENDIX A

ATMOSPHERIC ATTENUATION PROGRAM

```
    5  %D=8.68589
    7  G.705
   10  IN."NUMBER OF DATA SETS"F
   20  FDIM %RR(F),%SS(F),%QQ(F),%GG(F),%
HH(F)
   30  FOR M=1 TO F
   35P.'"DATA SET #"M,'
   40  FIN."P."%RR(M)
   50  FIN."T."%SS(M)
   60  FIN."H."%QQ(M)
   70  N.M
   80  FOR M=1 TO F
   90  %P=%RR(M);%T=%SS(M);%H=%QQ(M);GOS.
a;%GG(M)=%B;%HH(M)=%V;N.
  100  FOR M=1 TO F
  110  @=3;P.M;@=11;FP." ATT="%GGM"DB",'
  115  FP."      WVD="%HHM"GM-3" ';LINK#FFE3
;N.
  120  E.
  705  REM look up tables
  710  FDIM %AA(44),%BB(44),%CC(44),%DD(4
4),%EE(44),%FF(44)
  720  FDIM %YY(44),%VV(50),%PP(22),%NN(2
2),%WW(22),%XX(22)
  730  FDIM %ZZ(6),%II(4),%TT(2)
  740  %AA3=56.2648;%AA4=118.7503;%AA5=58
.4466;%AA6=62.4863
  741  %AA7=59.591;%AA8=60.306;%AA9=60.43
48;%AA10=59.1642
  742  %AA11=61.1506;%AA12=58.3239;%AA13=
61.8002;%AA14=57.6125
  743  %AA15=62.4112;%AA16=56.9682;%AA17=
62.998;%AA18=56.3634
  744  %AA19=63.5685;%AA20=55.7838;%AA21=
64.1278;%AA22=55.2214
  745  %AA23=64.6789;%AA24=54.6711;%AA25=
65.2241;%AA26=54.13
  746  %AA27=65.7647;%AA28=53.5957;%AA29=
66.3021;%AA30=53.0668
  747  %AA31=66.8368;%AA32=52.5422;%AA33=
67.3695;%AA34=52.0212
  748  %AA35=67.9007;%AA36=51.503;%AA37=6
8.4308;%AA38=50.9873
  749  %AA39=68.9601;%AA40=50.4736;%AA41=
69.4887;%AA42=49.9618
  750  %EE3=1.64554;%EE4=1.59197;%EE5=1.4
4867;%EE6=1.46784
  751  %EE7=1.3595;%EE8=1.38218;%EE9=1.29
704;%EE10=1.31879
```

```
704;%EE10=1.31879
   752  %EE11=1.24768;%EE12=1.26637;%EE13=
1.20682;%EE14=1.22107
   753  %EE15=1.17073;%EE16=1.18061;%EE17=
1.13859;%EE18=1.14418
   754  %EE19=1.10823;%EE20=1.11031;%EE21=
1.07754;%EE22=1.07892
   755  %EE23=1.04859;%EE24=1.04859;%EE25=
1.01865;%EE26=1.01865
   756  %EE27=.99577;%EE28=.99577;%EE29=.9
6653;%EE30=.96653
   757  %EE31=.94421;%EE32=.94421;%EE33=.9
1566;%EE34=.91566
   758  %EE35=.88749;%EE36=.88749;%EE37=.8
6605;%EE38=.86605
   759  %EE39=.83857;%EE40=.83857;%EE41=.8
177;%EE42=.8177
   780  %VV1=2.8627;%VV2=3.0971;%VV3=3.348
4;%VV4=3.6177
   781  %VV5=3.9061;%VV6=4.2148;%VV7=4.545
1;%VV8=4.8981;%VV9=5.2753
   782  %VV10=5.678;%VV11=6.1078;%VV12=6.5
662;%VV.13=7.0547
   783  %VV14=7.5753;%VV15=8.1294;%VV16=8.
7192;%VV17=9.3465
   784  %VV18=10.013;%VV19=10.722;%VV20=11
.474;%VV21=12.272
   785  %VV22=13.119;%VV23=14.017;%VV24=14
.969;%VV25=15.977;
   786  %VV26=17.044;%VV27=18.173;%VV28=19
.367;%VV29=20.63
   787  %VV30=21.964;%VV31=23.373;%VV32=24
.861;%VV33=26.43
   788  %VV34=28.086;%VV35=29.831;%VV36=31
.671;%VV37=33.608
   789  %VV38=35.649;%VV39=37.796;%VV40=40
.055;%VV41=42.43
   790  %VV42=44.927;%VV43=47.551;%VV44=50
.307;%VV45=53.2
   795  %R=1.434
   798  G.10
   845a%T=%T-273.15
   850  K=%T+11;L=K+1
   860  %E=(%T-K+11)*(%VV(L)-%VV(K))+%VV(K
)
   870  %W=%E*%H/100
   880  %H=.62069*(%W/(%P-%W))
   890  %Q=(%P-%W)^2*.000001
   900  %T=%T+273.15;%V=216.5*%W/%T
   932  FOR W=1 TO 2
   934  IF W=1 T. %F=53.975
   936  IF W=2 T. %F=58.11875
   940  F.J=3 TO 42
   950  IF J=(J/2)*2 T. G.980
   960  I=(J+1)/2;%WW(I)=%EE(J);G.990
   980  I=J/2;%XX(I)=%EE(J)
   990  N.J
  1000  %Z=L.(300/%T);%G=.48*E.(.89*%Z)
  1010  %FF21=0;%CC21=0;%AA1=0;%AA2=0;%AA4
3=0;%AA44=0
  1020  %Y=E.(.9*%Z);%BB21=%G-%WW21*%Y
  1040  %DD21=%G-%XX21*%Y;%PP1=0;%NN1=0
  1060  F.J=1 TO 19;I=21-J
  1070  A=2*(I-1)+1;B=A+1;C=A+B
  1080  %A=(C/(C-4))*E.(-4.138*(C-2)/%T)
  1090  %FF(I)=%BB(I+1)*%A
  1100  %BB(I)=%G-%WW(I)*%Y-%FF(I)
  1110  %GC(I)=%DD(I+1)*%A
```

```
 1120  %DD(I)=%G-%XX(I)*%Y-%CC(I)
 1130  %PP(I+1)=SQR((A*(C+2))/(B*C))
 1140  %NN(I+1)=SQR((B*(C-2))/(A*C));N.J
 1160  %PP2=.912871;%NN2=.816496
 1170  %BB1=0;%DD1=0
 1175  %PP22=0;%NN22=0
 1180  F.J=3 TO 42
 1190  IF J=(J/2)*2 T. G.1250
 1200  I=(J+1)/2
 1210  %I=(2*%PP(I-1)*%BB(I))/(%AA(J)-%AA
(J-2))
 1220  %I=%I-%G*(1/%AA(J)+1/(%AA(J)+60))
 1230  %I=(%I+(2*%PP(I+1)*%FF(I))/(%AA(J)
-%AA(J+2)))*(1/%PP(I))
 1234  %YY(J)=%I
 1240  G.1280
 1250  I=J/2;%I=%G*(1/%AA(J)+1/(%AA(J)+60
))
 1260  %I=(2*%NN(I-1)*%DD(I))/(%AA(J)-%AA
(J-2))-%I
 1270  %I=(%I+(2*%NN(I+1)*%CC(I)/(%AA(J)-
%AA(J+2)))*(1/%NN(I))
 1275  %YY(J)=%I
 1280  N.J
 1290  %N=%F;%TT(W)=0;%C=0;GOS.d
 1293  N.W
 1295  %B=(%TT2-%TT1)*.65
 1330  RETURN
1340d%D=L.(300/%T)
 1350  %K=1+1.6111*%H;%L=1+1.3*%H
 1360  %M=%L*EXP(.9*%D)
 1370  %O=.48*%M;%ZZ3=%N;GOS.e;%S=.7*%X/%
O/%T
 1400  F.I=3 TO 42
 1410  IF I<>(I/2)*2 T. G.1450
 1420  %O=%M*%EE(I)
 1430  %II3=%II1*(%II2-2)/(%II0*%II2)
 1440  %ZZ1=%O*%II3;%ZZ4=%ZZ5/%O/%O;G.150
0
 1450  %O=%M*%EE(I);%II0=I-2
 1460  %II1=%II0+1;%II2=%II1+%II0
 1470  %ZZ5=%II2*EXP(-2.0685*%II0*%II1/%T
)/(.725*%T*%T)
 1480  %II3=%II0*(%II2+2)/(%II2*%II1);%ZZ
1=%O*%II3
 1490  %ZZ4=%ZZ5/%O/%O
 1500  %ZZ2=%YY(I)*%L;%ZZ3=%AA(I)-%N;GOS.
e
 1510  %S=%S+%ZZ4*(%ZZ1-%ZZ3*%ZZ2*%II3)*%
X
 1520  %ZZ3=%AA(I)+%N;GOS.e
 1530  %S=%S+%ZZ4*(%ZZ1-%ZZ3*%ZZ2*%II3)*%
X;N.I
 1540  %TT(W)=%TT(W)+%R*%N*%N*%S*1000*%K/
(1+%H)
 1550  %O=5.84*%N*E.(.626*%D)*(1+6.272*%H
/%K);%ZZ3=494.402-%N*%N
 1560  GOS.e;%U=((7.9E9)*E.(-644/%T)*%X/%
O+30.7*%O*%Q)
 1570  %TT(W)=%TT(W)+(%H/(1+%H))*68.339*%
N*%U/(%T*%T*SQR(%T));R.
1580e%X=(%O*%O*%Q/%K/%K)
 1585  %X=%X/(%T*(%X+%ZZ3*%ZZ3));R.
 1590  E.
```

APPENDIX B

Microwave Reflection Properties of a Rotating Corrugated Metallic Plate used as a Reflection Modulator

by

Gordon E. Peckham and Robert A. Suttie

Microwave Reflection Properties of a Rotating Corrugated Metallic Plate Used as a Reflection Modulator

GORDON E. PECKHAM AND ROBERT A. SUTTIE

Abstract—The performance of a simple microwave modulating retro-reflector based on a rotating corrugated metallic plate has been analyzed theoretically and compared with laboratory measurements. Fields within the corrugations are described by waveguide modes and free space fields by Floquet modes. The periodicity of the grooves is represented through the reciprocal lattice corresponding to the periodic structure. The accuracy of the calculation is analyzed as a function of the number of modes used to describe the electromagnetic field. Graphs are given for the design of a modulator for any wavelength. This type of modulator has applications in the measurement of atmospheric propagation and of antenna beam patterns for both linearly and circularly polarized radiation.

Introduction

A ROTATING grooved metallic plate may be used to modulate linearly or circularly polarized radiation. This reflector plate (Fig. 1) carries a series of parallel rectangular grooves or corrugations with period less than a wavelength to avoid diffraction of the normally incident microwave radiation. The groove width is less than half a wavelength so that linearly polarized radiation with electric field parallel to the corrugations cannot propagate, and reflection occurs from the front of the plate. When the plate is rotated in its plane through a right angle, radiation propagates to the back of the grooves and reflection occurs behind the front face of the plate. If the depth of the grooves is a quarter wavelength, a 180° phase change results. This simple analysis must be modified to take account of fringe field effects but we will show that it is still possible to choose a groove shape to give a 180° phase change.

The reflector acts as an optical half-wave plate. Linearly polarized radiation remains linearly polarized, but the electric field direction is reflected in the plane parallel to the direction of the corrugations so that the plane of polarization of the reflected radiation rotates at twice the speed of rotation of the plate. A useful reduction of stray reflections can be made by polarizing the receiver at right angles to the transmitter. Steady rotation of the plate at frequency Ω then results in sinusoidal modulation of the reflected amplitude at frequency 2Ω. Circularly polarized radiation is reflected with no change of sense, i.e., clockwise incident gives rise to clockwise reflected polarization. Since a change of sense occurs on reflection from a plane metallic reflector some attenuation of stray reflection occurs if the receiver is sensitive only to the polarization reflected by the modulator. The frequency of the reflected radiation is changed by 2Ω. This single-sideband modulation may be detected conveniently by a homodyne receiver.

Measurements of atmospheric attenuation or antenna beam patterns are usually made with widely separated transmitter and receiver. Accurate measurements of receiver gain and transmitter power are necessary or at least these quantities must be highly stable. Use of a retro-reflector allows the receiver to be placed close to the transmitter so that bridge methods may be used to measure transmission loss. However, unwanted stray reflections from other objects in the field of view of transmitter and receiver can cause severe problems. Use of a modulating retro-reflector and coherent synchronous detection can largely eliminate these problems. A large aperture modulating retro-reflector may be made by placing a small corrugated plate modulator at the focus of a Cassegrain antenna system. This arrangement also avoids the need for accurate alignment as the reflector is a true retro-reflector.

Calculation of the Reflection Coefficients for a Corrugated Plate

Rayleigh [1] obtained expressions for the reflected velocity potential field arising from a plane sound wave reflected by a sinusoidally corrugated reflector. He described the reflected field as a superposition of diffracted plane waves known as Bloch or Floquet modes. Lamb [2] applied similar methods to the reflection and transmission of electromagnetic waves by a thin metallic grid. Chen [3] has extended this method for grids of finite thickness by introducing waveguide modes to describe the field within the grid apertures. This approach has proved very successful [4] and has been applied to the case of a corrugated plate by Deriugin [5], [6]. We introduce waveguide modes to describe the field within the rectangular grooves and obtain the amplitudes of the Floquet modes by requiring the two descriptions to be continuous across the front face of the corrugated plate. We formulate the solution for the general case of nonnormal incidence by introducing the reciprocal lattice corresponding to the periodic corrugations. Details are given in the Appendix. In the case that the period of the corrugations is less than the wavelength for normal

Manuscript received October 29, 1986, revised June 16, 1987. This work was supported by the Science and Engineering Research Council.

The authors are with the Department of Physics, Heriot-Watt University, Riccarton, Edinburgh EH14 4AS, Scotland

IEEE Log Number 8820221.

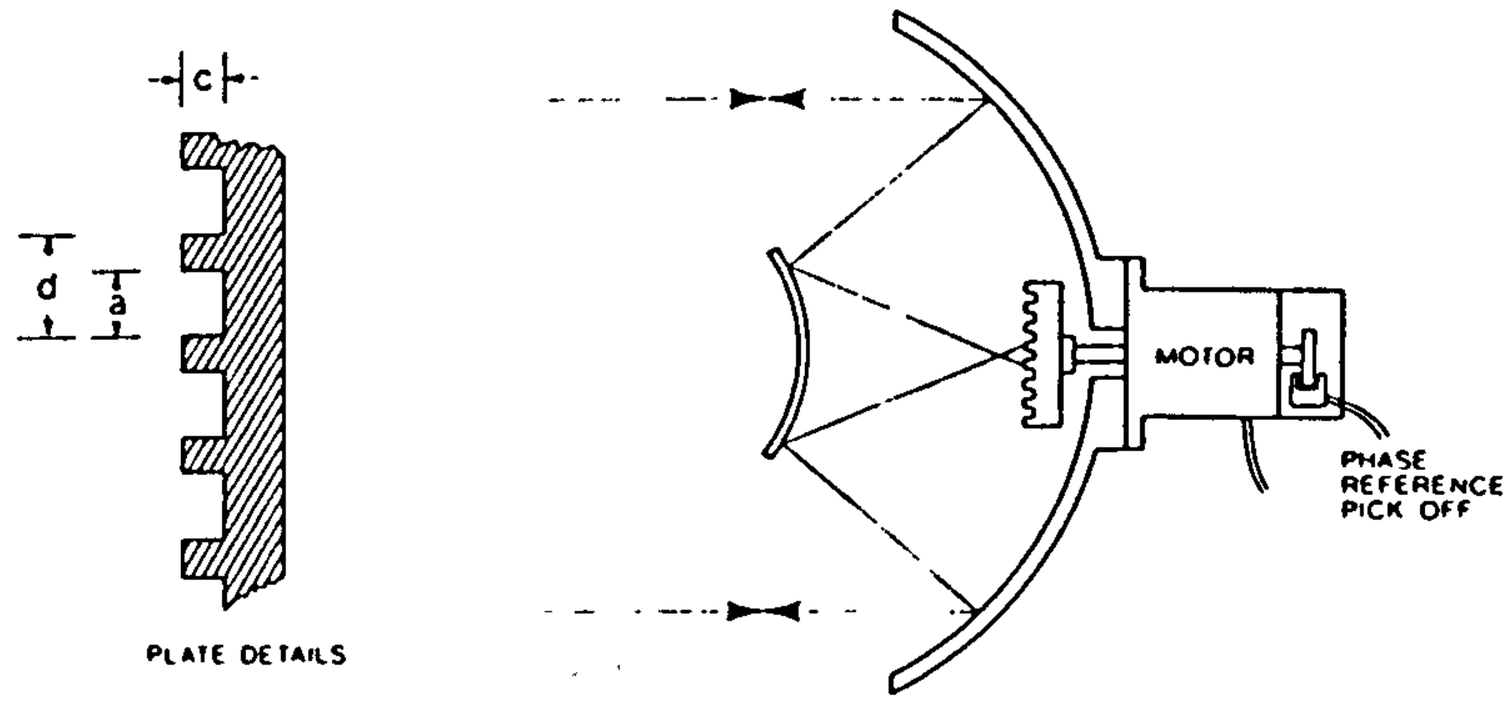

PLATE DETAILS

MODULATING CASSEGRAIN RETROREFLECTOR

Fig 1 The corrugated plate modulator

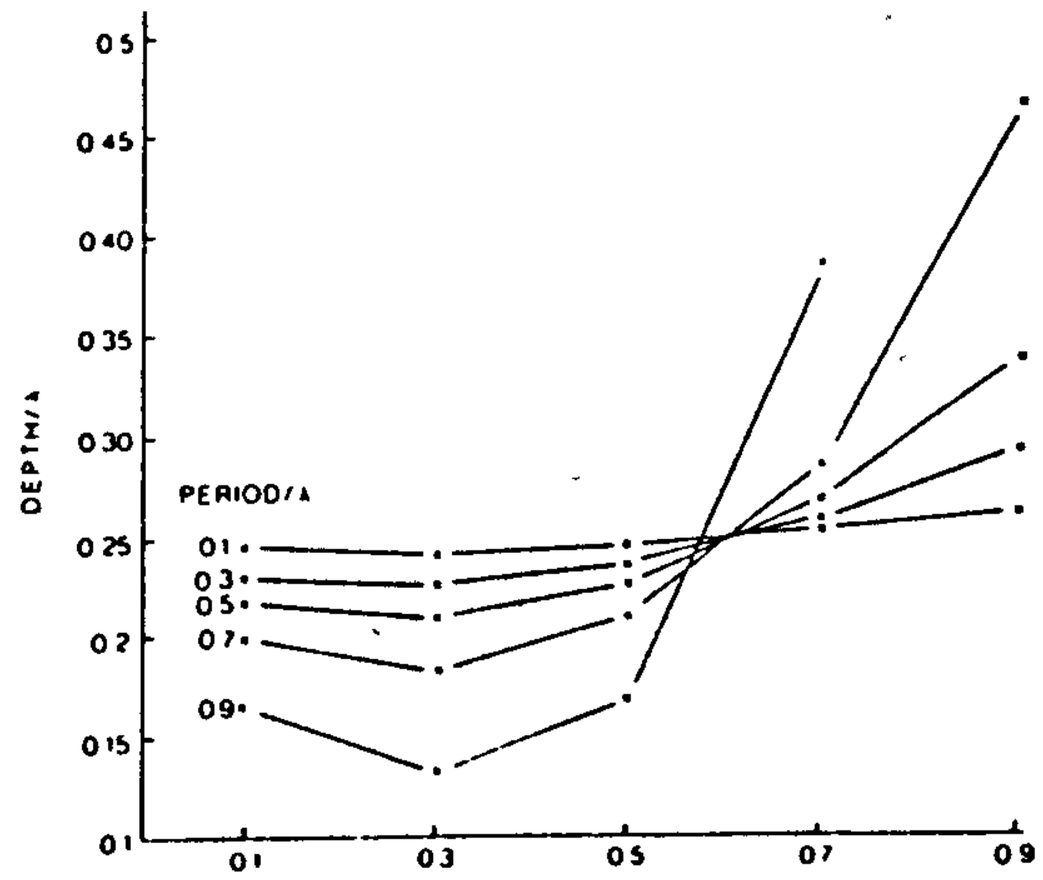

Fig 2 Depth of rectangular groove as a function of aspect ratio to give 180° phase shift between TM and TE orientations

incidence, only one mode propagates away from the plate to form the reflected beam, but nonpropagating evanescent modes make an important contribution to the field near the plate.

Reflectivities have been calculated for normal incidence only. The phase of the reflection is a function of the corrugation depth, period, and aspect ratio (groove width/repeat distance). In Fig. 2 we plot the corrugation depth as a function of aspect ratio to give 180° phase difference between the normal incidence reflected waves for electric field parallel and perpendicular to the corrugations. Plots are made for various values of the period. The required depth is seen to be quite close to the quarter-wavelength value indicated by simple theory for period of 0.1 of a wavelength or less. For larger values of the period the required depth becomes dependent on aspect ratio. However, an aspect ratio of 0.61 and a groove depth of a quarter wavelength give approximately 180° phase difference for all periods less than about 0.7 wavelengths. This graph provides the information needed to design a corrugated plate modulator for any wavelength.

TABLE I

CALCULATED PHASES (DEGREES) FOR TE AND TM WAVES REFLECTED FROM A CORRUGATED SHEET WITH GROOVE PERIOD 0 9λ, DEPTH 0 25λ, AND ASPECT 0.5

Number of Floquet Modes	Number of Waveguide Modes 1	2	5	10	20	
1	-118.28	-101.49	-99.67	-99.49	-99.45	TM
	135.76	134 37	133.93	133.86	133.85	TE
2	-118.28	-106.69	-104.74	-104.55	-104.50	TM
	142 96	137.85	137.02	136 90	136.88	TE
5	-119.30	-111.50	-108.08	-107.70	-107.63	TM
	142 43	140.55	139.10	138.93	138.88	TE
10	-119.39	-111.76	-109.52	-108.76	-108.64	TM
	142 63	140.95	140.01	139.53	139.46	TE
25	-119.44	-111.87	-109.85	-109.43	-109.14	TM
	142.68	141.02	140.19	139.96	139.80	TE
50	-119.44	-111.89	-109.89	-109.49	-109.25	TM
	142.68	141.04	140.22	140.01	139.92	TE
100	-119.44	-111.90	-109.90	-109.51	-109.37	TM
	142.69	141.04	140.23	140.02	139.94	TE
200	-119.44	-111.90	-109.90	-109.51	-109.37	TM
	142.69	141.04	140.23	140.02	139.94	TE

Effect of Varying the Number of Waveguide and Floquet Modes Included in the Phase Shift Calculation

Since a monomodal (one waveguide mode only) approximation has been advocated for the related problem of the transmission through a metallic mesh [7], [8], it is of interest to examine how the calculated phase of the reflected wave depends on the number of modes included. Tables I and II give the calculated phase for the transverse magnetic (TM) and transverse electric (TE) mode reflections as a function of the numbers of waveguide and Floquet modes for two cases. In both cases, the approximation of using one waveguide and one free space mode gives a reasonable answer but a maximum error results if one waveguide mode is used with many Floquet modes, or one Floquet with many waveguide modes. As the width of the grooves becomes larger, more modes are needed to obtain an accurate value for the reflected wave phase.

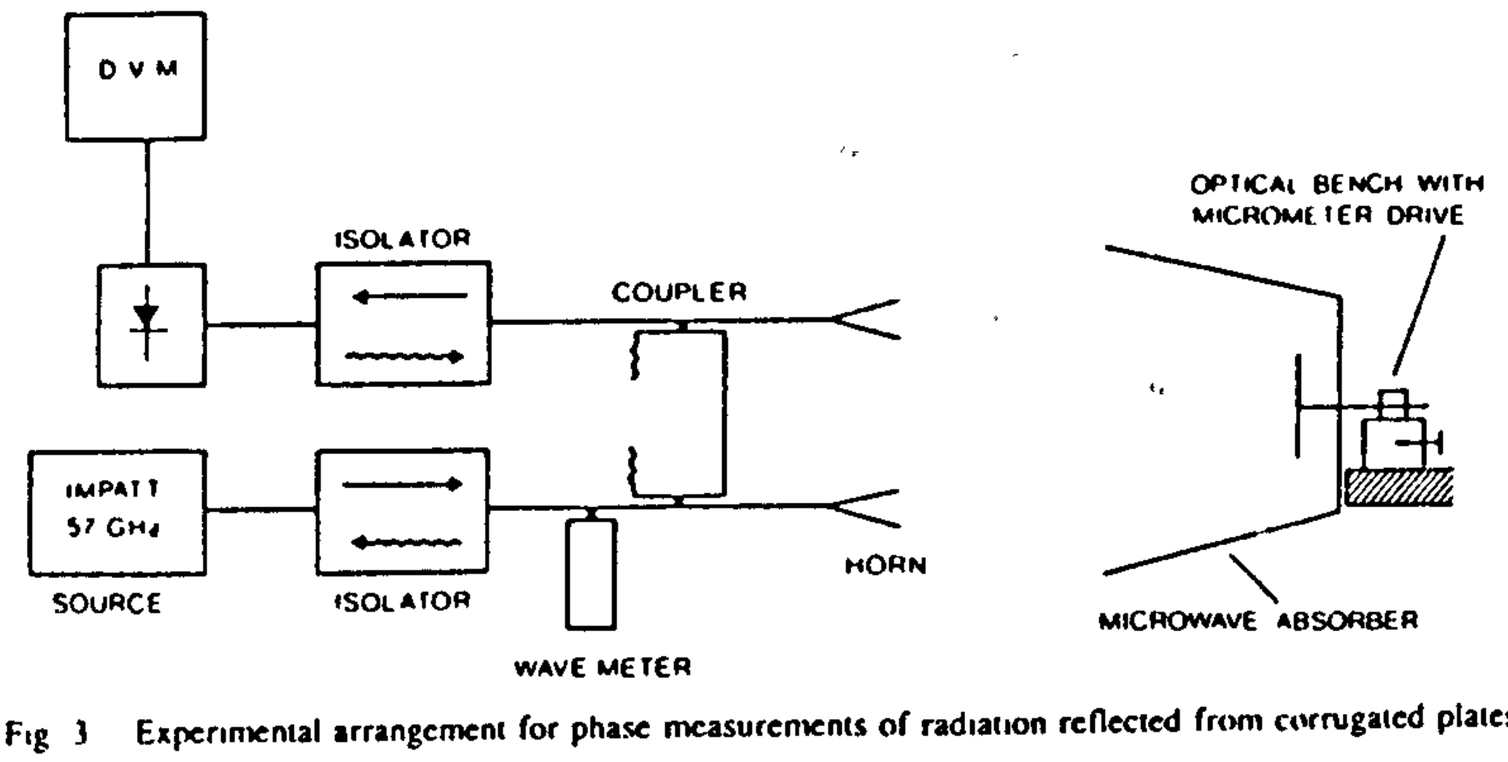

Fig 3 Experimental arrangement for phase measurements of radiation reflected from corrugated plates

TABLE II
CALCULATED PHASES (DEGREES) FOR TE AND TM WAVES REFLECTED FROM A CORRUGATED SHEET WITH GROOVE PERIOD 0.1λ, DEPTH 0.25λ AND ASPECT 0.62

Number of Floquet Modes	Number of Waveguide Modes 1	2	5	10	20	
1	-5.24	-3.87	-3.79	-3.78	-3.78	TM
	175.46	175.06	174.93	174.92	174.91	TE
2	-5.60	-5.12	-4.82	-4.80	-4.80	TM
	175.60	175.06	174.94	174.92	174.92	TE
5	-5.74	-5.34	-5.08	-5.04	-5.03	TM
	175.66	175.38	175.16	175.13	175.13	TE
10	-5.78	-5.39	-5.22	-5.14	-5.12	TM
	175.67	175.40	175.26	175.20	175.19	TE
25	-5.79	-5.41	-5.25	-5.20	-5.17	TM
	175.67	175.40	175.28	175.25	175.23	TE
50	-5.79	-5.41	-5.25	-5.21	-5.19	TM
	175.67	175.40	175.28	175.25	175.24	TE
100	-5.79	-5.41	-5.25	-5.21	-5.19	TM
	175.67	175.40	175.28	175.25	175.24	TE
200	-5.79	-5.41	-5.25	-5.21	-5.19	TM
	175.67	175.40	175.28	175.25	175.24	TE

Experimental Verification

The microwave system shown in Fig. 3 was used to verify the theoretical results. The system consists of an IMPATT oscillator transmitting at 57 GHz, followed by an isolator and wavemeter. The microwave radiation is transmitted via a horn to an aluminum-alloy corrugated plate, approximately 75 mm in diameter, mounted in front of a sheet of microwave absorber to reduce unwanted reflections. The plate was attached to a micrometer drive which was used to measure the phase shift of the reflected radiation. The micrometer was mounted on an optical bench to maintain alignment. The reflected signal enters the waveguide system via another horn and is mixed with a small amount of power leaked from the transmitter. The combined signals were passed through an isolator to a detector where the signal strength was observed using a digital voltmeter. The micrometer was adjusted to give a maximum signal strength.

The phases of the reflections from six plates were measured with respect to a flat reference plate of known thickness which was placed over the surface of the plate under test. The phase difference with the corrugations parallel and perpendicular to the electric field were also measured with and without the use of an intermediate reference plate.

Details of the plates together with the phase measurements are shown in Table III. Theoretical calculations use 20 waveguide modes and 200 Floquet modes. The errors in calculated values arise from inaccuracies in construction and measurement of the plates. Errors in measured phases mainly arise from determining the plate position for a maximum signal. The agreement between theory and experiment is within 12° for absolute phase measurements and within 6° for relative measurements of the phase difference for TE and TM configurations. This is consistent with estimated experimental errors.

Conclusion

The electromagnetic field reflected from a corrugated plate can be calculated accurately by matching plane wave and waveguide mode expansions at the surface of the plate. Although numerical results are presented for normal incidence only, the problem is formulated in the general case, making use of the reciprocal lattice corresponding to the periodic structure of the plate. Dimensions for the corrugations can be chosen so that on rotation the plate produces amplitude modulation in a linearly polarized system or single-sideband modulation in a circularly polarized system. The modulator, incorporated in a Cassegrain retro-reflector, has applications in field measurements of atmospheric transmission and of antenna patterns.

Appendix

Calculation of the Reflection Coefficients

In a region in which the electromagnetic properties of a medium are independent of the z coordinate, it is convenient to describe the electric and magnetic fields by their transverse $\mathbf{E}_t$, $\mathbf{H}_t$ and longitudinal E_z, H_z components. The substitution of a traveling wave, $\exp\{j(\omega t - \gamma z)\}$, leads to a separation of the time t, and longitudinal coordinate z, for modes with

TABLE III
MEASURED PHASES OF 57-GHz RADIATION REFLECTED FROM VARIOUS CORRUGATED PLATES

Plate No	Groove Aspect	Groove Depth/λ	Groove Period/λ	Calculated (degrees) TM	Calculated (degrees) TE	Calculated (degrees) Δ_1	Measured (degrees) TM	Measured (degrees) TE	Measured (degrees) Δ_2	Measured (degrees) Δ_1
1	0.821	0.285	0.489	−36	127	163	−44	126	170	165
2	0.719	0.271	0.559	−38	134	172	−46	138	184	178
3	0.548	0.285	0.734	−93	144	237	−102	135	237	237
4	0.400	0.236	0.175	2	177	175	+6	177	171	172
5	0.118	0.234	0.594	−114	179	293	−115	181	296	292
6	0.677	0.290	0.594	−62	137	199	−74	133	207	198
	Errors (standard deviations)			4	2	4	4	4	6	4

Δ_1 = phase difference, TE-TM.
Δ_2 = phase difference with metal plate as intermediate reference.
Δ_3 = phase difference with direct difference between TE and TM waves

transverse magnetic and transverse electric fields

$$E^{TM} = \{E_t^{TM}(r) + E_z(r)\} \exp(j\gamma z) \qquad H^{TM} = H_t^{TM}(r) \exp(j\gamma z)$$

$$E^{TE} = E_t^{TE}(r) \exp(j\gamma z). \qquad H^{TE} = \{H_t^{TE}(r) + H_z(r)\} \exp(j\gamma z)$$

The field amplitudes depend on the transverse position vector r, and the time dependence has been omitted. A general field can be described as a superposition of TM and TE modes. The longitudinal field components form scalar potentials for the transverse fields

$$\nabla E_z = j(\beta^2/\gamma)E_t^{TM} \qquad \nabla H_z = j(\beta^2/\gamma)H_t^{TE}$$

where ∇ is the two-dimensional gradient operator, $\beta^2 = \eta^2 - \gamma^2$, and $\eta = \omega(\epsilon\mu)^{1/2}$. For both modes, the transverse electric and magnetic fields are orthogonal.

$$H_t = \zeta(\hat{z} \times E_t)$$

where $\hat{z}$ is the longitudinal unit vector and the admittance $\zeta^{TM} = (\eta/\gamma)(\epsilon/\mu)^{1/2}$ for TM modes and $\zeta^{TE} = (\gamma/\eta)(\epsilon/\mu)^{1/2}$ for TE modes. If the medium is homogeneous, E_z and H_z obey identical two-dimensional wave equations

$$\nabla^2 E_z + \beta^2 E_z = 0 \qquad \nabla^2 H_z + \beta^2 H_z = 0.$$

The solutions of these equations, determined by the boundary conditions, form either a discrete set of localized functions, or a continuum of nonlocalized functions, or both. Each solution, or mode, is characterized by a particular value of β and hence γ.

A traveling wave incident on a transverse plane boundary between different media will be partially or wholly reflected. One method for the determination of the reflection and transmission coefficients is based on an expansion of the fields on each side of the boundary as a sum of TM and TE modes. The requirements that E_t and H_t should be continuous across the boundary and that E_t should be zero on any conducting surface in the boundary, together with conditions on the field at large z result in linear equations for the unknown mode amplitudes. The coefficients of these equations may be expressed in terms of overlap integrals between modes on opposite sides of the boundary. These expansions include nonpropagating modes which describe the fields in the vicinity of the boundary and are important in determining the interaction between modes.

In the case that the medium has properties which are periodic in a transverse plane, the fields may be expanded in Bloch or Floquet functions with a transverse wave vector k [9].

$$G = \Sigma_{mnr} g_{mnr} G_{mnr}(r) \exp\{j(-k \cdot l + \gamma z)\}$$

where G represents any of the TM or TE field components and the subscripts m, n, r identify the mode, with $r = 0$ for TM, and $r = 1$ for TE, modes. The modal functions have the periodicity of the structure

$$G_{mnr}(r + l) = G_{mnr}(r)$$

where l is a lattice vector.

If a plane wave propagating in a homogeneous medium occupying the half-space $z < 0$ impinges on the plane boundary with a periodic medium, the field within the homogeneous medium may be expanded in Bloch functions with transverse wave vector equal to that of the incident wave

$$E_t = \Sigma_{pq}\{f^+_{pqs} \exp(-j\gamma z) + f^-_{pqs} \exp(j\gamma z)\} \cdot F_{pq}(r) \exp(-jk \cdot l)$$

$$H_t = \zeta\Sigma_{pq}\{f^+_{pqs} \exp(-j\gamma z) - f^-_{pqs} \exp(j\gamma z)\} \cdot F_{pq}(r) \exp(-jk \cdot l).$$

f^+_{pqs} is the amplitude of a wave traveling in the direction of increasing z and f^-_{pqs} the amplitude of a wave traveling in the opposite direction. TM waves ($s = 0$) have magnetic fields, and TE waves ($s = 1$) electric fields, perpendicular to the

plane of incidence. p and q are integers and

$$F_{pq}(\mathbf{r}) = \exp\{-j(p\mathbf{a}^* + q\mathbf{b}^* + \mathbf{k}) \cdot \mathbf{r}\}$$

where $\mathbf{a}^*$ and $\mathbf{b}^*$ are basis vectors of the reciprocal lattice related to the direct lattice basis vectors $\mathbf{a}$ and $\mathbf{b}$ by

$$\mathbf{a}^* = (2\pi/v)\mathbf{b} \times \hat{\mathbf{z}}$$

$$\mathbf{b}^* = (2\pi/v)\hat{\mathbf{z}} \times \mathbf{a}$$

and $v = \mathbf{a} \cdot (\mathbf{b} \times \hat{\mathbf{z}})$. The convention that

$$\gamma = \{\eta^2 - |\mathbf{k} + p\mathbf{a}^* + q\mathbf{b}^*|^2\}^{1/2}$$

is positive real or negative imaginary, with $f^+_{pqs} = 0$ unless $p = q = 0$, ensures correct boundary conditions for large z and a single incident wave. As before, matching the tangential field components at the boundary leads to linear equations for the mode amplitudes, but now the overlap integrals extend over the unit cell only.

Chen [3] has used this technique to calculate the transmission through a screen perforated periodically with apertures. We apply the same method to calculate the reflection coefficient for a conducting plate with regularly spaced parallel rectangular grooves

If the front of the plate is in the plane $z = 0$ and the grooves, which are parallel to the y-axis, have depth c, width a, and repeat distance d, the waveguide modes which satisfy the boundary conditions within a groove have fields:

$$E_z = j(\beta/\eta) \sin \beta x \cos \gamma(z-c) \qquad H_z = j(\beta/\eta) \cos \beta x \sin \gamma(z-c)$$

$$E_x^{TM} = -j(\gamma/\eta) \cos \beta x \sin \gamma(z-c) \qquad H_x^{TE} = -j(\gamma/\eta) \sin \beta x \cos \gamma(z-c)$$

$$H_y^{TM} = (\epsilon/\mu)^{1/2} \cos \beta x \cos \gamma(z-c) \qquad E_y^{TE} = (\mu/\epsilon)^{1/2} \sin \beta x \sin \gamma(z-c)$$

where $\beta = m\pi/a$ with $m = 0, 1, 2, \cdots$, $\gamma = (\eta^2 - \beta^2)^{1/2}$, and the common phase factor $\exp\{-j(\mathbf{k}\cdot\mathbf{l} + k_y y)\}$ has been omitted where $\mathbf{l}$, a point on the edge of the groove, is the origin of the transverse coordinates for this groove. In the plane $z = 0$, the field is expanded as a sum of waveguide modes

$$E_t = \sum_{m=0}^{\infty} g_{mr} G_{mr}(x) \qquad H_t = \sum_{m=0}^{\infty} g_{mr} \xi_{mr} G_{mr}(x)$$

omitting the common phase factor are

$$E_t = \sum_{p=-\infty}^{\infty} (f^+_{ps} + f^-_{ps}) F_p(x) \qquad H_t = \sum_{p=-\infty}^{\infty} (f^+_{ps} - f^-_{ps}) \zeta_{p0} F_p(x)$$

where $F_p(x) = \exp(-j(\beta + k_x)x)$ and $\beta = 2\pi p/d$ with $p = 0, \pm 1, \pm 2, \cdots$.

For TM waves H_t is perpendicular to the plane of incidence and $\zeta_{p0} = (\eta/\gamma)(\epsilon/\mu)^{1/2}$ while for TE waves E_t is perpendicular to this plane and $\zeta_{p1} = (\gamma/\eta)(\epsilon/\mu)^{1/2}$ where $\gamma = \{\eta^2 - (\beta + k_x)^2 - k_y^2\}^{1/2}$.

If the angle between the x-axis (perpendicular to the grooves) and the plane of incidence is θ, the conditions for continuity of tangential field at the boundary are as follows.

E_t over the aperture:

$$\sum_{p=-\infty}^{\infty} (f^+_{p0} + f^-_{p0}) F_p(x)$$

$$= \sum_{m=0}^{\infty} \{g_{m0} G_{m0}(x) \cos\theta + g_{m1} G_{m1}(x) \sin\theta\}$$

$$\sum_{p=-\infty}^{\infty} (f^+_{p1} + f^-_{p1}) F_p(x)$$

$$= \sum_{m=0}^{\infty} \{-g_{m0} G_{m0}(x) \sin\theta + g_{m1} G_{m1}(x) \cos\theta\}.$$

E_t over the conducting surface:

$$\sum_{p=-\infty}^{\infty} (f^+_{p0} + f^-_{p0}) F_p(x) = 0$$

$$\sum_{p=-\infty}^{\infty} (f^+_{p1} + f^-_{p1}) F_p(x) = 0.$$

H_t over the aperture:

$$\sum_{p=-\infty}^{\infty} \{(f^+_{p0} - f^-_{p0}) \zeta_{p0} F_p(x) \cos\theta - (f^+_{p1} - f^-_{p1}) \zeta_{p1} F_p(x) \sin\theta\} = \sum_{m=0}^{\infty} g_{m0} \xi_{m0} G_{m0}(x)$$

$$\sum_{p=-\infty}^{\infty} \{(f^+_{p0} - f^-_{p0}) \zeta_{p0} F_p(x) \sin\theta + (f^+_{p1} - f^-_{p1}) \zeta_{p1} F_p(x) \cos\theta\} = \sum_{m=0}^{\infty} g_{m1} \xi_{m1} G_{m1}(x).$$

where, for TM modes, $E_x = E_t$, $H_y = H_t$, $\xi_{m0} = -j(\eta/\gamma)(\epsilon/\mu)^{1/2} \cot(\gamma c)$, and $G_{m0}(x) = \sqrt{2} \cos(\beta x)$ except $G_{00} = 1$, while for TE modes, $E_x = E_t$, $H_y = -H_t$, $\xi_{m1} = -j(\gamma/\eta)(\epsilon/\mu)^{1/2} \cot(\gamma c)$, and $G_{m1}(x) = \sqrt{2} \sin(\beta x)$. The fields derived from the free space Bloch functions at the boundary

The equations may be written in matrix notation by introducing the overlap integrals

$$C_{pmr} = \frac{1}{d} \int_0^a F_p^*(x) G_{mr}(x)\, dx$$

and noting the orthonormality conditions

$$\frac{1}{d}\int_0^d F_p^*(x)F_q(x)\,dx=\delta_{pq}$$

and

$$\frac{1}{a}\int_0^a G_{mr}^*(x)G_{ns}(x)\,dx=\delta_{mn}\delta_{rs}.$$

$$\mathbf{f}^+ + \mathbf{f}^- = \mathbf{C}\,\mathbf{g}$$

$$\mathbf{C}^*\,\mathbf{Z}(\mathbf{f}^+ - \mathbf{f}^-) = \frac{a}{d}\,\Xi\mathbf{g}.$$

The components of the vectors f and g are

$$f_{2p+s}=f_{ps},\quad g_{2m+r}=g_{mr}$$

while the matrix element

$$C_{2p+s,2m+r}=C_{pmr}\cos\left(\theta+(s-r)\frac{\pi}{2}\right)$$

and $\mathbf{C}^*$ is the Hermitian transpose of C.

The admittance matrices Z and Ξ are diagonal with

$$Z_{2p+s,2p+s}=\zeta_{ps}\text{ and }\Xi_{2m+r,2m+r}=\xi_{mr}.$$

These equations may be solved by rewriting them as

$$\{\mathbf{C}^*\mathbf{Z}\mathbf{C}+(a/d)\Xi\}\,\mathbf{g}=2\mathbf{C}^*\mathbf{Z}\mathbf{f}^+$$

$$\mathbf{f}^- = \mathbf{C}\mathbf{g}-\mathbf{f}^+$$

and noting that $f_{ps}^+ = 0$ for $p \neq 0$ while f_{00}^+ and f_{01}^+ are the amplitudes of the incident TM and TE waves, respectively.

In evaluating the overlap integrals, the symmetry of the waveguide modes is emphasized by a change of origin to the center of the groove.

$$C_{pmr}=\frac{\sqrt{2}}{d}\int_{-a/2}^{a/2}\exp\left\{j\left(\frac{2\pi p}{d}+k_x\right)x\right\}\cdot\cos\left\{\frac{m\pi x}{a}+(m-r)\frac{\pi}{2}\right\}dx,\qquad m\neq 0$$

$$\left.\begin{aligned}C_{pm0}&=\frac{\sqrt{2}}{\pi}\frac{a}{d}\sin\left(\frac{h\pi}{2}\right)\frac{2h}{h^2-m^2}\\ C_{pm1}&=j\frac{\sqrt{2}}{\pi}\frac{a}{d}\sin\left(\frac{h\pi}{2}\right)\frac{2m}{h^2-m^2}\end{aligned}\right\}\ m\text{ even},\ m\neq 0$$

$$\left.\begin{aligned}C_{pm0}&=j\frac{\sqrt{2}}{\pi}\frac{a}{d}\cos\left(\frac{h\pi}{2}\right)\frac{2h}{h^2-m^2}\\ C_{pm1}&=-\frac{\sqrt{2}}{\pi}\frac{a}{d}\cos\left(\frac{h\pi}{2}\right)\frac{2m}{h^2-m^2}\end{aligned}\right\}\ m\text{ odd}$$

where

$$h=2p\frac{a}{d}+\frac{k_x a}{\pi}.$$

For the case $m = 0$

$$C_{p00}=\frac{2a}{\pi dh}\sin\frac{h\pi}{2}\quad\text{and}\quad C_{p01}=0.$$

At normal incidence, the TM and TE polarizations of the incident wave may be chosen parallel to the corresponding polarization for the waveguide modes, thus separating the equations for TM and TE modes. The overlap integrals become symmetric or antisymmetric in the index p and, taking positive and negative values of p together, the coefficients of the linear equations corresponding to products of symmetric and antisymmetric functions are found to vanish in this way separating the equations for even and odd m. Modes with even m only are excited in the TM case and modes with odd m in the TE case.

Numerical results are presented for the case of normal incidence. The coefficients of the linear equations for the waveguide mode amplitudes g_{mr} were formed directly thus avoiding the introduction of matrices of dimension P, the maximum value of the index p. The waveguide admittance can become indefinitely large (e.g., for half-wave-deep slots) causing numerical problems. This may be avoided by scaling the equations. The admittances may be expressed in terms of trigonometric or hyperbolic functions.

$$\left.\begin{aligned}\xi_{m1}&=-j\frac{\eta}{\gamma}\left(\frac{\epsilon}{\mu}\right)^{1/2}\frac{\cos(\gamma c)}{\sin(\gamma c)}\\ \zeta_{m1}&=+j\frac{\eta}{\gamma'}\left(\frac{\epsilon}{\mu}\right)^{1/2}\frac{1}{\tanh(\gamma' c)}\end{aligned}\right\}\qquad\left.\begin{aligned}\xi_{m1}&=-j\frac{\gamma}{\eta}\left(\frac{\epsilon}{\mu}\right)^{1/2}\frac{\cos(\gamma c)}{\sin(\gamma c)}\\ \zeta_{m1}&=-j\frac{\gamma'}{\eta}\left(\frac{\epsilon}{\mu}\right)^{1/2}\frac{1}{\tanh(\gamma' c)}\end{aligned}\right\}$$

where $\gamma = j\gamma'$. For γ real, the trigonometric forms were used and the rows and columns of the equations were scaled by $\{(\gamma/\eta)\,|\sin\gamma c|\}^{1/2}$ for TM modes and by $|\sin\gamma c|^{1/2}$ for TE modes. For γ imaginary, the hyperbolic form was appropriate and the equations were scaled by $\{(\gamma/\eta)\tanh(\gamma' c)\}^{1/2}$ and $\{\tanh(\gamma' c)\}^{1/2}$ for TM and TE modes, respectively. The set of complex linear equations was solved by NAG [10] library routine F04ADF on a Burroughs B6930 computer.

REFERENCES

[1] Lord Rayleigh, *Theory of sound*. London, UK: Macmillan, 1896.

[2] H. Lamb, "On reflection and transmission of electric waves by a metallic grating," *Proc. London Math. Soc.*, vol. 29, pp. 523-544, 1898.

[3] C. C. Chen, "Transmission through a conducting screen perforated periodically with apertures," *IEEE Trans. Microwave Theory Tech.*, vol. MTT-9, pp. 627-632, 1970.

[4] H. M. Pickett, J. Farhoomand, and A. F. Chiou, "Performance of metal meshes as a function of incidence angle," *Appl. Opt.*, vol. 23, pp. 4228-4282, 1984.

[5] L. N. Deriugin, "Reflection of plane transversly polarized wave from rectangular grid," *Radiotechnika*, vol. 15, pp. 15-26, 1960 (in Russian), also *Radio Eng.*, vol. 15, pp. 25-41, 1960 (English translation).

[6] L. N. Deriugin, "Reflection of a longitudinally polarized wave from a rectangular comb," *Radiotechnika*, vol. 15, pp. 9-16, 1960 (in Russian), also *Radio Eng.*, vol. 15, pp. 12-23, 1960 (English translation).

[7] R. C. McPhedran and P. Maystre, "On the theory and solar application of inductive grids," *Appl. Phys.*, vol. 14, pp. 1-20, 1977.

[8] M. S. Durschlag and T. A. de Temple, "Far-IR optical properties of free standing and dielectrically backed meshes," *Appl. Opt.*, vol. 20, pp. 1245-1243, 1981.

[9] L. Brillouin, *Wave Propagation in Periodic Structures*. New York: Dover, 1953.

[10] NAG, Numerical Algorithms Group, Oxford, England, 1981.

Gordon E. Peckham was born in Bristol, England, in 1936. He received the B.Sc. degree in physics from the University of Cambridge, Cambridge, U.K., in 1960 and the M.A. and Ph.D. degrees in 1964 for research on the scattering of thermal neutrons from crystalline solids.

As a Research Assistant and then Lecturer at the University of Reading, U.K., he worked on the development of infrared radiometers later flown on Nimbus 4 and 5 satellites. Since 1971 he has held posts of Lecturer then Reader in the Physics Department at Heriot-Watt University, Edinburgh, Scotland. His current research interests center on the use of microwaves for remote sensing the earth's atmosphere.

Robert A. Suttie was born in Perth, Scotland, U.K. He received the B.Sc. degree in applied physics from Dundee University, Dundee, Scotland, in 1973.

He was an Engineer with Ferranti Microwave Division from 1973 to 1978. Since 1978 he has held a Research Associate position at Heriot-Watt University, Physics Department, Edinburgh, working primarily on microwave and millimeter instruments.

APPENDIX C

MODULATOR CONTROL CIRCUIT

The frequency of the modulation of the retroreflector (Section 4.2) was controlled to a preset value to avoid interference of the modulation frequency or its harmonics with the modulation frequency of the waveguide chopper in the reference path and to maintain a stable frequency.

The dc motor driving the corrugated modulator was frequency controlled by the circuit in Fig. C.1. The dc power supply for the circuit is via a half kilometre long cable from the laboratory to the retroreflector. The dc power is regulated to +12V for the control electronics but maintaining the higher voltage to drive the dc motor. Local regulation for the control is essential as the voltage at the input to the circuit will change with the current over such a long cable length. The 1 mH inductor in parallel with the 680 Ω resistor is used as a block for the reference pulse which also uses the power supply line. The inductor stops the reference pulse from re-entering the circuit and interfering with the operation of the circuit.

The motor was fitted with a chopper to modulate an infrared transmission sensor. The signal from the sensor is then squared up by the first schmitt trigger, resulting in a pulse shape as shown at point 'A' in the timing diagram, Fig. C.2. The chopper had approximately equal mark to space segments but this is not important to the functioning of the circuit.

The schmitt triggers are all in a single IC, a CD40106 which is a hex inverting CMOS 4000 series schmitt trigger. The rest of the schmitt triggers are used to produce timing pulses to control FET switches used in the comparison of the period of the modulation with a reference. The signal at point 'A' is differentiated to point 'B' and a schmitt trigger produces a short squared pulse at point 'C'. This signal is used in three ways:

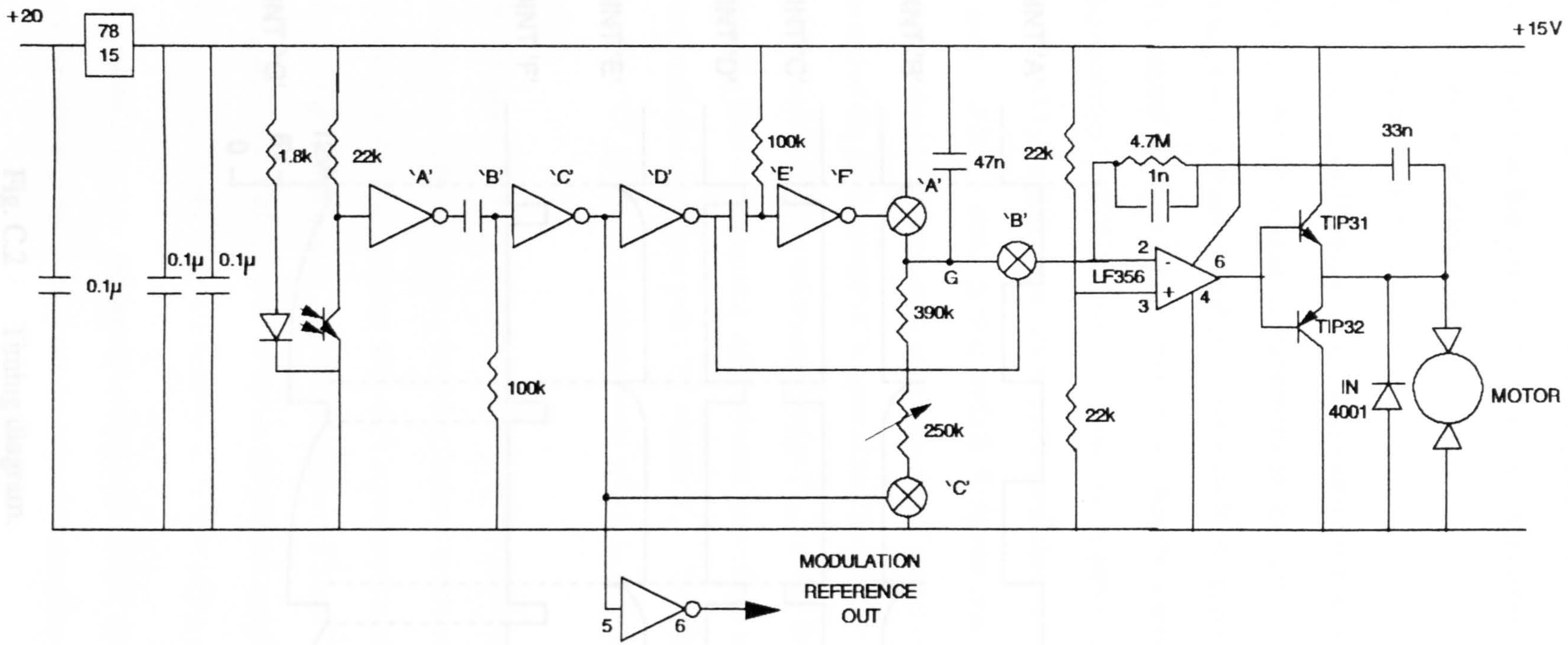

Fig. C.1 Corrugated modulator motor speed control circuit.

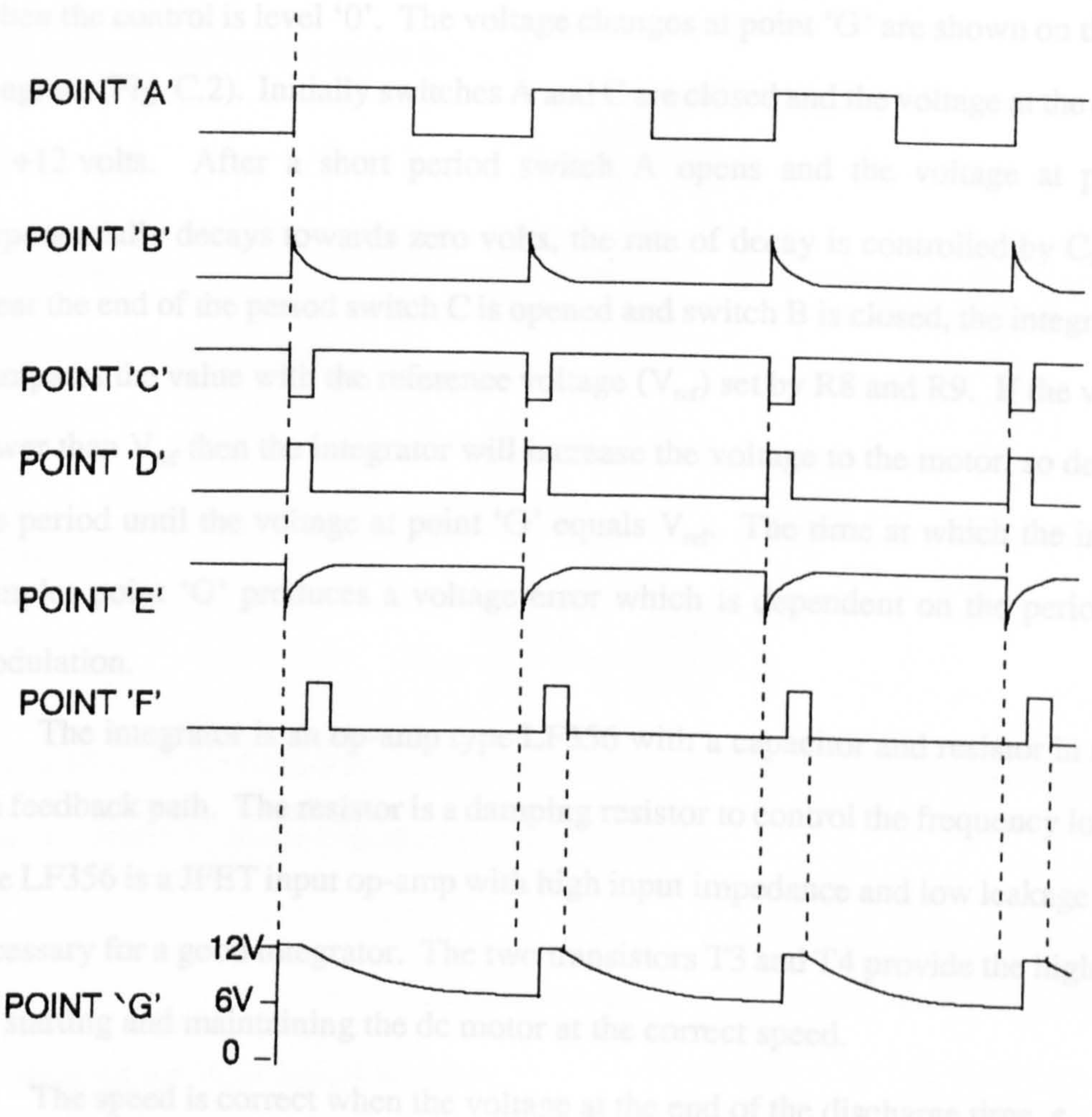

Fig. C.2 Timing diagram.

(a) a reference signal is fed via another schmitt trigger used as buffer to an npn BC337 transistor which modulates a frequency reference onto the dc power supply line. The reference is detected and fed into the demodulator by a circuit in the power supply line in the laboratory.

(b) the signal controls switch 'C'.

(b) the signal is inverted to point 'D' to produce the control signal for switch 'B'.

The signal at point 'D' is again differentiated to detect the falling edge of the pulse and squared to provide a short control pulse for switch 'A' at point 'F'.

The 'closed' position for the switches is when the control is a level '1' and 'open' when the control is level '0'. The voltage changes at point 'G' are shown on the timing diagram (Fig. C.2). Initially switches A and C are closed and the voltage at the capacitor is +12 volts. After a short period switch A opens and the voltage at point 'G' exponentially decays towards zero volts, the rate of decay is controlled by C_T and R_T. Near the end of the period switch C is opened and switch B is closed, the integrator now compares the value with the reference voltage (V_{ref}) set by R8 and R9. If the voltage is lower than V_{ref} then the integrator will increase the voltage to the motor, so decreasing the period until the voltage at point 'G' equals V_{ref}. The time at which the integrator samples point 'G' produces a voltage error which is dependent on the period of the modulation.

The integrator is an op-amp type LF356 with a capacitor and resistor in series in the feedback path. The resistor is a damping resistor to control the frequency lock loop. The LF356 is a JFET input op-amp with high input impedance and low leakage current, necessary for a good integrator. The two transistors T3 and T4 provide the high current for starting and maintaining the dc motor at the correct speed.

The speed is correct when the voltage at the end of the discharge time, τ_0, is equal to the voltage reference on the non-inverting input of the op-amp. If the period is too long then the error will be τ which can be related to a differential change in voltage as

$$V_1 = -k\tau$$

where k is the gain, and τ is the error in the period. V_1 is the voltage at the end of the decay period where the rate of decay is controlled by C_T(C4) and R_T(R6 & R7). R_T adjusts the frequency of operation. τ_0 is the time taken for the voltage across C_T to decay from 15 V to the 7.5 V reference on the op-amp when the period of the chopper is correct. The charge at -ve input to op-amp is

$$q = CV = -k\tau C_T$$

$$\text{Frequency} = \frac{1}{\tau_0 + \tau}$$

where τ is the error in the period.

The current into the integrator is I = qf

$$I = \frac{-k\tau C_T}{\tau_0}$$

assuming $\tau << \tau_0$, true for frequencies near lock. The voltage at the output of the integrator, V_2 is given by

$$V_2 = -RI - \frac{1}{c}\int I.dt$$

substituting

$$V_2 = \frac{Rk\tau C_T}{\tau_0} + \frac{1}{c}\int \frac{k\tau C_T}{\tau_0}.dt$$

The final section of the loop is the motor, which is like a VCO in other applications, relates voltage V_2 to the period error τ with a gain g.

$$\tau = -gV_2$$

$$\text{or } V_2 = -\tau/g$$

Substituting for V_2 in equation above.

$$\frac{k\tau RC_T}{\tau_0} + \int \frac{k\tau C_T}{c\tau_0}.dt = -\tau/g$$

re-arranging

$$\tau\left(\frac{1}{g}+\frac{kRC_T}{\tau_0}\right)+\int\frac{k\tau C_T}{c\tau_0}.dt=0$$

Differentiating τ with respect to time

$$\frac{d\tau}{dt}\left(\frac{1}{g}+\frac{kRC_T}{c\tau_0}\right)+\frac{k\tau C_T}{c\tau_0}=0$$

a solution of the differential equation is

$$\frac{d\tau}{dt}=-\alpha\tau$$

or

$$\tau=\tau_0 e^{-\alpha\tau}$$

$$\therefore\alpha=\frac{kC_T}{c\tau_0}.\frac{1}{(\frac{1}{g}+\frac{RkC_T}{\tau_0})}$$

$$=\frac{gkC_T}{c(\tau_0+gkRC_T)}$$

Therefore α will always be positive, i.e. the integrator will damp the system.

$$\text{time constant}=1/\alpha=\frac{c(\tau_0+gkRC_T)}{gkC_T}$$

$$=RC+\frac{c\tau_0}{gkC_T}$$

The value of the variables in the above equation are $R = 4.7\ M\Omega$; $C = 33\ nF$; $\tau_0 = 14.3$ ms for operation at 70 Hz; $g = 2.1 \times 10^{-3}$ s/V; $k = 363$ V/s. This gives a value for the time constant of 169 mS. The time constant is primarily controlled by R and C. The time constant was chosen such that the inertia of the motor would be insignificant in the dynamics of the frequency control. The capacitors C and C_T were low leakage and low temperature coefficients.

APPENDIX D

OFFSET OSCILLATOR

The offset oscillator was so called because the output frequency is only ~ 0.0001% offset from the system reference frequency. The reference frequency is 106.250 MHz and the chosen offset frequency was 841.384 Hz. The offset frequency appears a peculiar frequency to choose but it was chosen because there was a divider available which when supplied with 10.625 MHz produced 841.384 Hz. The frequency was convenient as the intermediate frequencies (IF's) in the downconversion were very similar for the two operating frequencies, as is shown in Section 4.5.

Fig. D.1 shows the overall schematic of the offset oscillator. The reference frequency of 106.250 MHz comes from the ovenised crystal oscillator supplied with the Hughes millimetre wave sources (Chapter 4). This is divided by 10 to give a frequency of 10.625 MHz which is then further divided by 12628 to produce the offset frequency of 841.384 Hz. This frequency is then compared with the downconverted frequency from the VCO in the phase detector. The integrator controls the dynamic response of the phase lock loop.

D.1 Voltage Controlled Oscillator

The voltage controlled oscillator (VCO) is shown in Fig. D.2. A VCO is an oscillator whose output frequency can be controlled by a voltage. The VCO here is an overtone crystal oscillator based on emitter coupled logic (ECL) design from Motorola [ref. D.1]. The MC10116 contains three line receivers which have two inputs and two complementary outputs. The dual-in-line package offers sufficient units to produce the oscillator with buffers. The oscillator has a crystal in the feedback loop with a varactor in series to allow the frequency to be adjusted by an external voltage. There is also a tuned tank circuit on the input to the "MC10116" with one terminal referenced to V_{BB}. V_{BB} is a reference voltage of - 1.3 V available on pin 11 of the IC to ensure the voltages

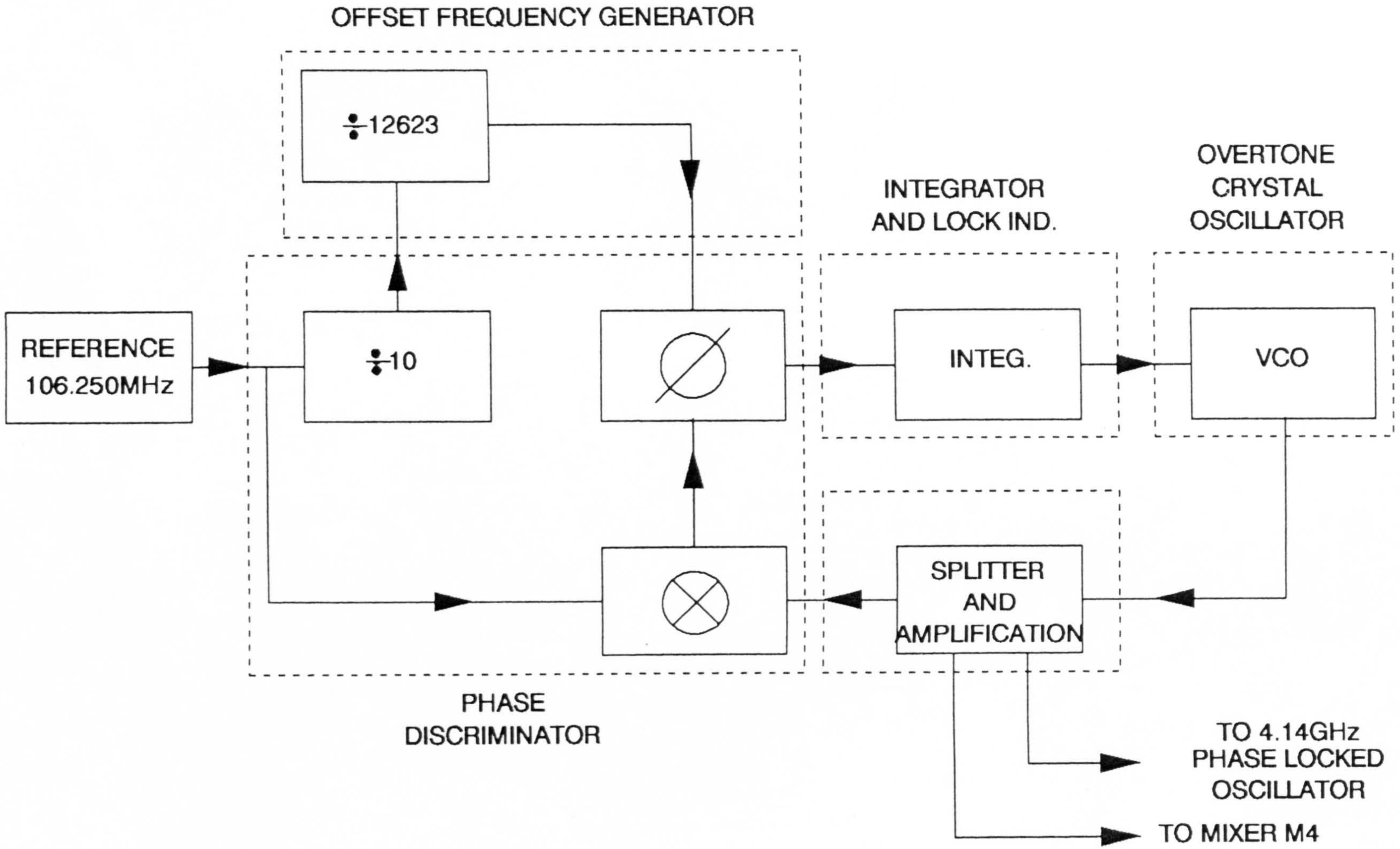

Fig. D.1 Offset oscillator schematic.

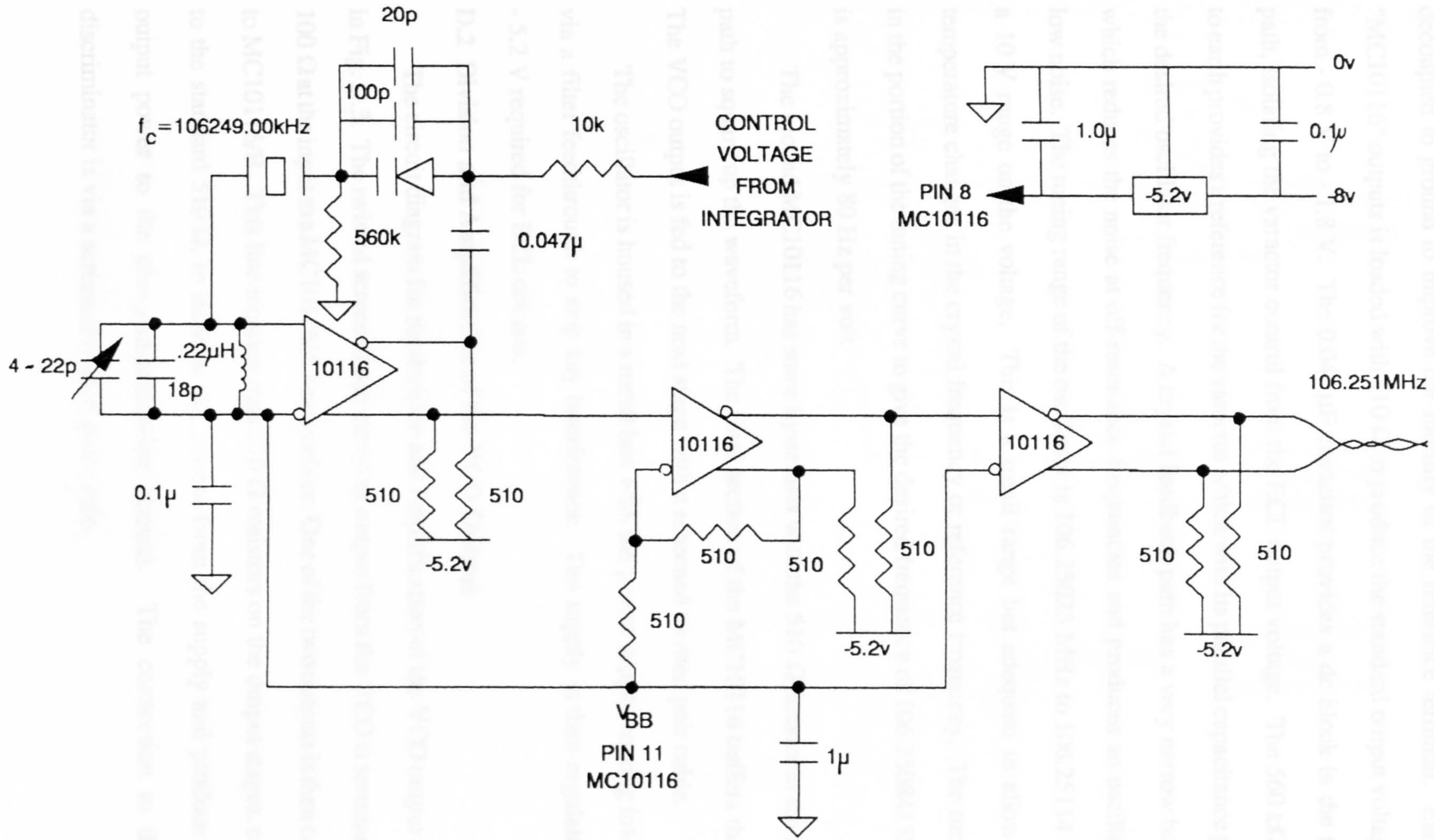

Fig. D.2 Overtone crystal oscillator.

are within the operating range of the input terminals. One of the input terminals is decoupled to ground to improve the stability of the reference terminal. Each of the "MC10116" outputs is loaded with 510 Ω to produce the standard output voltage swing from - 0.8 V to - 1.8 V. The 0.047 μF capacitor provides a dc block in the feedback path, isolating the varactor control from the ECL output voltage. The 560 kΩ resistor to earth provides a reference for the varactor which with its parallel capacitance produces the desired oscillator frequency. A crystal feedback path has a very narrow bandwidth which reduces the noise at off-resonance frequencies and produces an oscillator with low noise. The tuning range of the oscillator is 106.25023 MHz to 106.25114 MHz for a 10 V range on the voltage. This is a small range but adequate to allow for any temperature changes in the crystal frequency or reference frequency. The tuning rate, in the portion of the tuning curve to give the desired frequency of 106.250841384 MHz, is approximately 80 Hz per volt.

The second MC10116 has some hysteresis with the 510 Ω resistor in the feedback path to square up the waveform. The final section of the MC10116 buffers the output. The VCO output is fed to the next stage with a screened twisted pair cable.

The oscillator is housed in a metal box with the power supply coming into the box via a filter feedthrough to stop any interference. The supply is then regulated to the - 5.2 V required for ECL circuits.

D.2 Division and Amplification of the VCO Output

The circuit diagram for the division and amplification of the VCO output is shown in Fig. D.3. The twisted screened pair carrying output from the VCO is terminated with 100 Ω at the input to a MC10116/A line receiver. One of the two outputs is then connected to MC10116/B. This line receiver uses 270 Ω resistors on the output stages, compared to the standard 510 Ω, to increase the current from the supply and produce a higher output power to the phase discriminator circuits. The connection to the phase discriminator is via a screened twisted pair cable.

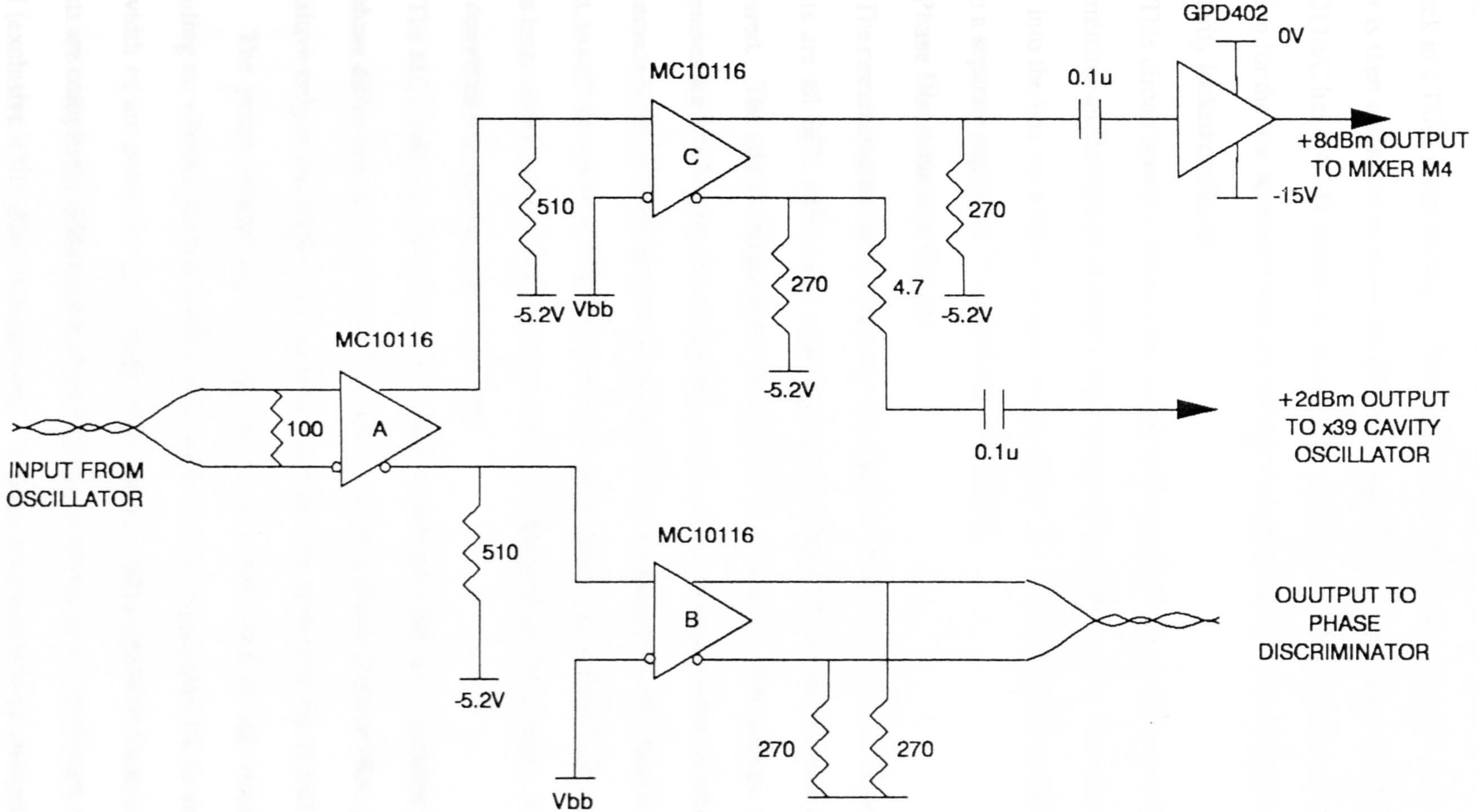

Fig. D.3 VCO division and amplification.

The other output from MC10116/A is fed to the remaining line receiver in the package MC10116/C. One of the outputs is ac coupled to a GPD 402, an amplifier from Avantek in a TO-8 metal package. The amplifier increases the power level to + 8 dBm which is then sufficient to correctly drive the mixer M3. The other output from the MC10116/C has a 4.7 Ω resistor in series with the capacitor coupling to provide some isolation for the line receiver from any noise transmitted back the coaxial line from the x39 cavity locked oscillator.

This circuit board is housed in a separate aluminium box from the VCO, phase discriminator and integrator to reduce the pick up of spurious noise. The power supply is fed into the box via a filter can and regulated to - 5.2 V for the ECL circuits. There is also a separate supply of 15 volts for the GPD 402.

D.3 Phase Discriminator Circuit

The circuit diagram for the phase discriminator is shown in Fig. D.4. The integrated circuits are all ECL due to the switching speeds required for the frequencies being compared. The phase comparator (MC12040) is also ECL even though the input frequencies are 841 Hz, i.e. the offset frequency. In a previous version of this circuit a low frequency phase comparator was used but this produced too much jitter on the VCO output, to such an extent as to be almost useless. The introduction of the ECL comparator gave a large improvement in jitter due to the fast edge speed of ECL logic. It was also more convenient to maintain the ECL logic.

The MC12040 is a phase-frequency detector intended for use in systems requiring zero phase difference at lock. The MC12040 is a type II phase detector (Ref. [D.2]). It is sensitive only to the relative timing edges between the reference signal and the VCO input. The phase comparator circuitry generates either lead or lag output pulses depending on whether the transitions of the reference or signal waveforms occur first. The width of the pulses is equal to the time between the respective transitions. The outputs are completely independent of the duty cycle of the input waveforms, unlike the type I (exclusive -OR) phase comparators. The two waveforms to be compared are

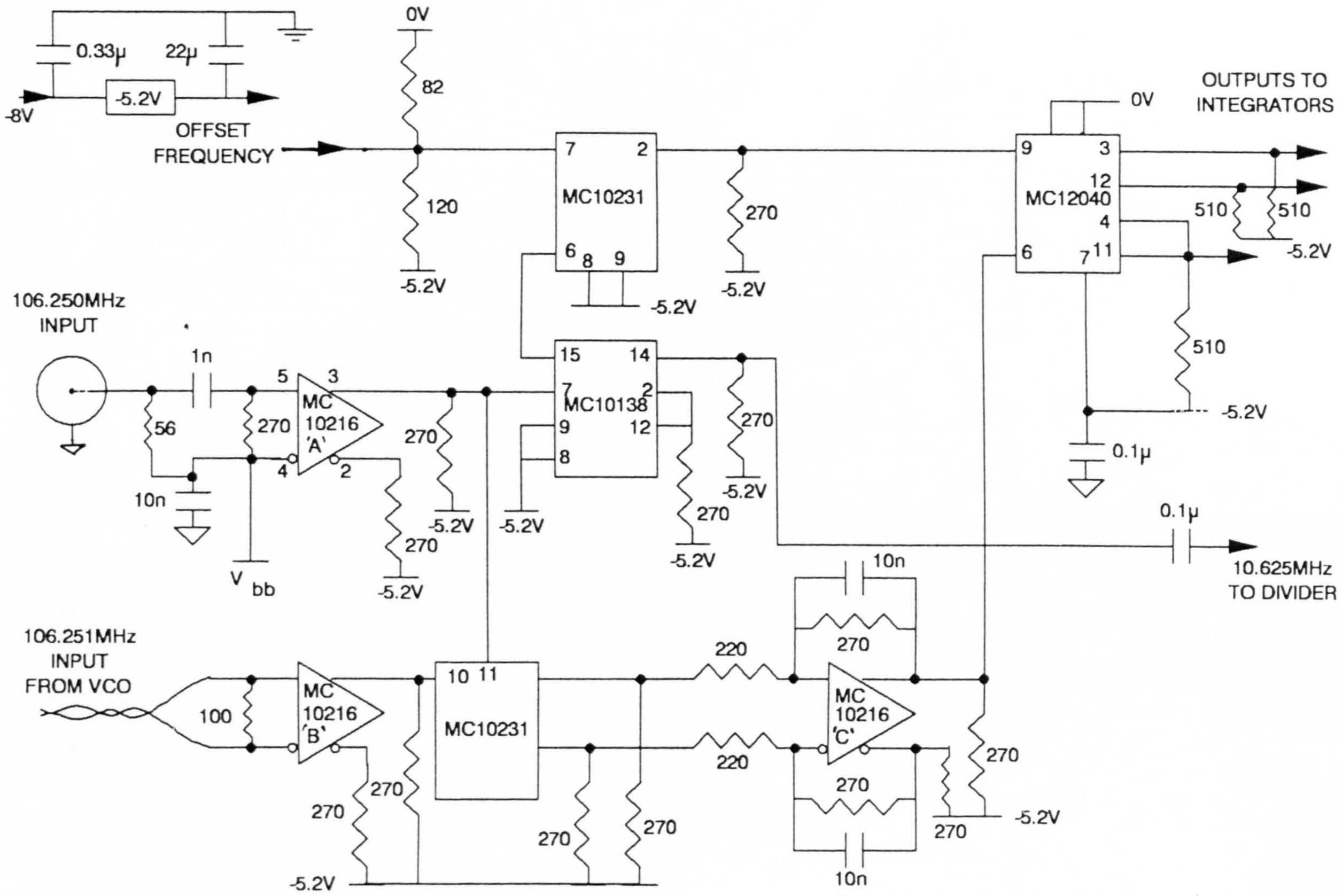

Fig. D.4 Phase discriminator circuit.

(a) the offset frequency which is derived from the reference frequency of 106.250 MHz, divided by ten in the MC10138 and further divided by 12628 in a divider unit. The offset signal is then clocked through D-type flip-flop (MC10231) to pin 9 of the MC12040. The output states of the flip-flop change on the positive transition of the clock. A change in the information present at the data input will not affect the output at any other time due to master-slave construction.

(b) the waveform from the VCO is buffered by MC10216/B into a D-type flip-flop which is being clocked at the reference frequency. The output of the D-type is then the difference frequency between these, i.e. 841 Hz, if the VCO is at the correct frequency. The output from the D-type is squared up by the line receiver MC10216/C before being fed into pin 6 of the phase discriminator (MC12040). The MC12040 is the ECL equivalent of the CMOS 4046 without the integral VCO. There are four outputs from the phase discriminator (MC12040). Pulses appear on either the D or $\bar{D}$ or the U + $\bar{U}$ outputs depending on whether one phase is advanced or retarded compared to the other. The pulse width is also dependent on the extent of the phase error. Digital phase discriminators, type II, have infinite capture range unlike most of the analogue types and some digital types which have a very restrictive capture range. One other important feature of the type II discriminator is that the output pulses disappear completely when the two signals are in lock, i.e. there are no pulses to generate periodic phase modulation in the loop.

The $\bar{U}$ and $\bar{D}$ were used to provide information of phase error to the integrator. The U and D outputs were combined to provide a lock indicator as shown in Fig. D.5. If there are a significant number of pulses on either U or D outputs, then the transistors will be turned off, which will allow sufficient voltage to develop across the light emitting diode (LED) to cause it to emit light, as a warning of an out of lock condition.

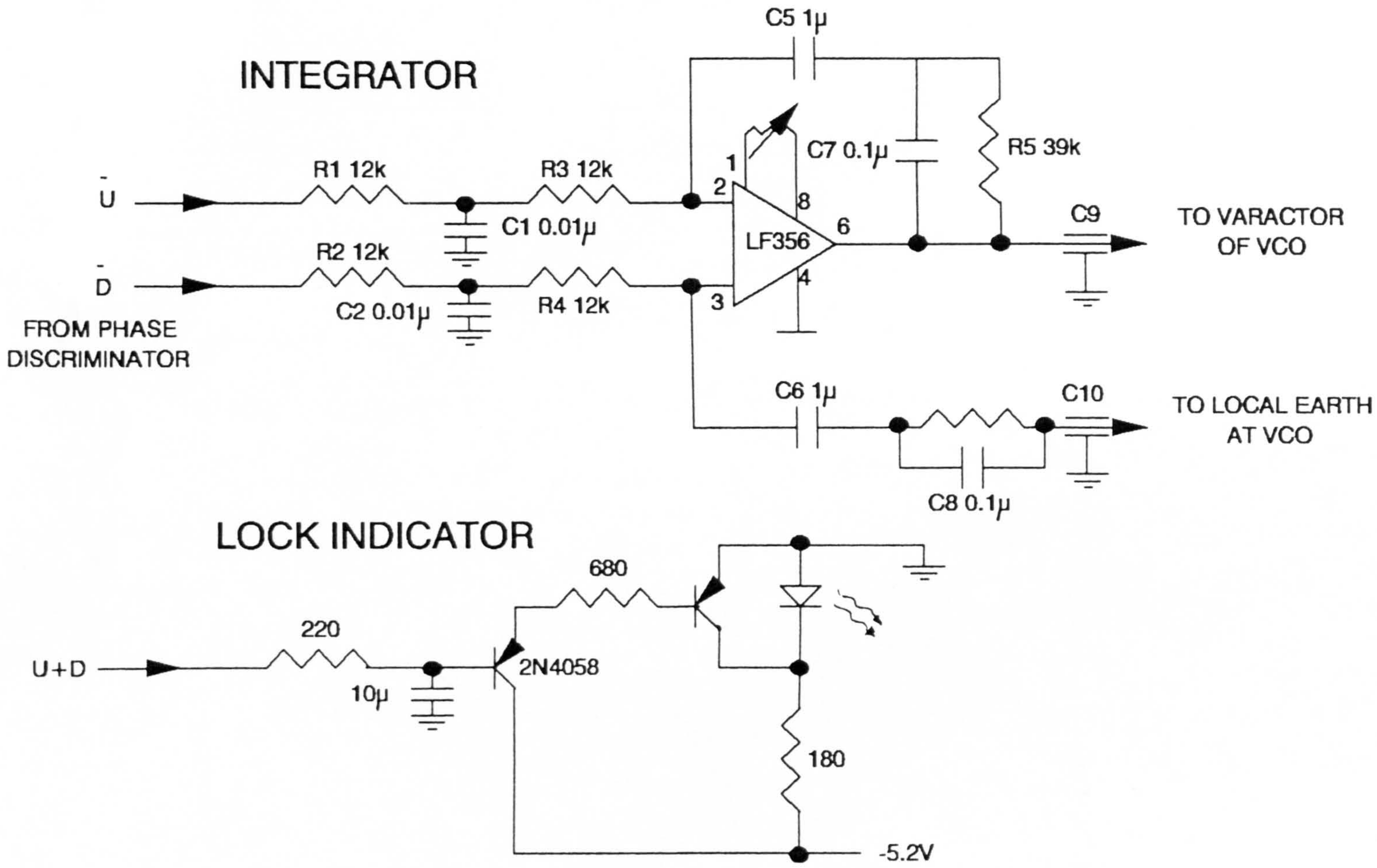

Fig. D.5 Integrator and lock indicator circuits.

D.4 Integrator Circuit

The integrator, in all phase locked loops (PLL's) is the element which controls the voltage input of the voltage controlled oscillator in response to the phase error signal from the phase discriminator. This is not a straightforward feed back problem but has an input which is phase dependent and an output voltage which has frequency dependence. Phase is the integral of frequency. The integrator is a low pass filter which reduces the phase noise and controls the dynamic response of the PLL.

Various filters are used in PLL's, the simplest is the first order RC low pass, shown in diagram (a) in Fig. D.6. The most commonly used is the lead-lag low pass shown in diagram (b), this has substantial advantages in control of the loop. The phase noise is reduced and there is "flywheel action". Flywheel action means that if the signal is removed or experiences a large change then the filter will maintain at the last value for a short period and will not instantly change. These filters produce phase locked loops with longer capture times, but this is not normally a problem especially where the phase locked oscillator is used to multiply frequencies for mixer local oscillators from a fixed reference frequency.

The filter in the offset oscillator is an active filter of the type shown in diagram (c) in Fig. D.6. The loop frequency and damping factor are controlled by the feedback components [ref. D.3]. The integrator circuit shown in Fig. D.5 is active lead-lag filter with differential inputs and differential outputs. One of the outputs is coupled to the VCO varactor control via a capacitive feedthrough, the other output is earthed at the VCO board, via a capacitive feedthrough to maintain the best possible immunity to interference and noise.

The differential input is required to level shift the ECL output from the normally high outputs of the $\bar{U}$ and $\bar{D}$ outputs of the phase discriminator [ref. D.4]. The quiescent differential voltage to the operational amplifier is zero assuming the $\bar{U}$ and $\bar{D}$ outputs are the same. The phase error pulses are first filtered by the RC network of R1C1 and R2C2 to increase the response of the integrator to the very narrow correctional pulses from the phase discriminator when the VCO is in phase lock.

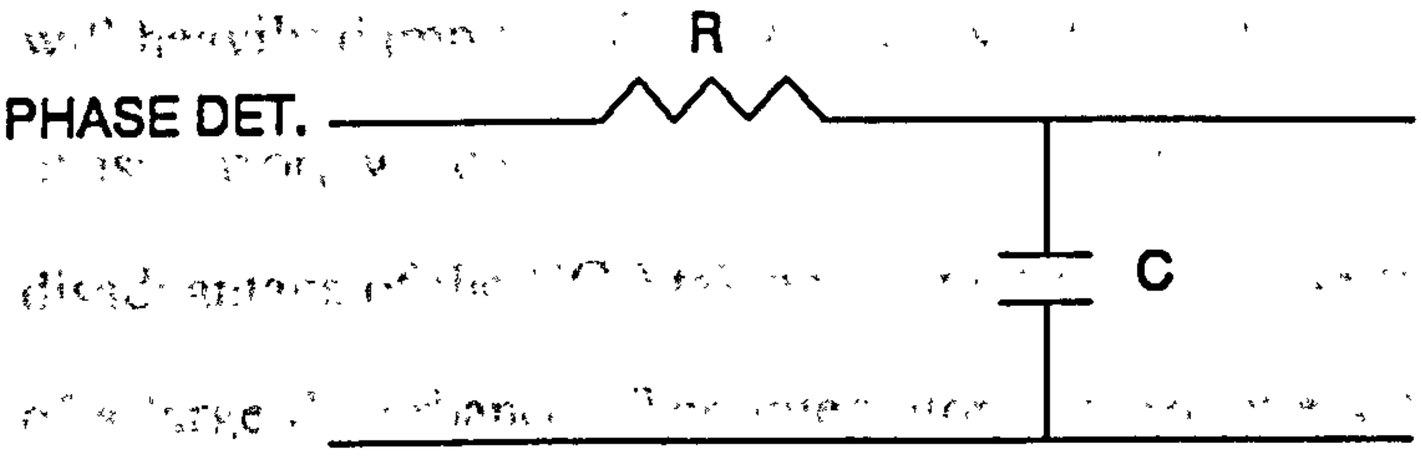

(a) LOW PASS RC FILTER

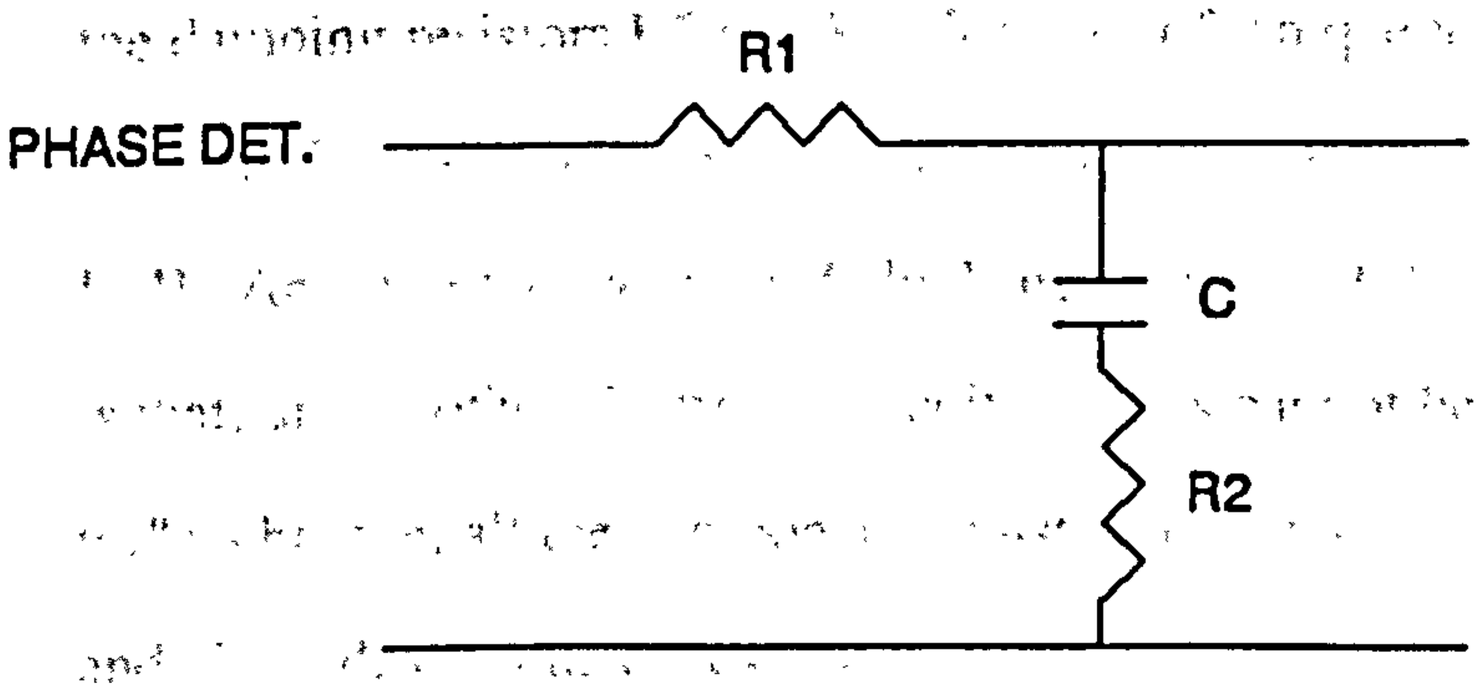

(b) LEAD-LAG LOW PASS FILTER

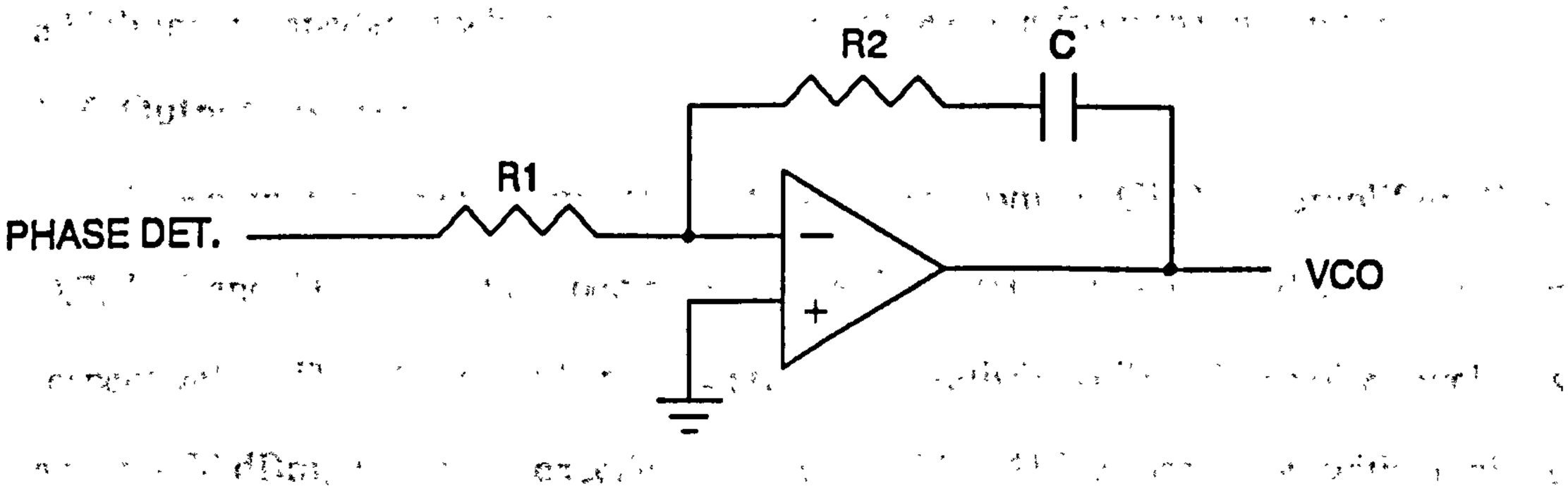

(c) ACTIVE LEAD-LAG LOW PASS FILTER

Fig. D.6 Loop filters.

The overall low pass filtering is controlled by C5 × (R1 + R2) and C6 × (R2 + R4) [ref. D.5]. The values shown in Fig. D.5 were to provide a low pass cut-off frequency of 6.6 Hz. This frequency allows the phase lock to react to small disturbances in the VCO or reference. Any changes in the reference should be small as it is derived from an ovenised crystal.

The damping factor was chosen to be quite a high value of 1.1. Such a high value will heavily damp the phase locked loop reducing the rate of change of the VCO to a phase error, which is ideal for this application. A large damping factor has the disadvantage of the VCO taking a long time to phase lock at switch on or as the result of a large disturbance. The integrator can become saturated due to long phase error pulses reducing the gain of the integrator and possibly causing ringing in the phase lock loop. These conditions can be inhibited by adding capacitors C7 and C8 in parallel to the damping resistors R5 and R6. The cut-off frequency for this RC combination was set at 40 Hz. Too low a value would also cause ringing of the phase locked loop [ref. D.4]. An important point made by Harowitz and Hill [ref. D.2] on phase locked loops is that, unlike other electronic circuits, PLL's cannot be made to operate by a "cut and try" technique, all the components must be calculated from measurements of the VCO and phase discriminator responses.

The integrator uses an LF356 operational amplifier operating from a - 15 volt supply. The LF356 has low voltage offsets keeping any phase offsets to a minimum and a high input impedance which minimises current leakage from the integrator.

D.5 Output Spectra

The output spectra were measured at the output from the GPD 402 amplifier. Figs. D.7, D.8 and D.9 show the spectrum with a 200 MHz, 20 MHz and 200 kHz span respectively. The offset oscillator operated very satisfactorily. The noise level was about - 70 dBm, which is excellent for a 106.250841 Hz oscillator with a phase comparison frequency of 841 Hz.

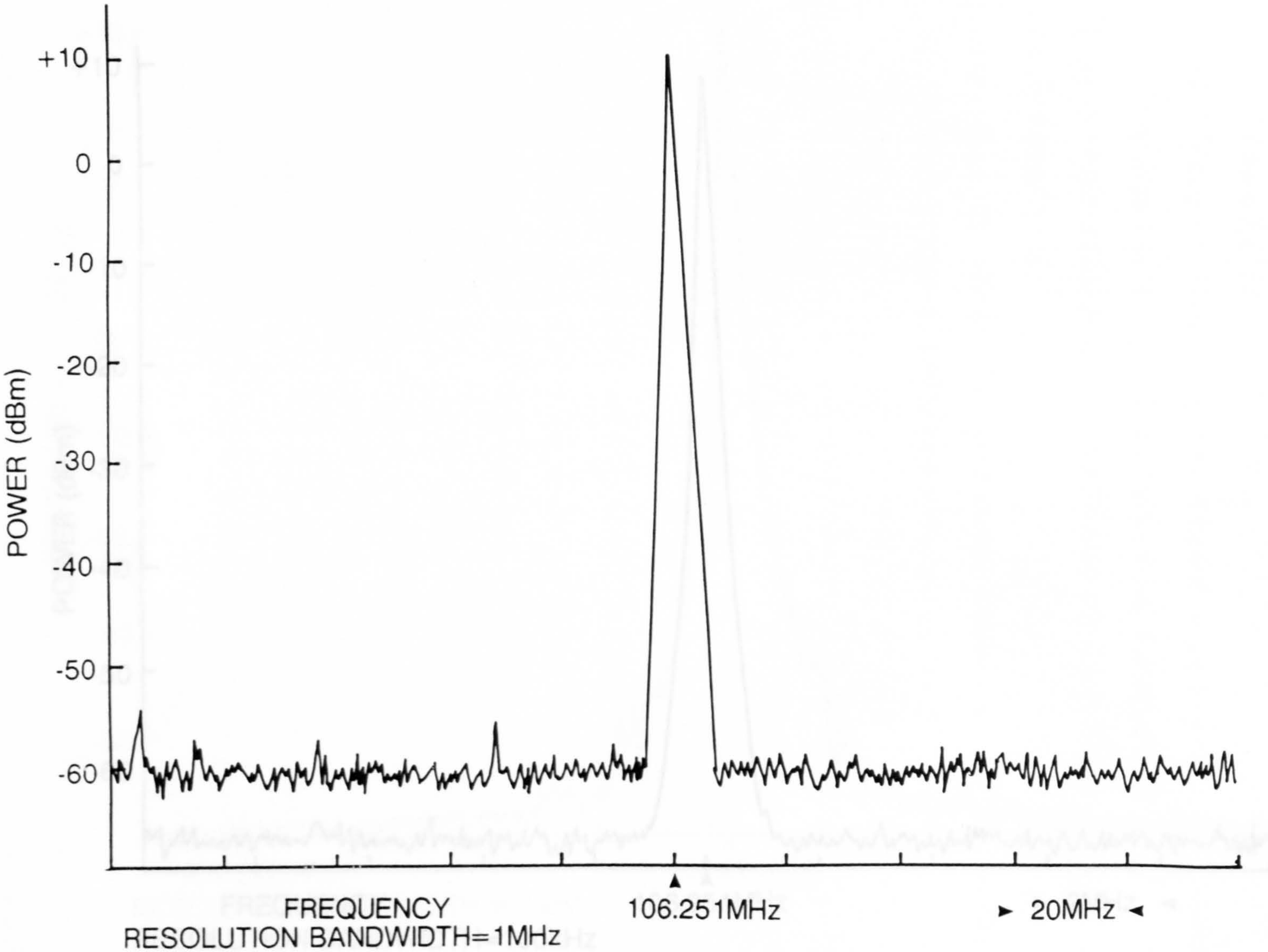

Fig. D.7 Offset oscillator output spectrum - 200 MHz span.

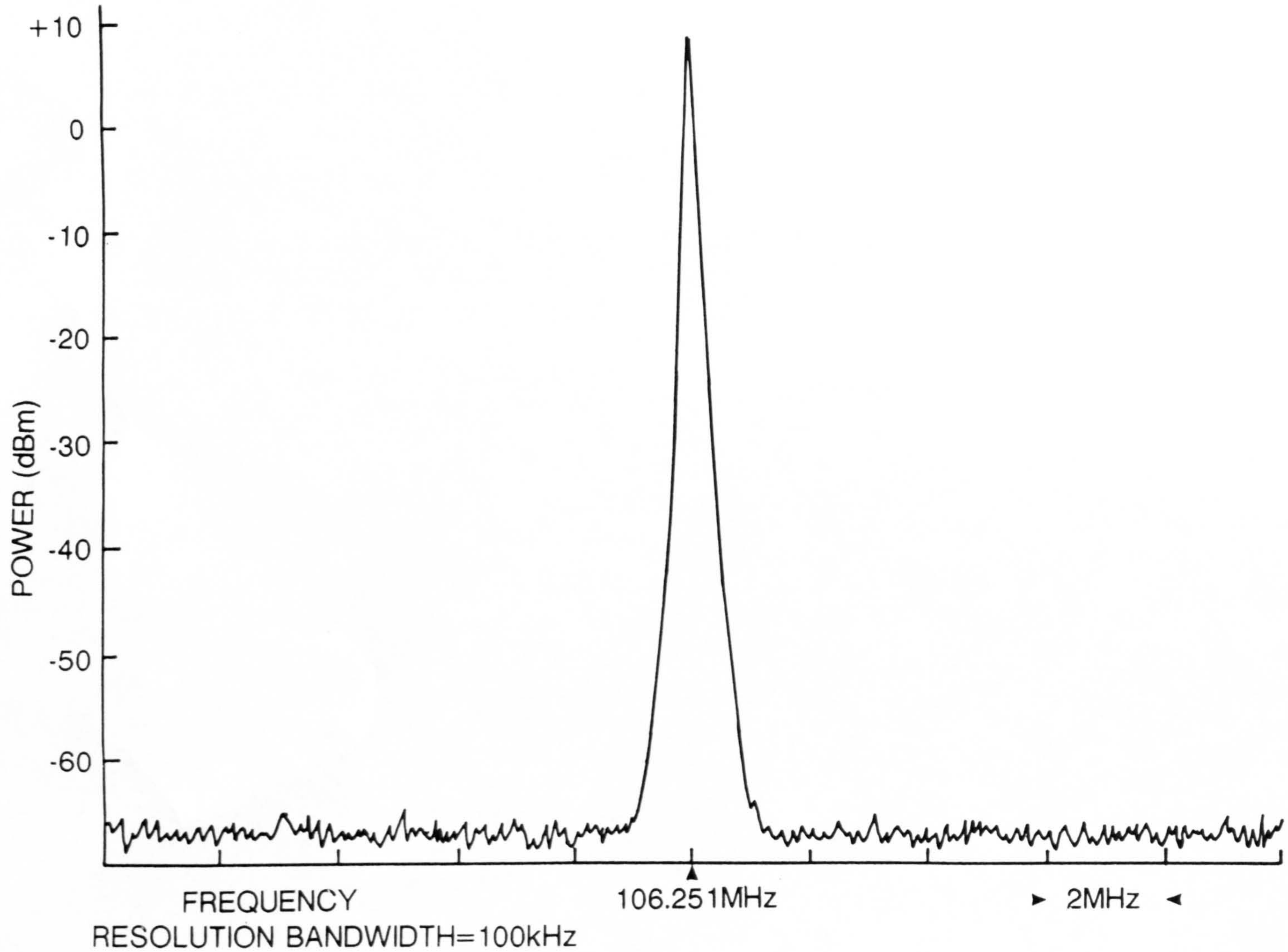

Fig. D.8 Offset oscillator output spectrum - 20 MHz span.

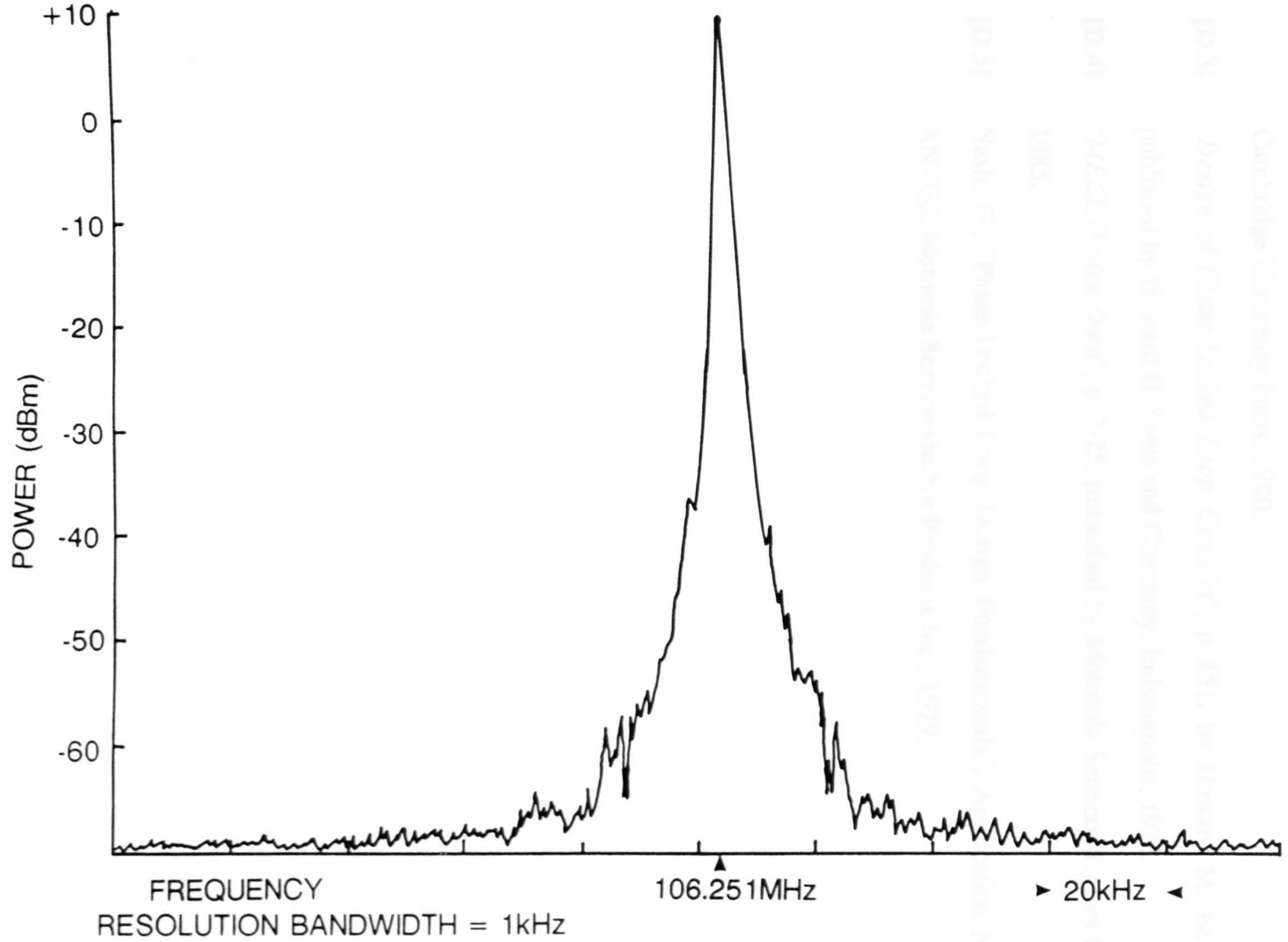

Fig. D.9 Offset oscillator output spectrum - 200 kHz span.

References

[D.1] "*MECL System Design Handbook*", Third Edition, p. 216, published by Motorola Semiconductor Products Inc., 1980.

[D.2] "*The Art of Electronics*", p. 429, by P. Horowitz and W. Hill, published by Cambridge University Press, 1980.

[D.3] "*Design of Phase-Locked Loop Circuits*", p. 151, by Howard M. Berlin, published by Howard H. Sams and Company, Indianapolis, 1978.

[D.4] "*MECL Device Data*", p. 7-25, published by Motorola Semiconductors Inc., 1985.

[D.5] Nash, G., "Phase-Locked Loop Design Fundamentals", Application Note AN-535, Motorola Semiconductor Products Inc., 1979.

APPENDIX E

SIGNAL AND LO CIRCUITS IN FINAL DOWNCONVERTION STAGE

The circuits described here are the signal amplifier and filter for the RF signal to mixer M5 (Section 4.5). The notch filter on the mixer output and the LO amplification and filtering circuits are also described.

E.1 Signal Amplifier, Filter and Mixer M5

The RF amplifier and filter circuit is shown in Fig. E.1. The amplifier has a differential input to reduce any common mode noise on the coaxial line carrying the signal. The 51 Ω resistance (R1) provides the correct terminating impedance for the coaxial line, R2 provides a reference to keep the input voltages within the operating range of the amplifier. The input and output is ac coupled to prevent any dc signals flowing from one part of the system to another. R3 is a 33 Ω resistor to increase the output impedance of the amplifier to 100 Ω to match the filter input impedances.

The filter is a 3 pole Butterworth LC bandpass filter [ref. E.1]. The transformation from low pass to bandpass gives the equation to calculate the filter components as

$$\omega_0 C = \frac{1}{\omega_0 L} = \frac{g\omega_0}{\omega_1 - \omega_2} \cdot \frac{1}{Z_0}$$

where ω_0 is the centre frequency, ω_1 and ω_2 are the 3 dB points, C is the capacitance, L the inductance, Z_0 the terminating impedance (100 Ω) and g is the element value for a doubly terminated Butterworth filter.

$$g_1 = g_3 = 1.0 \qquad g_2 = 2.0$$

The values on the circuit diagram provided a filter with centre frequency at 444 kHz and a bandwidth of 80 kHz. This is sufficient bandwidth to pass the carrier with modulation

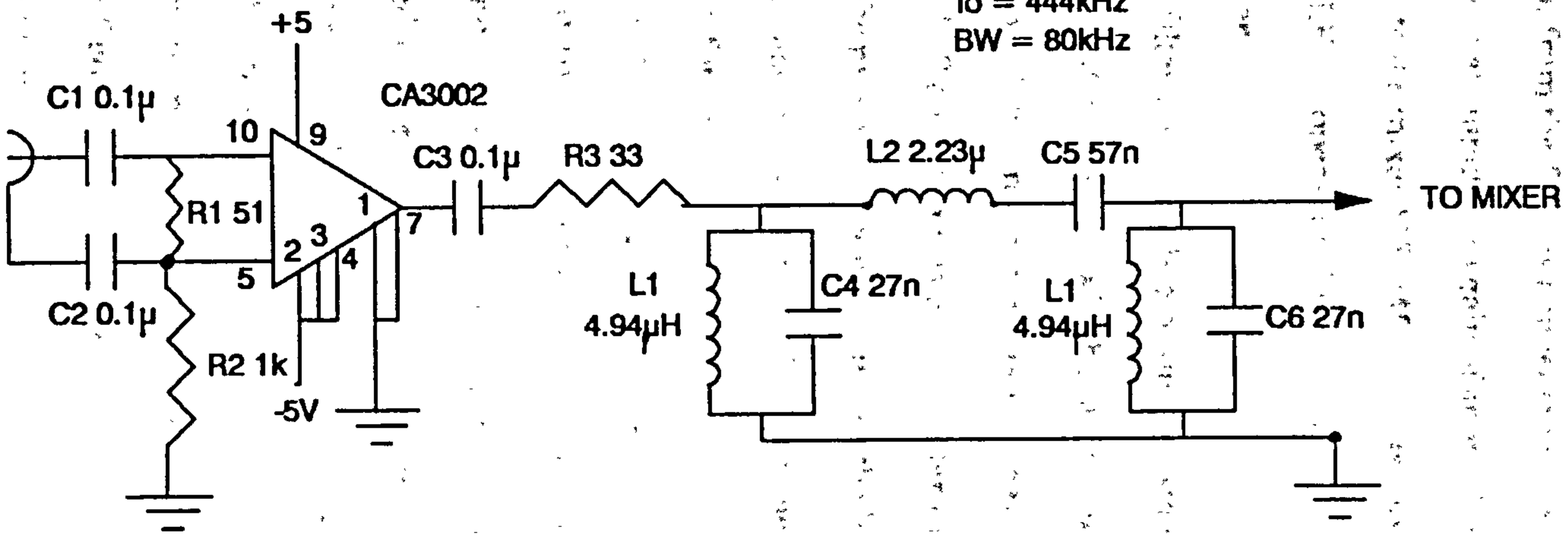

Fig. E.1 I.F. bandpass filter.

sidebands for the two operating frequencies of the RF signals. The amplifier gives a gain of 5 and isolates the mixer M3 from reflected signals from the filter. The filter rejects the higher frequency mixing products and any low frequency noise.

The output from the filter is connected to an amplifier (NE592) with a differential input and differential output and a gain of approximately 100. The output of the amplifier couples directly to the mixer M5 (MC1596) as shown in Fig. E.2. The mixer output was buffered by an LF356 operational amplifier.

E.2 Notch Filter

The notch filter was initially a bi-quad or state variable circuit but was replaced by a National Semiconductor MF10 which is a dual switched capacitor filter with the centre frequency controlled by a reference clock signal. The 841 Hz carrier was used as the clock and the MF10 configures as a notch filter to form a notch which exactly follows any changes in the reference frequency unlike the bi-quad circuit which relied on a stable carrier frequency and temperature stable components.

The circuit for the switched capacitor notch filter is shown in Fig. E.3. The configuration used is as described in the National Semiconductor literature [ref. E.2] as mode 3a. The MF10 is a dual filter IC but only one half is required to form a notch with an external operational amplifier. The operational amplifier from the other half of the filter IC was used as the external op amp. So the whole notch filter is constructed around one integrated circuit. The MF10 requires a clock frequency at 100 times the notch frequency which is provided by the CD4046 and the CD4518. The CD4046 is a phase lock loop integrated circuit with a voltage controlled oscillator (VCO) incorporated. The offset reference frequency (carrier frequency) is connected to one input of the phase comparator, the other input comes from the output of the VCO divided by 100 by the dual divide by ten integrated circuit CD4518. The loop is controlled by resistors R5, R6 and capacitor C1. The resistors on the input of the CD4046 change the reference voltage waveform to the required voltage levels to operate the phase comparator.

The notch frequency (f_n) is not solely controlled by the clock frequency (f_{clk}) but also by the resistor R_h and R_l by the equation

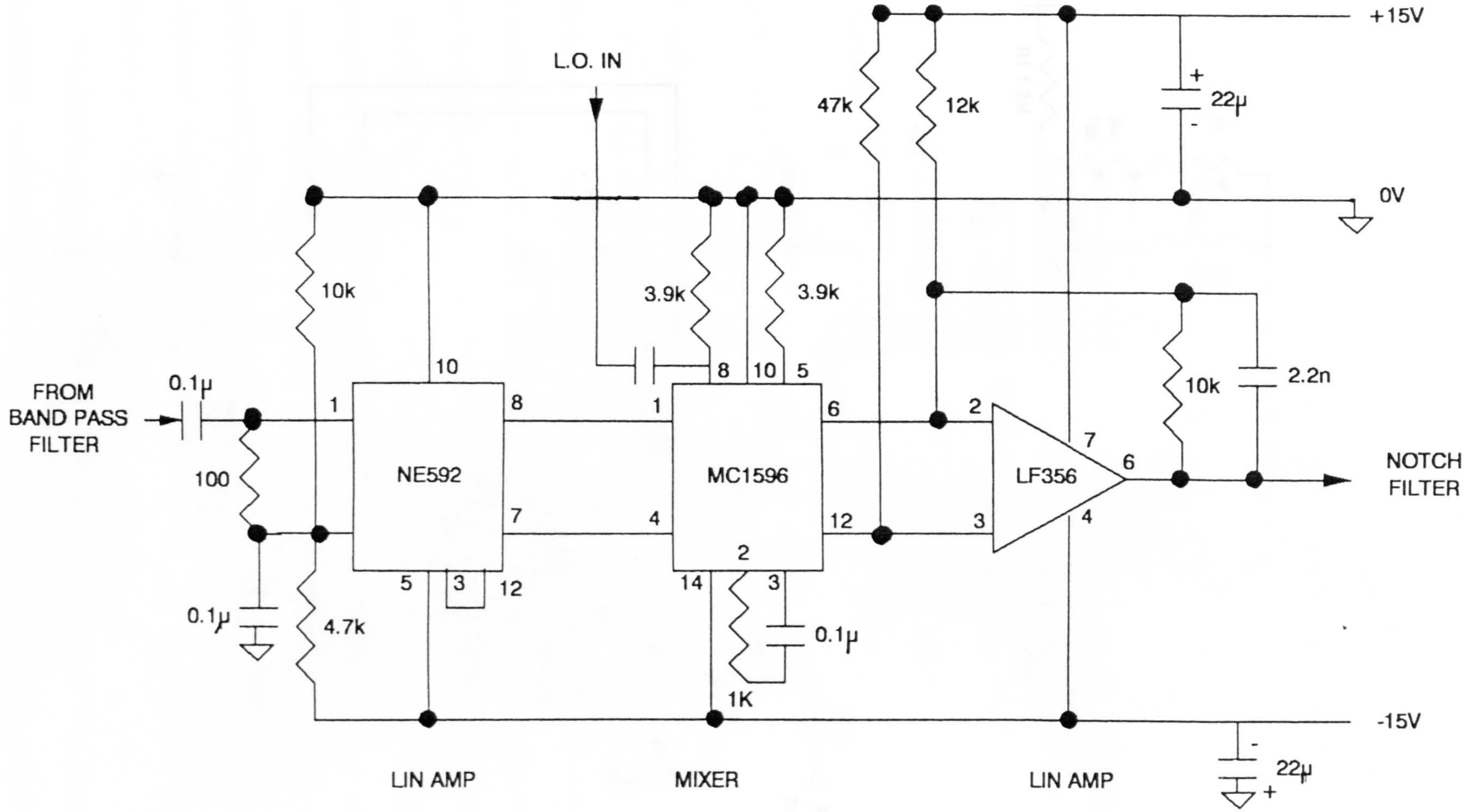

Fig. E.2 Mixer M5 circuit diagram.

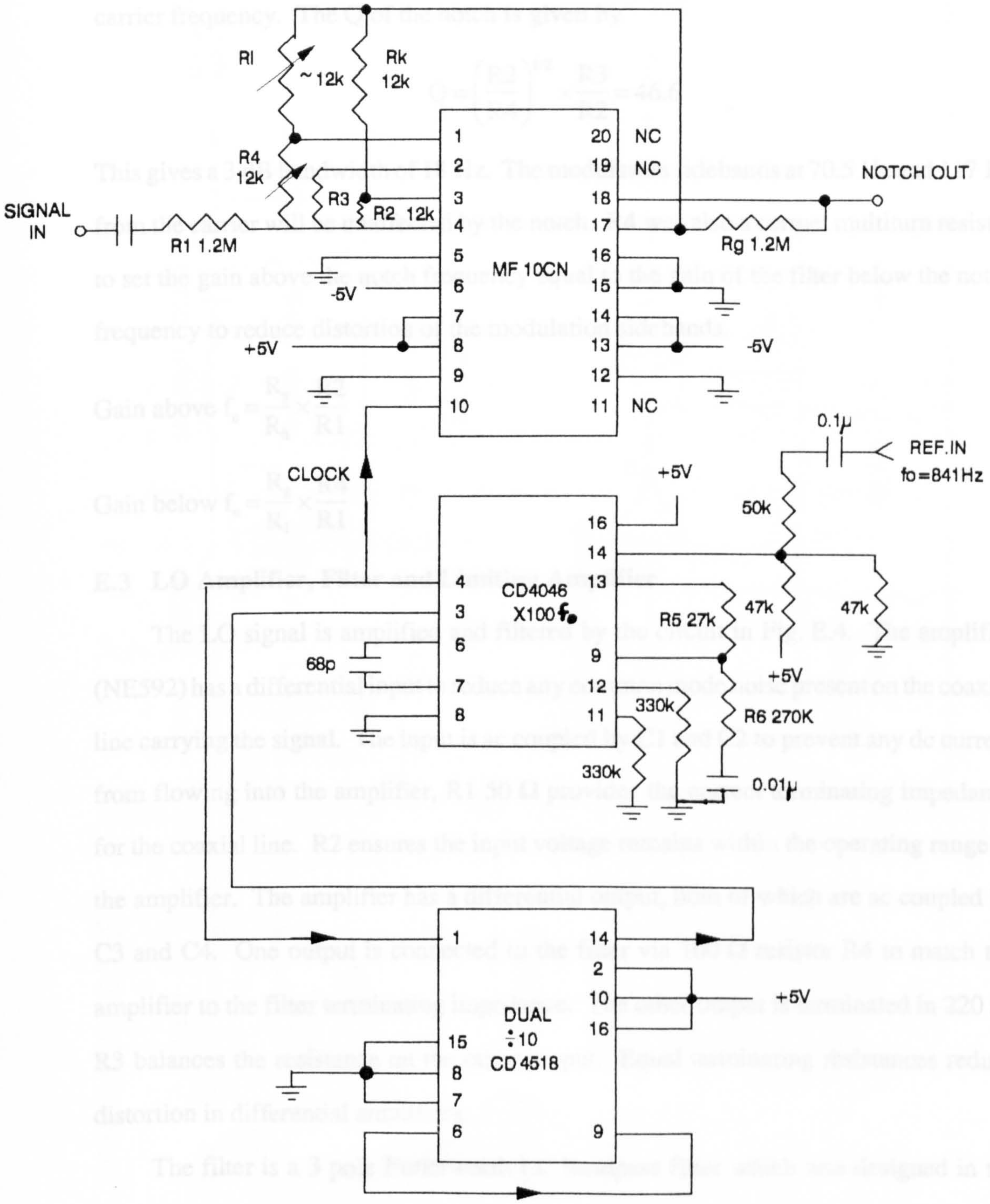

Fig. E.3 Switched capacitor notch filter circuit.

$$f_n = \frac{f_{clk}}{100} \cdot \left(\frac{R_h}{R_l}\right)^{1/2}$$

R_l was a cermet multiturn resistor to set the notch frequency at exactly the carrier frequency. Once the resistors have been set then the notch frequency will follow the carrier frequency. The Q of the notch is given by

$$Q = \left(\frac{R2}{R4}\right)^{1/2} \times \frac{R3}{R2} = 46.6$$

This gives a 3 dB bandwidth of 18 Hz. The modulation sidebands at 70.5 Hz and 117 Hz from the carrier will be unaffected by the notch. R4 was also a cermet multiturn resistor to set the gain above the notch frequency equal to the gain of the filter below the notch frequency to reduce distortion of the modulation sidebands.

$$\text{Gain above } f_n = \frac{R_g}{R_h} \times \frac{R2}{R1}$$

$$\text{Gain below } f_n = \frac{R_g}{R_l} \times \frac{R4}{R1}$$

E.3 LO Amplifier, Filter and Limiting Amplifier

The LO signal is amplified and filtered by the circuit in Fig. E.4. The amplifier (NE592) has a differential input to reduce any common mode noise present on the coaxial line carrying the signal. The input is ac coupled by C1 and C2 to prevent any dc current from flowing into the amplifier, R1 50 Ω provides the correct terminating impedance for the coaxial line. R2 ensures the input voltage remains within the operating range of the amplifier. The amplifier has a differential output, both of which are ac coupled by C3 and C4. One output is connected to the filter via 100 Ω resistor R4 to match the amplifier to the filter terminating impedance. The other output is terminated in 220 Ω, R3 balances the resistance on the other output. Equal terminating resistances reduce distortion in differential amplifiers.

The filter is a 3 pole Butterworth LC bandpass filter which was designed in the same manner as described above. The centre frequency is the same but the inductances

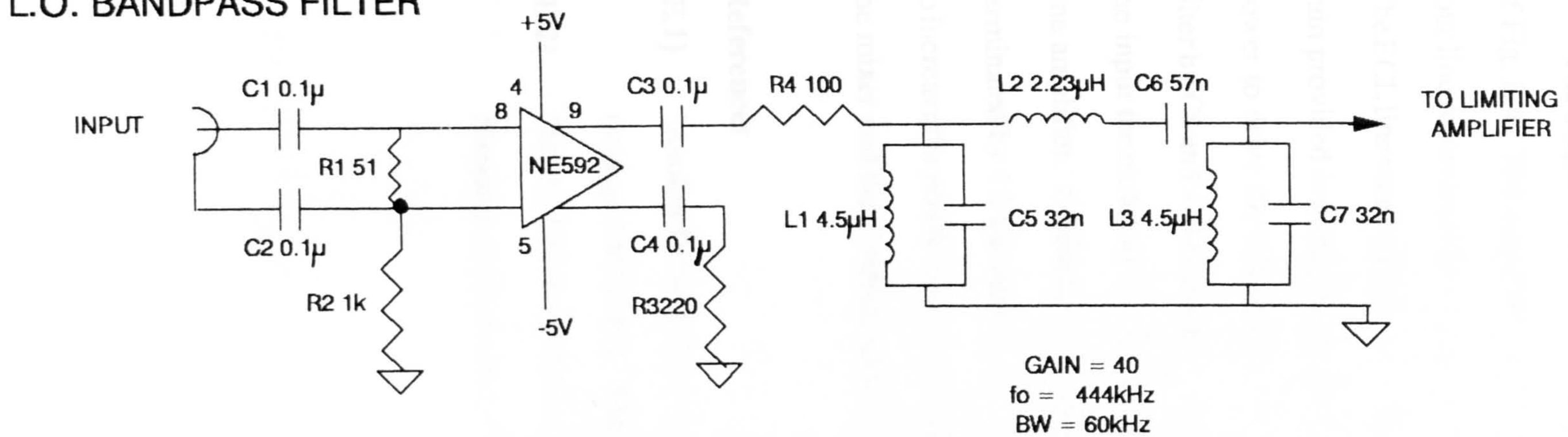

Fig. E.4 L.O. bandpass filter and limiting amplifier circuits.

and capacitances are slightly different due to the difficulty in winding ferrite inductors to a prescribed value. The overall performance of the amplifier and filter is a gain of 40, a centre frequency of 444 kHz and bandwidth 60 kHz.

The output of the filter is connected to a limiting amplifier shown in the lower half of Fig. E.4. The amplifier is based on a quad ECL line receiver, type MC10115. The four line receivers are connected in series to produce a maximum available gain of 625. The ECL line receivers will saturate and limit the output to a 1 Volt swing. The maximum gain provided is substantially greater than the gain required to produce a steady output power to drive the mixer M5. The input of the limiting amplifier is ac coupled to the filter by C8 and a terminating impedance for the filter of 100 Ω (R5) is connected across the input terminals of the first line receiver. R6 provides some hysteresis for the first line amplifier. Capacitor C9 decouples the input to ground. All the line receivers are terminated by 1.2 kΩ resistor except the last amplifier which has a 510 Ω resistor (R11) to increase the power output to the mixer. Resistor R12 provides some isolation between the mixer and the limiting amplifier.

References

[E.1] "*Analog Filter Design*", p. 411, by M.E. Von Valkenburg, published by CBS College Publishing, 1982.

[E.2] "MF10 Universal Monolithic Dual Switched Capacitor Filter", published by National Semiconductor Corp., 1981.

APPENDIX F

DIGITAL DEMODULATOR: FILTERS, HARDARE AND SOFTWARE

Details of the digital demodulator hardware, software and digital filters are discussed in the following sections.

F.1 Digital Filter

Digital filtering is based on arithmetic processes on discrete samples at fixed intervals in time. The digital filter in this case was derived from the analogue version of the Butterworth low pass filter. In analogue systems the Laplace transform can be used to describe the frequency domain transfer function where s is the Laplace variable. The transform into the s-plane is achieved by letting $s = j\omega$. The z-transform is useful in describing the filter response in a digital system, where $s = \exp(j\omega T)$, ω is the angular frequency and T is the sample period. The imaginary axis in the s-plane corresponds to the unit circle in the z-plane. The poles and zeroes in the z-plane must be obtained to determine the filter response.

Following Lynn and Fuerst [ref. F.1] the magnitude of the analogue Butterworth filter is given by

$$|H(\omega)| = \frac{1}{\left\{1 + \left(\frac{\omega}{\omega_c}\right)^{2n}\right\}^{1/2}} \qquad (F.1)$$

where n is the filter order and ω_c is the cut-off frequency. To transform this equation to a useful digital form the bilinear transform below is used

$$F(z) = \frac{z-1}{z+1} \qquad (F.2)$$

The transform is bilinear as the numerator and denominator are both linear in z. Other linear transforms are possible, but this version leads to realisable digital filters. By replacing z by exp(jΩ) in eqn. (F.2) we obtain

$$F(\Omega)=\frac{\exp(j\Omega)-1}{\exp(j\Omega)+1}$$

where $\Omega = \omega T$. Rearranging

$$F(\Omega)=\frac{\exp(j\Omega/2)\,[\exp(j\Omega/2)-\exp(-j\Omega/2)]}{\exp(j\Omega/2)\,[\exp(j\Omega/2)+\exp(-j\Omega/2)]}$$

$$=\frac{2j\sin(\Omega/2)}{2\cos(\Omega/2)}=j\tan(\Omega/2)$$

$F(\Omega)$ is purely imaginary, and periodic. If $F(\Omega) = j\tan(\Omega/2)$ is substituted for $j\omega$ in eqn. (F.1) we obtain

$$|H(\Omega)|=\left\{1+\left[\frac{\tan(\Omega/2)}{\tan(\Omega_c/2)}\right]^{2n}\right\}^{-1/2}$$

where Ω and Ω_c are again in terms of the sampling period. This expression has exactly the same values as Ω varies from 0 to π as in the original expression where ω varies from 0 to ∞. The scale has been compressed. As shown by [ref. F.2], the bilinear transformation is valuable in deriving digital Butterworth filters as the amplitude properties of the filter are preserved, there is no aliasing of the analogue frequency response and the method yields a recursive filter which is computationally efficient.

A second order Butterworth low pass digital filter has two poles and a second order real zero at z = -1. The positions of the poles in the z-plane are given by R_m and jI_m, [ref. F.1], where

$$R_m=(1-\tan^2(\Omega_c/2))/d$$

$$I_m=2\tan(\Omega_c/2)\sin(m\pi/n)/d \qquad m=0,1,2,..2n-1$$

$$d=1-2\tan(\Omega_c/2)\cos(m\pi/n)+\tan^2(\Omega_c/2) \qquad \text{(F.3)}$$

if n is even, then $m\pi/n$ is replaced by $(2m+1)\pi/2n$.

The transform can now be written in terms of zeroes and poles as

$$H(z) = \frac{(z+1)(z+1)}{(z-(R_m+j\,I_m))(z-(R_m-j\,I_m))}$$

$$= \frac{z^2+2z+1}{z^2-2R_m z+(R_m^2+I_m^2)}$$

Multiplying top and bottom by z^{-2}

$$H(z) = \frac{1+2z^{-1}+z^{-2}}{1-2R_m z^{-1}+(R_m^2+I_m^2)\,z^{-2}} = \frac{Y(z)}{X(z)}$$

In the digital filter, z^{-1} is equivalent to a time delay of one sample

$$\therefore\ y(n) = x(n) + 2x(n-1) + x(n-2) + 2R_m\,y(n-1) - (R_m^2 + I_m^2)\,y(n-2)$$

$$= a_o\,x(n) + a_1\,x(n-1) + a_2\,x(n-2) + b_1\,y(n-1) + b_2\,y(n-2)$$

where y(n) is the filter output and x(n) is the filter input.

The realisation diagram is shown in Fig. F.1, where

$a_0 = 1$

$a_1 = 2$

$a_2 = 1$

$b_1 = 2\,R_m$

$b_2 = -\,(R_m^2 + Im^2)$

b_1 and b_2 can be found by choosing the cut-off and sampling frequencies and evaluating eqns (F.3). The cut-off frequency was 13 Hz and the sampling frequency was 841 Hz. This gave

$b_1 = 1.98895$

$b_2 = -0.98901$

In digital filters it can be difficult to use precise coefficients when the number of bits is small. In this case an arithmetic multiplier with a large number of bits, allowed precise coefficients to be used. The analogue coefficients were multiplied by 2^{14} for the computation.

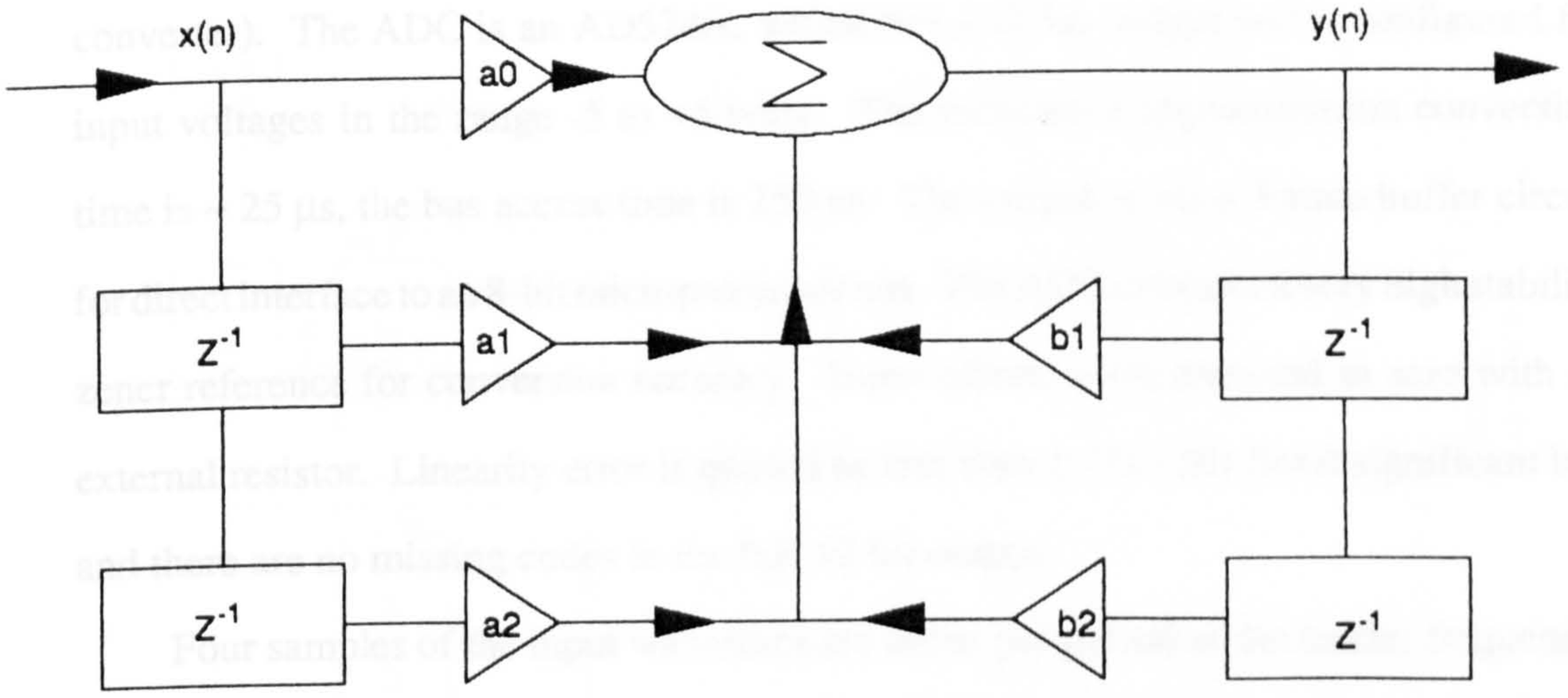

Fig. F.1 Recursive digital filter.

F.2 Hardware

A schematic of the digital modulator is shown in Fig. F.2, excluding the computer which controls the unit. The signal from the downconvertion stages is fed through a buffer amplifier and a low pass fifth order active Butterworth filter [ref. F.3]. The filter is required to remove any higher order harmonics of the carrier produced by the previous downconvertion stage (and is known as an anti-aliasing filter). The circuit diagram is shown in Fig. F.3. The op-amps are TL074s, the resistor and capacitor values are all derived from standard tables as per [ref. 5.3] above. The cut-off frequency is 1310 Hz, this gives approximately 11 dB attenuation at the second harmonic of the carrier frequency and 28 dB attenuation at the third harmonic. The signal is then sampled and held during the analogue to digital conversion process in the ADC (analogue to digital converter). The ADC is an AD574A, which has a 12 bit output and is configured for input voltages in the range -5 to +5 volts. The successive approximation conversion time is ~ 25 μs, the bus access time is 250 ns. The output is via a 3-state buffer circuit for direct interface to an 8-bit microprocessor bus. The ADC contains a very high stability zener reference for conversion accuracy. Input offsets were trimmed to zero with an external resistor. Linearity error is quoted as less than ± 1/2 LSB (least significant bit) and there are no missing codes in the full 12 bit output.

Four samples of the input waveform are taken per period of the carrier frequency. The timing of the start of a conversion is controlled by a signal from the synchroniser circuit (marked as 'SYNCH' on Fig. F.2). The SYNCH has two inputs. One is derived from a reference from the offset generator of the final carrier frequency and provides the timing reference to demodulate the signal. The other input to the SYNCH is from a counter that tells the processor at what part of the modulation cycle the sample has been taken. The synchronisation is required so that the counter output will be latched during conversion periods. The SYNCH output causes the sample and hold (S/H) to hold the signal and the analogue to digital converter to start. The phase of the sample with respect to each of the modulation cycles is derived from counters driven by phase locked oscillators operating at 1024 times the modulation frequency. The outputs of

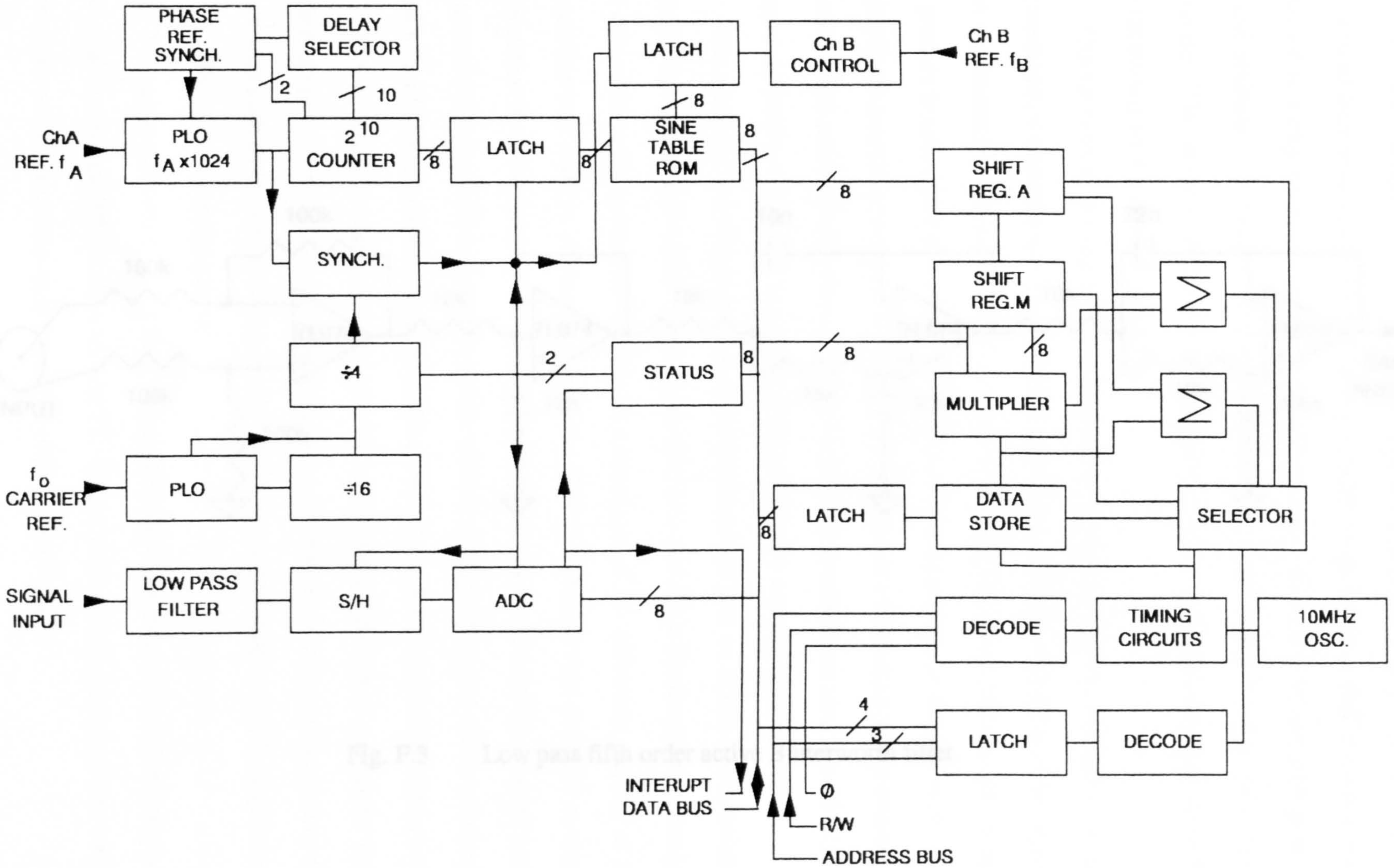

Fig. F.2 Digital demodulator schematic.

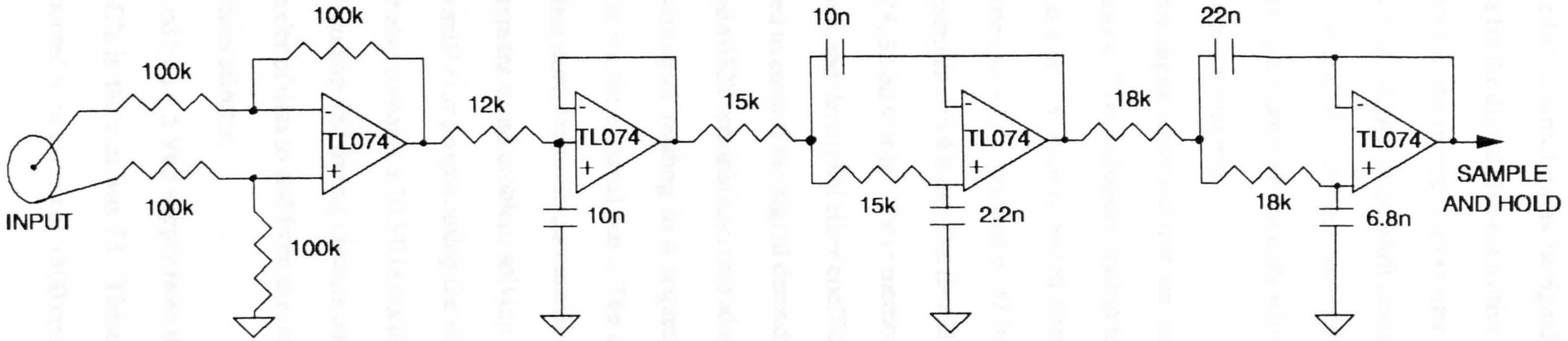

Fig. F.3 Low pass fifth order active Butterworth filter.

these counters are latched at the same time as the signal is sampled. The phase information for each of the channels for the digital phase sensitive detector is read from the sine table ROM (read only memory) for the appropriate counter value. The modulation was phased to the reference by means of a digital phase shift circuit in the feedback loop of the phase locked oscillator. At the end of each conversion the ADC sends an interrupt to the computer. The computer program then controls which arithmetic functions are carried out depending on the status at that time.

Calculations in the digital demodulator are carried out by the multiplier, shift registers and accumulators. The multiplier multiplies a 32 bit word by a 16 bit word with the convention that a binary point is placed after 12 bits of the 16 bit word. A 46 bit product is accumulated which is rounded to 32 bits on storage in the data store. A multiplication can be completed in 4.8 μs. The data store is a 4k random access memory (RAM) which holds 128, 32 bit words. These memory locations are used to hold ADC outputs, sine table values and the digital filter coefficients and the running totals.

The computer used to control the digital demodulator was an Acorn Atom, which has a 6502 processor and a 6522 versatile interface adaptor (VIA). The computer controls the demodulator by writing or reading to a sequence of 16 addresses, starting at a presettable base address via the external bus . The demodulator was designed so that information from the data store, multiplier, accumulators, sine table ROM and ADC can be accessed by the computer to aid problem solving during debugging and to allow as great a flexibility as possible for programming the unit to perform other functions.

The demodulator also contains a 10 MHz oscillator which acts as a clock for the timing circuits. The decoding and timing circuits control the latches and the timing of operations such as transfer of data to and from the multiplier, data store, accumulators, along with the data stream selector.

The unit is powered by a + 5 Volt supply from the computers mains power supply. The total number of IC's in the unit was 75. These were connected using wire wrap techniques which amounted to in excess of 1500 connections.

F.3 Software

The computer program to control the digital demodulator and calculate the relative amplitudes of the atmospheric and reference signals is attached at the end of the Appendix. A section of the program is written in assembly language to make the control and computation as fast as possible to allow a second order recurrence digital filter to be used. Annotation of the programme was removed to improve the computation speed. The program description is as follows:

line 100	setting up arrays
line 110-350	assembly language, which controls the digital demodulator, interrupt service routines, sampling, digital filters, PSD and loads data on to bus to be passed to the computer
lines 360-390	sets up interrupt service routing, presetting of VIA registers and loading digital filter coefficients into the demodulator RAM
lines 400-450	Basic program to control which program function is used
line 460	Alarm to keep operator awake
lines 555-630	Subroutine A. Interrupts enabled. Amplitude for channels A & B accumulated over 100 interrupts
lines 700-790	Data manipulation, commands to change frequency, calculation of relative attenuation between 58 GHz and 54 GHz frequencies

For each value input to subroutine A, there are 128, 4 element samples of the waveform fed to the PSD/digital filter accumulators, i.e. channel A and B, phase and quadrature, has each received 128 samples each time the information is passed to the computer. For each frequency the process was performed 8 times in each full measurement cycle. The final output being the relative attenuations for the two millimetre wave signals. The pattern of the measurements was to do 4 blocks of the 54 GHz signal, then 8 blocks of the 58 GHz signal and a further 4 blocks of the 54 GHz signal to minimise any effects due to drifts in the system or atmospheric condition. The atmospheric temperature,

pressure and humidity was recorded during the central portion of the 58 GHz signal measurement section. A measurement could be made every 8 minutes. The total integration time for each frequency was approximately 2 minutes.

References

[F.1] "*Digital Signal Processing*", p. 176, by P.A. Lynn and W. Fuerst, published by John Wiley and Sons, 1989.

[F.2] "*Digital Processing of Signals*", Second Edition, p. 179, by Maurice Bellanger, published by John Wiley and Sons, 1989.

[F.3] "*Analog Filter Design*", p. 178, by M.E. Van Valkenburg, published by CBS College Publishing, 1982.

DIGITAL DEMODULATOR COMPUTER PROGRAM

```
100DIM LL(7),W(24),P(-1);V=£4000
110[:LL0 CLI;RTS
120:LL1 LDA @£20;AND £B80D;BEQ LL7
122STA £B80B;LDA @£20;STA £B80D;PLA;CLI;RTI
124:LL7 LDA @£10;STA £B80E;CLI
125LDA W+2;AND @2;BNE LL2
130LDA @£7F;STA V+1;LDA W+2;AND @1;ORA @£88;STA V+1
140LDA W+2;AND @3;BNE LL3
150LDA V+8;AND @4;BEQ LL4
160DEC W+1;BNE LL3;LDA W;STA W+1
170LDA @1;STA W+7;TXA;PHA;LDX @0
180:LL5 TXA;LSR A;LSR A;STA V+1
185ORA @4;STA V+2
190LDA V+£D;LDA V+£D
200LDA V+£D;STA W+8,X;INX
210LDA V+£D;STA W+8,X;INX
220EOR @£80;ASL A;LDA @£FF;ADC @0
230STA W+8,X;INX;STA W+8,X;INX
240CPX @16;BNE LL5;PLA;TAX
250:LL3 INC W+2
260:LL4 SEI;LDA @£80;STA £B80E;LDA @£10;STA £B80D;PLA;CLI;RTI
270:LL7 TXA;PHA;LDA W+2;AND @5;TAX
280AND @1;ORA @8;STA V+1
290LDA @£FF;STA V+2;LDA @£BA;STA V+1
300:LL6 LDA V+£E;LDA @£7A;STA V;STX V+3
310LDA @£7B;STA V;TXA;EOR @4;STA V+3
320LSR A;AND @1;ORA @£7C;STA V;LDA @£A;STA V+3
330TXA;EOR @£84;STA V+1
340INX;INX;AND @2;BEQ LL6
350PLA;TAX;JMP LL3;]
360LINK £FFE3;P.';?£0204=LL1;?£0205=LL1/256
365?£B80C=£10;?£B80D=£7F
370W'0=128;W'4=0;W!8=32587;W!12=-16204
375I=?(V+£E);?(V+4)=W?8;?(V+4)=W?9;?V=£FA
380?(V+4)=W?12;?(V+4)=W?13;?V=£FB
385FORI=£80TO£87;?(V+1)=I;N.I
390LINK LL0
400 P.$12,''''WHICH PROGRAM FUNCTION?",'
410P."1  MEAS.",","2  MON.""3  END"'
420 INPUT F;IF F=1 T.6.700
421IF F=2 T.6.450
422IF F=3 T.E.
430G.400
450 GOS.a;;G.450
460bFOR R=1 TO 5;FOR S=40 TO 80 STEP 4;BEEP S.1;N.S;N.R;R.
555a?£B80B=£E0;?£B808=£C1;?£B809=£01
556WAIT;WAIT;WAIT;WAIT
557?£B804=£00;?£B805=£39
560?£B80E=£90
570A=0;B=0;W?3=0
580FOR I=1TO100
590IF W?7=0 T.G.590
600W?7=0;X=W'8;Y=W!12;A=A+X*X+Y*Y
610X=W!16;Y=W!20;B=B+X*X+Y*Y
620W?3=W?3;W?7;N.I
625WAIT;?£B80E=£7F;?£B80B=0
630@=1;P.W?3;@=10;P.A,B,A/(B/1000)';RETURN
700 P."54GHZ MEASUREMENTS"'"PRESS SPACE-BAR TO CONTINUE"
705ZI=0;ZY=0;ZR=0;ZS=0
710LI.£FFE3;P.';FOR J=1 TO 4;GOS.a;ZX=ZX+A/B;ZR=ZR+A;N.J;GOS.b
720P."CHANGE TO 58GHZ"'"PRESS SPACE-BAR TO CONTINUE"
730LI.£FFE3;P.';FOR J=1 TO 4;GOS.a;ZY=ZY+A/B;ZS=ZS+A;N.;GOS.b
740 P."CHANGE PHASE SHIFTER"'"PRESS SPACE-BAR TO CONTINUE"
750LI.£FFE3;P.';FOR J=1 TO 4;GOS.a;ZY=ZY+A/B;ZS=ZS+A;N.;GOS.b
760 P."CHANGE TO 54GHZ"'"PRESS SPACE-BAR TO CONTINUE";LI.£FFE3
770P.';FOR J=1 TO 4;GOS.a;ZX=ZX+A/B;ZR=ZR+A;N.;GOS.b
775FP.''ZR/8,"  "ZS/8,''
777FP.ZX/8,"  ",ZY/8
780 FP.'''"ATTEN.=",4.34265*(L.ZY-L.ZX),'''
790LI.£FFE3;G.400
```

APPENDIX G

TEMPERATURE SENSING UNIT

The temperature sensing device (LM134H) was a three terminal current source in which the current is directly proportional to the absolute temperature [ref. G.1]. The sensor has a true floating current source with no separate power supply connection. The LM134H can be operated from a two wire system and the current is not sensitive to changes in the series resistance, within a certain limit. The current is given by

$$I_{SET} = \frac{(227\,\mu V/^{\circ}K) \times T}{R_{SET}}$$

where I_{SET} is the current through the device, T is the temperature in degrees Kelvin and R_{SET} is a resistor which controls the current range.

The current can be sensed by measuring the voltage across a load resistor, i.e.

$$V_{OUT} = \frac{(227\mu V/^{\circ}K) \times T \times R_L}{R_{SET}} \qquad (G.1)$$

where V_{OUT} is the measured voltage and R_L is the load resistance. A useful feature of the LM134H is that because the output extrapolates to zero at 0°K, then gain adjustment is only required at one temperature. Two temperature points have been defined by zero Kelvin and the adjustment temperature, and all other points are linearly related. The gain can then be adjusted by either R_{SET} or R_L. In this case R_{SET} was fixed and R_L was an adjustable resistor. Fig. G.1 shows the overall temperature sensing circuit. The circuit is supplied with a + 12 V supply. R_L which is the preset resistor was made up from a 9.1 kΩ fixed and a variable 1 kΩ resistor in series. The current through R_L is controlled by the LM134H which is temperature dependent. The FET, 2N3822 provides local regulation. The voltage across the LM134H is between 1 and 2 volts which reduces the heating effect in the temperature sensor. The current through the LM134H was about 0.3 mA and is defined by R_{SET} which was a 221 Ω precision metal film resistor. R_{SET}

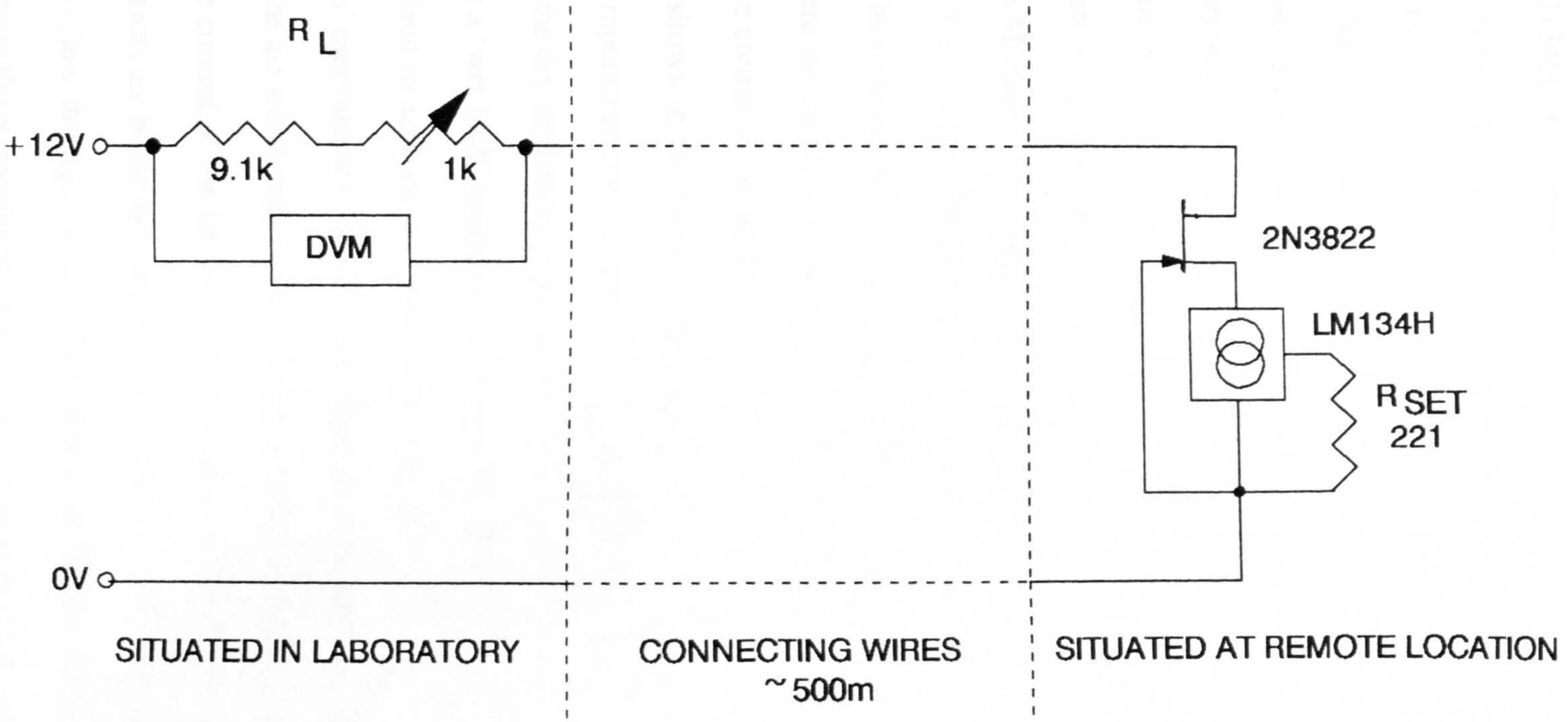

Fig. G.1 Temperature sensor.

and R_L were low temperature coefficient resistors (15 ppm/°C). As can be seen from eqn. (G.1), changes in both R_L and R_{SET} affect the measured output voltage. R_{SET} is the most important resistor in this respect as it will experience changes in temperature similar to the LM134H. The contribution of the resistor temperature coefficient to the measured temperature over the expected range of observed temperatures is less than 0.04 K, using the maximum possible value of the temperature coefficient. The resistors that make up R_L (~ 9.7 kΩ) are less important as they only experience the small temperature fluctuations of the laboratory. The mechanical stability of the adjustable resistor with time necessitates a high quality component, a multiturn cermet 1k Ω was used. Any changes in resistance of the wires connecting the sensor to the laboratory has no effect on the current except if there is an exceptionally large change. The stability and accuracy of the DVM (digital volt meter) is also important to the temperature measurements. A $4^{1/2}$-digit Sinclair DT450 was used. The temperature sensor was calibrated against a mercury bulb thermometer and compared at regular intervals for changes in calibration. There were no changes required in the calibration of any of the temperature sensors during the course of the project.

As shown in the circuit diagram, Fig. G.2, the remote thermometer unit consists of two temperature sensors and a fan. Two temperature sensors were incorporated to measure the dry air temperature and one sensor was fitted with a wick carrying distilled water for a 'wet bulb' temperature to measure the relative humidity of the air. The fan was required to aspirate the wet and dry sensors. The fan is not only necessary to the 'wet bulb' measurement but it is important that the air from outside the unit is measured and not the air which may have been warmed by the fan or electronics in the unit.

The control of the fan was via the supply to the temperature sensors. When any of the sensors are being measured the power FET (type VN46AF) is biased 'on' allowing current to flow through the fan. The power for the fan comes from the supply to the modulator on the retroreflector, for the unit situated on the reflector tower. A unit outside the laboratory had its own separate supply. The fan supplies were all regulated to 12 volts near the fan to maintain a steady air flow over the temperature sensors.

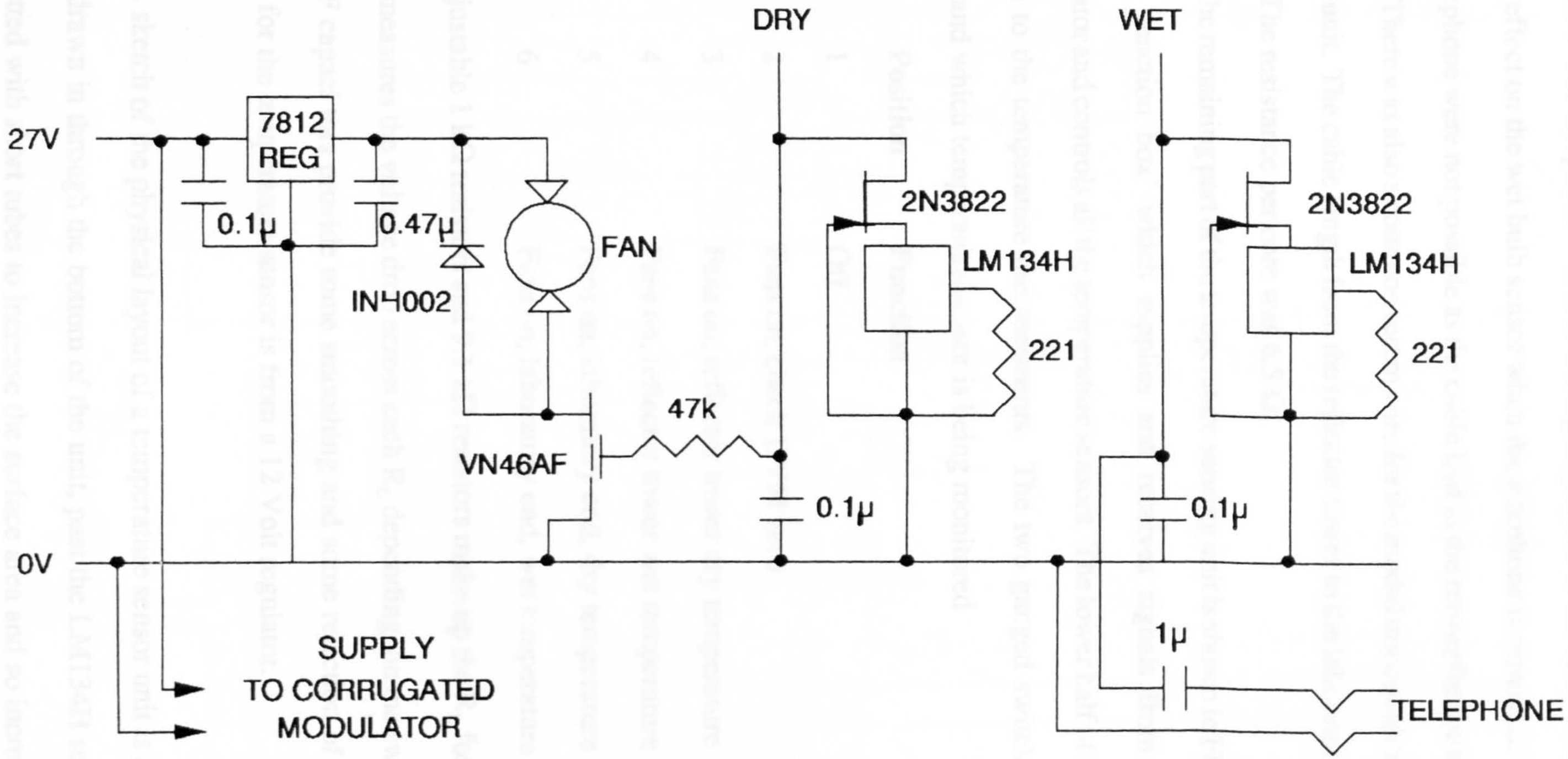

Fig. G.2 Remote temperature sensor circuit.

The temperature unit at the reflector was also fitted with a socket for a two-way telephone. The telephone was used during alignment of the retroreflector and the socket has no effect on the wet bulb sensor when the telephone is removed. Separate wires for the telephone were not possible as the cable laid to the retroreflector tower had only four cores. There was also a common return wire for the modulator circuit and the temperature sensor unit. The cable length from the reflector tower to the laboratory was about 500 m long. The resistance per core was 6.5 Ω.

The remaining part of the temperature sensing unit is shown in Fig. G.3. The circuit is the 'junction box' which supplies and receives signals from the retroreflector modulator and controls all the temperature sensors. The lower half of the circuit diagram applies to the temperature measurements. The two ganged switches control the fan on-off and which temperature sensor is being monitored

Position	Function
1	Off
2	Fans on, check DVM zero
3	Fans on, reflector tower dry temperature
4	Fans on, reflector tower wet temperature
5	Fans on, laboratory end, dry temperature
6	Fans on, laboratory end, wet temperature

The adjustable 1 kΩ resistors and 9.1 kΩ resistors make up the R_L for each sensor. The DVM measures the voltage drop across each R_L depending on the switch position. The 0.47 μF capaci tors provide some smoothing and some rejection of interference. The supply for the temperature sensor is from a 12 Volt regulator.

A sketch of the physical layout of a temperature sensor unit is shown in Fig. G.4. Air is drawn in through the bottom of the unit, past the LM134H sensors, which have been fitted with short tubes to increase the surface area and so increasing the coupling between the air and the sensor. The air then passes through the fan (Micronel Type

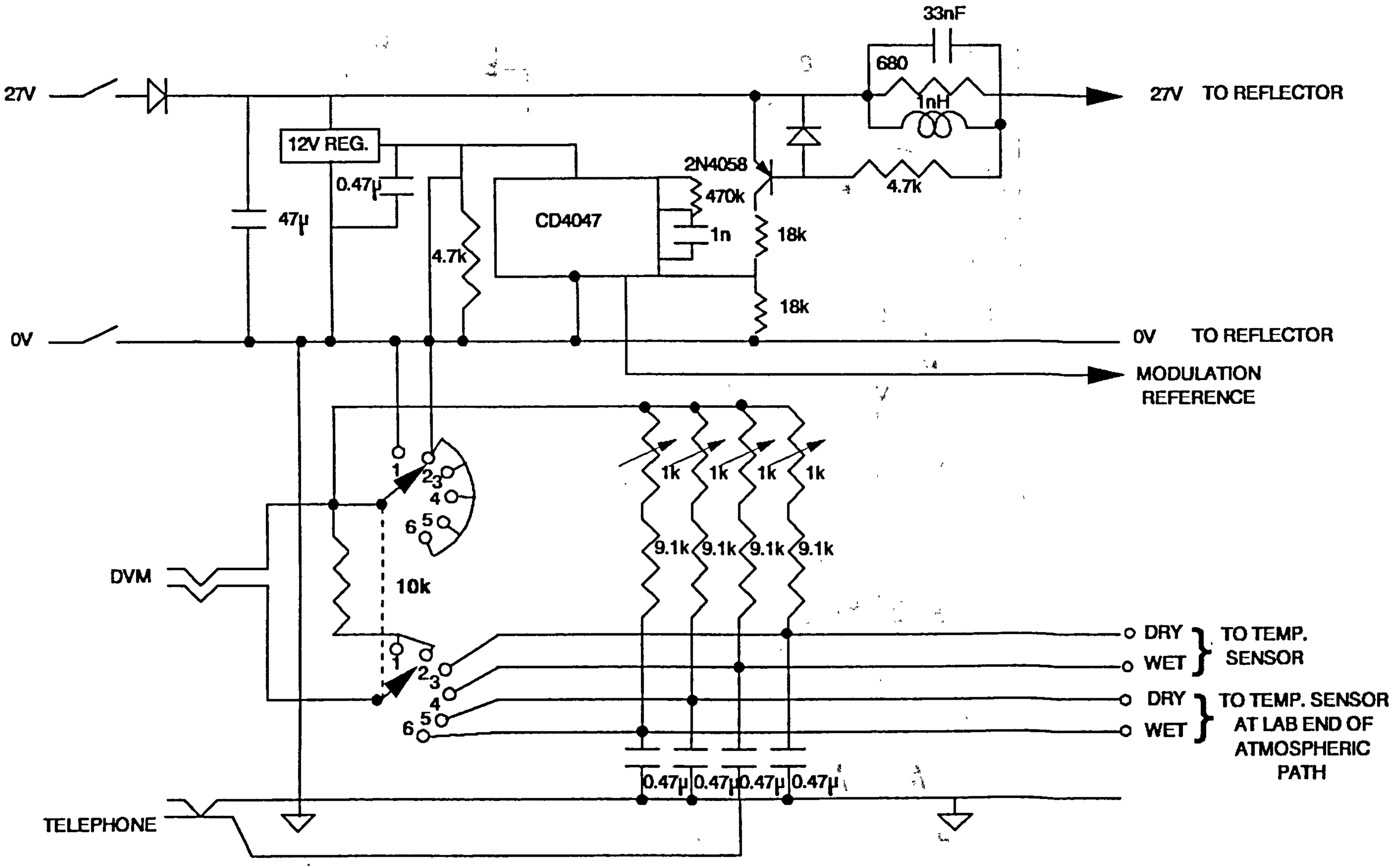

Fig. G.3 Junction box circuit.

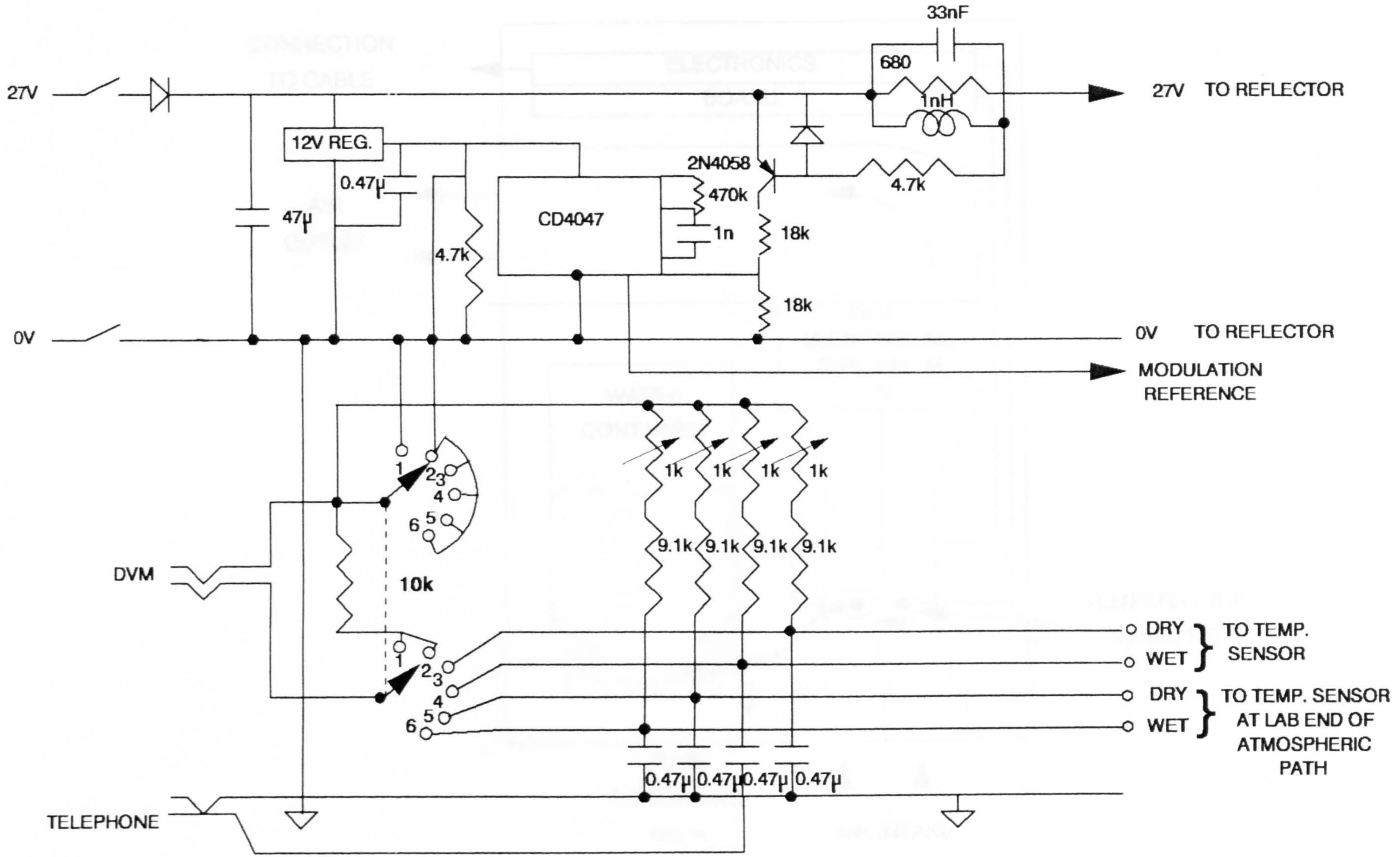

Fig. G.3 Junction box circuit.

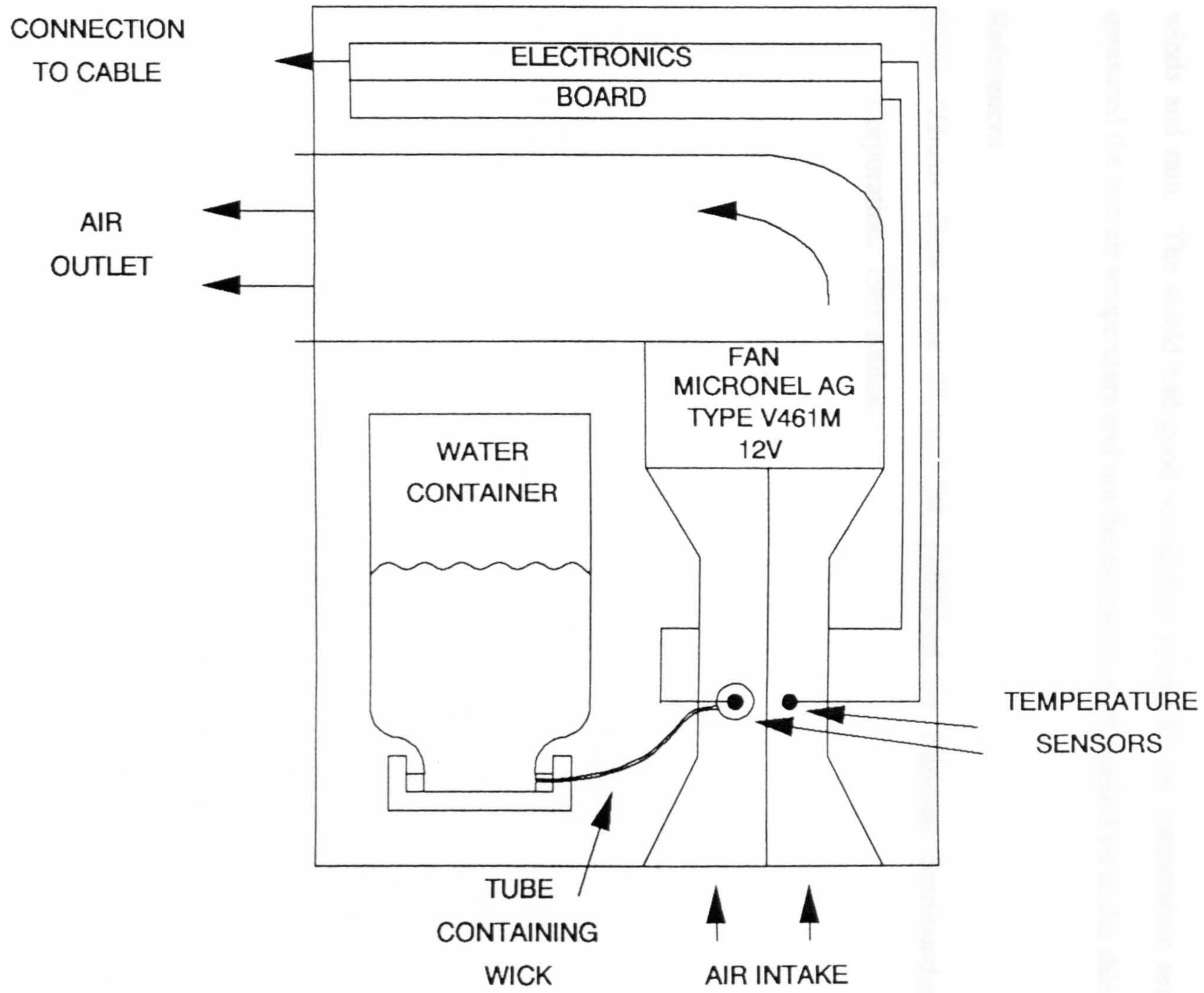

Fig. G.4 Remote temperature sensor unit schematic.

V461M) and is expelled through an aperture away from the inlet. A bottle containing distilled water was connected to one of the sensors via a small pipe and a cotton wick to provide a wet bulb temperature measurement. The unit is in a metal case with another white painted shield around the unit to protect the sensor assembly from sunlight, strong winds and rain. The shield had good ventilation to ensure the temperature sensor measured the true air temperature and not the temperature of trapped air in the shield.

References

[G.1] *"Linear Data Book 2"*, p. 7-20, published by National Semiconductor Corporation. 1988 edition.